UNIVERSITY OF ADELAIDE.

DEPARTMENT OF ELECTRICAL ENGINEERING.

SURFACE ACOUSTIC WAVE SCATTERING AT A PERIODICALLY

MASS-LOADED SURFACE.

by

Percy Victor Harvey SABINE, B.Sc., B.E. (Hons.)

A thesis submitted to the Faculty of Engineering of the University
of Adelaide for the degree of Doctor of Philosophy.

Adelaide.   October, 1972.

TABLE OF CONTENTS.

VI

VII

CHAPTER XI -

THE APPLICATION OF PERIODIC MASS
LOADING OF A SURFACE ACOUSTIC WAVE
PROPAGATION SURFACE TO MICROSONIC
COMPONENT DESIGN

LIST OF FIGURES.

SUMMARY

This thesis is primarily concerned with a theoretical and an experimental study of some important aspects of the behaviour of a surface acoustic wave incident upon a region of periodic mass-loading deposited upon the propagation surface. In particular attention is focussed upon that range of frequencies for which the wave vectors of the input signal and of the surface perturbation satisfy, or nearly satisfy, the first order Bragg relation; under these conditions a strong interaction occurs and a surface acoustic wave of large amplitude is coherently scattered from the mass-loaded region. But in exploring this topic, contributions to several other facets of surface acoustic wave technology are made.

Initial investigations of Rayleigh wave attenuation, due to scattering into volume modes, at a periodically roughened surface provide, for the first time, theoretical verification of previously published experimental measurements. The same study suggests a novel design for a surface acoustic wave directional coupler - the so-called "crossbar" coupler in which periodic mass-loading of the propagation surface supplies coupling between an input and an output wave. The fabrication and testing of a "crossbar" directional coupler forms a convenient focal point around which the wider aim of the research program, namely an examination of the periodic surface mass-loading interaction, can be pursued.

An analysis of surface acoustic wave motion on anisotropic and piezoelectric single crystal materials allows the development of two computer programs which prove of great value in assessing the utility

of a substrate for a specific microsonic device application. These programs are used to characterise surface waves travelling on an AT cut quartz crystal. Until now this cut generally has been overlooked in surface wave studies. It is noted that a substrate of this orientation offers some attractive features, with regard to surface acoustic wave component design, not found in other more commonly employed cuts of quartz. The desirable properties of the AT cut quartz surface are exploited in the final design and fabrication of a microsonic "crossbar" directional coupler.

A detailed theoretical study of the performance of this surface acoustic wave directional coupler is undertaken. Analytical methods "borrowed" from electromagnetic microwave theory are combined with a perturbation treatment of the surface mass-loading interaction to derive expressions for the amplitudes of the coupled waves. Experimental response curves plotted from extensive measurements made with several models of the "crossbar" coupler show close agreement, in relation to both the strength and the frequency dependence of the coupled signal, with the predicted behaviour.

In a concluding chapter consideration is given to the many potential surface acoustic wave device applications of the periodic surface mass-loading coupling mechanism. Included in the discussion, which compares the projected device performance with that of existing designs, are surface wave directional couplers, delay line taps, filters and reflectors.

Statement of Originality.

This thesis contains no material which has been accepted for the award of any degree or diploma in any University.   To the best of the author's knowledge and belief, this thesis contains no material previously published or written by another person, except when due reference is made in the text.

(H. SABINE.)

CHAPTER I

INTRODUCTION

1.1 Surface Acoustic Waves.

The properties of surface acoustic waves were determined first by Rayleigh (1) who, in 1885, described mathematically the properties of an elastic wave propagating on the plane surface of a semi-infinite isotropic elastic half-space. Rayleigh foresaw that the wave motion he had succeeded in describing would be significant in the interpretation of earthquake disturbances because the natural attenuation of a wave which diverges from a source along the two dimensional space provided by a propagation surface is less than that of a wave which spreads out into a three dimensional volume.

1.2 Historical Background.

This prediction proved true and for the next half-century most studies of surface acoustic waves were undertaken as an aid to seismological research. Investigations of the progress of these waves through the earth's mantle led to analyses of propagation on curved surfaces (2), (3) and in laminated media (2), (4). In both instances the surface wave phase velocity was shown to become frequency dispersive, in contrast to the simpler non-dispersive situation considered by Rayleigh.

During the mid-1950's surface acoustic waves found their first commercial application in the field of non-destructive materials testing (5), (6). Volume (longitudinal and shear) acoustic waves had been utilized for some time in the ultrasonic inspection of manufactured articles. The development of the wedge transducer (5), (7) provided a convenient means for launching and detecting surface waves, generally

at frequencies less than a few megahertz, so that these waves, too,
could be employed to examine material surfaces for manufacturing
flaws. By the early 1960's wedge and comb (7) type transducers,
both of which depend upon mode conversion from volume to surface
waves, were being used to propagate surface waves in a wide variety
of materials. This experimental work stimulated analytical studies
of surface wave motion in situations of increasing complexity -
principally in anisotropic media (8) - (12). At about the same
time White (13) and Foster (14), (15) developed volume wave transducers
capable of fundamental mode operation at several hundreds of megahertz.
This extended the practical frequency range of volume acoustic wave
delay lines (16), which had been in service for nearly twenty years,
into the UHF region, where it was noted that certain glasses and
single crystal materials continued to exhibit extremely low acoustic
loss (17) - (20). The primary factor which hampered the application
of surface waves to this role, in which they offer the very real
advantage, over volume mode devices, of signal accessability, was
the high insertion loss associated with existing transduction schemes.

1.3 Application to Communications Engineering.

This barrier was removed when, in 1965, White and Voltmer (21)
introduced the interdigital conducting electrode array transducer,
which provides an efficient two dimensional structure for generating
and detecting surface acoustic waves over broad communication band-
widths at centre frequencies ranging typically from five to five
hundred megahertz. As illustrated in Figure 1.1 the transducer
operates on a single crystal or on an oriented poly-crystalline
piezoelectric material. Coupling to the surface acoustic wave is
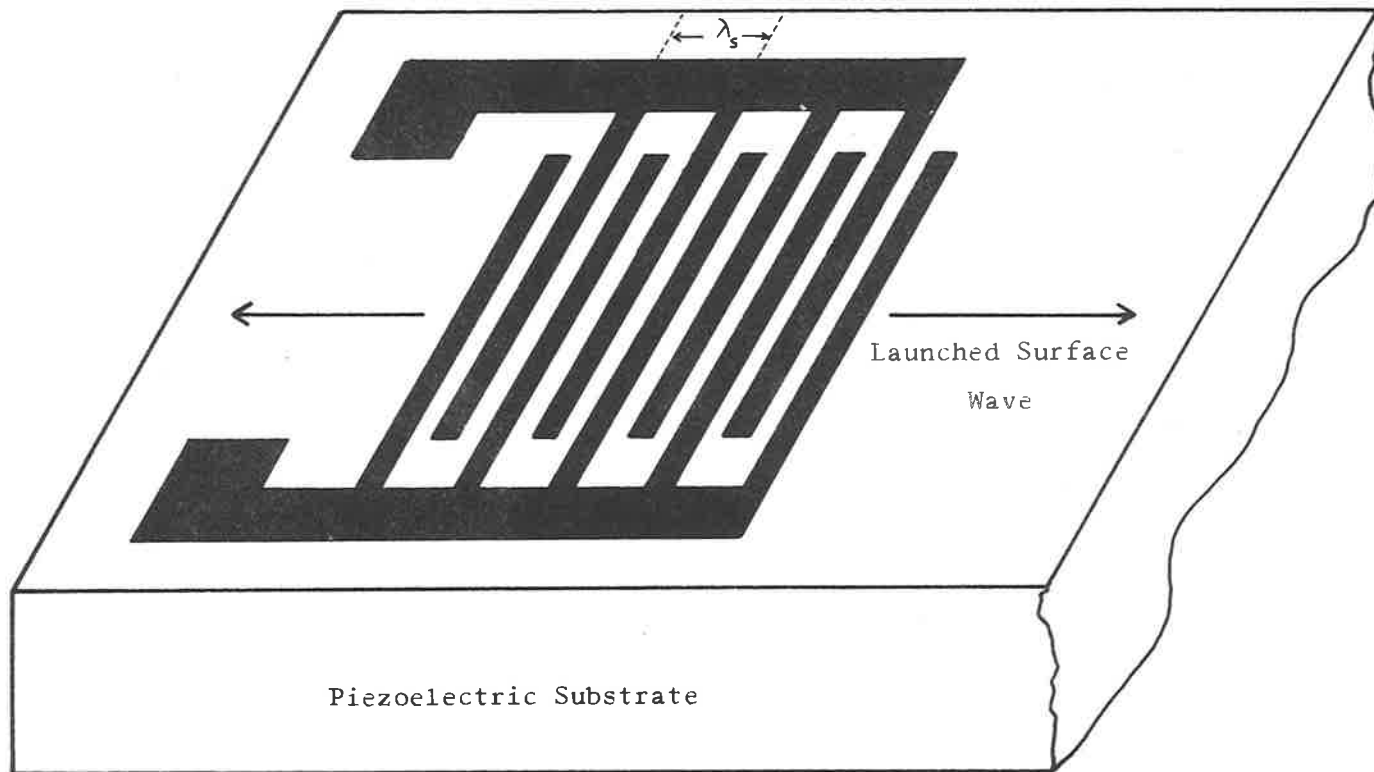
Figure 1.1

An interdigital electrode array transducer (IDT).

λ_s = surface acoustic wavelength.

achieved through the piezoelectrically induced stress arising from the electromagnetically excited electrode pattern, the periodicity of which is chosen to match the surface wavelength at the desired operating frequency. The practical success of these interdigital transducers ushered in a sudden upsurge of interest in the high frequency applications of surface acoustic waves. In addition it encouraged theoreticians to broaden existing analyses of anisotropic surface wave propagation (12) to include the effects of piezoelectricity (22) - (25), thus facilitating the search for substrate materials and orientations of high acoustoelectric coupling.

As a result, the last half-decade has seen a rather remarkable growth in surface acoustic wave technology as it applies to communications engineering. Today a basic range of surface wave devices is being manufactured on a commercial scale and this component range is being extended steadily. Recent widespread interest in this technology has arisen primarily because it may lead to an efficient and compact means for signal processing in radar or communications systems. It is appropriate, at this juncture, to summarise the principle features of surface acoustic waves which suggest this possibility.

In some media acoustic waves provide unusually high quality (Q) factors, of 10^5 or more at 500 MHz (17) - (20), which allow complex processing operations to be performed without frequent regeneration of the signal. At the same time the conveniently low surface wave phase velocity, of typically 3Km./sec., ensures that distributed parameter systems occupy very little space. Because a wide variety of both linear processes, such as filtering (26) - (29), storage (30) - (34) and amplification (35) - (38), and non-linear processes,

such, as frequency translation (39) - (41), can be performed on signals

in the surface acoustic mode there exists the hope that virtually

complete UHF receivers can be built using this technology.   Finally

a surface wave propagates on the stress-free boundary of a medium

and 95% of the acoustic energy is contained within one wavelength of

the free surface (42).   Thus not only is a signal encoded in the

surface acoustic mode always accessable, but also planar device

fabrication techniques can be employed.

Although delay lines operating at a fundamental frequency of

several gigahertz have been fabricated (43), (44) most sober assess-

ments (45) of surface wave technology place the useful frequency range

between a few tens of MHz and 500 MHz.   To date most commercial

implementations of these waves have centred on delay-line (46) and

filter (26) - (28) applications.   However considerable research effort

has been devoted as well to the design and testing of microsonic

devices which are the acoustic analogues of familiar electromagnetic

microwave components.   Included in this category are surface acoustic

waveguides (47) - (50), directional couplers (47), (49), (51), resonators

(31) - (33), (52), phase shifters (53) and travelling wave amplifiers

(35) - (38).   Many of these components are at an early stage of

development, and further study is required before a true assessment

of device utility can be made.

1.4 Aim of Thesis.

The principal aim of this thesis is to describe a study of the

behaviour of a surface acoustic wave incident upon a region of periodic

mass-loading deposited upon the propagation surface.   Both the

experimental and theoretical aspects of this investigation are

described with a view to exploiting this interaction in the design of
a surface wave directional coupler. Although most of this thesis is
concerned with the design, development, fabrication, testing and
theoretical performance evaluation of such a coupler, the surface
acoustic wave-periodic mass-loading interaction has, as is discussed
in the concluding chapter, far wider application in microsonic com-
ponent design.

In treating all facets of practical and theoretical directional
coupler performance it will be necessary to give detailed considera-
tion to many different aspects of surface wave technology. Included
are analyses of anisotropic propagation, assessment of substrate
utility, the establishment of a theory to predict device performance,
the development of photolithographic fabrication techniques, and the
determination of suitable testing procedures to allow practical
measurements of coupler response.

CHAPTER II

EVOLUTION OF A SURFACE WAVE DIRECTIONAL COUPLER DESIGN.

2.0 Introduction.

Details of preliminary experimental and theoretical studies
which suggested the design of a directional coupler based upon the
coupling provided by periodic mass-loading of a propagation surface
are presented in this chapter. This serves a two-fold purpose.
Firstly it provides an opportunity to indicate the link between two of
the main avenues along which the research programme has progressed.
Secondly it forms a useful basis for discussion of certain features of
the practical coupler performance, details of which appear in Chapter
X.

2.1 Scattering of Surface Acoustic Waves.

Experience in the field of non-destructive materials testing,
using surface waves, furnished qualitative information regarding the
effect, on wave motion, of isolated defects in the propagation surface
(5), (6). Viktorov (54) added to this knowledge through experimental
studies of surface wave behaviour in the vicinity of models of single
surface defects.

The more urgent need as far as communications engineers, interested
in the VHF and UHF applications of the technology, were concerned, was
an understanding of propagation on a continuously roughened surface.
This was of importance in determining the quality of substrate surface
finish required to ensure low loss propagation at the higher frequencies.
There existed the hope, too, that the opposite situation, in which areas
of the surface were deliberately roughened, would lead to techniques
for acoustically isolating sections of the substrate and to practical

microsonic band rejection filters (55).

Brekhovskikh (56), in 1958, had produced a first order perturbation treatment of surface wave scattering, into longitudinal and shear waves, at a region of periodic surface roughness. Bykov and Shneider (57), (58) conducted some practical studies of the dependence of acoustic attenuation upon surface preparation, but the first attempt to verify Brekhovskikh's analytical results was undertaken by Rischbieter (59), who, in 1965, performed a series of carefully executed experiments. He measured the attenuation of a surface wave normally incident upon a series of many shallow triangular grooves machined into the surface of an aluminium block. The damping of the wave thus recorded exhibited the expected frequency response, but the magnitude of the attenuation was, in general, more than one order of magnitude smaller than predictions based upon Brekhovskikh's analysis.

In simple experiments modelled on the work of Rischbieter, the present author used a wedge transduction scheme to measure surface acoustic wave attenuation on the periodically roughened surface of a large aluminium block (60) and of a ridge acoustic waveguide (61). The observed attenuation was of the same order of magnitude as reported by Rischbieter. At about this time a publication by Humphryes and Ash (62) confirmed the discrepancy between theoretical and experimental results. As the evidence now pointed strongly towards an error in Brekhovskikh's analysis, it was decided to rely upon Rischbieter's practical response curves - considerable time would have been consumed in establishing such a refined experimental procedure - and to re-examine the theory of surface wave scattering.

A thorough check of the analysis disclosed an error in the

theoretical expression for the damping factor (60), (63). Figures 2.1 and 2.2 show that calculations based on the corrected theory provided, for the first time, results in close agreement with the experimental measurements of Rischbieter. As would be expected of a perturbation treatment, the analytical curves more closely represent the practical results in situations of weak coupling, (Figure 2.1), and differ considerably at the attenuation peaks.

2.2 Coherent Reflection of Surface Acoustic Waves.

It should be noted that Brekhovskikh's analysis of surface wave scattering at a periodically roughened surface considers only the energy removed from the incident beam due to mode conversion into longitudinal and shear waves, whose propagation vectors are directed at non-zero angles to the plane of the free surface:- no account is taken of energy which may be lost as a surface wave scattered in some direction (within the free surface) other than that of the incident wave. The nature of the scattered wave is governed by the need to satisfy the conservation conditions relevant to a surface situation, namely

$$(\beta_i + n \beta_p + \beta_s).r = 0 \qquad n = 1,2,3,... \qquad (2.201)$$

$$\text{and} \quad \omega_i = -\omega_s \qquad (2.202)$$

Here ω_i and β_i are the frequency and wave vector, respectively, of an incident wave, ω_s and β_s are the corresponding parameters of the scattered wave, β_p is the wave vector describing the surface roughness perturbation, and r is a unit vector in the plane of the unperturbed propagation surface. These two restraints must pertain in order that the interaction be cooperative in both its spatial and time dependences.

Rischbieter studied experimentally the behaviour of a surface wave launched at normal incidence to a region of one dimensional
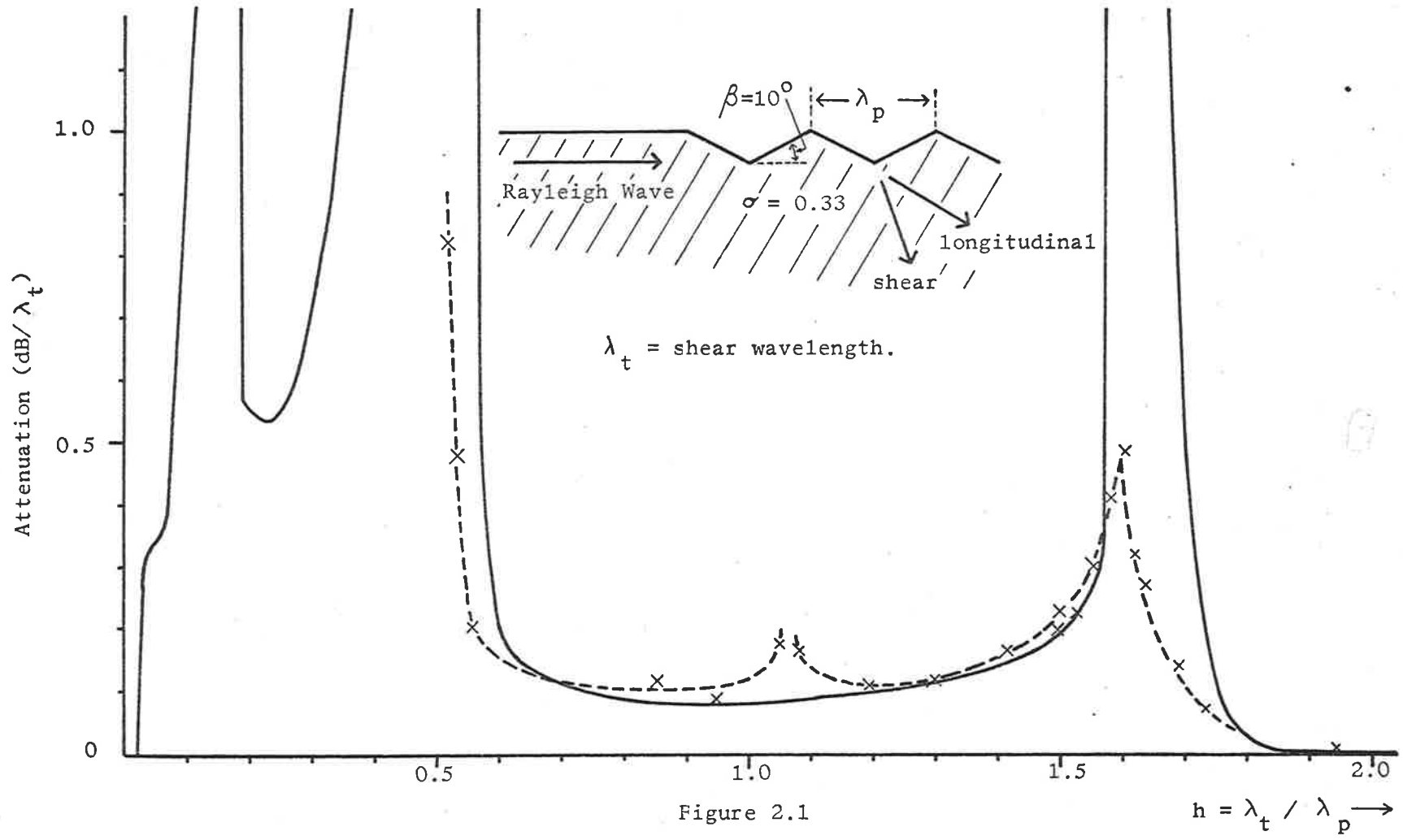
Figure 2.1

Rayleigh wave attenuation at a periodically roughened surface

———— Theoretical results   ✕──✕ Rischbieter's experimental results.
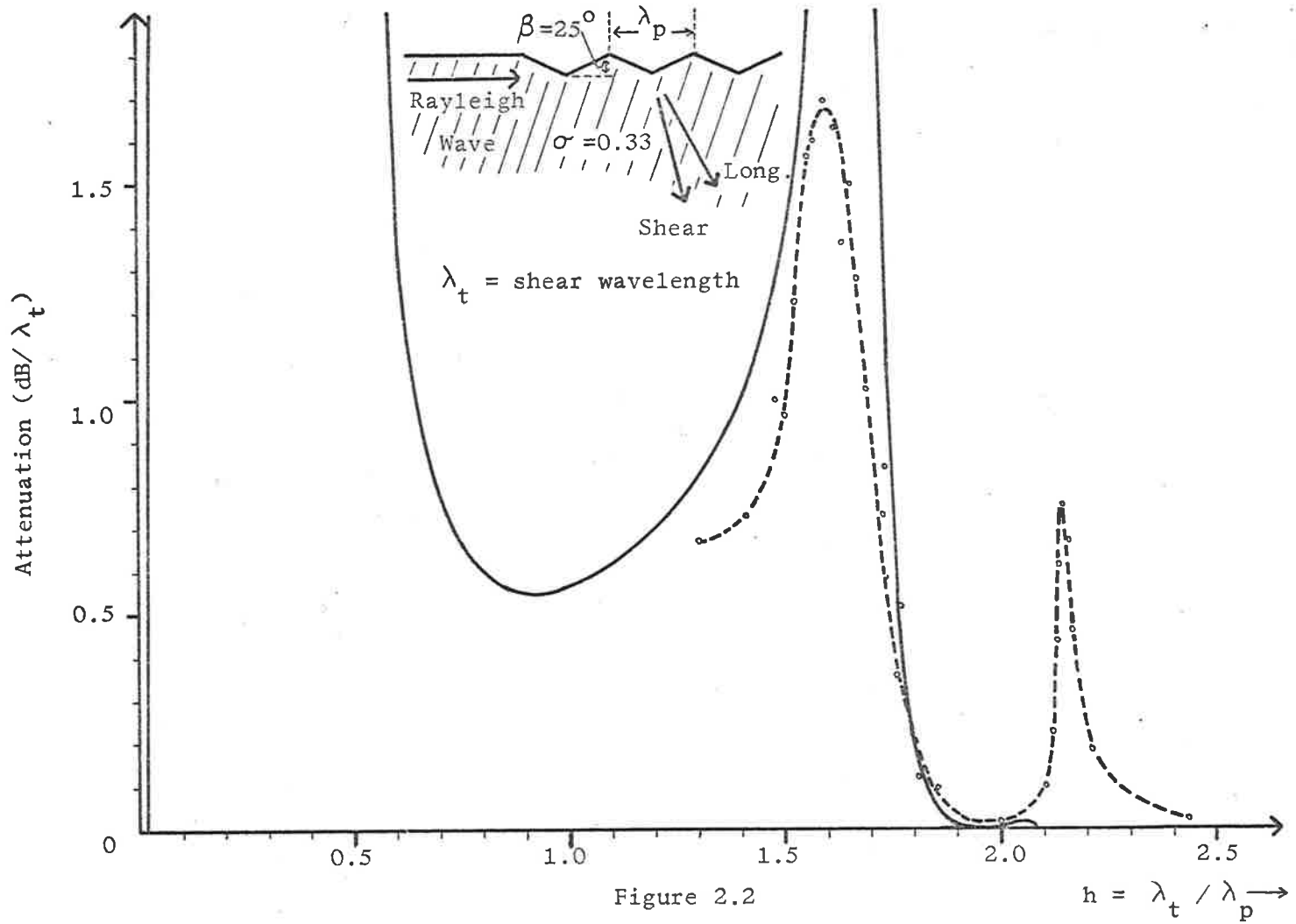
Figure 2.2

Rayleigh wave attenuation at a periodically roughened surface

———Theoretical results ⌐o⌐⌐Rischbieter's experimental results

periodic roughness. If attention is focussed on those situations

for which the scattered wave is also a surface acoustic wave, the

conservation relations, (2.201) and (2.202), require that

$$n\lambda_i /2 = \lambda_p \qquad n = 1,2,3,... \qquad (2.203)$$

where λ_i is the wavelength of the incident signal and λ_p is the

periodicity of the surface roughness. Equation (2.203) is a state-

ment of the conditions for which Bragg reflection (64) of a normally

incident wave motion may be observed. For input signals of a

frequency satisfying this relation, a surface acoustic wave of com-

paratively large amplitude will be reflected from the periodic surface

perturbations such that it travels in the opposite direction to the

incident wave. It is this reflected signal which contributes to the

more severe damping measured by Rischbieter at h = 1.07, (i.e. $\lambda_i = \lambda_p$),

in Figure 2.1, and which is solely responsible for the attenuation

peak at h = 2.14, (i.e. $\lambda_i = 2\lambda_p$), in Figure 2.2. This latter point

is most interesting because it indicates that at the fundamental

Bragg frequency (n = 1 in equation (2.203)) a surface wave is strongly

reflected from a region of periodic surface roughness with, theoretically,

no energy scatter into volume acoustic modes. Rischbieter investigated

this phenomenon by measuring the standing wave ratio at a point in

front of the roughened area. In this way he was able to record the

reflection coefficient and to assess the dependence of the frequency

response of the reflected signal upon the length of the interaction

region.

2.3 Application to Surface Wave Directional Coupler Design.

In order to observe independently the reflected wave, the crude

experiment sketched in Figure 2.3 was arranged (60); this enabled a
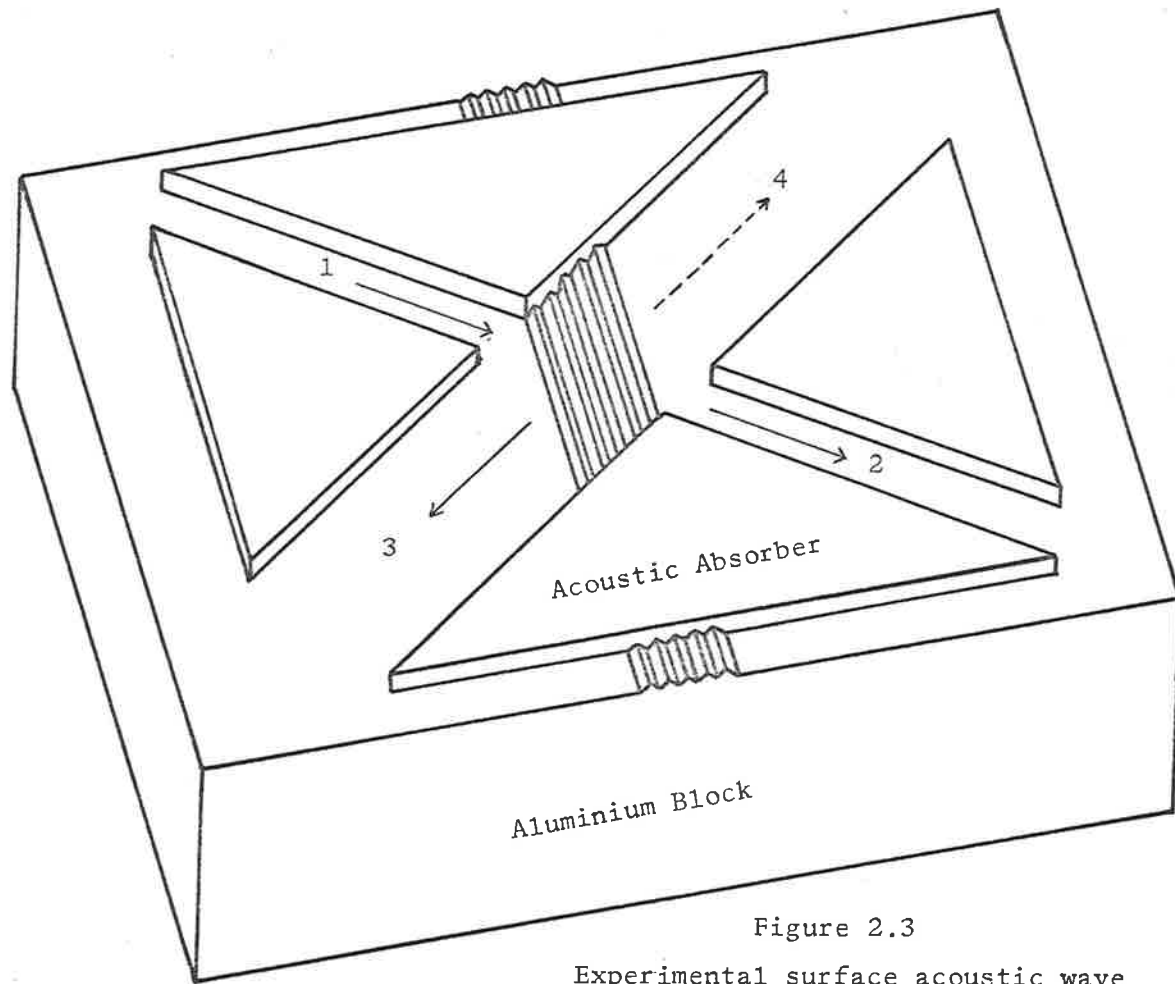
Figure 2.3

Experimental surface acoustic wave

directional coupler.

study of the Bragg reflection of surface waves at non-normal incidence.
The aluminium block used in the exploration was that machined to study
the scattering of surface waves, into volume modes, at regions of
periodic surface roughness. Acoustic absorbing material, (modelling
clay), was applied to the perturbed surface to define input and exit
beam paths.

A surface acoustic wave was launched, at an angle of 45° to the
perturbations, by a wedge transducer located in port one. When the
frequency of the input signal, (1.0 - 2.0 MHz), was adjusted to satisfy
the fundamental Bragg condition, a reflected signal of large amplitude
was recorded at a receiving wedge transducer placed in port three.
This was expected, as an analysis, using two dimensional surface wave
scattering theory (60), had shown that under these conditions, as in
the one dimensional situation discussed in section 2.2, scattering to
volume waves is negligible. Plots of the frequency response of the
reflected signal were made, but accuracy was hampered by the following
two factors.

> 1) Signal amplitudes were highly dependent upon the quality
>   of the acoustic coupling between the wedge transducers
>   and the substrate.
>
> 2) The "make-shift" experimental set-up forced the input
>   and output beams, as illustrated in Figure 2.3, to be of
>   different widths.

For these reasons the practical results (60) must be regarded as
providing only qualitative information.

Rischbieter's experiments had shown that a comparatively long
interaction region of periodic surface roughness could act effectively

as a reflector of surface acoustic waves, although no existing analysis
could predict the relative amplitude of the reflected signal. During
the course of practical measurements at non-normal incidence, it was
observed that a considerably shorter interaction length permitted the
device depicted in Figure 2.3 to behave as a surface wave directional
coupler (60). Energy incident in port one was, in part, coherently
reflected to port three, the remainder of the acoustic power being
received, undeviated, in port two. As required by the conservation
conditions, very little energy was detected as a back-scattered wave
in port four. In this device the strength of coupling is determined
mainly by the number, N, and depth (relative to a surface acoustic
wavelength) of the surface perturbations. The frequency response is
basically of sinx/x dependence, where $x = N\pi(\omega-\omega_o)/\omega_o$ and ω_o is the
centre (Bragg) frequency; this provides a 3dB fractional bandwidth
of approximately 7/8N.

2.31 Surface Wave Directional Coupler Design using a Periodic Surface Roughness Interaction.

Hence a surface acoustic wave directional coupler design
exploiting the previous experimental results (60) might appear as
shown in Figure 2.4, in which Ash's slot guide structures (47), (48),
(55) define the four ports. But the efficient generation and detection
of surface waves and adherence to a planar device technology necessitates,
as noted in section 1.3, the use of interdigital transducers (IDTs) on
a piezoelectric substrate. Because the common piezoelectric materials
such as quartz, lithium niobate and PZT ceramics are both difficult to
machine (with regard to cutting periodic grooves of specified width
and depth into the substrate surface) and to etch, the design does not
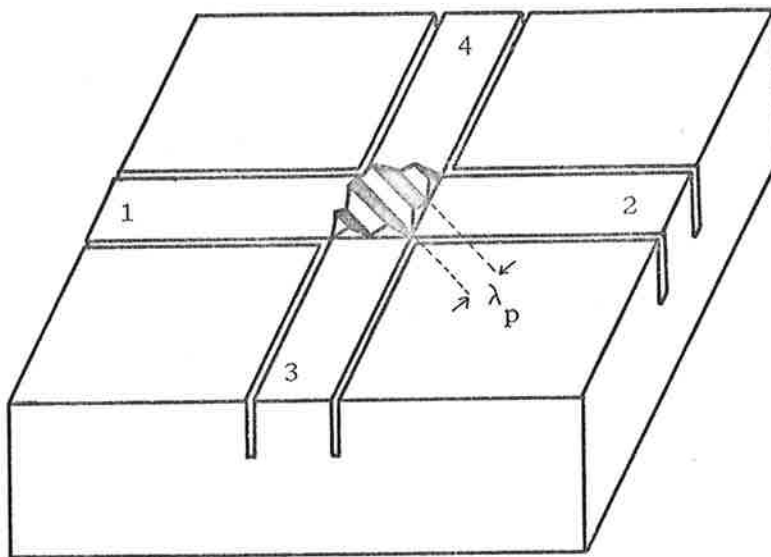
Figure 2.4

Surface acoustic wave directional coupler design.
Coupling provided by periodic surface roughness.

$$\lambda_p = \lambda_s / \sqrt{2}$$

lend itself readily to practical implementation.

2.32 <u>Surface Wave Directional Coupler Design using a Periodic</u>

<u>Surface Mass-Loading Interaction.</u>

The search for a design more suited to fabrication by the well-
established photo-lithographic techniques of the integrated circuit
industry led to the design illustrated in Figure 2.5.   Here the
substrate is assumed to be piezoelectric, so that IDTs can launch
and receive the surface wavesignals in the various ports.   Although
this coupler is similar in concept to that sketched in Figure 2.4,
there is one significant difference:- the interaction region of
periodic surface roughness has been replaced by a central grid which
provides periodic mass-loading of the propagation surface.   These
mass-loading strips, which can be etched from a deposited layer of a
material whose elastic properties may or may not differ considerably
from those of the substrate, can be formed during the same photo-
lithographic processes needed to fabricate the transducers.
Intuitively one would expect the behaviour of this device to be
similar to, but the design more versatile than, the coupler described
in section 2.31.

In 1967 Tseng (23) had published a brief report of the experimental
observation of the Bragg reflection of surface acoustic waves employing
essentially the arrangement shown in Figure 2.5.   However he did not
explore the response of the device in any detail, in either a theoretical
or a practical sense, but was content to note that this reflection
could be the source of a significant aberration from ideal performance
in IDTs.   More importantly, as discussed in sections 10.8 and 11.1,
the interaction utilized in Tseng's experiment was almost entirely
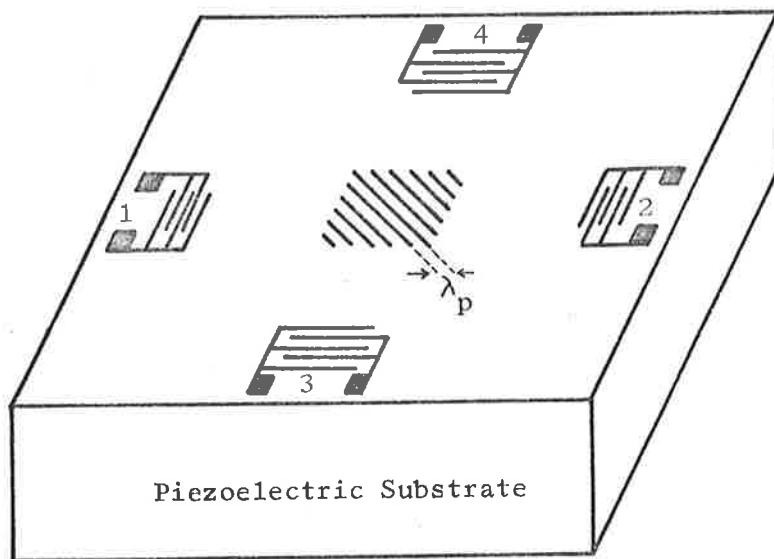
Figure 2.5

Surface acoustic wave directional coupler design.

The "crossbar" coupler - coupling provided by

periodic surface mass-loading.

$$\lambda_p = \lambda_s / \sqrt{2}$$

acousto-electric, the coupling being introduced by the combined effects of a strongly piezoelectric substrate, PZT-4, and a periodic conducting grating, fabricated from a thin layer of the low mass density metal, aluminium. Hence the periodic surface mass-loading interaction can be shown to have made a negligibly small contribution to Tseng's measurements.

The remainder of this thesis is concerned, therefore, with describing the design, fabrication and testing of the so-called microsonic "crossbar" coupler, the fundamental concepts of which are illustrated in Figure 2.5. It is concerned, as well, with the development of an understanding of the effect, on surface acoustic wave propagation, of periodic surface mass-loading, and thus with the establishment of a theory to evaluate coupler performance.

CHAPTER III

SUBSTRATE ASSESSMENT - ANALYTICAL

3.0 <u>Introduction</u>.

Frequently the most crucial problem facing the designer of micro-sonic components is the selection of a substrate possessing all the properties needed for design implementation.   As was decided in the preceding chapter, the substrate on which the crossbar coupler is to be built should be piezoelectric, to allow efficient electromechanical transduction using IDTs, while in order to ensure low propagation loss the material should be a single crystal rather than an oriented poly-crystalline piezoelectric medium.   Furthermore the high cost of even small plates of some piezoelectrics, (notably lithium niobate), as compared with the much lower cost and ready availability of large single crystal synthetic quartz determines that, if possible, the coupler should be fabricated on a suitable cut of the latter material.

Substrate piezoelectricity affords the advantage of design using IDTs, but the accompanying elastic anisotropy of single crystal media introduces the problem of coping with the more complex analyses needed to describe surface wave motion.   Buchwald (11), (12) and others (8) - (10) first developed theories to study waves travelling on the surfaces of single crystal media of high order elastic symmetry (cubic). These analyses were extended by Tseng (22), (23) to include the effects of piezoelectricity, as exhibited by some hexagonal crystals.   In their theoretical investigation of surface wave propagation on various cuts of quartz, which belongs to the low order trigonal elastic symmetry class, Coquin and Tiersten (24) described methods of widespread applicability.   Their work demonstrated techniques which can be used

to analyse surface wave propagation in any direction on a surface of arbitrary orientation cut from a crystal of any symmetry class.

In contrast to the simple elastically - isotropic situation treated by Rayleigh (1), iterative numerical procedures on a digital computer are necessary to calculate the surface wave phase velocity and details of acoustic power flow and electroacoustic coupling on aniso-tropic materials. Lim and Farnell (65), (66) report, following an extensive survey based on these numerical methods, that no combination of surface, wave vector orientation or crystal symmetry has been found for which an unattenuated surface wave, satisfying the stress-free boundary conditions, cannot be propagated. Slobodnik and Conway (67) have produced computer programmes exploiting the analytical methods developed by Coquin and Tiersten (24) and Campbell and Jones (25) and thus have determined numerical data characterising surface wave motion on various cuts of many single crystal materials (67), (68).

A designer of surface acoustic wave components seeks propagation directions and substrate orientations possessing three main properties.

1) To enable the fabrication of IDTs operating at a specified frequency, the surface wave phase velocity, v_s, should be known accurately.

2) Acoustic power flow and wave vectors should be colinear; - i.e. the misalignment angle, ϕ, between these vectors should be zero to avoid "transducer misfire" (24), (67), (68), (69).

3) In order to obtain efficient electromechanical transduction over wide bandwidths with IDTs, the chosen propagation path should exhibit a high electroacoustic coupling factor,

k^2 (70) - (72).

De Klerk (73) and others (25) note that the electroacoustic coupling factor can be evaluated directly from a knowledge of the elastic, piezoelectric and dielectric constants of the medium. But because the surface wave phase velocity must be calculated as part of the required component design data, the method of Campbell and Jones (25) frequently proves more attractive. They offer the conjecture that

$$k^2 \propto |\Delta v/v|$$

(3.001)

where $|\Delta v/v| = (v_f - v_m)/v_f$

v_f being the surface wave phase velocity on a free boundary of the piezoelectric medium, while v_m is the velocity on the same, but ideally-metallised, surface. The postulation of Smith et al. (70) that

$$k^2 = 2F |\Delta v/v|$$

(3.002)

wherein F is a factor approximately equal to unity, is verified by the more detailed analysis of Auld and Kino (72).

A feature of the surface acoustic wave directional coupler design illustrated in Figure 2.5 is that two propagation paths of relatively large angular separation and each offering the three properties described above are needed on the one substrate surface, which economic reasons dictate should be cut from a quartz crystal. Slobodnik and Conway (67) have computed curves of v_s, ϕ and $|\Delta v/v|$ as functions of wave vector orientation on the X, Y and Z crystal cuts of quartz. Their results show that an X-cut surface has four directions along which $\phi = 0$, but all possess only weak electroacoustic coupling. Two well-separated paths, namely those along the X and Z crystal axes, for which the misalignment angle is zero are to be found on a Y cut quartz surface, but unfortunately the Z axis direction has an essentially zero value of

$|\Delta v/v|$. The Z cut crystal, which displays three fold elastic

symmetry appears, at first, to provide all the wanted substrate features.

Two of the three propagation directions which afford colinearity of the

wave and power flow vectors occur in regions where the $|\Delta v/v|$ curve

is approaching a maximum. But closer examination reveals that the

overall electroacoustic coupling factor for Z cut quartz is more than

an order of magnitude less than is available on the Y and X cuts.

Thus not one of these three crystals is particularly well suited

to implementation of the crossbar directional coupler design. For

this reason it was decided to conduct a theoretical study of surface

wave propagation on other common cuts of a quartz crystal, in the hope

of discovering a more appropriate substrate. This segment of the

research programme relies almost entirely upon analyses formulated by

other workers (24), (25) so that the theory is presented only in

sufficient detail to facilitate an interpretation of the numerical data

appearing later in this chapter, and to assist in analyses of the

surface mass-loading and coupler performance as contained in Chapter

IX. With these latter ends in view, a brief description of surface

wave propagation in isotropic media is included.

3.1 Isotropic Propagation.

As mentioned briefly in section 1.1, the equations governing

surface wave motion on the stress-free boundary of a semi-infinite,

isotropic, perfectly-elastic solid were derived first by Rayleigh (1);

for this reason a surface acoustic wave propagating under these condi-

tions is referred to as a Rayleigh wave (5), (42).

3.11 Coordinate Notation.

Throughout the following analyses, unless otherwise stated, the

surface wave is assumed to be travelling in the direction of the
positive x_1 axis on thefree surface $x_2 = 0$. This coordinate notation
is depicted in Figure 3.1 which shows, additionally, that the particle
displacement amplitudes are assumed to decay with increasing positive
values of x_2. A careful distinction must be made between the propaga-
tion coordinate system, x_i, and the coordinate system defined by the
crystal axes:- the latter is variously represented as the (X,Y,Z)
system and, in tensor relations, as the x_i' coordinate system.

3.12 Fundamental Isotropic Equations.

The fundamental equations determining the allowable modes of
propagation for elastic waves in isotropic solids are (74), (75);

Stress-Strain Relationship.

$$T_{ij} = \lambda \delta_{ij} S_{kk} + 2 \mu S_{ij} \qquad (3.121)$$

T_{ij} is stress tensor

S_{ij} is strain tensor

λ, μ are Lamé's elastic constants

δ_{ij} is Kronecker delta.

Strain-Particle Displacement Relationship.

$$S_{ij} = \tfrac{1}{2} (u_{i,j} + u_{j,i}) \qquad (3.122)$$

u_i is component of particle displacement
along x_i coordinate axis.

$,i$ implies $\partial / \partial x_i$

Equations of Motion.

$$\rho \ddot{u}_i = (\lambda + 2\mu) u_{j,ji} + \mu u_{i,jj} \qquad (3.123)$$

ρ = mass density

Perhaps the most convenient method of solution expresses the
particle displacement components, u_i, in terms of a scalar and a vector
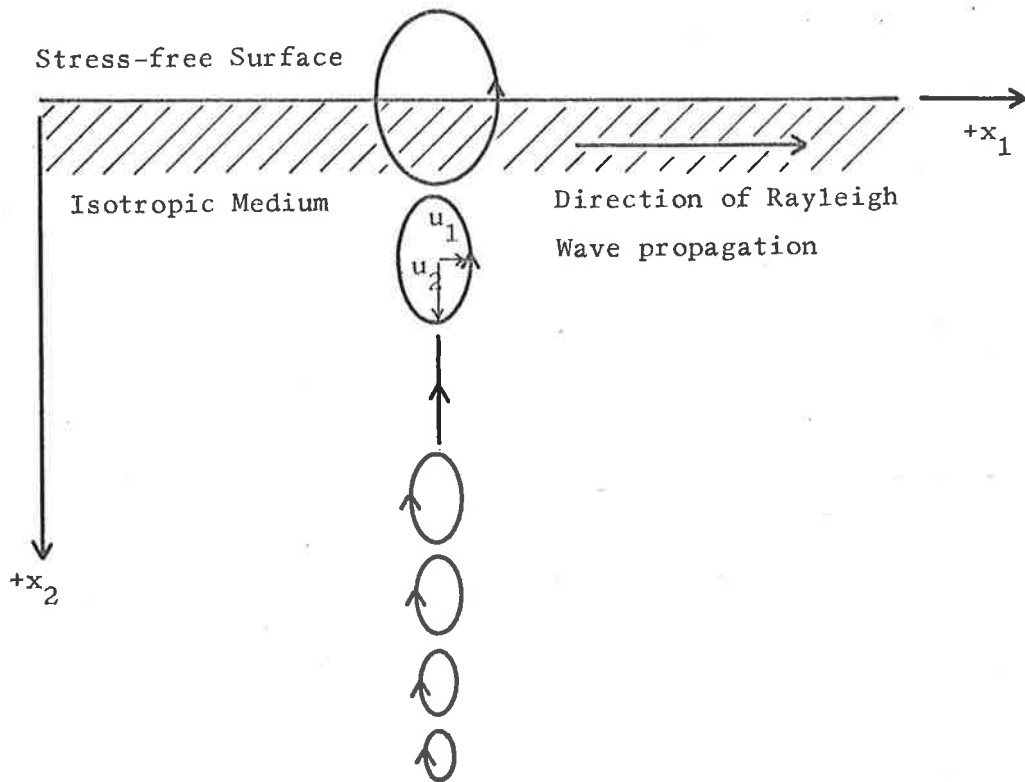
Figure 3.1

Particle displacements for Rayleigh wave motion.

potential (75). By substituting for the particle displacements in the equations of motion it is a simple matter to show that the potentials must be solutions of the well-known longitudinal and shear wave equations (4), (75).

3.13 Boundary Conditions.

With the further assumption that the wave motion is independent of the transverse (x_3) coordinate, trial solutions for the potentials can be established. These may be inserted into the boundary condition equations, viz

$$T_{2j} = 0 \quad \text{at} \quad x_2 = 0 \qquad (3.131)$$

which obtain for a traction-free surface. The need to have non-zero displacement amplitude coefficients leads, from the expanded form of equation (3.131), to the Rayleigh wave characteristic equation

$$K^6 - 8K^4 + (24 - 16\eta^2) K^2 + 16(\eta^2 - 1) = 0 \qquad (3.132)$$

in which $K = v_s/v_t$ and $\eta = v_t/v_1$, v_s, v_t and v_1 being the surface, shear and longitudinal wave velocities, respectively, in the medium.

3.14 Rayleigh Wave Velocity.

The two volume acoustic wave velocities are calculable from the mass density and Lamé's elastic constants for the isotropic material;

$$v_t = (\mu/\rho)^{\frac{1}{2}} \qquad v_1 = \left[(\lambda + 2\mu)/\rho\right]^{\frac{1}{2}} \qquad (3.141)$$

Their ratio can be expressed in terms of the Poisson's ratio, σ, of the medium;

$$\eta = v_t/v_1 = \left[(1 - 2\sigma)/(2 - 2\sigma)\right]^{\frac{1}{2}} \qquad (3.142)$$

In specific situations the precise surface wave phase velocity can be computed from the bi-cubic characteristic equation (3.132), or can be deduced, with a maximum error of 0.5%, from the simple approximation

(76)

$$v_s = v_t \ (0.87 + 1.12\,\sigma)/(1 + \sigma) \qquad\qquad (3.143)$$

3.15 Rayleigh Wave Particle Displacements.

Figure 3.1 shows that the particle displacements associated with a Rayleigh wave are two dimensional, describing a retrograde ellipse at the stress-free surface and reverting to prograde a short distance below, and are confined to the sagittal plane. The displacement components, u_1, parallel to the wave vector, and u_2, normal to the plane surface, can be written as (42)

$$u_1 = A \left[e^{-\alpha_1 \beta x_2} - 2\,\frac{\alpha_1 \alpha_2}{(\alpha_2^2 + 1)}\, e^{-\alpha_2 \beta x_2} \right] \sin(\omega t - \beta x_1)$$

$$\qquad\qquad (3.151)$$

$$u_2 = -A \alpha_1 \left[e^{-\alpha_1 \beta x_2} - \frac{2}{(\alpha_2^2 + 1)}\, e^{-\alpha_2 \beta x_2} \right] \cos(\omega t - \beta x_1)$$

where A is an arbitrary amplitude constant, β is the surface wave vector and α_1, α_2 are real decay constants;

$$\alpha_1 = (1 - v_s^2/v_1^2)^{\frac{1}{2}}$$

$$\qquad\qquad (3.152)$$

$$\alpha_2 = (1 - v_s^2/v_t^2)^{\frac{1}{2}}$$

3.16 Power Flow.

Because a Rayleigh wave is characterised by two-dimensional particle displacements, there being no component transverse to the direction of propagation, the wave and power flow vectors are always colinear in isotropic materials.

3.2 Anisotropic Propagation.

Summarised below are the analytical techniques developed by Coquin and Tiersten (24); the notation established is theirs, and is vital to

an understanding of the calculations performed in sections 9.3 and
9.5.

3.21 Fundamental Anisotropic Equations.

In a non-piezoelectric, but possibly anisotropic, material the
fundamental equations of elasticity are:-

Stress - Strain Relationship

$$T_{ij} = c_{ijkl} \, S_{kl} \tag{3.211}$$

c_{ijkl} is elastic constant tensor

Strain - Particle Displacement Relationship

$$S_{ij} = \tfrac{1}{2} (u_{i,j} + u_{j,i}) \tag{3.212}$$

Stress Equations of Motion

$$T_{ij,j} = \rho \, \ddot{u}_i \tag{3.213}$$

It is assumed, for the moment, that the propagation coordinate axes,
x_1, x_2 and x_3 coincide with the X, Y and Z crystal axes, respectively;
hence elements of the general fourth order elastic constant tensor,
c_{ijkl}, take their normal values referred to these crystal axes (77).

3.22 Analytical Procedure.

A trial formulation for the particle displacements is

$$u_i = \beta_i e^{-\alpha \omega x_2 / v_s} e^{j\omega(t - x_1/v_s)} \qquad i = 1,2,3 \tag{3.221}$$

where ω is the angular frequency of the surface wave motion. Sub-
stitution of this expression into equations (3.211), (3.212) and
finally into (3.213) allows the latter to be expanded as three linearly
independent equations in the β_i. Non-trivial solutions for these
amplitude factors can exist only if the determinant of the 3x3 matrix
of coefficients is zero. This determinantal equation produces a
sixth order polynomial in $s = -j\alpha$ of the form

$$A_6 s^6 + A_5 s^5 + A_4 s^4 + A_3 s^3 + A_2 s^2 + A_1 s + A_0 = 0 \qquad (3.222)$$

in which the A_n are real and are calculable in terms of the c_{ijkl}.
The structure of equation (3.222) is such that roots of s are real,
or occur in complex conjugate pairs; this in turn forces roots of α
to be either pure imaginary or to occur in pairs, with positive and
negative real parts. Since the particle displacement amplitudes,
equation (3.221), must approach zero as $x_2 \to \infty$, the three valid
solutions for $\alpha^{(j)}$, $j = 1,2,3$, (i.e. three decay constants with
positive real parts) are selected. Amplitude factors, $\beta_i^{(j)}$,
corresponding to each $\alpha^{(j)}$ can be deduced from the three equations of
motion.

To satisfy the boundary conditions of zero stress components on
the propagation surface, viz

$$T_{2j} = 0 \qquad \text{at } x_2 = 0 \qquad (3.223)$$

all three valid solutions for the decay constants are required. Thus
the general expression for surface wave particle displacements in
anisotropic media becomes

$$u_i = \sum_{j=1}^{3} C_i^{(j)} e^{-\alpha^{(j)} \omega x_2 / v_s} e^{j\omega(t - x_1/v_s)}$$

$$\qquad (3.224)$$

wherein $\qquad C_i^{(j)} = B^{(j)} \beta_i^{(j)}$

Equations (3.211), (3.212) and (3.224) permit rearrangement of the
boundary condition equations (3.223) as a set of three linearly
independent relationships in the $B^{(j)}$; i.e. as

$$\sum_{j=1}^{3} L_i^{(j)} B^{(j)} = 0 \qquad i = 1,2,3. \qquad (3.225)$$

the $L_i^{(j)}$ being known in terms of the c_{ijkl}, $\alpha^{(j)}$ and $\beta_i^{(j)}$.

The 3x3 matrix of coefficients, $L_i^{(j)}$, must be of a format which leads

to non-zero solutions for the $B^{(j)}$, which introduces the restraint that

$$\left| L_i^{(j)} \right| = 0 \qquad\qquad i,j = 1,2,3. \qquad\qquad (3.226)$$

When this condition is fulfilled, the relative amplitude factors,

$B^{(j)}$, can be calculated from equation (3.225). A brief description

of the computational procedure is given in section 3.25, a more detailed

treatment being provided elsewhere (78) - (80).

3.23 Comparison of Anisotropic and Isotropic Propagation.

A solution for surface wave propagation in anisotropic materials

generally involves three complex decay constants, in contrast to the

two real decay constants which characterise the isotropic disturbance,

and three components of particle displacement, compared with the two-

dimensional motion analysed by Rayleigh. Only in certain discrete

directions, sometimes predictable from elastic symmetry considerations,

does anisotropic surface wave motion simplify to the two-dimensional

form. In anisotropic media there arise certain situations in which

a "pseudo" or "leaky" surface wave, with a phase velocity very close to

that of the true surface wave, can exist (12), (65), (66), (81).

This "leaky" wave leads to the withdrawal of acoustic energy from the

free surface, by virtue of one of its decay constants being purely

imaginary, so that propagation directions characterised by near-

equality of these phase velocities should be avoided in component

design.

3.24 Acoustic Power Flow in Anisotropic Media.

The presence, in anisotropic media, of a transverse component of

surface wave particle displacement creates a component of acoustic

power flow in the plane of the free surface, but normal to the wave

vector. The component, P_i, of acoustic power density per unit surface area directed along the x_i coordinate axis is

$$P_i = -\tfrac{1}{2} \int_0^\infty \text{Real Part} \left[T_{ij} \, \dot{u}_j^* \right] dx_2 \qquad (3.241)$$

where $*$ indicates a complex conjugate term. The P_i can be evaluated by using equations (3.211), (3.212) and (3.224) to expand the above expression. For the coordinate notation adopted here, (Figure 3.1), $P_2 = 0$ but generally, in anisotropic materials, $P_3 \neq 0$ so that as shown in Figure 3.2, the nett surface acoustic power flow is directed at an angle, ϕ, to the wave vector, the "misalignment angle" being

$$\phi = \arctan \ (P_3/P_1) \qquad (3.242)$$

The same diagram emphasises the importance of this parameter. The combination of a propagation path for which ϕ is considerable and a comparatively large spatial separation of transmit and receive transducers can cause the launched energy to miss entirely the detecting array. Therefore the microsonic component designer seeks orientations for which the misalignment angle is zero.

3.25 Techniques for Numerical Solution.

Provided that the most general form of the elastic constant matrix, c_{ijkl}, is employed, the foregoing analysis is applicable to materials of any elastic symmetry. But to study a surface acoustic wave travelling in some chosen direction on a crystal cut of specified orientation these elastic constants must take values related to the propagation coordinate system, x_i:- recall, from section 3.21, that until now the coordinate systems defined by the propagation and crystal axes have been assumed coincident. The required elastic constants are determined
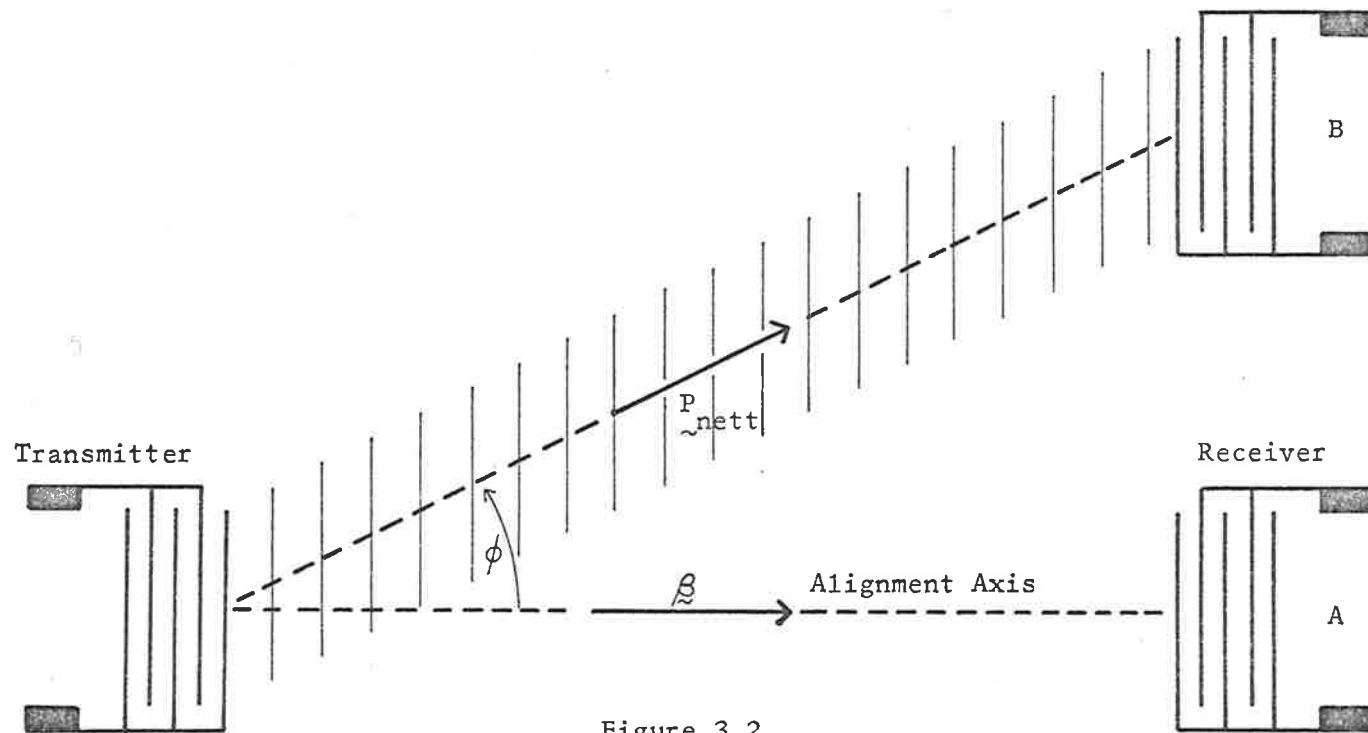
Figure 3.2

Anisotropic surface wave propagation in a direction
characterised by non-colinearity of wave and power flow
vectors.

by the transformation

$$c_{ijkl} = a_{ir} \, a_{js} \, a_{kt} \, a_{lu} \, c'_{rstu} \qquad (3.251)$$

in which $a_{ir} = \cos(x_i, x'_r)$, the x'_i being the crystal axes (77).

Iterative numercial methods involving a digital computer must be utilised in order to examine surface acoustic wave motion in a given anisotropic situation. Program "Anisom", based on the analytical techniques outlined in this section, was developed for this purpose. This computer program uses the most general theoretical approach, and so is capable of analysing surface acoustic wave propagation in any direction on a substrate of any orientation cut from a material of any elastic symmetry class. A flow chart of "Anisom" is contained in Appendix I, together with typical data outputs. More detailed results, drawn from this program, for specific cuts of a quartz crystal are presented in section 3.5, while complete program listings have been provided also (79).

3.26 Application of Analysis to Weakly Piezoelectric Materials.

For materials, such as quartz, which possess small electroacoustic coupling, microsonic component design data, including surface wave phase velocity, decay constants and misalignment angle can be calculated to sufficient accuracy by the analytical methods described above, which neglect piezoelectricity. However to estimate the electroacoustic coupling factor through the technique of Campbell and Jones (25), or to study strongly piezoelectric materials, such as lithium niobate (45), (67), (68), (71), an analysis which takes account of the piezo-electric and dielectric properties of the medium is necessary.

3.3 Anis&tropic Piezoelectric Propagation.

In their analysis of surface acoustic waves travelling on single crystal quartz Coquin and Tiersten (24) give separate consideration to the problems of determining propagation parameters and of calculating the efficiency of coupling to the wave motion using IDTs. Campbell and Jones (25) extend the propagation analysis to include piezoelectric and dielectric terms, and, through the assertion discussed in section 3.0, show that an evaluation of the electroacoustic coupling can be undertaken simultaneously with studies of the phase velocity and particle displacements in piezoelectric materials. This analytical approach, which is summarised in the following sections, is applicable to both strong and weak coupling materials.

3.31 Fundamental Piezoelectric Equations.

A surface acoustic wave launched on the face of a piezoelectric crystal is accompanied, both inside the medium and above the stress-free surface by electroacoustic fields (22). To encompass piezoelectric effects, the stress-strain relationship for anisotropic materials, equation (3.211), must be replaced by the

Piezoelectric Equations of State,

$$T_{ij} = c_{ijkl}S_{kl} - e_{kij}E_k \qquad (3.311)$$

$$D_i = e_{ijk}S_{jk} + \epsilon_{ij}E_j \qquad (3.312)$$

in which the E_i are electroacoustic fields,

D_i are electric displacements,

e_{ijk} are piezoelectric constants,

and ϵ_{ij} is permittivity tensor.

The other fundamental anisotropic elastic equations, namely the Strain-

Particle Displacement relation, (3.212), and the Stress Equations of Motion, (3.213), are retained in their original form.

3.32 Analytical Procedure.

A trial substitution for the particle displacements, equation (3.221), must be supplemented by an additional relation which describes the total scalar electric potential, ψ;

$$\psi = \beta_4 e^{-\alpha \omega x_2 / v_s} e^{j\omega (t-x_1/v_s)} \qquad (3.321)$$

These trial expressions for the particle displacements and electric potential, combined with equations (3.212), (3.311) and (3.312), enable the equations of motion, (3.213) to be expanded as three linear equations in the amplitude coefficients, β_i (i= 1,2,3,4). Gauss's Law, as it applies to the insulating crystal medium, adds the further constraint that

$$\underset{\sim}{\nabla} \cdot \underset{\sim}{D} = 0 \qquad\qquad x_2 \geqslant 0 \qquad\qquad (3.322)$$

which provides, on expansion, a fourth linearly independent equation in the β_i. The usual requirement that the 4x4 coefficient matrix must have a zero determinant in order to yield non-trivial values of β_i leads to an eighth order polynomial, of similar structure to (3.222), in the decay constant, α. Solution of this polynomial produces four decay constants, ($\alpha^{(j)}$, j=1,2,3,4), with real parts of the correct sign to ensure that the acoustic field quantities approach zero as $x_2 \longrightarrow \infty$. Values of $\beta_i^{(j)}$ corresponding to each $\alpha^{(j)}$ may be obtained from the expanded forms of equations (3.213) and (3.322).

Hence the most general descriptions of the particle displacements and the electroacoustic potential associated with a propagating surface wave on a piezoelectric crystal are;

$$u_i = \sum_{j=1}^{4} C_i^{(j)} e^{-\alpha^{(j)}\omega x_2/v_s} e^{j\omega(t-x_1/v_s)}$$

$$\psi = \sum_{j=1}^{4} C_4^{(j)} e^{-\alpha^{(j)}\omega x_2/v_s} e^{j\omega(t-x_1/v_s)} \Bigg\} \, x_2 \geqslant 0$$

$$\text{(3.323)}$$

where
$$C_i^{(j)} = B^{(j)} \beta_i^{(j)}$$

The usual boundary conditions of a traction free propagation surface, equation (3.223), still pertain and provide, on substitution of the above expressions for the particle displacements and electroacoustic potential, three linear relations in the four amplitude factors, $B^{(j)}$. A fourth boundary condition is imposed by the continuity of the electroacoustic potential across the crystal-air interface; i.e.,

$$\psi(x_2=0^+) = \psi(x_2=0^-) \tag{3.324}$$

Once again the 4x4 matrix of coefficients, $L_i^{(j)}$, of the boundary condition equations must be singular; i.e.,

$$\left| L_i^{(j)} \right| = 0 \qquad\qquad i,j = 1,2,3,4 \tag{3.325}$$

When this restriction is fulfilled, the correct surface wave phase velocity and decay constants are known and the $B^{(j)}$ can be determined from the four linearly independent boundary condition relations.

3.33 Comparison of Piezoelectric and Non-Piezoelectric Propagation.

There are a number of important differences between the numerical results obtained from the analytical procedure described above, (computational techniques being detailed in section 3.35), and those derived from the method of section 3.2 applied to the equivalent elastic, but non-piezoelectric, material. The analysis which includes piezoelectric phenomena finds four complex decay constants, compared to the three noted previously, and computes a surface wave phase velocity

which is raised by a small amount due to "piezoelectric stiffening".
In addition, theoretical descriptions of the electroacoustic fields
accompanying the wave motion emerge from the treatment of section 3.3.

3.34 Acoustic Power Flow in Piezoelectric Media.

Because surface wave propagation in single crystal piezoelectrics
generally involves three components of particle displacement, there is
usually a non-zero misalignment angle, ϕ , between the wave and power
flow vectors.   For crystal cuts possessing strong electromechanical
coupling, accurate determinations of misalignment angle can be made
only by taking account of the piezoelectric properties of the material.
This can be achieved through the normal power flow equations, (3.241)
and (3.242), in which the piezoelectric equation of state, (3.311),
is used to evaluate the stresses.

3.35 Techniques for Numerical Solution.

These are the same as described in section 3.25 for investigations
of non-piezoelectric media, except for the obvious difference that
piezoelectric and dielectric, as well as elastic, constants must be
incorporated.   Precise values for these extra parameters, in relation
to the propagation coordinates, must be calculated through the trans-
formations

$$e_{ijk} = a_{ir} \, a_{js} \, a_{kt} \, e'_{rst} \qquad\qquad (3.351)$$

$$\text{and} \quad \epsilon_{ij} = a_{ir} \, a_{js} \, \epsilon'_{rs} \qquad\qquad (3.352)$$

where, as before, $a_{ir} = \cos(x_i, x'_r)$ and the x'_i coordinate system defines
the crystal axes (77).

Iterative numerical techniques must be used again to examine the
wave motion in specific situations.   Program "Pianm", which implements

the analytical methods described above, is a general purpose computer
program capable of returning numerical data characterising surface
wave propagation on a piezoelectric surface of any orientation cut from
a single crystal of any symmetry class. A flow chart of "Pianm"
contained in Appendix II shows the similarities between the computa-
tional procedures for piezoelectric and non-piezoelectric media.
Included in the same appendix are typical numerical data outputs, while
more comprehensive results for specific cuts of a quartz crystal are
presented in section 3.5. A complete listing of "Pianm", which
highlights the structural similarities and differences between itself
and "Anisom", is available (79). Because these two programs were
developed to study various crystal cuts of weakly piezoelectric quartz,
"Pianm", as originally conceived (78), (79), did not compute the
misalignment angle, ϕ , this task being undertaken by "Anisom". At
a later stage "Pianm" was extended to allow calculations of ϕ to
include piezoelectric contributions;- hence values of this parameter
appear in the outputs of Appendix II.

3.4 <u>Propagation on an Ideally Metallised Piezoelectric Surface.</u>

Equations (3.001) and (3.002) recall that perhaps the most con-
venient method for assessing the strength of electroacoustic coupling
between an IDT and a surface acoustic wave on a particular propagation
path is to know the phase velocity in that direction for both the free
and ideally metallised crystal surface. The free surface velocity,
v_f, which must be calculated by a method which includes the piezo-
electric properties of the substrate, is available through the analytical
processes of section 3.3. As will now be shown, the phase velocity,
v_m, on the metallised piezoelectric surface can be computed with only

minot modifications to the analysis.

The metal overlay is assumed ideal in the sense that it is mass-
less, which permits retention of the familiar stress-free surface
boundary conditions, and is of zero resistivity.   Whereas in an
investigation of propagation on a free piezoelectric surface equation
(3.324) forces the electroacoustic potential to be continuous across
the crystal-air interface, the metal film short-circuits the piezo-
electric fields at the free surface, so that the boundary condition
reduces to

$$\psi\ (x_2 = 0)\ =\ 0 \tag{3.401}$$

A comment inserted in the program listing (79) describes the
simple alteration which must be effected before "Pianm" can be applied
to studies of propagation on ideally metallised piezoelectric surfaces.
Typical data outputs from "Pianm" for the coated surface situation are
to be found in Appendix II, while the curves of electroacoustic coupling
factor presented in section 3.5 are plotted from complete analyses of
the free and metallised substrate surface.

3.5 Numerical Results.

The information obtained from theoretical studies of surface
wave propagation on particular substrates using computer programs
"Anisom" and "Pianm" is illustrated here by focussing attention upon
the Y and AT cut quartz surfaces.   Figure 3.3 indicates the relation-
ships that these surfaces bear to the other principal cuts of a quartz
crystal, and establishes the coordinate notation for the remainder of
this section.

3.51 Y Cut Quartz.

Summarised in the graphs of Figure 3.4 are the most significant
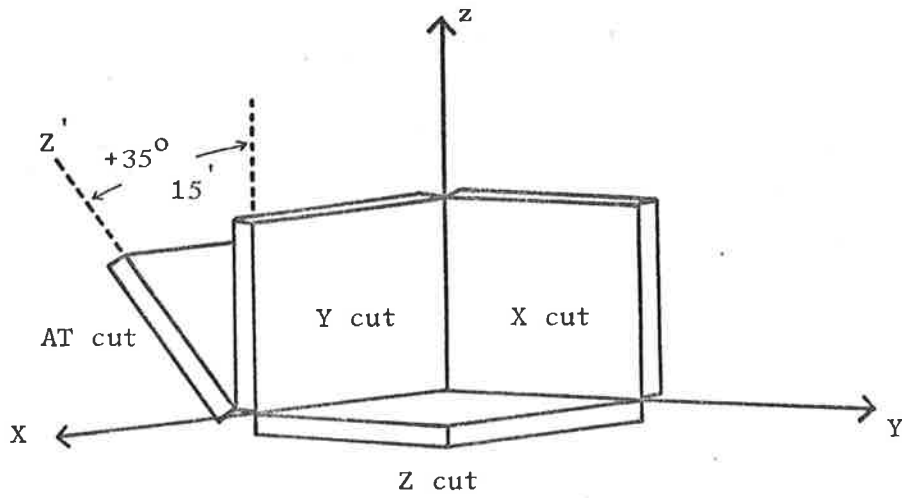
(a) Principal quartz crystal cuts
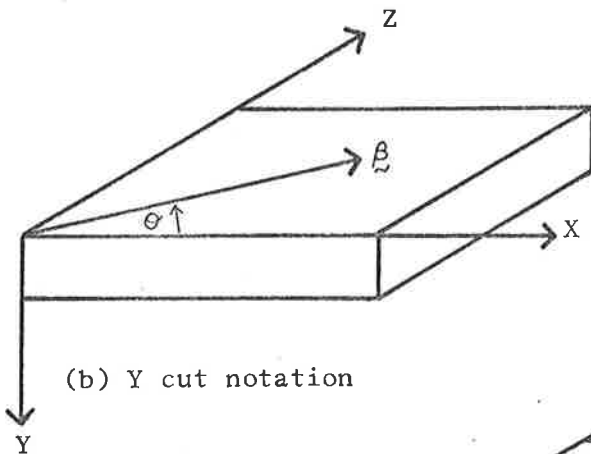
(b) Y cut notation
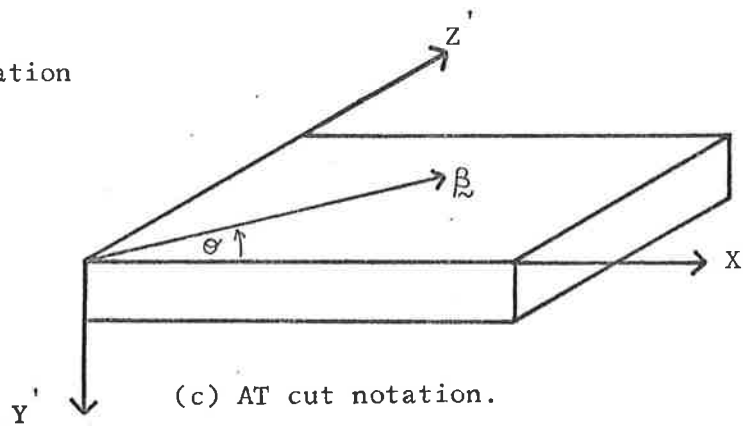
(c) AT cut notation.

Figure 3.3

Principal quartz crystal cuts and coordinate notation.

X, Y, Z are crystal axes.
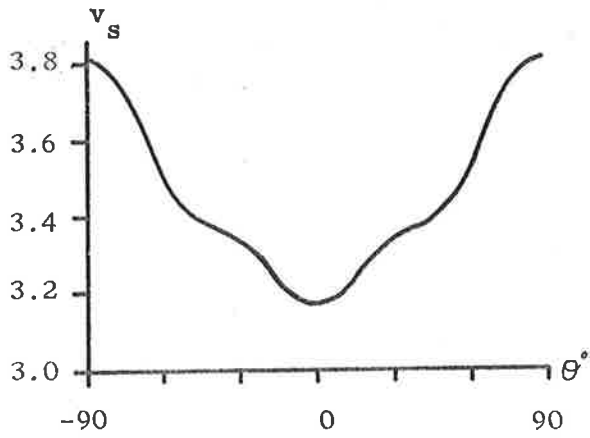
(a) Phase velocity (km/sec).
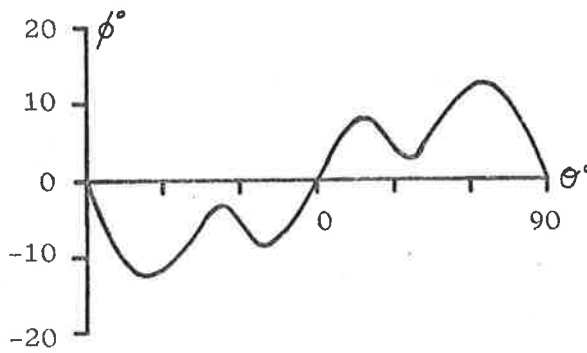
(b) Misalignment angle (degrees)
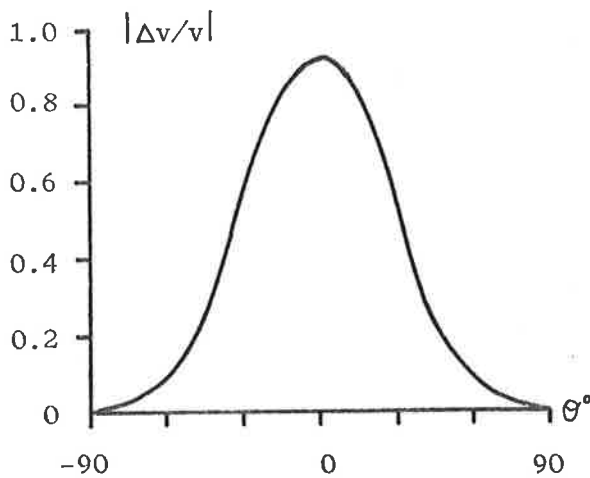
(c) Electroacoustic Coupling

(x10) (%)

Figure 3.4

Surface acoustic wave propagation on Y cut quartz.

properties of acoustic waves propagating in various directions on

the surface of a Y cut quartz crystal.   Curves (a) and (b) which

represent, respectively, surface wave phase velocity and misalignment

angle as functions of the angle, θ, between the wave vector and the

X crystal axis, are plotted from results supplied by "Anisom".   The

variation of electroacoustic coupling factor as a function of θ is

depicted in curve (c), which is drawn from data output by "Pianm".

Due to the symmetry of the material properties about the X and Z

crystal axes, all three graphs are symmetrical about these directions.

A comparison of Figure 3.4 (78) with corresponding results for Y

cut quartz published a short time earlier by Slobodnik and Conway (67)

discloses that the two sets of analytical data are in excellent agree-

ment.   Furthermore the theoretically determined values of phase

velocity are in harmony with the experimental measurements of Engan

et al. (81).   The two aforementioned factors instil confidence in the

accuracy with which the analysis is programmed in "Anisom" and "Pianm".

3.52 AT Cut Quartz.

Figure 3.3 indicates that an AT cut quartz surface is a Y cut

crystal which undergoes a single positive rotation of $+35^{\circ}$ $15'$ about

the X crystal axis.   Thus surface acoustic wave propagation on an AT

cut crystal can be studied theoretically by the simple step of inserting

one additional coordinate rotation [refer equations (3.251),(3.351) and

(3.352)] into the programs used to analyse the Y cut surface.

The analytical results obtained for the AT cut of quartz are shown

in Figure 3.5, in which curves (a) and (b) of surface wave phase

velocity and misalignment angle are derived from "Anisom" while the

electroacoustic coupling factor, curve (c) is drawn from the output
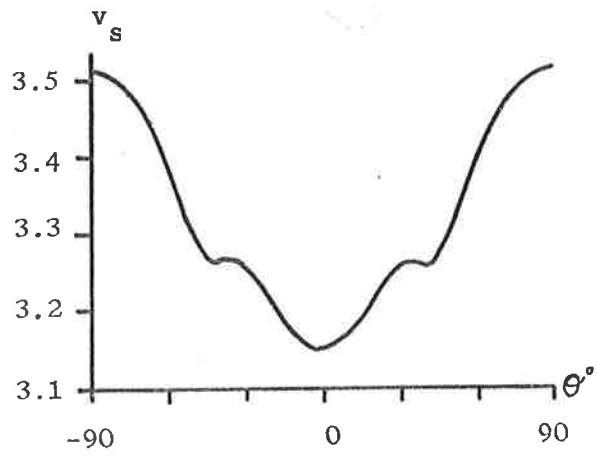
43.

(a) Phase velocity (km/sec)
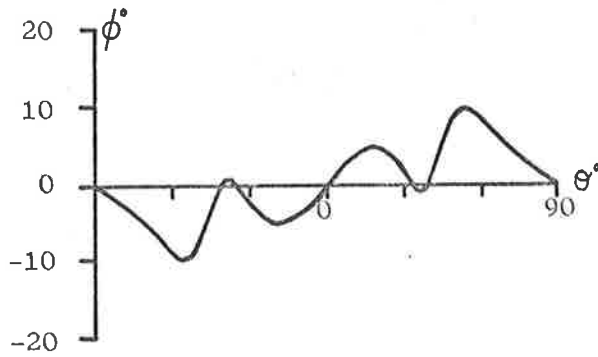
(b) Misalignment angle (degrees)
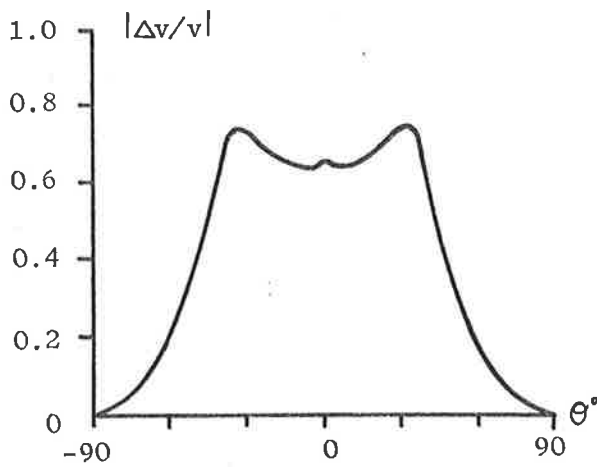
(c) Electroacoustic coupling

(x10) (%)

Figure 3.5

Surface acoustic wave propagation on AT cut quartz.

supplied by "Pianm". As noted in the investigation of surface waves
travelling on a Y cut substrate, each graph is symmetrical about the
X and Z' (refer Figure 3.3) crystal axes. By considering, separately,
the three curves of Figure 3.5, important characteristics of the AT
cut surface emerge.

3.521 Phase Velocity.

Figure 3.5(a) indicates that the surface wave phase velocity on
AT cut quartz ranges from 3.147 Km/sec along the X crystal axis, $\Big[$
which compares favourably with the value of 3.16 Km/sec calculated by
Deresiewicz and Mindlin (82) and a similar result which can be extracted
from the graphs of Coquin and Tiersten (24) (Figure 3)$\Big]$, to 3.512
Km/sec along the Z' axis. Note that these velocities are calculated
by a procedure which neglects substrate piezoelectricity, so that the
actual phase velocities may be raised by small amounts, ($< \cdot 1\%$), due
to piezoelectric stiffening. The phase velocity does not increase
monotonically with θ, but undergoes local maxima and minima in the
region $32^{\circ} < |\theta| < 42^{\circ}$. This suggests the existence, within these
angular limits, of orientations for which the wave and power flow vectors
are colinear.

3.522 Misalignment Angle.

Curve (b) of Figure 3.5 shows that there are indeed paths on the
AT cut crystal characterised by a zero misalignment angle; these occur
along the X and Z' axes and in the four directions defined by $\theta = \pm 34^{\circ}$
and $\theta = \pm 40.5^{\circ}$. Reference to the previous graph verifies that each
of these orientations is associated with a local maximum or minimum
in the surface wave phase velocity. The greatest misalignment,
$\phi \doteqdot 10^{\circ}$, arises when $\theta = \pm 54^{\circ}$.

3.523 Electroacoustic Coupling Factor.

The dependence of electroacoustic coupling factor, represented by $|\Delta v/v|$, upon wave vector orientation on the AT cut quartz surface, is illustrated in Figure 3.5(c). This plot indicates that the coupling is satisfactorilly high, with regard to available bandwidth and electro-mechanical conversion losses using IDTs (70), (71), over the range $-45° < \Theta < 45°$, for these paths to be of practical device utility. A peak of electroacoustic coupling, where $|\Delta v/v| \doteq \cdot075\%$, is available in the vicinity of $\Theta = {}^+_-34°$. Outside of this useful region the coupling decreases steadily and becomes essentially zero along the Z' axis.

3.524 Utility in Microsonic Component Design.

Because of their widespread application in volume mode crystal oscillators, AT cut quartz plates are readily available at comparatively low prices. It is somewhat surprising, therefore, that this particular cut has received little attention, of either a theoretical or an experimental nature, in the surface acoustic wave context (82), (83).

Table 3.1 summarises the characteristics of surface acoustic waves propagating in those directions, on an AT cut quartz crystal, which provide colinearity of the wave and power flow vectors. In view of the discussion in section 3.0, it is clear from this table that the Z' axis, ($\Theta = 90°$), is totally unsuited to most practical device designs because of an essentially zero value of electroacoustic coupling factor. On all of the other orientations listed, an IDT couples satisfactorilly to a surface wave.

Besides the three properties described in the introduction to this chapter, a further most useful quantity in assessing the utility

.Orientation Θ^o	Velocity (Km/sec)		ϕ^o	$\partial\phi/\partial\Theta$	$\|\Delta v/v\|$
	"Anisom"	"Pianm"			(%)
0	3.147	3.151	0	0.34	0.064
$^+_-34$	3.251	3.264	0	-0.45	0.074
$^+_-40.5$	3.248	3.261	0	0.50	0.064
90	3.512	3.512	0	-0.23	0.000

Table 3.1

Surface Acoustic Wave Propagation Characteristics for

Colinear Directions on AT Cut Quartz.

of a propagation path to microsonic component design is $\partial\phi/\partial\Theta$, the slope of the misalignment angle curve, Figure 3.5(c). This parameter decides the misalignment angle should the transmit-receive transducer pair be dis-oriented, during the photo-fabrication process, from the optimum path;- obviously the smallest possible value of $\|\partial\phi/\partial\Theta\|$ is an advantage. Although elastic anisotropy introduces the problem of acoustic "beam steering", i.e. of paths for which $\phi \neq 0$, its effect can be used to advantage to assist in controlling the diffraction of a surface wave beam from a transducer aperture (68), (84). In propagation directions for which $\partial\phi/\partial\Theta$ is negative, anisotropy narrows the launched acoustic beam relative to that which is radiated by the same transducer on an isotropic surface; the inverse effect arises for situations wherein $\partial\phi/\partial\Theta$ is positive.

In the light of this discussion, the paths on an AT cut quartz crystal which are most suited to the demands of microsonic component design are the two for which $\Theta = ^+_-34^o$. Along these directions $\partial\phi/\partial\Theta$ is small and negative:- hence even though Table 3.1 shows that

a misalignment angle of approximately one degree results from every two degrees of pattern disorientation, anisotropy tends to reduce the width of the launched surface acoustic wave beam.   For $\theta = {}^{+}_{-}34^{o}$ the electroacoustic coupling is quite high - in fact the largest available on an AT cut surface, and 72% of the maximum known for a quartz crystal, (which is for propagation along the X axis of a -20° rotated Y cut (24)). Finally these two paths are well separated, in an angular sense, by 68°, so they seem most useful for implementation of the basic crossbar surface wave directional coupler design of Figure 2.5.

CHAPTER IV

SUBSTRATE ASSESSMENT - EXPERIMENTAL

4.0 Introduction.

As stated in the closing remarks of the previous chapter the AT

cut of a quartz crystal appears to meet all the substrate requirements

needed for implementation of the crossbar directional coupler design.

But this conclusion has been reached solely from the analytical results

presented in section 3.5, for which little supporting evidence can be

found in the litterature (24), (82), (83). Measurements of surface

acoustic wave phase velocity as a function of wave vector orientation

on an AT cut crystal are deeply immersed in the velocity - temperature

dependence curves plotted by Schulz et al. (83), but considerable

effort would be required to extract numerical values of velocity from

their results, and this task could not be performed accurately from

the published graphs.

Because of the close agreement between the analytical results

produced in this study and those of Slobodnik and Conway (67) for

surface acoustic wave propagation on Y cut quartz, there is every

reason to have confidence in the results of Figure 3.5 for the AT cut

(which is a $+35^{o}15'$ rotated Y cut). However as many facets of the

projected research programme, including the design and performance

evaluation of the crossbar coupler, rested upon an accurate knowledge

of propagation conditions on the selected substrate it was deemed

advisable to seek some experimental confirmation of the analytical data.

The propagation parameter which can be measured most easily in

practice is the surface wave phase velocity, which can be determined

by constructing a simple delay line with one transmit and one receive

transducer. Reference to the flow charts of "Anisom" and "Pianm" contained in Appendices I and II shows that if experimental verification of the analytical velocity curve can be obtained, the accuracy of the most difficult segments of the computation has been established. Careful rechecking of the algebra and programming involved in the final step which calculates the misalignment angle will eliminate errors in this procedure.

4.1 Delay Line Fabrication on AT Cut Quartz.

Precise details of the delay line photofabrication procedure have been documented (78), so that only essential details are repeated here. The devices were formed on one inch square AT cut quartz crystals, of thickness one eighth of an inch, which, being in excess of ten surface acoustic wavelengths at the design centre frequency of approximately 9 MHz, guaranteed dispersionless propagation (75). Each IDT consisted of 5 electrode pairs[†] which determined a transducer quality factor, $Q_a = 5$ (70), (71). The centre electrodes of the two IDTs were 1.25 cms. apart in the final pattern, a separation which afforded a delay of approximately 4μ secs. Transducer apertures of 20 surface wavelengths ensured that all measurements were made under near field conditions (34).

A photographic mask of the hand-cut rubylith pattern of the transducer pair was taken initially on a Kodak high resolution plate and then, by contact printing, was transferred to Kodalith sheet film. This offered a simple, but comparatively accurate method for positioning the mask in relation to the substrate. The sheet film could be cut to

---

[†]An array of N electrode pairs contains (2N+1) fingers.

provide an edge making a selected angle to the axis of the transducer pair; this could be aligned with the sides of the crystal which were the X and Z' axes.   The IDTs were etched from a vacuum-deposited aluminium film, visually estimated to be only 0.03 microns thick - considerably less than the 0.1 micron layer planned.   Such a thin coating would have been of little use in transducer studies, because the large resistance per square of the metal overlay (85) would lead to significant departures from ideal performance (86).   But in the measurement of phase velocity, this problem would not be of importance.

In all five delay lines were fabricated (78), each on a separate substrate, with the transducers aligned nominally along the X and Z' crystal axes, and at angles of 30°, 45° and 60° to the X crystal axis. One such completed pattern is pictured in Figure 4.1.   Throughout the experimental phases of this surface wave study considerable time and effort was expended in the design and manual preparation of rubylith masks and in the development of successful (in terms of an acceptable device yield) procedures for each stage of the photofabrication process (78).   In fact, as will become more evident from the discussion of Chapter V, these procedures were being improved and up-dated continually in later device manufacture.

4.2 Transducer Bandwidth and Conversion Loss Considerations.

Smith et al. (70), (71), in their lossless three-port analysis of a surface acoustic wave IDT, show that for each propagation path and substrate material there is a transducer quality factor, Q_m, determined by the electroacoustic coupling factor, such that

$$Q_m = (f_o / \Delta f) = \left[\frac{\pi}{8 \, |\Delta v/v|} \right]^{\frac{1}{2}} \qquad (4.201)$$

Figure 4.1

(Opposite)

AT cut quartz crystal and a 9 MHz IDT pair.
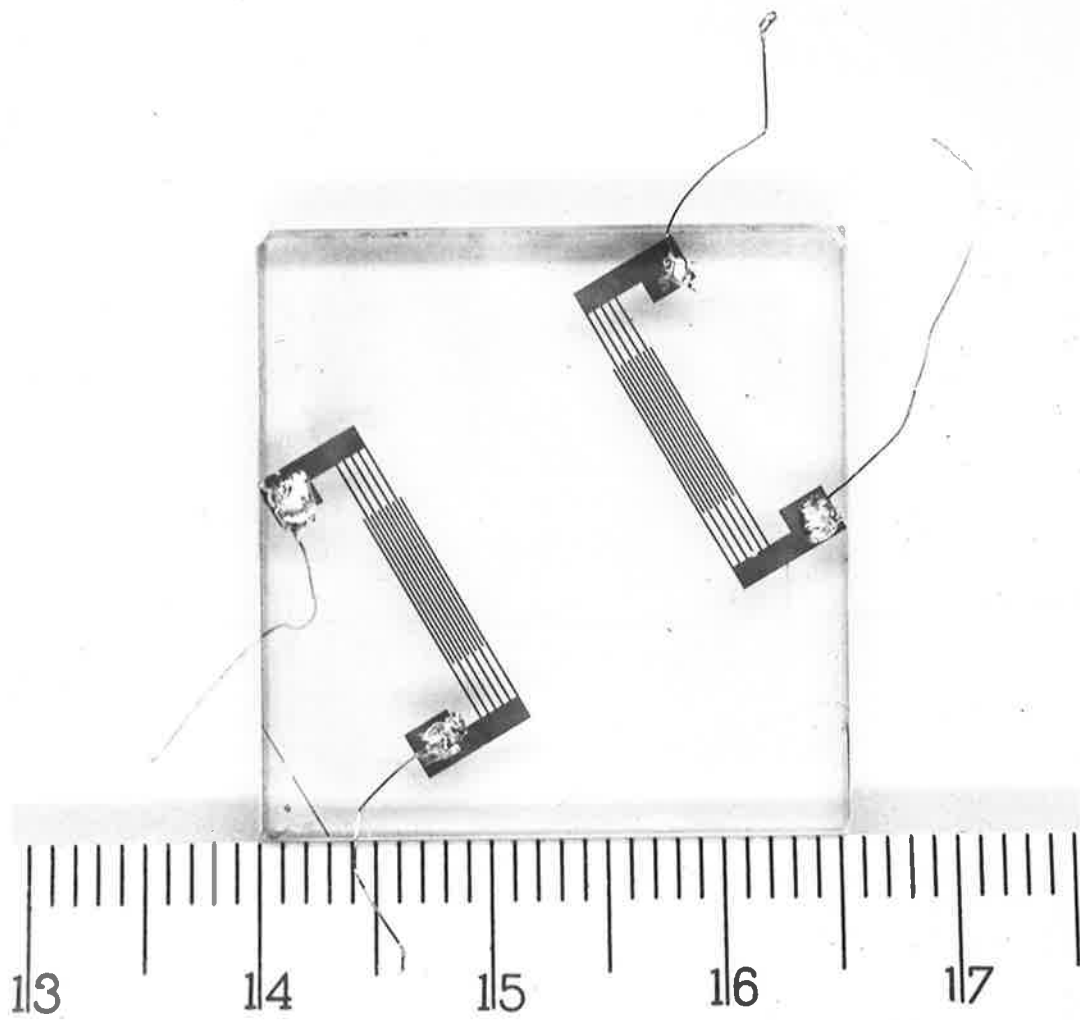
MM.

for which maximum bandwidth can be achieved with minimum electro-
mechanical conversion loss. This means that for the simple uniform
IDT of Figure 1.1, which consists of N electrode pairs, the minimum
one-way electromechanical conversion loss of 3dB (due to bidirectional
launching) can be achieved when $N = Q_m$. On paths of strong electro-
acoustic coupling Q_m is small, so that a mimimum conversion loss
transducer offers a comparatively high fractional bandwidth, $\Delta f/f_o$;
e.g., for a surface wave propagating along the Z crystal axis on Y cut
lithium niobate, $|\Delta v/v| = 2.5\%$, so that $\Delta f/f_o = 0.25$ (71).

The analysis of Smith et al. (70), whose results are replotted in
Figure 4.2 in a manner which facilitates discussion of weak coupling
situations, indicates that this bandwidth can be broadened by external
loading, the price paid being an increased conversion loss. In this
approach it is possible to draw upon the considerable volume of research
which treats the insertion loss-bandwidth trade-offs in broadband
matching to arbitrary impedances (87), (88) and to volume mode piezo-
electric transducers (89) - (92). That external circuit loading can
be effective in widening the bandwidth of IDTs on a strongly piezo-
electric material has been demonstrated clearly by practical measure-
ments of insertion loss for broadband surface wave delay lines on
lithium niobate substrates (71), (26), (93).

This technique assumes even greater importance when the medium
possesses low electroacoustic coupling. For example, consider the
propagation paths angled at $\pm 34^o$ to the X crystal axis on AT cut quartz.
In this situation, Table 3.1 shows that $|\Delta v/v| = 0.075\%$, so that for
an IDT with 3dB conversion loss the fractional bandwidth is, from
equation (4.201), 0.045. This bandwidth is insufficient for many

Figure 4.2

(Opposite)

Lossless three-port characteristics of a surface acoustic wave IDT.

[after (70), Figure 10]

C_E^2 is twice the electromechanical conversion loss

R_A is the acoustic reflection loss

T_A is the acoustic transmission loss

$Q_i = \pi/4k^2N = Q_m^2/N$ is an internal (radiation) quality factor deter-
mined by the electroacoustic coupling factor, k^2, of the medium,
and the number of electrode pairs, N, in the IDT.

$Q_e = \omega R_g C_T$ is the transducer quality factor due to external circuit
connections. R_g is the external damping resistance, and C_T is the
capacitance of the IDT.

Minimum electromechanical conversion loss for a particular N results
when $Q_e = Q_i$.
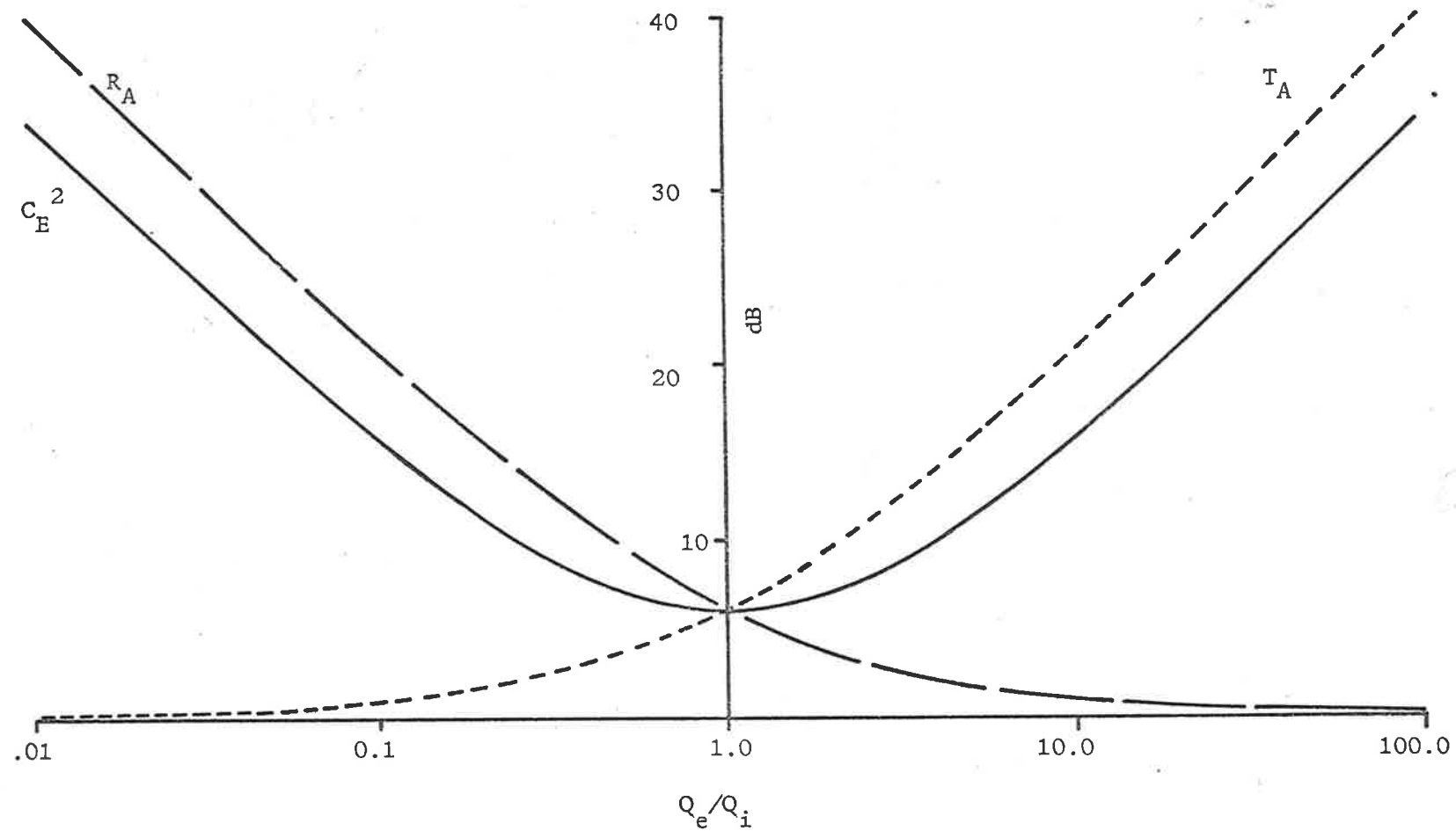
Figure 4.2

Lossless three-port characteristics of a surface acoustic wave IDT.

[after (70), Figure 10]

practical applications - e.g. the transmission of carrier frequency pulses of short time duration - and must be extended by loading the transducer with external circuit elements. To date the main utilization of weakly piezoelectric materials has been as substrates in multitap surface wave delay lines (28), (29). In these devices the taps are simple bidirectional IDTs, of few electrode pairs, which remain untuned to minimise the amount of energy which is withdrawn from the main acoustic signal. Perhaps this is why, with rare exception (94), details of transducer tuning and matching circuits, used in experimental studies of surface waves on low coupling media are not provided in general.

The following section describes the design approach adopted throughout the current investigation to increase the bandwidth of, and to impedance match, surface wave IDTs operating on quartz. An attempt is made to relate the behaviour of these broad-banded arrays to the theoretical performance predictions (70).

4.21 Tuning and Impedance Matching of Transducers.

In Figure 4.3(a) an IDT is represented by a shunt equivalent circuit comprising a capacitance, C_T, and a parallel resistance, R_a, (71), where

$$C_T = \text{transducer capacitance}$$

and R_a = transducer radiation resistance.

The transducer is tuned and matched to its external circuit connection, (represented by the voltage generator, e_s, of source impedance, R_s, normally of 50 ohms), by means of a transformer, the secondary winding inductance, L_s, of which resonates the transducer capacitance at the operating frequency, ω ; i.e.,
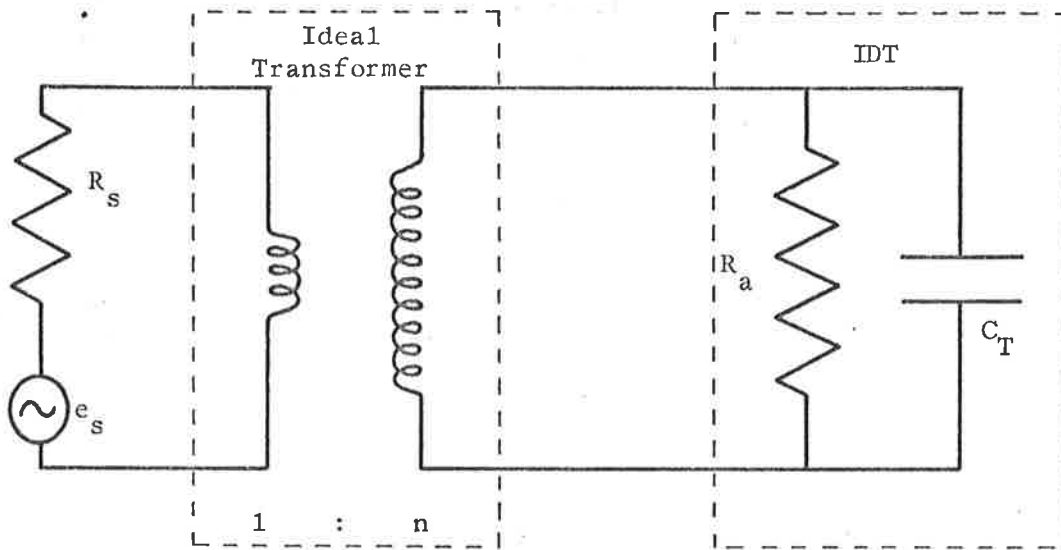
(a) Equivalent circuit for a tuned and matched IDT.
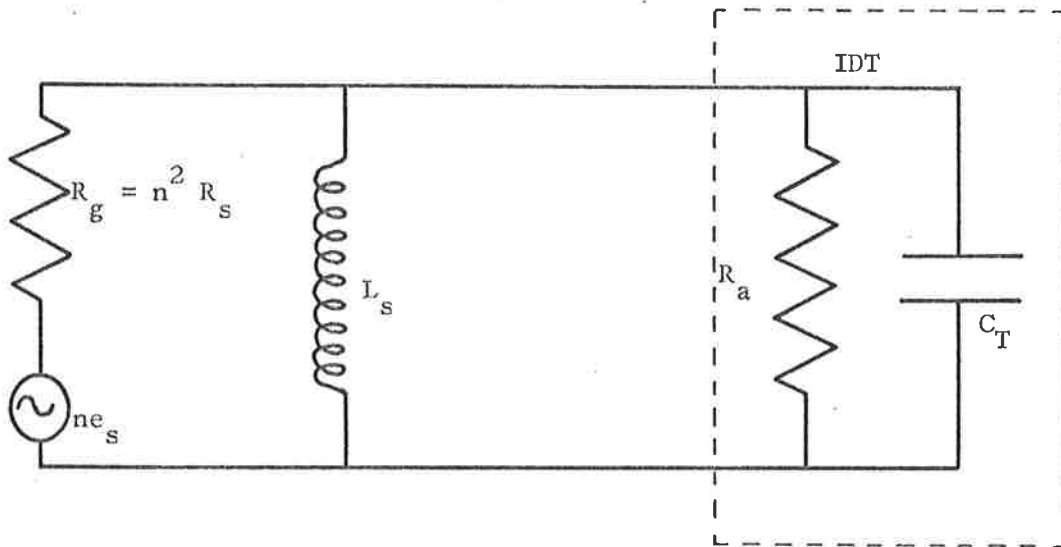
(b) Simplified equivalent circuit for a tuned and matched IDT.

Figure 4.3

Tuning and impedance matching of interdigital

array transducers.

$$L_s = 1/\omega^2 C_T \tag{4.211}$$

In this shunt representation the radiation resistance is (70)

$$R_a = \pi/4k^2 N C_T \omega \tag{4.212}$$

where k^2 ($\doteq 2 \ |\Delta v/v| \ $) is, as usual, the electromechanical coupling

factor. Thus associated with the transducer and its equivalent circuit

of Figure 4.3(a) is an internal (radiation) quality factor defined to

be

$$Q_i = \omega C_T R_a$$

which, from equation (4.212), has the value

$$Q_i = \pi/4k^2 N \tag{4.213}$$

By assuming that the matching transducer is ideal and has a unity

coupling factor the equivalent circuit may be rearranged into the more

convenient form shown in Figure 4.3(b). This diagram indicates that

the quality factor due to the external circuit connections is

$$Q_e = \omega R_g C_T \tag{4.214}$$

where $R_g = n^2 R_s$, due to impedance transformation, and n is the secondary

to primary turns ratio. The loaded circuit quality factor becomes

$$Q_L = Q_i Q_e / (Q_i + Q_e) \tag{4.215}$$

From the equivalent circuit of Figure 4.3(b) it is clear that the

power radiated by the transducer is

$$P_R = \left[\frac{n e_s}{R_g + R_a} \right]^2 R_a \tag{4.216}$$

while the available source power is

$$P_A = e_s^2 / 4R_s \tag{4.217}$$

If a resistance ratio, R, is defined to be

$$R = R_g / R_a = Q_e / Q_i \tag{4.218}$$

then the radiated to available power ratio can be written as

$$P_R/P_A = 4R/(1 + R)^2 \qquad (4.219)$$

which is a maximum when $R = 1$; i.e. when $Q_i = Q_e = 2Q_L$.

In surface acoustic wave propagation directions for which the electroacoustic coupling factor is small, equation (4.213) shows that a high value of Q_i is encountered, which leads, in turn, to large values of Q_L required for optimum power transfer. This Q_L may be too great to accomodate, without severe envelope distortion, the short rectangular pulses (typically 1-2 μsec bursts of 10 MHz RF) commonly launched in microsonic devices. The only way to reduce Q_L is to lower Q_e by reducing R_g. An inevitable consequence is, as emphasised by equations (4.218) and (4.219), a reduced radiated to available power ratio and hence large amounts of energy are dissipated in the external circuit elements. The technique is, therefore, to select a suitable value of Q_L (= 2 for AT cut delay lines) which, in a given situation, fixes the necessary Q_e and which further determines, through equation (4.214), the secondary to primary turns ratio. A surface wave delay line whose transmit and receive transducers have been tuned and matched by this procedure is pictured in Figure 4.4.

4.22 Electromechanical Conversion Losses.

In all experimental aspects of this study it was assumed, under the constraint of operating with short signal pulses, that bandwidth was of primary importance, so that moderately high electromechanical conversion losses were tolerated. By way of example consider once again the performance of two IDTs, each of 5 electrode pairs, operating on the path which makes an angle of 34° to the X crystal axis on AT cut quartz. The external quality factor for each array is $Q_e = 0.5$,

Figure 4.4

(Opposite)

Tuned and matched surface acoustic wave delay

line (9 MHz) on an AT cut quartz crystal.
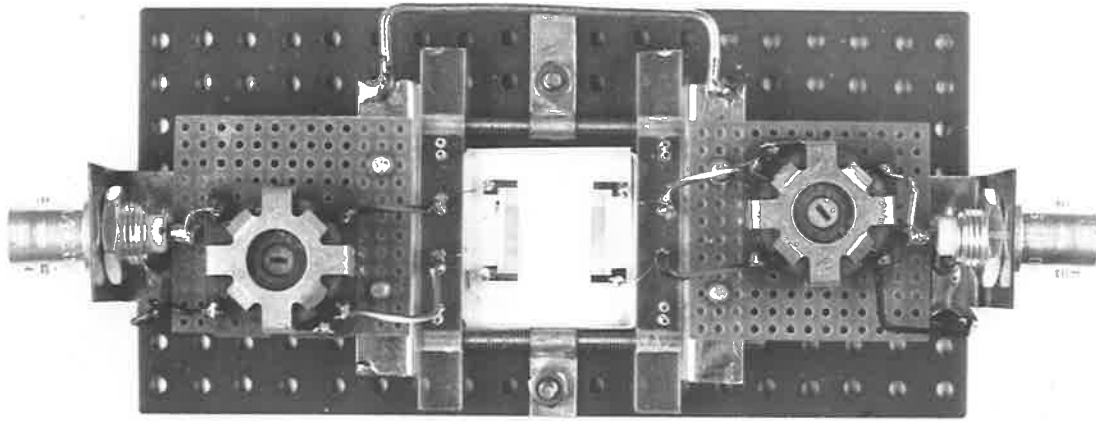
Propagation along
X axis.

while each has a radiation quality factor, calculable from equation
(4.213), of $Q_i \doteq 100$, so that $Q_e / Q_i \doteq 0.005$. The analytical results
plotted in Figure 4.2 (70) predict a two-way electromechanical conver-
sion loss of 40dB for this transducer pair, and an acoustic reflection
loss of 46dB at each array. As is discussed in greater detail in
section 5.34, a two-way conversion loss of 42.5dB was recorded experi-
mentally under the afore-stated conditions.

4.23 Testing of Delay Lines.

The five delay lines were tested by applying a 1μsec pulse of
RF carrier to the transmitting array and observing the signal received
at the second transducer (78). For four of the delay lines a surface
acoustic wave signal of large amplitude was detected at the receiving
IDT, the strongest response being for centre frequencies in the vicinity
of 9MHz, the approximate design centre frequency. But for the crystal
whose transducers were aligned along the Z' axis, no surface wave signal
could be detected. In view of the analytical curve of Figure 3.5(c),
which shows that the electroacoustic coupling between a surface wave
and an IDT is essentially zero for this wave vector orientation, this
result was not surprising. For extremely weak coupling situations the
discussion of sections 4.21 and 4.22 reveals that a very large delay
line insertion loss arises - so great, in this particular instance,
that no surface wave signal could be observed at the receiver.

4.3 Phase Velocity Measurement Procedure.

The simplest method of determining surface wave phase velocity is
to measure accurately the distance, L, between corresponding points on
the transmit and receive transducers and the elapsed time, T, between
excitation of the launching array and detection of the propagated

signal at the receiving array; the desired velocity can then be calcula-
ted as

$$v_s = L/T \qquad\qquad\qquad (4.301)$$

For the four useful AT cut quartz delay lines the predicted largest

velocity difference, namely that between the waves propagating along

the X crystal axis and at 60° to this axis, can be seen, from Figure

3.5(a), to be only 6%.   Hence quite an accurate practical procedure

is needed to observe the small changes in velocity for different delay

lines.

A block diagram of the equipment used in this experiment is presented

in Figure 4.5 while the photograph of Figure 4.6 pictures the actual

items.   An extremely short pulse, of 0.7μsecs duration and of 9MHz

carrier frequency, was applied to the transmitting transducer of a

delay line.   The "A intensified by B" and "Delay Time Multiplier"

facilities of the Tektronix 585 CRO, (the latter having been calibrated

previously using a stable RF source and frequency counter), allowed

the time delay, T, to be measured to an accuracy of 0.2% (T $\doteqdot 4\mu$secs).

A Nikkon Measurescope enabled the distance, L, between the centre

electrodes of the two IDTs to be recorded as 12.485 $^+_-$0.2mm.   From

these two results and equation (4.301), the surface wave phase velocity

was calculated.

The four working delay lines were subjected to this experimental

procedure.   Each step of the process was repeated several times and

the results averaged to improve accuracy further.   The precise orienta-

tions of the delay lines were measured by means of the Nikkon Measure-

scope, which permitted a determination of the angular separation between

the delay line axis and the crystal edges.   But during machining of

Figure 4.6

(Opposite)

Items of equipment used in surface acoustic wave phase

velocity measurements.
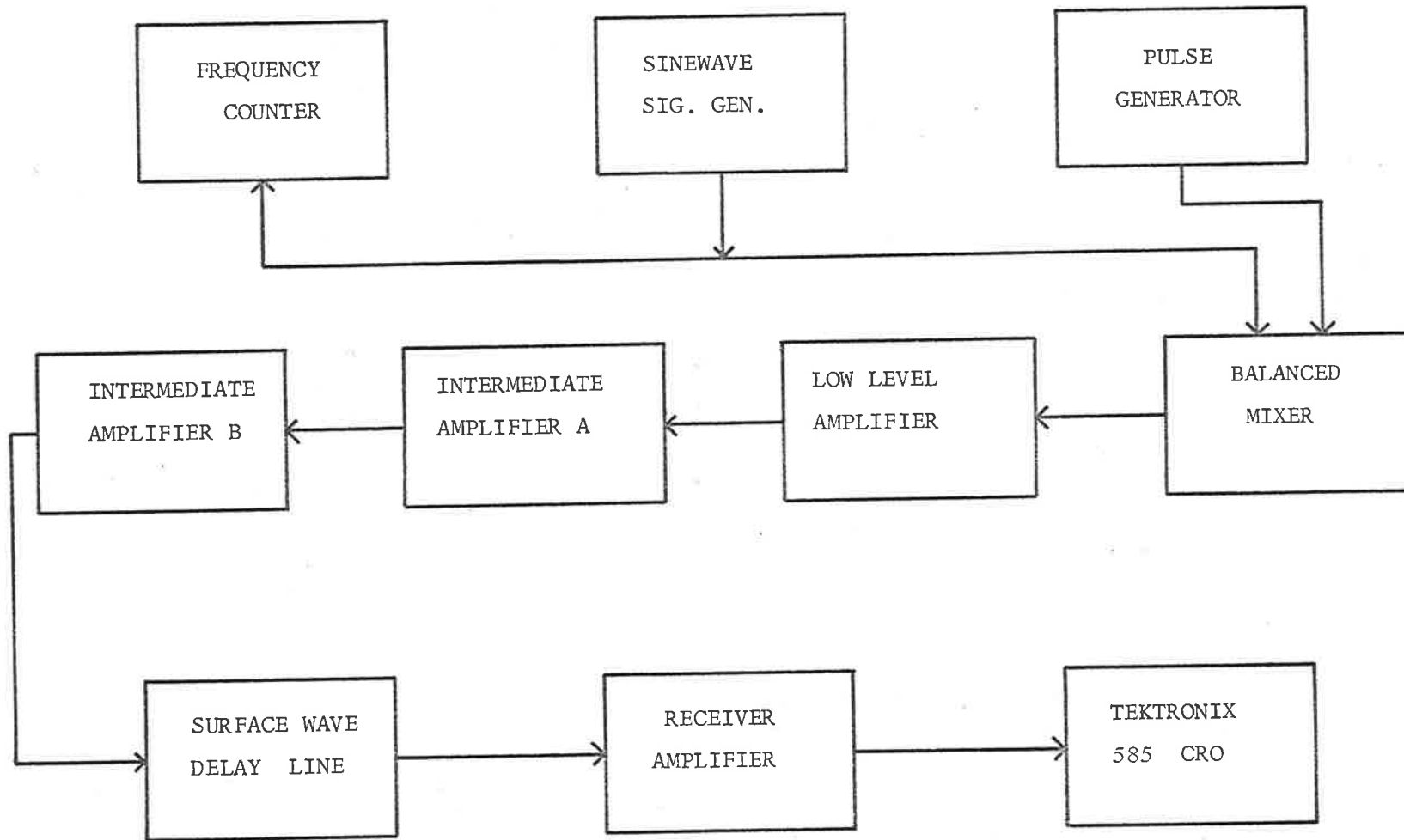
Figure 4.5

Block diagram of experimental arrangement for measurements of surface
wave phase velocity.

Figure 4.6

(Opposite)

Items of equipment used in surface acoustic wave phase

velocity measurements.
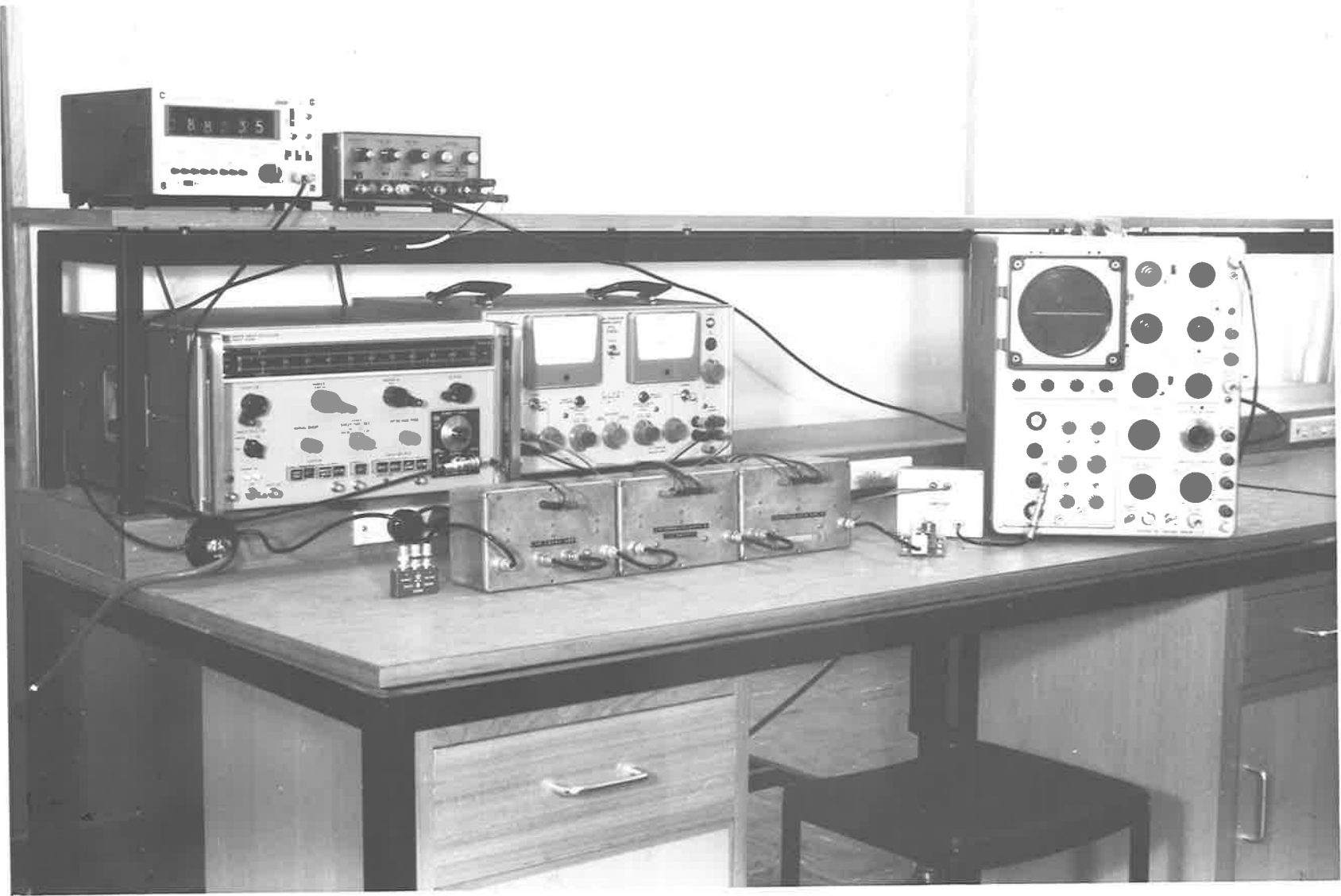
the AT cut substrates from the original crystal, the edges of each
plate were oriented with the X and Z' axes only to within $\pm 1^\circ$.

The single quantity which can be recorded least accurately in the
above method is the time delay, T; this can be removed from the final
calculation of surface wave phase velocity by resorting to phase
interference techniques (95), (96). This indeed was done, and the
measured velocities showed close agreement not only with those observed
by the simpler "elapsed time-distance" procedure but also with the
analytical values. However it was realized later that a number of
uncertainties, which could have been resolved only by detailed equiva-
lent circuit analyses of the now-dismantled transducer tuning circuits,
could have introduced small phase shifts which would have a minor, but
noticeable (in terms of the desired experimental accuracy of approx.
0.3%) effect on the measured velocities; for this reason these results
are not presented here. Alternatively, to avoid the necessity of a
detailed circuit analysis, phase interference measurements should
have been taken at two frequencies corresponding to adjacent maxima or
minima (95) or two receiving transducers should have been employed (96).

4.4 Results of Surface Wave Velocity Measurements on AT Cut Quartz.

The four experimentally recorded surface wave phase velocities
are plotted in Figure 4.7, together with an analytical velocity curve
drawn from the results of "Pianm" applied to free surface propagation.
All of the measured values show a discrepancy of less than 0.3% with
the theoretical velocities. Clearly the $\pm 1.0^\circ$ angular tolerance
described in section 4.3 could not significantly influence this agree-
ment. The harmony of these theoretical and practical phase velocities
engenders further confidence in the analysis and computational procedures,
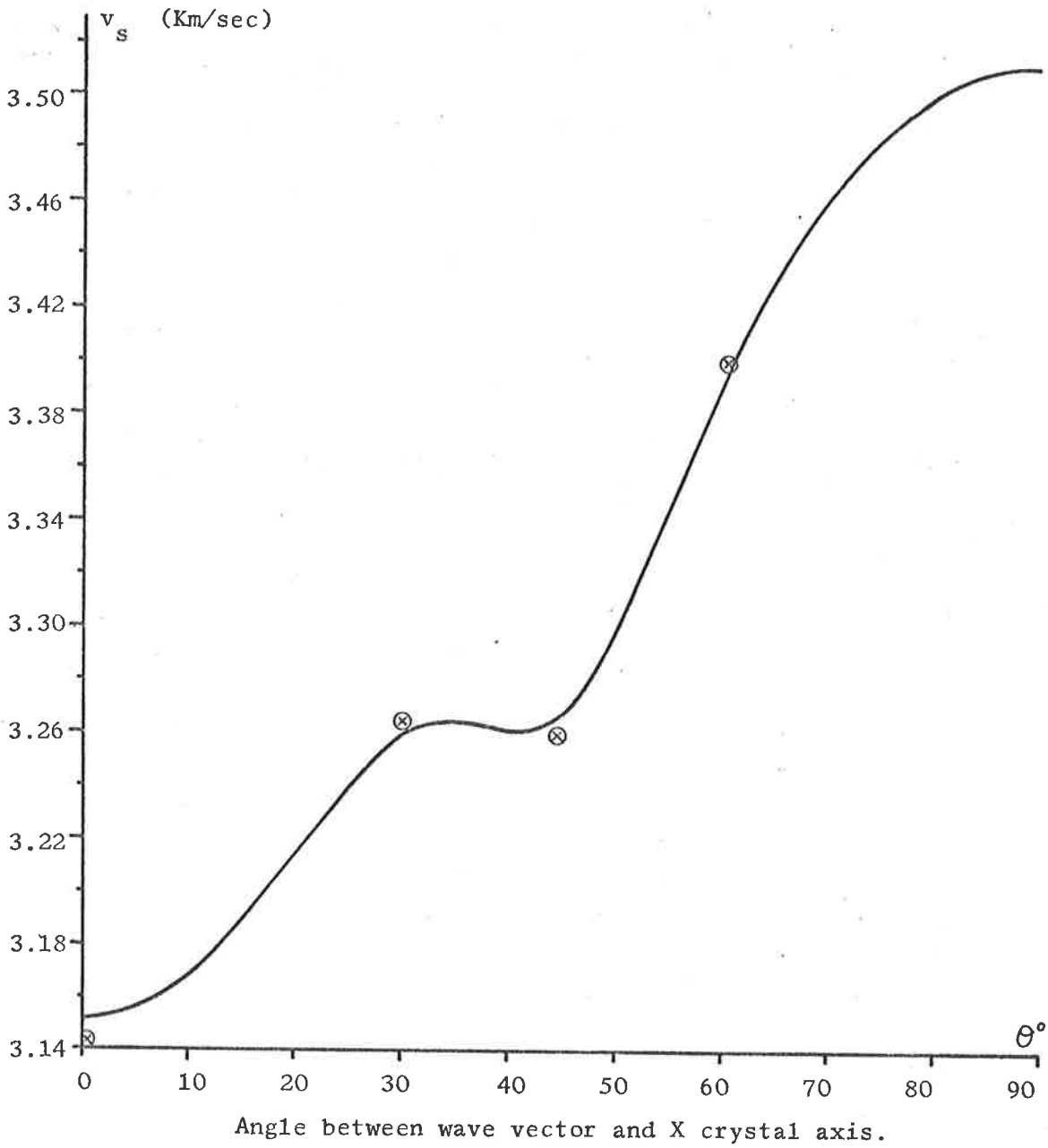
Figure 4.7

Surface acoustic wave phase velocity on AT cut quartz.

⊗ Experimental measurements.

━━━Analytical results from "Pianm".

and, as discussed in section 4.0, provides strong justification for the design of microsonic components on AT cut quartz using the analytical data summarised in Figure 3.5.

CHAPTER V

DESIGN AND FABRICATION OF A MICROSONIC CROSSBAR COUPLER.

5.0 Introduction.

Chapters III and IV have discussed at length the properties of
surface acoustic waves propagating on an AT cut quartz crystal. They
lead to the conclusion that this particular substrate can be utilized
effectively in the construction of a microsonic directional coupler
which exploits periodic mass-loading of the propagation surface as the
coupling mechanism. Attention is now focussed upon the design and
fabrication of such a device. Details of practical device performance
do not follow immediately but are deferred so that subsequent chapters
can develop an analysis of coupler behaviour based on the intimate
description of the device contained here. This allows theoretical and
experimental coupler response curves to be presented together and to be
compared closely in Chapter X.

5.1 Design of Metal Overlay Patterns for the Crossbar Coupler.

Throughout experimental studies of the surface acoustic wave cross-
bar directional coupler two separate and slightly different masks were
used to fabricate the metal overlay patterns. These are pictured in
Figure 5.1, parts (a) and (b), and are labelled as style A and style B
respectively. Both are essentially identical in their geometry, and
both evolved from the same design strategy. The only important
difference between the two masks is that style B includes an additional
IDT, which permits the amplitude of a launched surface acoustic wave
to be monitored before it encounters the region of periodic surface
mass-loading. Although couplers of style B have five transducers, they
are four port devices. Because of the basic similarities between the

Figure 5.1

Surface acoustic wave crossbar directional coupler pattern on

AT cut quartz.

(a) (Opposite) Photograph of device mask, style A.

(b) (page 68) Photograph of device mask, style B.

Port 3 Port 2

Port 1 Port 4

34°
34°

X crystal axis

d

IDT 3

IDT 2

34°
34°

X crystal axis

d

IDT 5

IDT 1

IDT 4

68
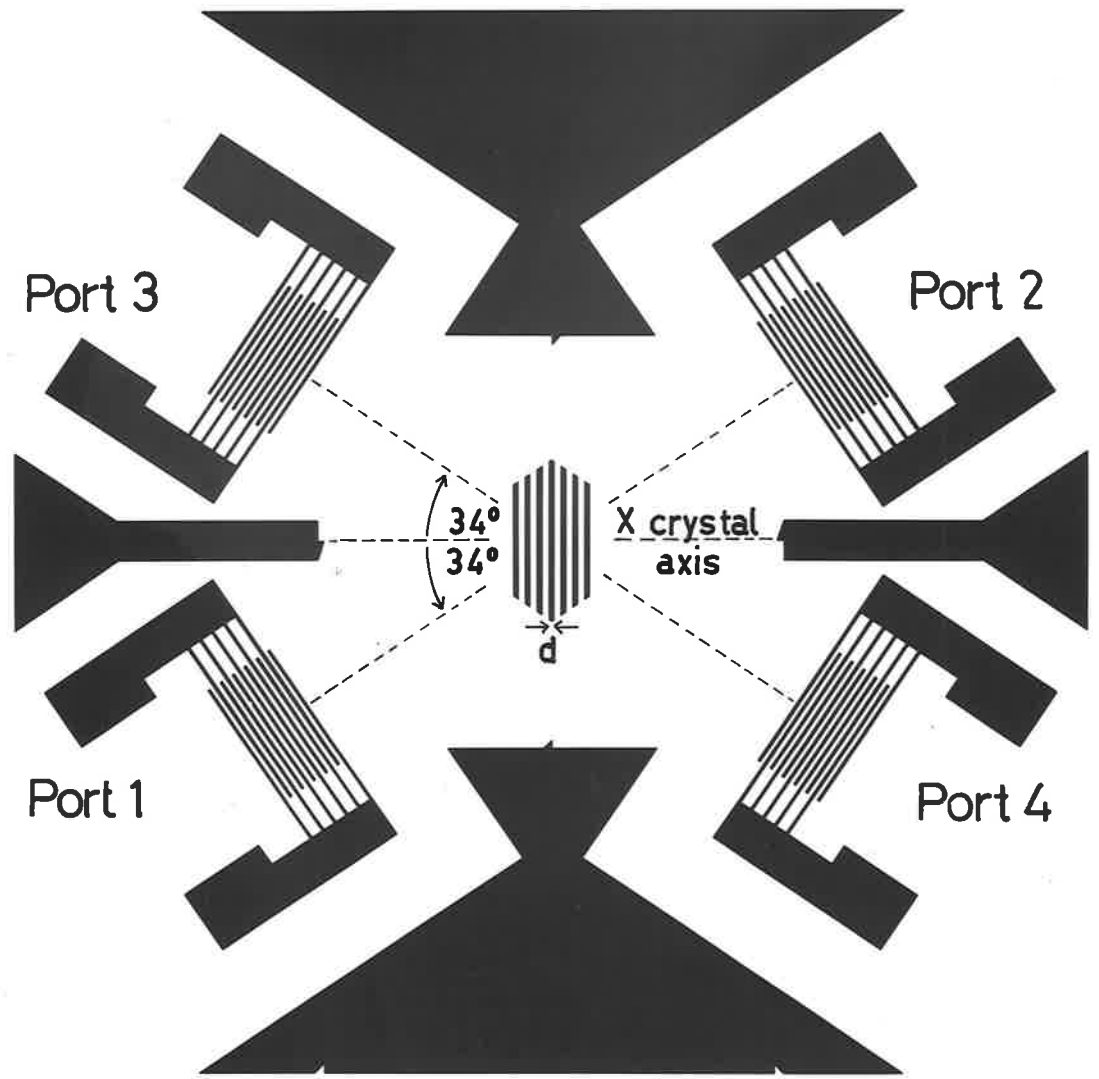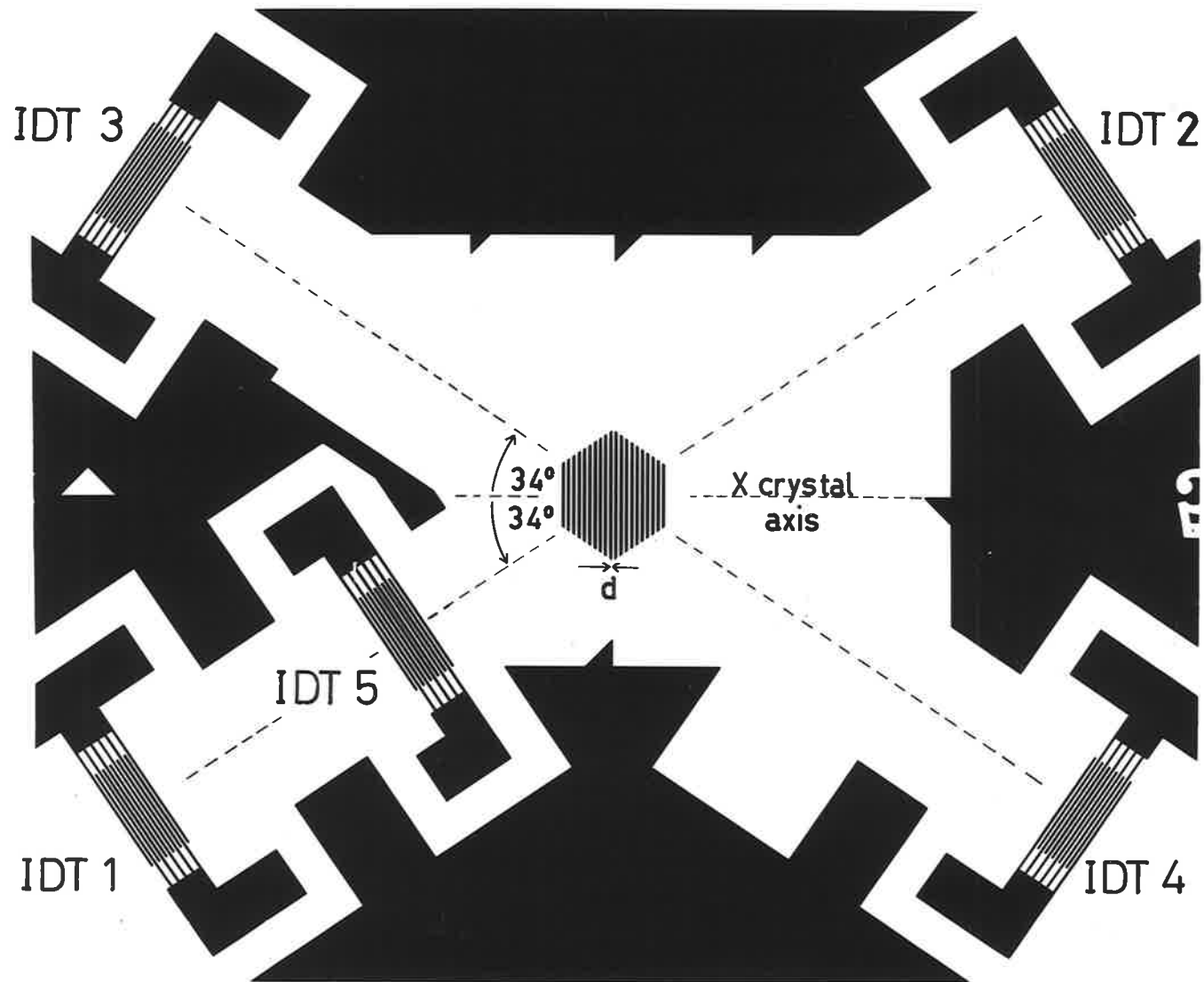
two patterns, the design concepts from which they emerged will be

discussed jointly.

5.11 <u>Orientation of Transmission Paths</u>.

For the reasons detailed in section 3.524, the main transmission

paths of the crossbar coupler, (i.e. between ports 1 and 2 and between

ports 3 and 4) are, as illustrated in Figure 5.1, placed at angles of

$\pm 34^{\circ}$ to the X crystal axis on AT cut quartz.   Furthermore it may be

recalled from section 3.52 that because of the inherent symmetries in

this particular cut, surface acoustic waves propagating in these two

directions have identical characteristics.

5.12 <u>Periodicity of Surface Mass-Loading Perturbation</u>.

The fundamental principles upon which the coupling mechanism of

the crossbar coupler, as pictured in Figure 5.1, depends were introduced

in section 2.3.   A surface wave launched in port 1, say, is, in part,

coherently scattered through interaction with the region of periodic

surface mass loading into a surface wave which is detected at port 3.

The balance of the acoustic energy is transmitted directly to port 2,

there being virtually no signal back-scattered to port 4, or, theoret-

ically, converted to volume modes.   In this particular context, where

both the incident and scattered signals are surface waves, the general

conservation conditions, equations (2.201) and (2.202), reduce to

$$\underset{\sim}{\beta_i} + \underset{\sim}{\beta_p} + \underset{\sim}{\beta_s} = 0 \tag{5.121}$$

$$\text{and} \quad \omega_i = -\omega_s \tag{5.122}$$

where fundamental frequency operation has been assumed.   The notation

is as established in section 2.2; viz ω_i and $\underset{\sim}{\beta_i}$ are the frequency and

wave vector of the incident wave , ω_s and $\underset{\sim}{\beta_s}$ are the corresponding

parameters of the scattered wave and $\underset{\sim}{\beta_p}$ is the wave vector of the

periodic surface perturbation. Figure 5.2 depicts the wave vector

diagram drawn from equation (5.121) and related to the centre frequency

behaviour of the coupler whose geometry is shown in Figure 5.1.

From this diagram it is clear that a necessary band centre condition

which must be fulfilled in order that the coupling interaction be

cooperative in terms of spatial dependence, is that

$$|\beta_p| \quad = \quad 2 \quad |\beta_i| \quad \cos\theta \qquad\qquad (5.123)$$

in which, as indicated in Figure 5.1, $\theta = 34°$. Thus the width, d,

of each mass-loading strip must be

$$d \quad = \quad (\lambda_o \sec\theta) / 4 \qquad\qquad (5.124)$$

λ_o being the wavelength of the incident wave at the device centre

frequency. The surface mass-loading perturbation is composed, there-

fore, of elements which are a factor of $\sec\theta$ wider than the electrode

fingers of the IDTs in each of the ports and which are placed normal to

the X crystal axis, (refer Figure 5.1), so that $\underset{\sim}{\beta_p}$ is colinear with

this axis, as shown in Figure 5.2.

This choice of $\underset{\sim}{\beta_p}$ ensures that a signal of large amplitude is

coupled to port 3 when port 1 is excited. At the same time it means

that the amplitude of the directivity wave, back-scattered to port 4,

is small, because the wave vector of this signal cannot satisfy the

conservation relation (5.121) and thus cannot arise from an interaction

which is cooperative in its time and spatial dependences.

5.13 Frequency Response Considerations.

Intuitively the coupling mechanism could be expected to exhibit

a predominantly sin x/x frequency dependence, where $x = N\pi(\omega - \omega_o)/\omega_o$,

N being the number of mass-loading strips in the interaction region

and ω_o the device centre frequency; this anticipated response provides
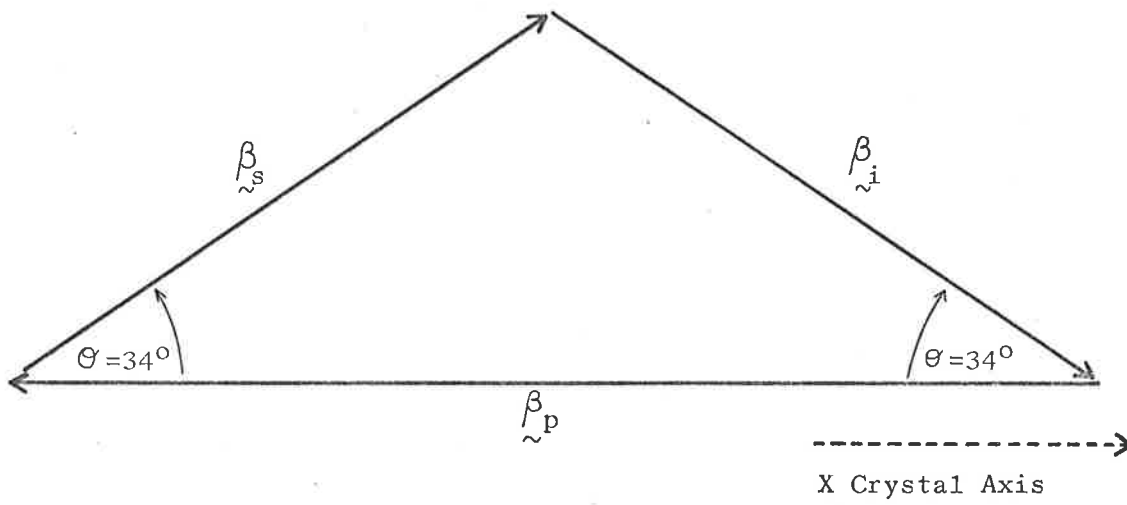
Figure 5.2

Centre frequency wave vector diagram for the
coupled signal in the microsonic crossbar coupler.

an approximate 3dB fractional bandwidth of (7/8N). Figure 5.1 shows

that couplers were fabricated with N = 10, (style A), or N = 20, (style

B), these values being thought to afford a suitable compromise between

bandwidth, (inversely proportional to N), and strength of coupled

signal (proportional to N). IDTs of five electrode pairs were to

provide the means of electromechanical conversion at the four ports

in both device styles. When externally tuned and loaded as described

in section 4.21, these transducers should possess a bandwidth - electro-

mechanical conversion loss characteristic suited to experimental studies

of the coupling mechanism:- most importantly they should provide

sufficient bandwidth to allow a complete exploration of the main lobe

of the coupling response while tolerating only small distortion of the

launched surface acoustic wave pulse envelope.

5.14 Preparation of Masks for Photofabrication Processes.

Techniques almost identical to those outlined in section 4.1

for the delay lines formed on AT cut quartz (78) were used to prepare

the original rubylith and final photographic masks for fabrication of

the crossbar couplers. A photographic reduction factor of 25:1 allowed

the mask for coupler style A, as illustrated in Figure 5.1(a), to fit

onto a one inch square substrate area, so that this device could be

constructed on the same AT cut crystals used in the delay line experi-

ments described in Chapter IV. Couplers of style A were designed to

function at a centre frequency of 10.3MHz and to have a separation

between ports (i.e. between transducers 1, 2 and 3, 4 in Figure 5.1(a))

of 1.3cms; the latter should allow propagation of pulse lengths

approaching 4μsecs without interference, at the receiving transducer,

due to a signal electromagnetically coupled from the input port. All

IDT apertures were of approximately ten surface wavelengths, so that all measurements could be made in the near field region (34).

Crossbar couplers of style B were planned to fit on a somewhat larger AT cut quartz plate of dimensions 2.0 inches along the X crystal axis, 1.5 inches along the Z' axis, and 0.15 inches thick. A photographic reduction of 20:1 from the original rubylith pattern to the final mask provided a design centre frequency of 10.6MHz and a transducer separation of approximately 4cms along the main transmission paths. Hence the main advantage of coupler style B, apart from the availability of an additional monitor transducer, was the provision of longer propagation distances, which should enable the detection of surface wave pulses in excess of $10\,\mu$secs duration without interference from an electromagnetically coupled signal. Thus practical measurements, which would have to be made in a pulse mode to avoid the build-up of spurious signals, (perhaps due to electromagnetic coupling or to surface wave reflection at the edges), would be more representative of CW performance in the improved coupler of style B. In keeping with the greater path lengths, the transducer apertures in this pattern were increased to thirteen surface wavelengths so that measurements could be taken once again under near field conditions (34).

In both coupler styles elements of the surface mass-loading grid were of a non-uniform length. Figure 5.1 illustrates that the perturbed surface area was that illuminated by both the launching transducer and by the transducer receiving the scattered wave (i.e. by IDTs 1 and 3 or 2 and 4). Another feature common to both styles A and B was the incorporation of large metallised areas of the substrate surface between ports:- when earthed these plated regions should reduce the

electromagnetic coupling between transducers.

5.2 Fabrication of the Crossbar Coupler.

All of the surface wave crossbar couplers were constructed by
the same photolithographic methods, although, as detailed below, these
differed somewhat from the procedures described in section 4.1 for delay
line fabrication (78).

5.21 Metal Overlay Deposition.

The material most commonly employed in IDT manufacture on a quartz
crystal is aluminium. This metal offers the advantages of good
adhesion and acoustic impedance matching to the quartz substrate (73).
But because the interaction in the crossbar directional coupler was
to be provided by surface mass-loading, a material of greater mass
density than aluminium, ($\rho = 2.7$) (97), was needed to obtain appreciable
coupling with moderate overlay film thickness. The obvious choice
was gold, whose mass density is $\rho = 19.3$ (97).

Initial attempts to fabricate the pattern of Figure 5.1(a) from
a gold film vacuum deposited upon an AT cut quartz surface were plagued
by poor metal adhesion. Two methods by which this problem could be
overcome were contemplated. Firstly an extremely thin interface layer
of a suitable material (chromium) could be applied to the quartz
surface before deposition of the gold. Although this method offered
a permanent and possibly the most ideal solution, it would have com-
pounded the problems of deposition, (only a single filament being
available in the vacuum chamber), and of etching (necessitating a more
sophisticated and perhaps a two-stage process). These factors
suggested that a concentrated effort should commence on the second
approach, which rested upon the belief that more elaborate substrate

cleaning procedures would substantially increase overlay adhesion.
The first improvement involved the design, construction and imple-
mentation of a vapour degreasing unit (trichlorethylene reflux bath)
to be used immediately following the normal cleaning procedures (78)
and immediately prior to sealing the substrates in the vacuum chamber.
Utilization of a recently installed glow discharge unit comprised
the second improvement to the cleaning procedures.   With these addi-
tional processes, a device yield in excess of 80% was obtained for the
frequency range of interest (a 10MHz centre frequency requires a line
width of approximately 75microns for one IDT electrode).

The fingers of an IDT are spaced at a periodicity conducive to
the coherent reflection, at subsequent electrodes, of a launched surface
acoustic wave (73) (refer Figure 1.1).   For this reason the whole of
the AT cut crystal surface was coated with a comparatively thin,
(typically 0.1micron), layer of gold; from this IDTs, which could be
expected to function with quite small inter-electrode reflections,
would be etched at a later stage.   A mask was lowered over the crystal
surface and a further thick film, (typically 0.5 - 2 microns), of gold
was deposited over a circular region at the centre of the substrate:-
from this the periodic surface mass-loading bars would be formed.

5.22 Preparation of Photoresist Mask.

KTFR photoresist was applied, exposed and the desired image
developed in the usual manner (78).   The photographic mask was oriented
relative to the substrate by the technique outlined in section 4.1; it
was found that with this method the transmission paths of the crossbar
coupler could, with care, be aligned to within $\pm 0.5^{\circ}$ of their exact
location as determined by the crystal edges.   Thus the overall

tolerance in siting the main coupler paths at $\pm34^{\circ}$ to the X crystal

axis became $\pm1.5^{\circ}$ (refer section 4.3).

5.23 <u>Etching of Metal Overlay Pattern</u>.

An iodine solution (98), (10g. I_2, 20g.KI, 400ml. H_2O), diluted

as stated to provide a controllable etch rate of approximately .08 microns/

minute at $68^{\circ}F$, yielded the desired pattern from the photoresist mask

on the gold overlay.   Because of the disparity in thickness of the two

gold films, on placing the quartz crystal into the etch the IDTs

rapidly formed from the thin overlay, but considerable time was required

for the mass-loading bars to be etched from the much thicker central

region.   It was observed that if this mass-loading film was too thick,

there was a tendency for the resist to be attacked, after a considerable

period of time, by the etch; this resulted in damage to the completed

transducer patterns.   Although this factor, together with the associated

problem of under-cutting, did not pose any serious problems in device

fabrication during this study, it does present a practical limitation

to the fabrication of strongly mass-loading grids by chemical processes.

After etching the remaining photoresist was removed by a commercial

stripping solution.   Completed directional coupler patterns of both

styles A and B are pictured in Figure 5.3.

5.3 <u>Preparation of Crystals for Experimental Device Studies</u>.

Additional tasks had to be undertaken to prepare the microsonic

crossbar couplers for experimental study.   These included steps to

reduce interference from spurious signals, the provision of external

circuit connections and the incorporation of suitable external tuning

and loading for the IDTs.

Figure 5.3

Completed surface acoustic wave crossbar coupler patterns

etched in gold on an AT cut quartz crystal.

(a) (Opposite) Coupler Style A on 1$''$ square AT cut

quartz crystal.

(b) (page 77) Coupler Style B on (2$''$ x 1.5$''$) AT

cut quartz crystal.
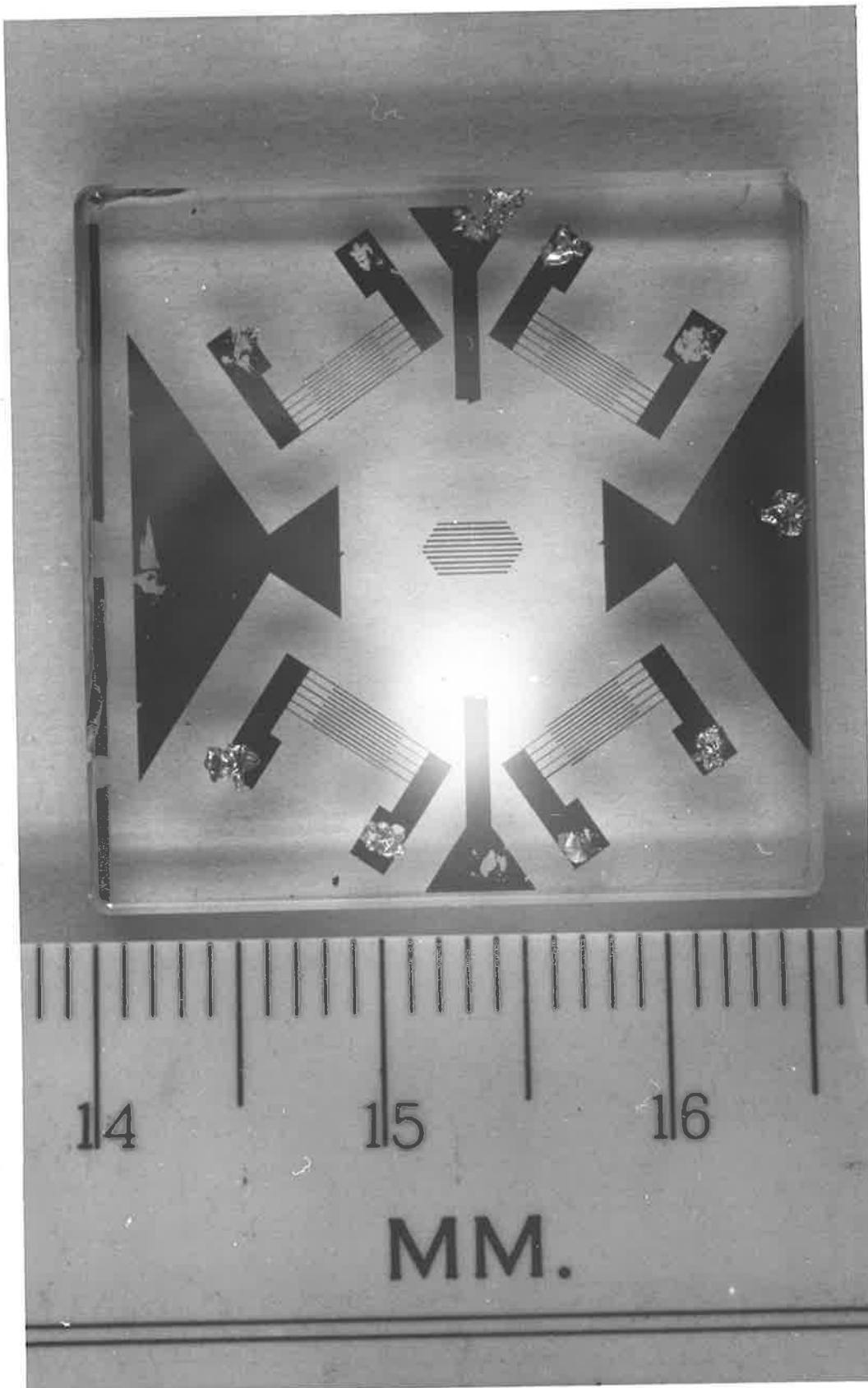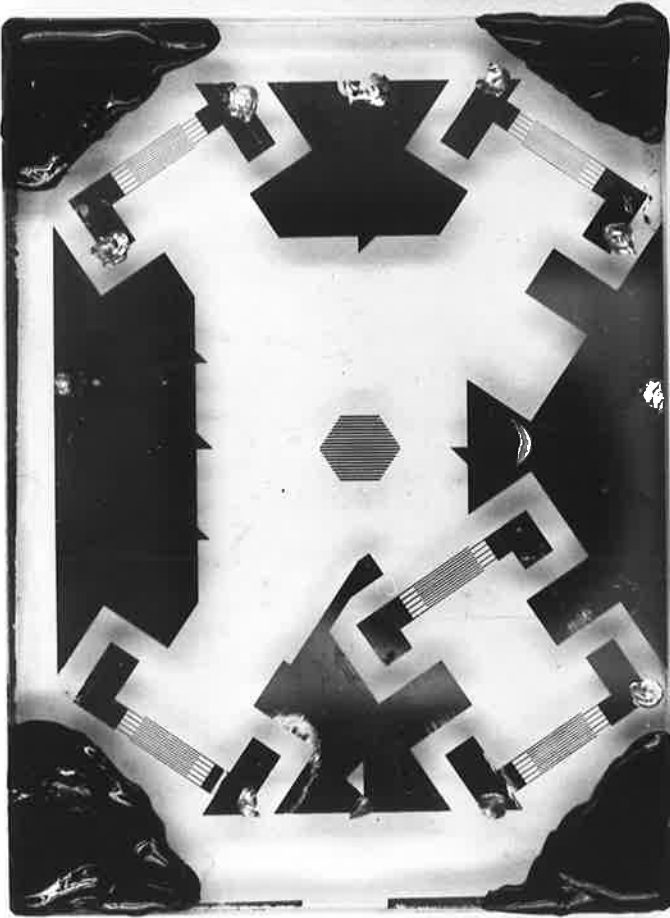
MM.

5.31 Suppression of Unwanted Surface Acoustic Wave Signals.

The photographs of the directional couplers contained in Figure 5.3 show that the transducers in each port were located quite near to the corners of the crystal.   In this situation one of the major sources of spurious acoustic signals was the surface wave, launched in the reverse direction by the bidirectional IDTs, which was reflected at the edges of the crystal (54), (78), (99) - (101) back towards the receiving transducer.   "Apiezon W", (black wax), (27), (102) small quantities of which were melted onto the substrate surface immediately behind each array, as depicted in Figure 5.3(b), damped these unwanted signals by more than 30dB.

5.32 External Circuit Connections.

Thin gold wires, 5 thousandths of an inch in diameter, soldered directly to the transducer terminals with pure indium, using a low temperature $(500^{o}F)$ soldering iron tip to avoid damaging the thin film overlay, proved the most effective means of providing external circuit connections.   Although commercial fluxes facilitated the creation of a neat, solid joint they were sufficiently corrosive to attack the gold film over a period of time.   Thus in all practical devices somewhat untidy, but good ohmic contacts were made without the aid of a flux.

5.33 Mounting of Crystals.

For the purpose of experimental study, the crystals on which couplers of style A had been fabricated were placed in the jig shown in Figure 5.4(a).   Because this was the first directional coupler to be investigated, the jig was quite simple.   Single tuned and matched input and output circuit connections were provided; measurements of

Figure 5.4

Surface acoustic wave crossbar directional couplers
mounted and tuned in preparation for experimental study.

(a) (Opposite) Coupler style A.

(b) (page 80) Coupler style B.
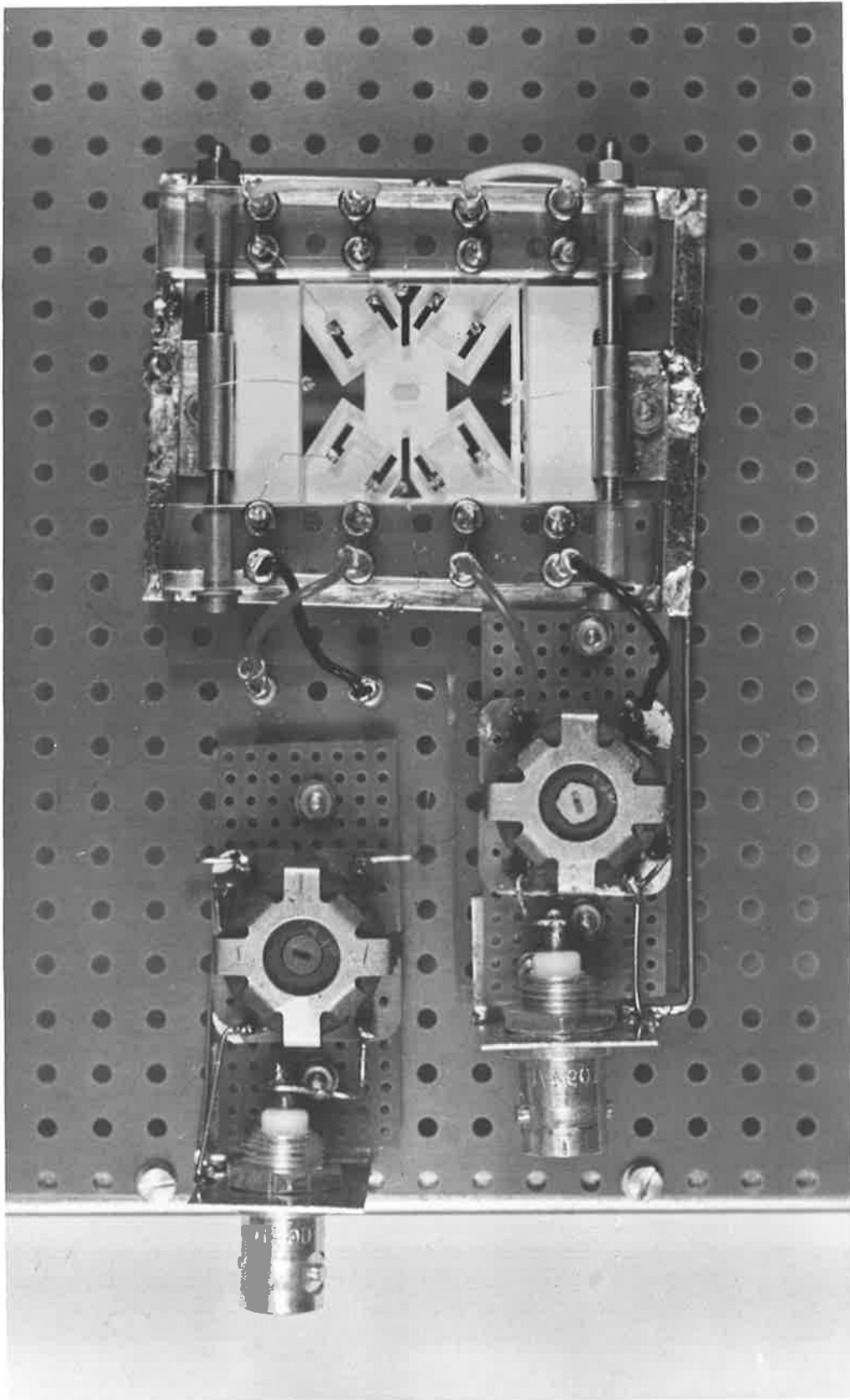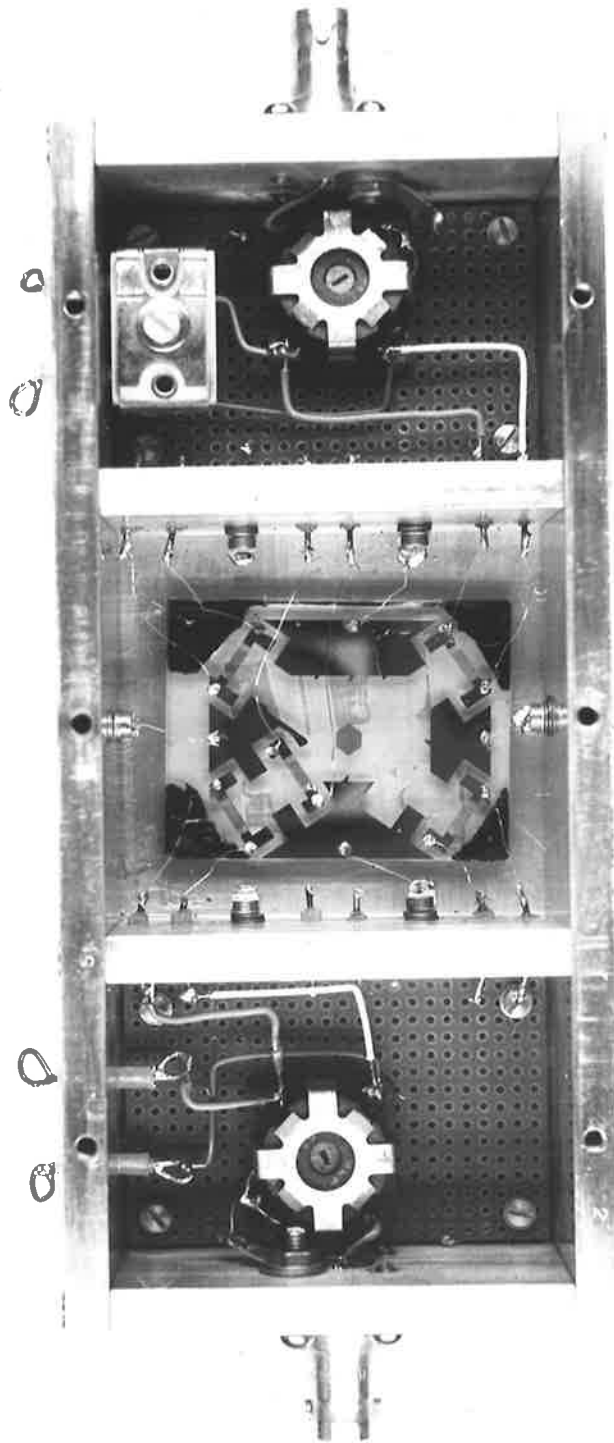
coupling factor were performed by connecting the same output circuit, in turn, to each of the detecting transducers. This experimental arrangement functioned quite satisfactorilly, but because of the lack of electromagnetic shielding, care had to be exercised to make certain that an electromagnetically coupled signal (of much greater amplitude than the propagated surface acoustic wave pulse) did not saturate the receiving amplifier.

To overcome this problem in the practical tests on couplers of style B, the crystals were housed in the more elaborate jig illustrated in Figure 5.4(b). The box was made from aluminium, and the crystal was held in place on the floor of the central compartment by adhesive tape - the proximity of the metal ground plane, on which the crystal rested, to the launching and receiving IDTs greatly reduced the amplitude of the electromagnetically coupled signal. Single input and output circuits were contained in separate compartments; access to the transducers was obtained by passing short lengths of wire through small holes drilled in the intervening walls.

5.34 Tuning and Matching of Transducers.

The transmitting and receiving IDTs were tuned and impedance matched by the basic method described in section 4.21. However, to facilitate tuning and to permit monitoring of the voltage applied to the launching transducer, a CRO probe (10 Megohm, 7 pf) was placed permanently across each transformer secondary winding, the required inductance of which became, therefore,

$$L_s = 1 / \omega^2 (C_s + C_T) \qquad (5.341)$$

where C_T represents, as before, the transducer capacitance and C_s is the total additional capacitance due to the CRO probe, wiring strays, etc.

.It is instructive to investigate, analytically, the effect of the capacitance, C_s, upon IDT performance. For this purpose the definitions of external load resistance, R_g, (Figure 4.3), external quality factor, Q_e, [equation (4.214)] , and transducer radiation quality factor, Q_i, [equation (4.213)] , are retained from the discussion of section 4.21, and the quantity

$$Q_s = \omega\, R_g\, C_s \qquad\qquad (5.342)$$

is introduced to take account of the extra capacitance. On propagation paths of weak electroacoustic coupling, $Q_i \gg Q_s$, Q_e so that from Figure 4.3 it can be seen that the loaded circuit quality factor is

$$Q_L \doteqdot (Q_e + Q_s)$$
$$\doteqdot \omega\, R_g\, (C_s + C_T) \qquad\qquad (5.343)$$

Experimental measurements on couplers of style B determined that $C_T = 1.1\,\text{pf}$ and $C_s = 11\,\text{pf}$. By providing the value of R_g required by the above relationship, each IDT was tuned to provide $Q_L = 5.0$, and hence $Q_e = 0.5$. As detailed in section 4.22, lossless three port junction theory predicts, for this situation $(Q_e / Q_i \doteqdot 0.005)$, a two-way electromechanical conversion loss of 40dB; in practical studies of style B crossbar couplers a 2-way conversion loss of 42.5dB was recorded. In view of the facts that the theoretical conversion loss is calculated from an analysis based upon the over-simplified equivalent circuit of Figure 4.3 and upon the assumption of an ideal transformer, this agreement is quite acceptable.

But it is important to note, from equation (5.343), that this predicted two-way conversion loss of 40dB can be achieved, in the presence of this particular capacitance, C_s, only with a loaded circuit quality factor of $Q_L = 5$. The analysis contained in section 4.21

indicates that in the absence of any additional capacitance, the same transducer performance can be obtained with $Q_L = 0.5(\doteqdot Q_e)$; i.e. the communication bandwidth can be increased by the factor $(C_s + C_T) / C_T$.

Although the comparatively low value of Q_e used in experimental studies of style B crossbar couplers introduced a high insertion loss, compensation in the form of adequate transmitter power and receiver amplification was available, and the relatively wide bandwidth afforded by working with $Q_L = 5$ ensured a range of frequency excursion suitable for the exploration of the complete main lobe of the coupled signal response.

CHAPTER VI

METHODS OF MICROWAVE ANALYSIS APPLIED TO ELECTROACOUSTIC

FIELD PROBLEMS

6.0 Introduction.

Perhaps the most useful analytical tools of microwave theory are

the reciprocity relation, the orthogonality condition for the normal

modes of an electromagnetic waveguide and the expression which describes

the amplitude of a normal mode excited by a known source distribution

(103) - (105).   Auld (106) has pioneered the application of these

concepts to studies of electroacoustic interaction systems.   His

fundamental paper which highlights the many similarities between the

electromagnetic and acoustic field equations, extends the three electro-

magnetic relationships to encompass the effects of elastic and piezo-

electric energy storage.   These techniques have been exploited by

Auld and other workers in analyses of various surface acoustic wave

phenomena:- included in this category are propagation (106), (107),

(108), transduction (72), (108), amplification (108), (109), surface

loading (108), (110) and scattering (108), (110), (111).   These

investigations proved quite fruitful and clearly demonstrated the power

and widespread applicability of this approach to electroacoustic field

problems.   In particular these methods offer a convenient means for

evaluating the theoretical performance of the surface acoustic wave

crossbar directional coupler.

This chapter develops expressions for the reciprocity relation,

the normal mode orthogonality condition and the amplitude of a coupled

normal mode as they relate to propagation in a piezoelectric waveguide.

In so doing it prepares a foundation upon which the crossbar coupler

analysis, as contained in Chapters VII, VIII and IX, can be built.

Derivations of the three relationships can be undertaken in either

of two formulations (112), (113); the "direct", which involves products

of the field variables, or the "mixed" or "complex", which involves

products of the field variables and their complex conjugates.   Closer

examination discloses that the two formulations provide results of

similar utility and, in determinations of the required expressions,

lead to analyses of similar complexities.   For definiteness this

chapter, and those which follow, are written within a "complex" frame-

work.   As emphasised by Waldron (107), a choice of this formulation

demands that, in extensions of the basic analysis to perturbation and

variational treatments, attention be given to the phase relationships

which exist between the field quantities.

Because the electroacoustic reciprocity relation, and descriptions

of the methods by which it may be derived from Maxwell's equations and

the fundamental piezoelectric field equations, have appeared several

times in the litterature (106), (108), (112), (113), in a number of

different forms, its validity will be assumed and the relationship will

not be verified from first principles.   An orthogonality condition

for the normal modes of a piezoelectric waveguide will be established

from the reciprocity relation.   These two results will be used to

determine an expression for the amplitude of a normal waveguide mode

excited by a known source distribution.   Although both the orthogonality

(34), (72), (106), (108), (111) - (114) and the coupled mode amplitude

relationships (34), (72), (106), (108), (109), (112), (113) are to be

found in the litterature as well, a detailed treatment is warranted in

order to present the expressions in the form most suited to the

ultimate goal:- i.e., analysis of the surface wave crossbar coupler.
Throughout this chapter opportunities to place the results in perspec-
tive with the work of other researchers are created.

Chapter VII takes the analysis developed here in an electroacoustic
waveguide context and modifies it to deal with interaction on a surface,
as encountered in the microsonic crossbar coupler.

6.1 Notation for Field Variables.

The principal field variables of propagating electroacoustic mode
"i" may be summarised as follows;

Electromagnetic

$\underset{\sim}{E}_i$ (3x1) vector $\longleftrightarrow$ electric field

$\underset{\sim}{H}_i$ (3x1) vector $\longleftrightarrow$ magnetic field

$\underset{\sim}{J}_i$ (3x1) vector $\longleftrightarrow$ current density

$\underset{\sim}{e}_{t_i}$ (3x1) vector $\longleftrightarrow$ transverse component of electric field

$\underset{\sim}{e}_{x_i}$ (3x1) vector $\longleftrightarrow$ longitudinal component of electric field

$\underset{\sim}{h}_{t_i}$ (3x1) vector $\longleftrightarrow$ transverse component of magnetic field

$\underset{\sim}{h}_{x_i}$ (3x1) vector $\longleftrightarrow$ longitudinal component of magnetic field

Acoustic

$\underset{\approx}{T}_i$ (3x3) matrix $\longleftrightarrow$ acoustic stress

$\underset{\sim}{v}_i$ (3x1) vector $\longleftrightarrow$ acoustic velocity

$\underset{\sim}{F}_i$ (3x1) vector $\longleftrightarrow$ acoustic body force density

t_{t_i} (3x1) vector ⟵———⟶ transverse component of acoustic stress on a surface of specified normal

t_{x_i} (3x1) vector ⟵———⟶ longitudinal component of acoustic stress on a surface of specified normal

v_{t_i} (3x1) vector ⟵———⟶ transverse component of acoustic velocity

v_{x_i} (3x1) vector ⟵———⟶ longitudinal component of acoustic velocity

All field quantities are capable of interpretation as the real parts of complex numbers containing the usual time variation factor; in the field expansions of section 6.34 the $e^{j\omega t}$ term has been omitted from both sides of the relation, but is included by implication.

Further general notation includes:-

ω_i angular frequency of mode i

β_i wave vector (real) of propagating mode i

$d\underset{\sim}{S}$ outward normal of surface S

σ material conductivity

ν material viscous damping coefficient

X^{*} complex conjugate of field quantity X

A^{T} transpose of matrix A

6.2 Complex Electroacoustic Reciprocity Relation.

The reciprocity relation is concerned with two field solutions, (E_i, H_i, T_i, v_i) and (E_j, H_j, T_j, v_j), of Maxwell's equations and the

basic electroacoustic equations describing a non-magnetic, piezoelectric

material possessing a linear conductivity relation. Field solutions

"i" and "j" are assumed to be of the same angular frequency, ω.

Gauss's divergence theorem (115) permits the reciprocity relation to

be expressed in the integral form (103), (106), (108), (112), (113)

$$\oint_S (E_i \times H_j^* + E_j^* \times H_i - T_i \cdot v_j^* - T_j^* \cdot v_i) \cdot dS$$

$$= \int_v (-E_i^T \cdot J_j^* - E_j^{*T} \cdot J_i + v_j^{*T} \cdot F_i + v_i^T \cdot F_j^*) dv \qquad (6.201)$$

The left hand side of this equation is an integral over the surface,

S which encloses volume v of the piezoelectric medium. Contained

within this volume are the electric current densities J_i, J_j and the

acoustic body force densities F_i, F_j which are the sources of the

electroacoustic fields. The above relationship is truly reciprocal,

with respect to field solutions "i" and "j", only if

$$J_r = \sigma E_r \qquad r = i,j \qquad (6.202)$$

and $F_r = -\nu v_r \qquad r = i,j \qquad (6.203)$

To satisfy these constraints the medium must have a linear conductivity

relation, and the only body force densities must be due to viscous

damping.

Several features of this reciprocity relation, equation (6.201),

are worthy of note. Firstly, for reasons which will become apparent

in Chapter VII, the usual quasi-electrostatic approximation (106),

(108) ($\nabla \times E = 0$, $E = -\nabla\psi$) has not been made. Secondly, the

surface integrand is the sum of Poynting-vector-type products; the

electromagnetic Poynting vector (103), P_e, and the acoustic Poynting

vector, (116), P_a, can be written in terms of the field variables as

$$P_e = E \times H^*$$ (6.204)

and $$P_a = -v \cdot T^*$$ (6.205)

Finally, although the reciprocity relation is applicable to a general

electroacoustic interaction system, the volume integral does not

contain any piezoelectric coupling terms.

6.3 An Orthogonality Condition for the Normal Modes of a Uniform Piezoelectric Waveguide.

Commencing with the complex reciprocity relation, equation (6.201),

this section proceeds to derive an orthogonality condition for the

normal modes of a piezoelectric waveguide.

6.31 A Uniform Piezoelectric Waveguide.

The propagation system envisaged in this and the subsequent

section of the analysis is a general piezoelectric waveguide, one

example of which is sketched in Figure 6.1. This structure has its

main axis along the x coordinate direction, and is assumed to be of

uniform geometry in both transverse directions. S_1 and S_2, located

at x_1 and x_2 respectively, are cross-sectional planes of the waveguide;

S_w comprises the total guide-wall surface between these reference

planes. The surface S, $(= S_1 + S_2 + S_w)$, whose outward normal is

n, encloses volume v of the guide.

6.32 Boundary Conditions at the Waveguide Walls.

In accordance with the usual electromagnetic and acoustic boundary

conditions, the waveguide walls are assumed to be perfectly conducting

and stress-free. These requirements can be met simultaneously by

the deposition of an infinitely-thin, perfectly-conducting metal over-

lay onto the piezoelectric wall surfaces. As discussed in section

3.4, this concept has been used widely in calculations of the strength
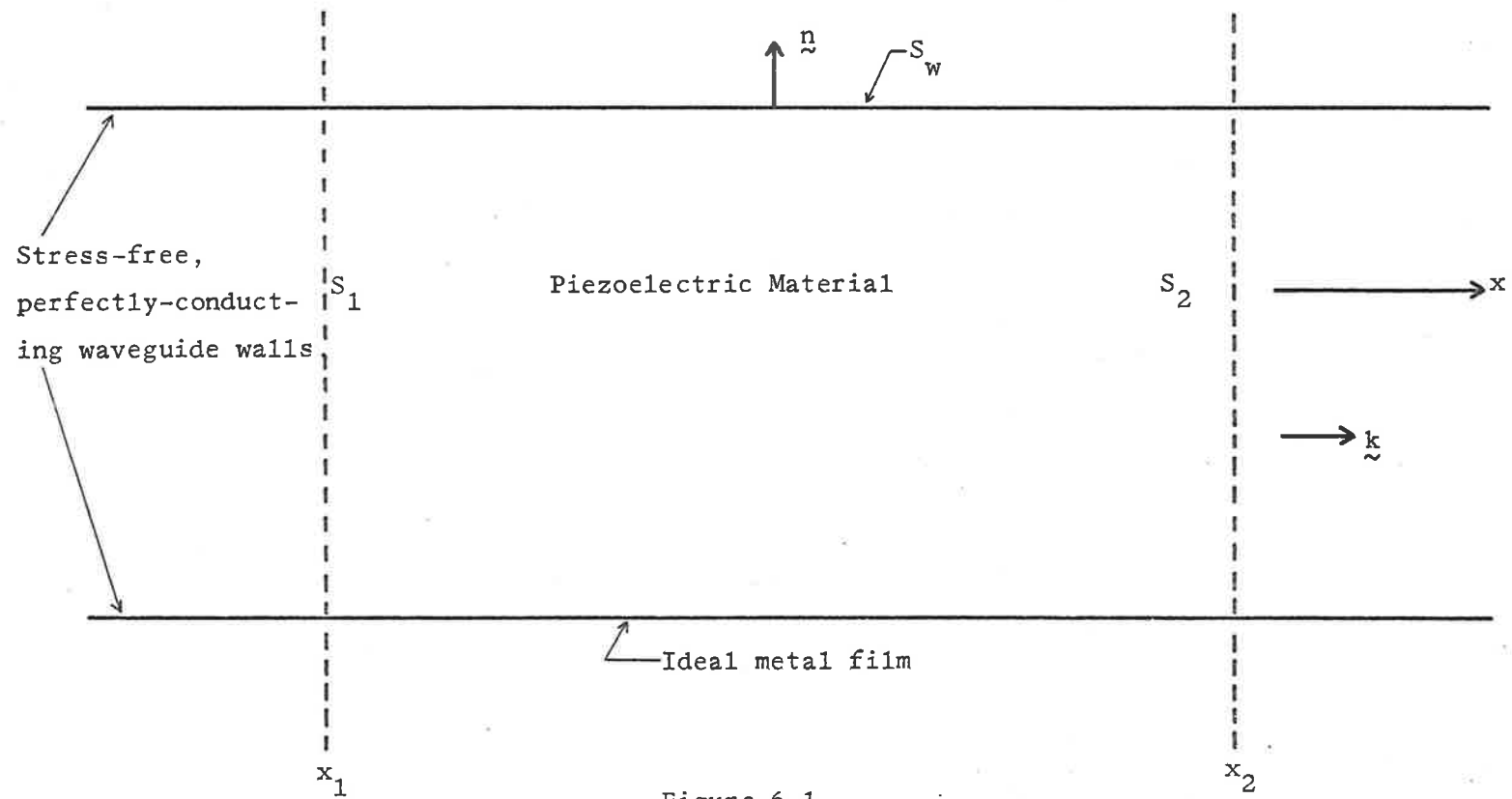
Figure 6.1

A uniform electroacoustic waveguide structure.

Closed surface $S = S_1 + S_2 + S_w$

of electroacoustic coupling between a surface acoustic wave and an IDT

(25), (67), (72).

6.33 Derivation of an Orthogonality Condition.

A derivation of the desired orthogonality condition is based upon

the complex reciprocity relation in which field solutions "i" and "j"

are replaced by normal waveguide modes "m" and "n"; as such these modes

are source-free solutions of the electroacoustic equations describing

propagation in the structure. Putting the current and body force

density sources equal to zero, i.e.

$$J_m = J_n = F_m = F_n = 0 \tag{6.331}$$

equation (6.201) reduces to

$$\oint_S (E_m \times H_n^* + E_n^* \times H_m - T_m \cdot v_n^* - T_n^* \cdot v_m) \cdot dS = 0 \tag{6.332}$$

The boundary conditions, which force the tangential components of

electric field and the components of stress to be zero at the waveguide

walls, ensure that there is no nett power flow across S_w. Hence

equation (6.332) becomes, with reference to Figure 6.1,

$$-\int_{S_1} (E_m \times H_n^* + E_n^* \times H_m - T_m \cdot v_n^* - T_n^* \cdot v_m) \cdot k \, dS$$

$$+ \int_{S_2} (E_m \times H_n^* + E_n^* \times H_m - T_m \cdot v_n^* - T_n^* \cdot v_m) \cdot k \, dS = 0 \tag{6.333}$$

where the sign of the integral over S_1 arises from the fact that the

outward normal on this surface is $-k$.

For the mth forward (+x) propagating normal mode the fields,

(E_m, H_m, T_m, v_m), have a spatial dependence of $e^{-j\beta_m x}$. It is clear,

from an examination of equation (6.333), that the integral over S_1

depends only on x_1, and the integral over S_2 depends only on x_2. Since

x_1 and x_2 can be chosen arbitrarily, it is necessary for each surface

integral to be identically zero, except when $\beta_m = \beta_n^*$, in which case the integrals are independent of x_1 and x_2 and cancel on substraction. Thus for propagating normal modes, (i.e. β real),

$$\int_{S_0} (\underset{\sim}{E}_m \times \underset{\sim}{H}_n^* + \underset{\sim}{E}_n^* \times \underset{\sim}{H}_m - \underset{\approx}{T}_m \cdot \underset{\sim}{v}_n^* - \underset{\approx}{T}_n^* \cdot \underset{\sim}{v}_m) \cdot k \, dS = 0$$

$$\beta_m \neq \beta_n \qquad (6.334)$$

S_0 being an arbitrary waveguide cross-section. The above relationship accomodates the situation in which $\beta_m = -\beta_n$; i.e. m and n are the same, but oppositely travelling, modes. When $\beta_m = \beta_n$, m and n are the same waveguide mode travelling in the same direction and

$$\int_{S_0} (\underset{\sim}{E}_m \times \underset{\sim}{H}_n^* + \underset{\sim}{E}_n^* \times \underset{\sim}{H}_m - \underset{\approx}{T}_m \cdot \underset{\sim}{v}_n^* - \underset{\approx}{T}_n^* \cdot \underset{\sim}{v}_m) \cdot \underset{\sim}{k} \, dS = 4P$$

$$\beta_m = \beta_n \qquad (6.335)$$

where

$$P = \tfrac{1}{2} \text{ Real Part} \left[\int_{S_0} (\underset{\sim}{E}_n \times \underset{\sim}{H}_n^* - \underset{\approx}{T}_n^* \cdot \underset{\sim}{v}_n) \cdot \underset{\sim}{k} \, dS \right] \qquad (6.336)$$

Providing that all field variables are peak values, P can be interpreted as the total power carried along the waveguide axis by normal mode n (103), (106), (116).

Combining the results of equations (6.334) and (6.335) yields the desired orthogonality condition;

$$\int_{S_0} (\underset{\sim}{E}_m \times \underset{\sim}{H}_n^* + \underset{\sim}{E}_n^* \times \underset{\sim}{H}_m - \underset{\approx}{T}_m \cdot \underset{\sim}{v}_n^* - \underset{\approx}{T}_n^* \cdot \underset{\sim}{v}_m) \cdot \underset{\sim}{k} \, dS$$

$$= 0 \quad \beta_m \neq \beta_n$$

$$= 4P \quad \beta_m = \beta_n \qquad (6.337)$$

Other workers (72), (106), (108) have derived this, or an almost identical, orthogonality relation for the normal modes of an electroacoustic waveguide. Equation (6.337) expresses the mode orthogonality condition

in the precise manner required in section 6.4 to deduce the amplitude

of a normal mode excited by a known distribution of sources.

6.34 Derivation of a Simplified Orthogonality Condition.

Although the relationships to be derived under this heading are

not needed in the main analysis, they are essential to an understanding

of the overall application of microwave analytical methods to studies

of electroacoustic interaction systems. They are vital, as well, to

the secondary aim of this chapter, namely to relate the results obtained

in this present treatment to those of other researchers in this field.

The procedure is to employ the techniques developed by Collin (103)

in the purely electromagnetic situation to simplify the orthogonality

equation (6.337). Through the notation introduced in section 6.1,

the fields of forward propagating normal piezoelectric waveguide mode

m can be expanded into transverse and longitudinal components:-

$$\underset{\sim}{E}_m = (\underset{\sim}{e}_{t_m} + \underset{\sim}{e}_{x_m}) \, e^{-j\beta_m x}$$

$$\underset{\sim}{H}_m = (\underset{\sim}{h}_{t_m} + \underset{\sim}{h}_{x_m}) \, e^{-j\beta_m x}$$

$$\underset{\sim}{k} \cdot \underset{\approx}{T}_m = (\underset{\sim}{t}_{t_m} + \underset{\sim}{t}_{x_m}) \, e^{-j\beta_m x} \qquad (6.341)$$

$$\underset{\sim}{v}_m = (\underset{\sim}{v}_{t_m} + \underset{\sim}{v}_{x_m}) \, e^{-j\beta_m x}$$

A corresponding expansion exists for the nth forward propagating mode.

Substitution of the expanded field forms for both modes m and n shows

that

$$\int_{S_0} \left[(\underset{\sim}{e}_{t_m} \times \underset{\sim}{h}_{t_n}{}^* + \underset{\sim}{e}_{t_n}{}^* \times \underset{\sim}{h}_{t_m}) \cdot \underset{\sim}{k} - \underset{\sim}{t}_{t_m} \cdot \underset{\sim}{v}_{t_n}{}^* - \underset{\sim}{t}_{x_m} \cdot \underset{\sim}{v}_{x_n}{}^* \right.$$

$$\left. -\underset{\sim}{t}_{t_n}{}^* \cdot \underset{\sim}{v}_{t_m} - \underset{\sim}{t}_{x_n}{}^* \cdot \underset{\sim}{v}_{x_m} \right] \, dS = 0 \qquad \beta_m \neq \beta_n \qquad (6.342)$$

$$= 4P \qquad \beta_m = \beta_n$$

This reduced expression results from the fact that all other vector

product terms in components of $\underset{\sim}{E}$ and $\underset{\sim}{H}$ are normal to $\underset{\sim}{k}$, thus vanishing

on formation of the scalar product, while all other mixed products of

the transverse and longitudinal components of $\underset{\approx}{T}$ and $\underset{\sim}{v}$ must be zero.

An equally valid substitution into the orthogonality equation

(6.337) is a forward (+x) travelling normal mode m, whose field expan-

sion is provided once again by equation (6.341), and a reverse (-x)

travelling normal mode n, whose field expansion is

$$\underset{\sim}{E}_n = (\underset{\sim}{e}_{t_n} - \underset{\sim}{e}_{x_n}) \, e^{j\beta_n x}$$

$$\underset{\sim}{H}_n = (-\underset{\sim}{h}_{t_n} + \underset{\sim}{h}_{x_n}) \, e^{j\beta_n x} \qquad\qquad (6.343)$$

$$\underset{\sim}{k} \cdot \underset{\approx}{T}_n = (-\underset{\sim}{t}_{t_n} + \underset{\sim}{t}_{x_n}) \, e^{j\beta_n x}$$

$$\underset{\sim}{v}_n = (\underset{\sim}{v}_{t_n} - \underset{\sim}{v}_{x_n}) \, e^{j\beta_n x}$$

A comparison of equations (6.341) and (6.343) reveals that the trans-

verse components of acoustic stress and magnetic field, and the longi-

tudinal components of acoustic velocity and electric field change sign

when the direction of propagation is reversed (103), (114). That these

phase relationships pertain for plane volume (longitudinal and shear)

and surface acoustic waves, at least in isotropic media, has been

verified (112). Inserting the field expansions of equation (6.341)

for mode m, and of equation (6.343) for mode n, into the orthogonality

relation (6.337) provides

$$\int_{S_0} \left[(-e_{t_m} \times h_{t_n}^* + e_{t_n}^* \times h_{t_m}) \cdot \underset{\sim}{k} - t_{t_m} \cdot v_{t_n}^* + t_{x_m} \cdot v_{x_n}^* \right.$$
$$\left. + t_{t_n}^* \cdot v_{t_m} - t_{x_n}^* \cdot v_{x_m} \right] dS = 0 \qquad \beta_m \neq \beta_n \qquad (6.344)$$

Note that because modes m and n are now propagating in opposite direc-
tions, the situation wherein $\beta_m = \beta_n$ cannot be considered in relation
to the above integral.

Subtracting the integrands of equations (6.342) and (6.344) leads
to the simpler orthogonality condition

$$\int_{S_0} \left[(e_{t_m} \times h_{t_n}^*) \cdot \underset{\sim}{k} - t_{t_n}^* \cdot v_{t_m} - t_{x_m} \cdot v_{x_n}^* \right] dS = 0$$
$$\beta_m \neq \beta_n \qquad (6.345)$$

for the normal modes of a piezoelectric waveguide. Omitting purely
acoustic terms, equation (6.345) becomes

$$\int_{S_0} (e_{t_m} \times h_{t_n}^*) \cdot \underset{\sim}{k} \, dS = 0 \qquad \beta_m \neq \beta_n \qquad (6.346)$$

which is the usual relation expressing the orthogonality of the power
carried by two non-degenerate normal propagating modes of an electro-
magnetic waveguide (103). Considering only the acoustic field terms
the same equation shows that

$$\int_{S_0} (-t_{t_n}^* \cdot v_{t_m} - t_{x_m} \cdot v_{x_n}^*) dS = 0 \qquad \beta_m \neq \beta_n \qquad (6.347)$$

which is the orthogonality relation quoted, without proof, by Oliner
et al. (114). But equation (6.347) is not a corresponding statement
of power orthogonality for two non-degenerate acoustic modes; however,
by invoking an assumption of elastic isotropy, this expression can be
processed further to produce such a result. Bertoni (111) proves the

power⋅orthogonality of surface acoustic waves directly from the original
orthogonality condition (6.337).

A final comment relates to the construction of equivalent circuits
for N-port electroacoustic interaction systems (112), (113).   The
field expansions of equations (6.341) and (6.343) for forward and
reverse propagating modes would seem to suggest a formulation in which
voltage represents electric field, at an electromagnetic port, and
velocity at an acoustic port.   For this convention, an impedance
interpretation (112), (113) of the reciprocity integrals determines an
expression of the form

$$Z_{ij} = -Z_{ji} \tag{6.348}$$

The more common reciprocity relation

$$Z_{ij} = Z_{ji} \tag{6.349}$$

results from a choice of equivalent voltage to represent stress at an
acoustic port and, as usual, electric field at an electromagnetic port.

6.4 An Expression for the Amplitude of a Normal Piezoelectric Waveguide
Mode Excited by a Known Source Distribution.

This section exploits the reciprocity relation, equation (6.201),
and the orthogonality condition, equation (6.337), to determine an
expression for the amplitude of the nth normal piezoelectric waveguide
mode launched by a known distribution of current and body force density
sources.

6.41 A Uniform Piezoelectric Waveguide Containing Sources.

The propagation structure under consideration is once again the
uniform piezoelectric waveguide illustrated in Figure 6.1.   Details of
the normal propagation modes of this guide, in the absence of any sources,

are assumed known. Suppose now that sources of electroacoustic fields, in the form of an electric current density, $\underset{\sim}{J}$, and an acoustic body force density, $\underset{\sim}{F}$, are introduced into a limited region of the waveguide, as sketched in Figure 6.2. The problem is to calculate expressions for the resulting fields, at least for those sections of the waveguide sufficiently far from the sources for the fields to be expanded as a linear superposition of normal propagating modes. One important concept in this derivation is drawn from electromagnetic theory (103) and provides that in the vicinity of reference planes 1 and 2 a complete solution for the fields of the perturbed waveguide can be obtained as an infinite sum of propagating and non-propagating normal modes.

If careful attention is paid to the location of the reference planes and to the methods of waveguide termination, this analytical process can be simplified considerably. Outwardly exponentially growing modes can be rejected from the solution on the basis that the guide terminations cannot produce suitable sources to sustain them. Placing the reference planes at a sufficiently large distance from the sources ensures that the amplitudes of outwardly exponentially decaying modes are negligible. Furthermore the inwardly propagating modes, shown dotted in Figure 6.2, can be eliminated on the assumption that the waveguide is so terminated as to allow no reflection for any of the outwardly propagating modes. Thus at reference planes 1 and 2 only outwardly propagating normal modes remain; representative members are labelled as $(\underset{\sim}{E}_i{}^-, \underset{\sim}{H}_i{}^-, \underset{\approx}{T}_i{}^-, \underset{\sim}{v}_i{}^-)$ and $(\underset{\sim}{E}_i{}^+, \underset{\sim}{H}_i{}^+, \underset{\approx}{T}_i{}^+, \underset{\sim}{v}_i{}^+)$ in Figure 6.2. Explicitly calculable expressions for the amplitudes, $C_i{}^-$ and $C_i{}^+$, of these modes are sought in the following section.

6.42 Derivation of the Coupled Normal Mode Amplitude.

E_i^-, H_i^-, T_i^-, v_i^-

C^-

S_1

F_i

J_i

Piezoelectric Material

S_w

n

E_i^+, H_i^+, T_i^+, v_i^+

C^+

S_2

x

k

Stress-free, perfectly-conducting walls

Ideal metal film

x_1

x_2
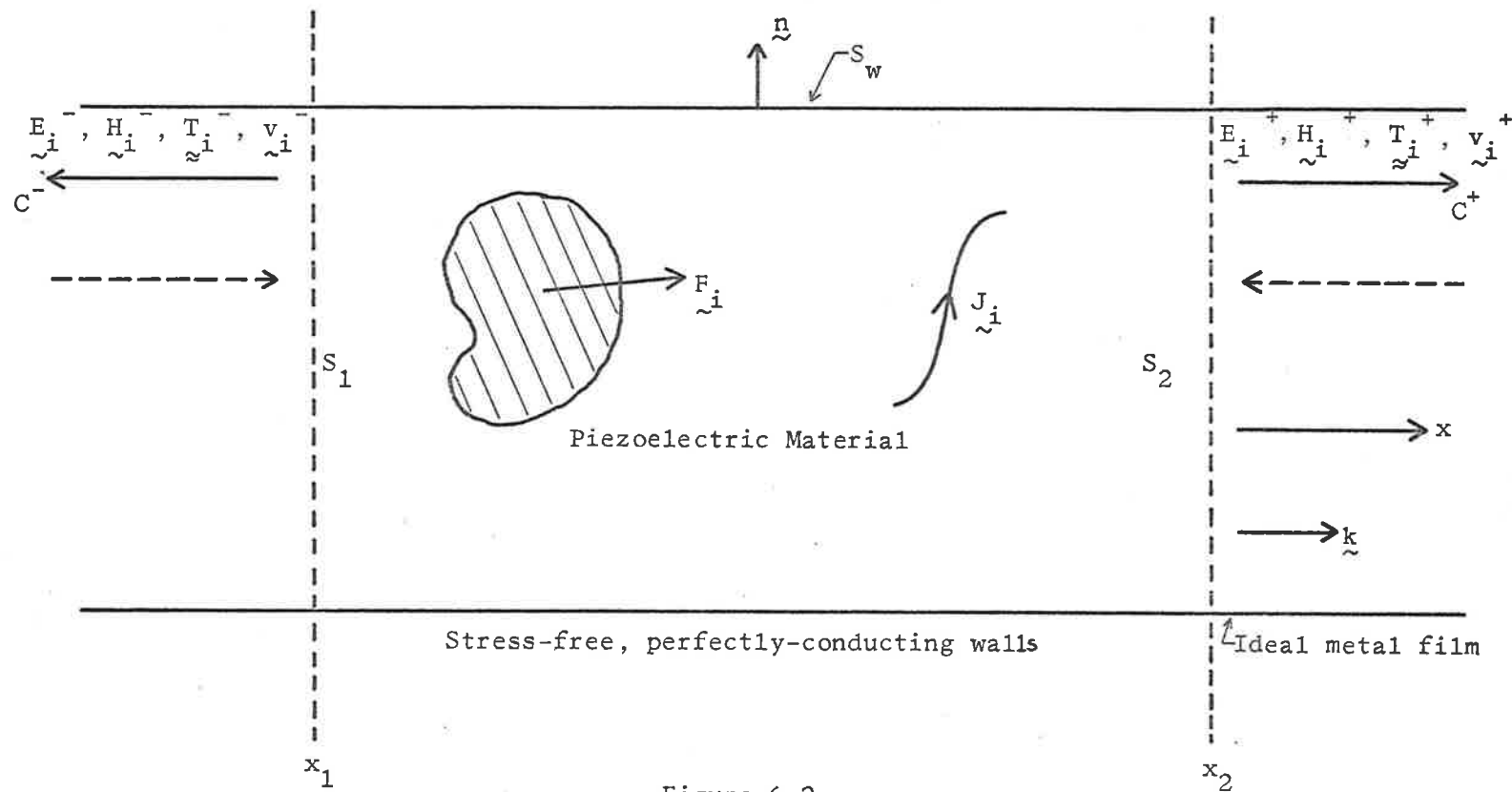
Figure 6.2

A uniform electroacoustic waveguide containing

sources.

98.

.Once more the derivation stems from the complex reciprocity relation of equation (6.201). Field solution "i" is that excited by a known distribution of sources, $J_{\sim i}$, of current density, and $F_{\sim i}$, of acoustic body force density. On the other hand field solution "j" is chosen to be a specific waveguide normal mode — in particular, the nth forward propagating mode, $(E_{\sim n}^{+}, H_{\sim n}^{+}, T_{\approx n}^{+}, v_{\sim n}^{+})$, where the superscript + denotes a wave travelling in the +x direction. This means that

$$J_{\sim j} = F_{\sim j} = 0 \qquad (6.421)$$

and the reciprocity relation simplifies to

$$\oint_{S} (E_{\sim i} \times H_{\sim n}^{+*} + E_{\sim n}^{+*} \times H_{\sim i} - T_{\approx i} \cdot v_{\sim n}^{+*} - T_{\approx n}^{+*} \cdot v_{\sim i}).dS_{\sim}$$

$$= \int_{V} (-E_{\sim n}^{+*T} \cdot J_{\sim i} + v_{\sim n}^{+*T} \cdot F_{\sim i})dv \qquad (6.422)$$

As noted in section 6.33, the perfectly-conducting, stress-free boundaries allow no contribution to the surface integral from the waveguide walls, so that equation (6.422) can be re-expressed as

$$\int_{S_2} (E_{\sim i} \times H_{\sim n}^{+*} + E_{\sim n}^{+*} \times H_{\sim i} - T_{\approx i} \cdot v_{\sim n}^{+*} - T_{\approx n}^{+*} \cdot v_{\sim i}).\underline{k}\, dS$$

$$- \int_{S_1} (E_{\sim i} \times H_{\sim n}^{+*} + E_{\sim n}^{+*} \times H_{\sim i} - T_{\approx i} \cdot v_{\sim n}^{+*} - T_{\approx n}^{+*} \cdot v_{\sim i}).\underline{k}\, dS$$

$$= \int_{V} (-E_{\sim n}^{+*T} \cdot J_{\sim i} + v_{\sim n}^{+*T} \cdot F_{\sim i})dv \qquad (6.423)$$

Section 6.41 details the method whereby the fields radiated by sources $J_{\sim i}$ and $F_{\sim i}$ can be expanded as an infinite sum of outwardly propagating modes; i.e. of reverse (-x) travelling modes in the region to the left of S_1, as shown in Figure 6.2, and of forward (+x) travelling modes in the region to the right of S_2. Hence

$$\underset{\sim}{E}_i = \sum_{m=1}^{\infty} C_m^+ \underset{\sim}{E}_m^+$$

$$\underset{\sim}{H}_i = \sum_{m=1}^{\infty} C_m^+ \underset{\sim}{H}_m^+$$

$$\underset{\approx}{T}_i = \sum_{m=1}^{\infty} C_m^+ \underset{\approx}{T}_m^+ \qquad\qquad x > x_2 \qquad\qquad (6.424)$$

$$\underset{\sim}{v}_i = \sum_{m=1}^{\infty} C_m^+ \underset{\sim}{v}_m^+$$

and

$$\underset{\sim}{E}_i = \sum_{m=-1}^{-\infty} C_m^- \underset{\sim}{E}_m^-$$

$$\underset{\sim}{H}_i = \sum_{m=-1}^{-\infty} C_m^- \underset{\sim}{H}_m^-$$

$$\underset{\approx}{T}_i = \sum_{m=-1}^{-\infty} C_m^- \underset{\approx}{T}_m^- \qquad\qquad x < x_1 \qquad\qquad (6.425)$$

$$\underset{\sim}{v}_i = \sum_{m=-1}^{-\infty} C_m^- \underset{\sim}{v}_m^-$$

Here positive mode numbers are assigned to modes propagating across S_2 in the +x direction, and negative mode numbers to modes propagating across S_1 in the negative x direction. Substitution of these normal mode expansions into equation (6.423) determines that

$$\int_{S_2} \sum_{m=1}^{\infty} C_m^+ \, (\underset{\sim}{E}_m^+ \times \underset{\sim}{H}_n^{+*} + \underset{\sim}{E}_n^{+*} \times \underset{\sim}{H}_m^+ - \underset{\approx}{T}_m^+ \cdot \underset{\sim}{v}_n^{+*} - \underset{\approx}{T}_n^{+*} \cdot \underset{\sim}{v}_m^+) \cdot \underset{\sim}{k} \, dS$$

$$- \int_{S_1} \sum_{m=-1}^{-\infty} C_m^- \, (\underset{\sim}{E}_m^- \times \underset{\sim}{H}_n^{+*} + \underset{\sim}{E}_n^{+*} \times \underset{\sim}{H}_m^- - \underset{\approx}{T}_m^- \cdot \underset{\sim}{v}_n^{+*} - \underset{\approx}{T}_n^{+*} \cdot \underset{\sim}{v}_m^-) \cdot \underset{\sim}{k} \, dS$$

$$= \int_V (-\underset{\sim}{E}_n^{+*T} \cdot \underset{\sim}{J}_i + \underset{\sim}{v}_n^{+*T} \cdot \underset{\sim}{F}_i) dv \qquad\qquad (6.426)$$

The normal mode orthogonality condition, equation (6.337), can be applied to this relationship to show that all contributions to the integral over S_1 are zero, and that the only non-zero contribution to

the integral over S_2 occurs when m and n are the same mode. Thus, from equation (6.426), emerges the following expression for the amplitude, C_n^+, of the nth forward propagating waveguide mode;

$$C_n^+ = \frac{1}{4P} \int_V (-\underset{\sim}{E}_n^{+*T} \cdot \underset{\sim}{J}_i + \underset{\sim}{v}_n^{+*T} \cdot \underset{\sim}{F}_i) dv \qquad (6.427)$$

where P is, as defined by equation (6.336), the total power carried by forward travelling mode n, and all field quantities are peak values. By choosing mode n to be the field of the reverse propagating normal mode and repeating the foregoing analytical procedures, the amplitude, C_n^-, of the nth (-x) travelling waveguide mode is determined to be

$$C_n^- = \frac{1}{4P} \int_V (-\underset{\sim}{E}_n^{-*T} \cdot \underset{\sim}{J}_i + \underset{\sim}{v}_n^{-*T} \cdot \underset{\sim}{F}_i) dv \qquad (6.428)$$

Equations (6.427) and (6.428) are the required expressions for the amplitudes of normal piezoelectric waveguide modes launched by a known distribution of sources, $\underset{\sim}{J}_i$ and $\underset{\sim}{F}_i$. Similar, and closely related, formulations of the same results have been published by Auld and Kino (72), (106), (108) and , for the specific case of piezoelectric surface waves, by Bertoni (111). But the treatment presented above leads to results which, as will be discovered in Chapter VII, can be applied more directly to an analysis of the microsonic crossbar coupler (112), (113).

CHAPTER VII

THE APPLICATION OF MICROWAVE METHODS TO AN ANALYSIS

OF THE SURFACE ACOUSTIC WAVE CROSSBAR COUPLER.

7.0 Introduction.

In this and the following chapter, the analytical techniques described previously in the context of an electroacoustic waveguide are re-examined and modified to permit their application to studies of propagation and interaction on a surface. This prepares the way for a theoretical investigation of the surface wave crossbar directional coupler, which culminates in the analytical predictions of device performance contained in Chapter IX.

Figure 7.1 illustrates the general surface coupling configuration upon which attention is currently focussed. A launching transducer, T_p, radiates an essentially uniform-width surface acoustic wave towards a perturbed area of the substrate surface. At this stage the interaction is not restricted to one due to periodic mass-loading of the propagation surface; this constraint is introduced in the next chapter, when the investigation is oriented more specifically towards analysis of the crossbar coupler. The shaded region of Figure 7.1 represents some general non-uniformity on the free surface, (perhaps due to surface roughness, material overlays, or other changes in the surface properties of the substrate), which causes scattering of an incident surface wave. Because, as is discussed in more detail in Chapter VIII, the calculations rest upon a first order perturbation treatment, the interaction region is assumed to have only a small effect upon a propagating surface wave. Hence most of the acoustic energy launched by transducer T_p is transmitted directly to the receiving transducer, T_q, but some is
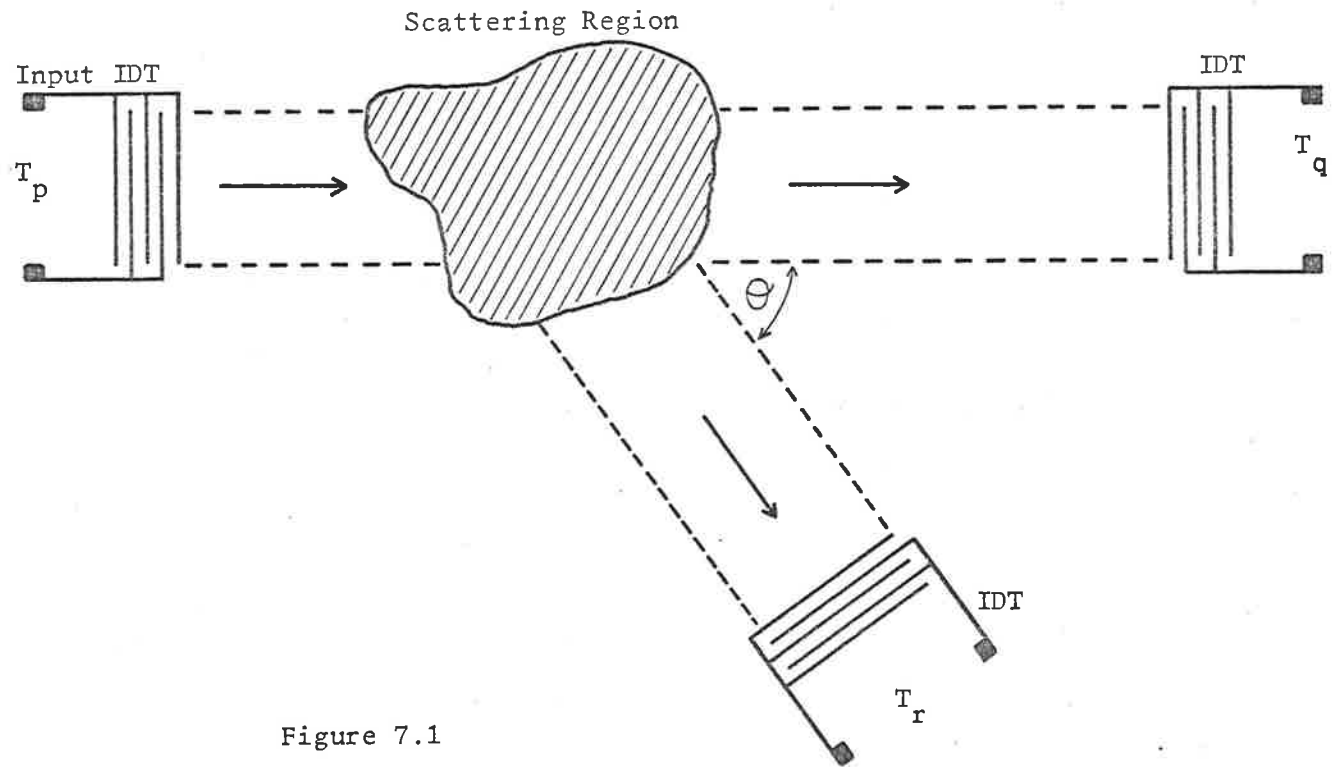
Figure 7.1

The general surface acoustic wave coupling
configuration.

scattered in all other directions. The question which the rest of this chapter seeks to answer is, "How much energy is scattered at a general angle θ, and is detected by transducer T_r?"

Chapter V describes the fabrication of the experimental crossbar couplers on an AT cut quartz crystal. This substrate material is only weakly piezoelectric and for present purposes can be replaced, in the analysis, by a non-piezoelectric medium possessing the same elastic properties. Thus in this investigation of surface scattering $\underset{\sim}{E}$ and $\underset{\sim}{H}$ fields are omitted and only the acoustic fields, $\underset{\approx}{T}$ and $\underset{\sim}{v}$ are retained. Both the practical and analytical results presented in section 10.3 support the validity and accuracy of this simplification.

Although the configuration of Figure 7.1 leads to the coupling of propagating modes on an interaction surface, a calculation by scattering to a set of normal modes is still possible. But the absence of a uniform cross-section waveguide allows the normal mode system on the surface to assume a different structure from the discrete normal mode set encountered previously. The first important task to be under-taken, therefore, is to separately establish the mode orthogonality conditions relevant to the surface situation. This step is made mathematically more tractable by the introduction of artificial periodic boundary conditions (112), (113). Once the desired mode orthogonality relation has been obtained, a calculation of the amplitudes of the normal modes scattered by the surface perturbation proceeds by a method completely parallel to that used in Chapter VI.

Clearly the determination of the amplitudes of artificial normal modes is not of practical interest. Quantities actually recorded in experiments are the ratios of the signal amplitudes launched at a trans-

mitting transducer and detected at each receiving transducer. The
second significant task is to show how the very many normal modes of
surface propagation relate to the transducer input and output. This
problem is facilitated by incorporating a scattering matrix notation
into the analysis; in so doing a convenient description of transducer
properties and, in particular, of the relationships between their
terminal voltages and the (artificial) normal mode fields which they
excite, is provided.

7.1 The Normal Modes of an Acoustic Propagation Surface.

On the free surface a continuum of normal modes, propagating in
all directions, displaces the discrete normal mode set of a uniform
waveguide.

7.11 Periodic Boundary Conditions.

An artificial assumption, common in quantum mechanical contexts
(117), (118), of periodic boundary conditions is necessary to introduce
the concept, essential to this style of analysis, of discrete normal
modes. Specifically this assumption is that the entire system of
substrate, transducers and scattering region has, as depicted in Figure
7.2, spatial periodicity of large periodic distance, L, in two dimensions.
Two useful effects result from this procedure. Firstly the normal
modes on the surface are forced to have wave vector components, in the
plane of the free surface and resolved parallel to the periodic
boundaries, which are integral multiples of $2\pi/L$ (117), (118). This
ensures that the normal modes form a discrete set and that an orthogon-
ality relation between different modes can be derived in terms of a
perimeter integral. Secondly the finite nature of this perimeter
integral promises that the normal mode amplitudes can be properly
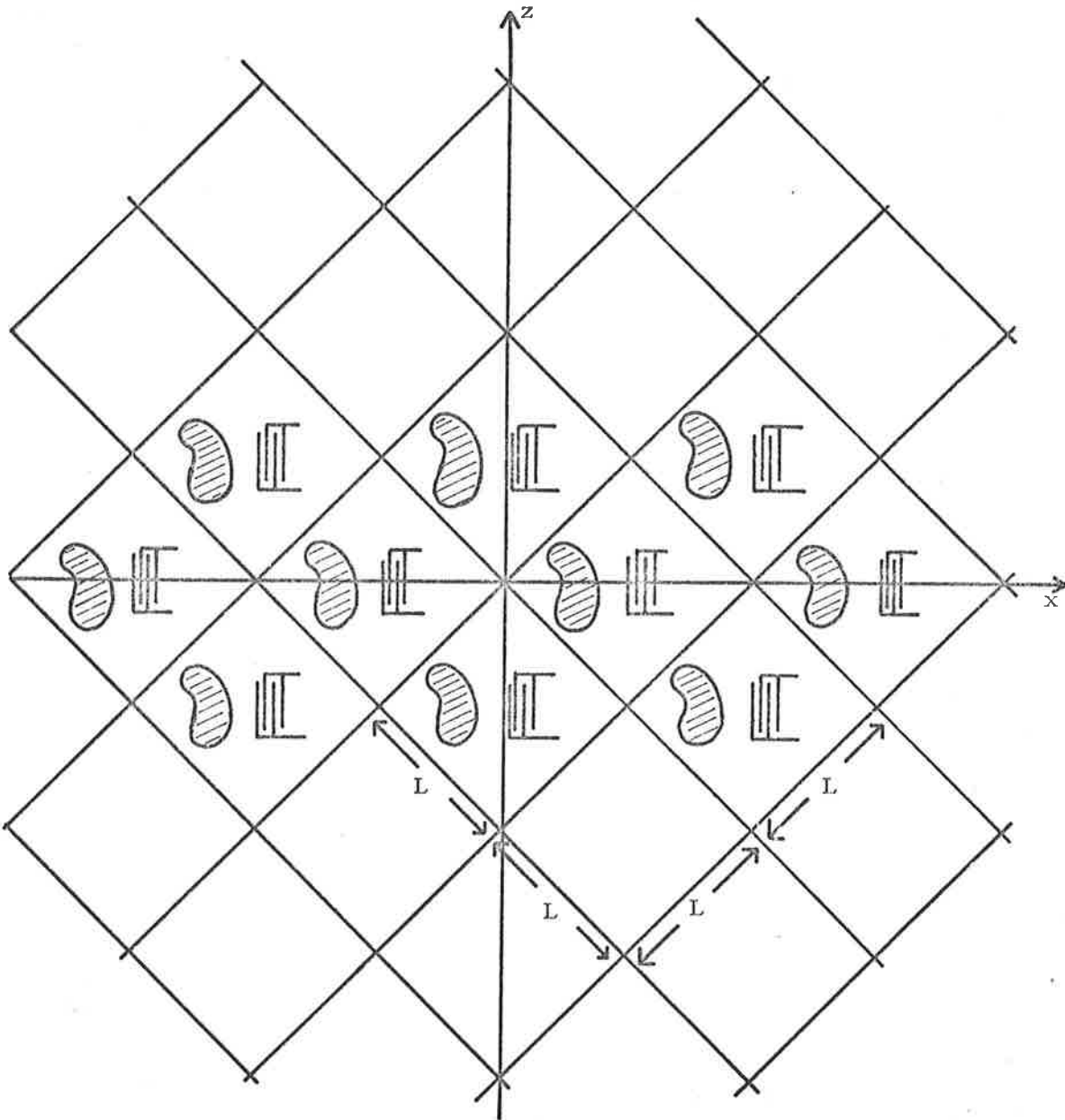
Figure 7.2

Periodic boundary conditions in the surface scattering problem.

normalised if so desired. Although the introduction of periodic

boundary conditions is a clear departure from the experimental device,

it will be observed that the distance L cancels from all subsequent

evaluations of quantities of interest. For such quantities it is

asserted that this artificial procedure nevertheless affords a

sufficiently accurate description of the experiment.

7.2 Transducer Scattering Matrix Notation.

To determine the way in which the very many possible surface

normal modes couple to the transducer input and output, the viewpoint

of Figure 7.3 is adopted. For simplicity the output transducer is

assumed to be a lossless, unidirectional IDT (71), (119) – (121) and

the periodic boundaries are so oriented that the normal modes of the

periodic boundary condition can be classified half as input modes to,

and half as output modes from, that transducer. This introduces the

multi-port representation of a transducer shown in Figure 7.4. The

behaviour of such a component can be characterised by the scattering

matrix $\underset{\approx}{S}$, where

$$\underset{\approx}{S} = \begin{bmatrix} S_{00} & \cdots & S_{0j} & \cdots & S_{0n} \\ \vdots & & & & \\ S_{-j0} & & & & \\ \vdots & & & & \\ S_{-n0} & & & & S_{-nn} \end{bmatrix}$$

Here the input transducer modes, which from Figure 7.3 can be seen to

have positive wave vector components, β_x, along the x coordinate axis,

are assigned positive mode numbers, j. The output modes, which have

negative x wave vector components, are ordered in the same fashion, but

are assigned negative mode numbers, -j. There is, of course, a one-
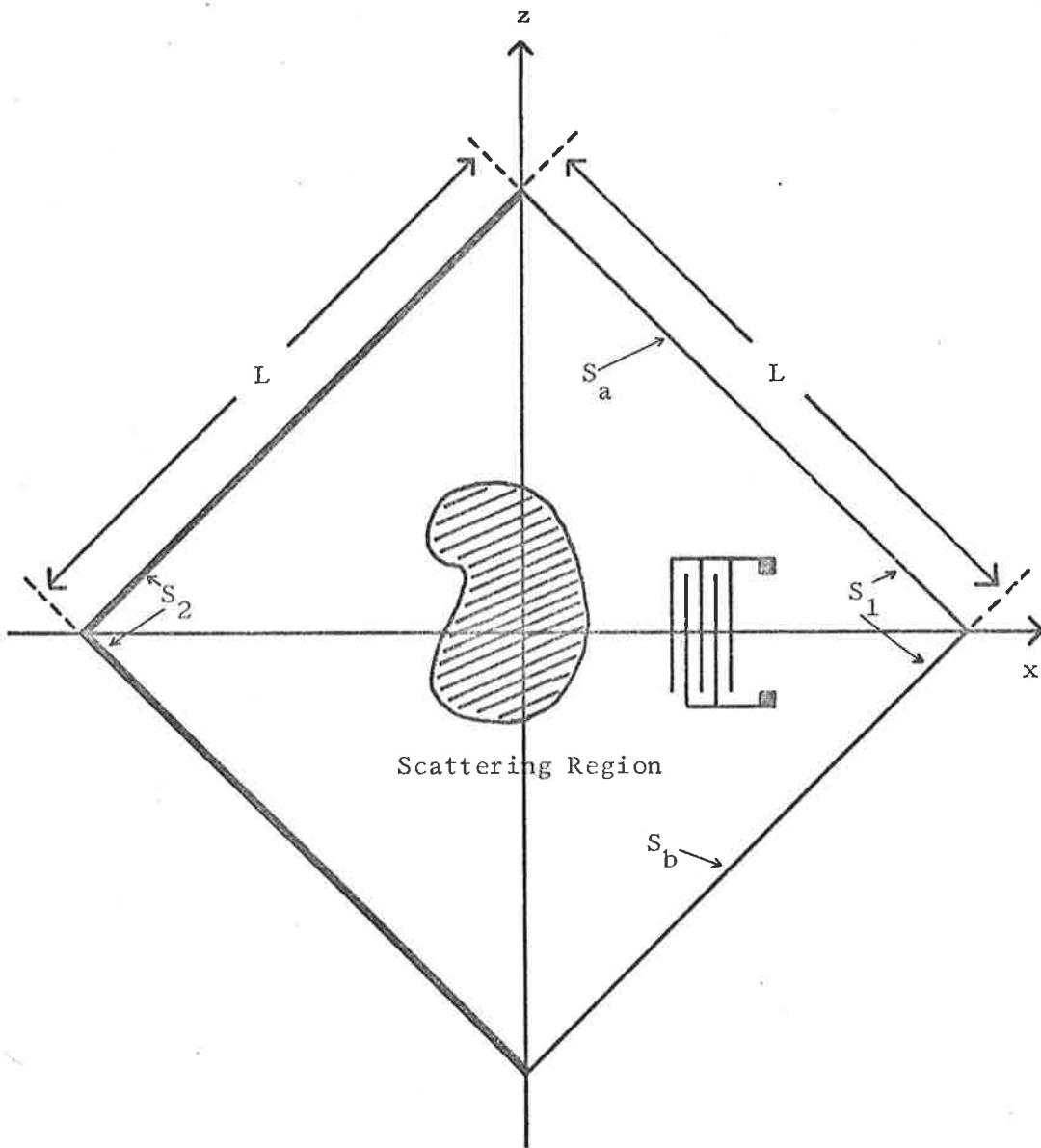
Figure 7.3

Periodic boundary coordinate notation.

Definition of surfaces: $S = S_0$ + upper and lower
closing surfaces.

$$S_0 = S_1 + S_2$$

$$S_1 = S_a + S_b$$

Electrical Port

Unidirectional IDT

Input Mode

Output Mode

x

Electrical Port

0

1

-1

2

-2

Lossless

Unidirectional

IDT

Acoustic Ports

(Input mode,
n +ve)

(Output mode,
n -ve)

n

-n
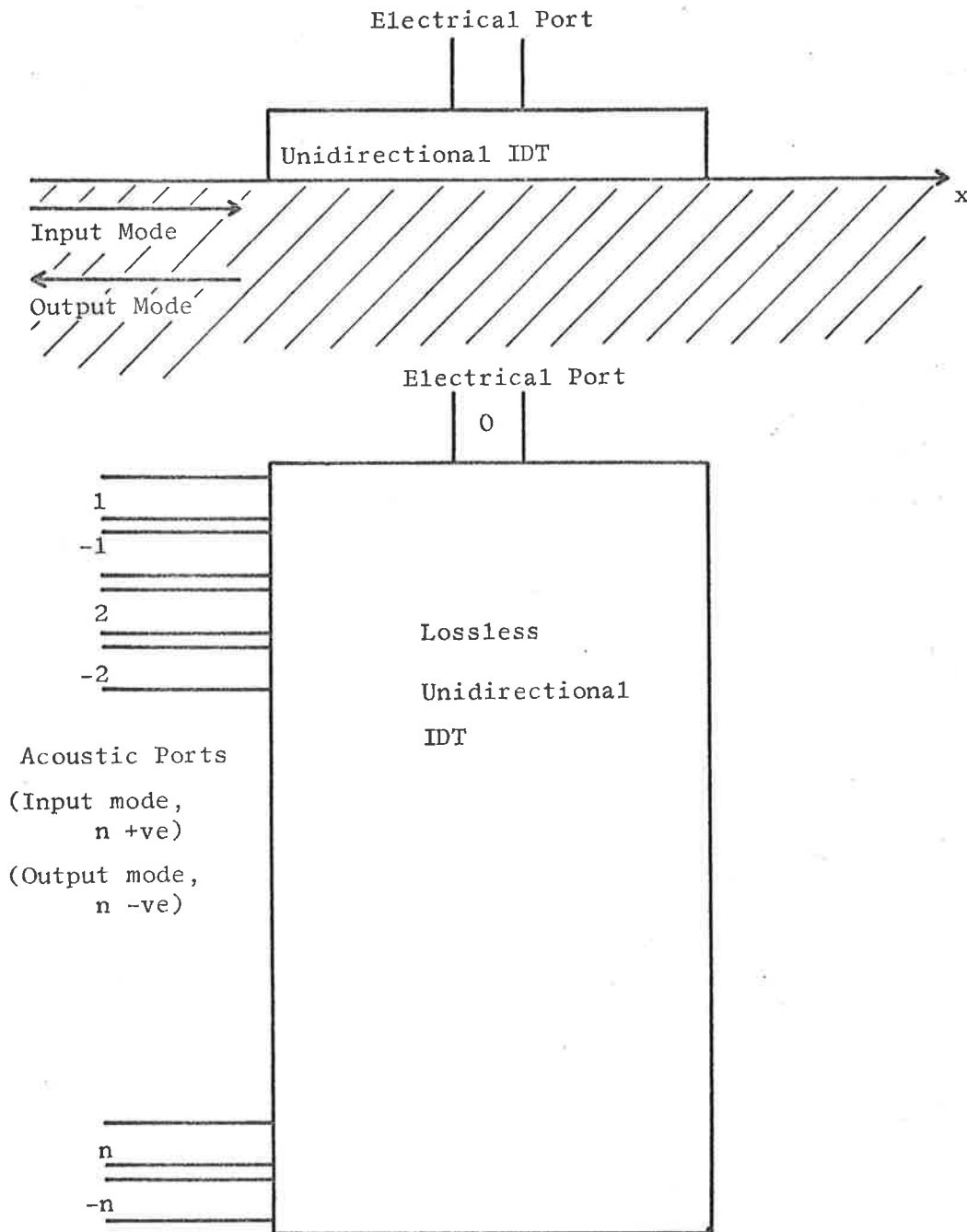
Figure 7.4

Multi-port representation of a unidirectional surface
acoustic wave IDT.

to-one correspondence between each input mode, i, and the companion
output mode, -i, which is obtained by reversing the wave vector of the
input mode.   In this scattering matrix formulation the index zero
refers, as indicated in Figure 7.4, to the electrical port, wherein
both input and output acoustic modes exist.

It is convenient, in equivalent circuit representations of the
surface acoustic wave IDT, to normalise all the equivalent voltages
and currents in the ports so that the power carried by each mode is
$k|C_n|^2$ where C_n is the amplitude of the nth normal mode, and k is a
constant applying to all modes.   By this normalisation process the
equivalent characteristic impedances at each port are set equal to
unity, so that the transducer scattering matrix exhibits the usual
symmetry,

$$S_{-i0} = S_{0i}$$

about the principal diagonal.   The orthogonality relation developed in
the following section preserves the consistency of characteristic
impedance between the acoustic ports, and a suitable selection of
scale for the impedance of the electrical port makes certain that the
power normalisation is maintained.

7.3 Derivation of an Orthogonality Relation for the Surface Normal Modes.

As in the electroacoustic waveguide analysis, the derivation of
an orthogonality relation proceeds from the complex reciprocity relation,
equation (6.201), in which field solutions "i" and "j" are replaced by
normal (source-free) surface modes m and n; i.e.,

$$\oint_S (-\underset{\approx}{T}_m \cdot \underset{\sim}{v}_n^* - \underset{\approx}{T}_n^* \cdot \underset{\sim}{v}_m) \cdot \underset{\sim}{dS} = 0 \qquad (7.301)$$

Figure 7.3 shows that the surface of integration consists of the surface

S_0, which comprises four cross-sectional planes directed into the material and passing through the periodic boundary perimeter, (normal to the substrate surface), together with closing surfaces formed by the propagation surface and a parallel plane deep in the material.

The stress-free nature of the propagation surface means that this does not contribute to the integral of equation (7.301). Similarly because the propagating modes, in this situation, are surface waves the integral over the parallel closing surface can be made zero by choosing a plane at a sufficient depth. Thus the above relationship reduces to

$$\int_{S_0} (-\underset{\approx}{T}_m \cdot \underset{\sim}{v}_n^* - \underset{\approx}{T}_n^* \cdot \underset{\sim}{v}_m) \cdot \underset{\sim}{dS} = 0 \qquad (7.302)$$

But this expression, as it stands, cannot be used as the basis of an orthogonality relation, since the right hand side states that the surface integral is always zero, for all mode combinations. In common with the electroacoustic waveguide study, an integral is sought over the partial perimeter surfaces S_1 and S_2, as defined in Figure 7.3, such that the result is zero for different modes, but is non-zero when the fields are derived from the same mode.

The integral to be examined is

$$\int_{S_1} (-\underset{\approx}{T}_m \cdot \underset{\sim}{v}_n^* - \underset{\approx}{T}_n^* \cdot \underset{\sim}{v}_m) \cdot \underset{\sim}{dS}_1 \qquad (7.303)$$

Altogether three separate combinations of wave vector pairs for modes m and n must be dealt with; these are treated as individual cases below.

Case 1: Modes m and n are the same mode, propagating in the same direction. (i.e. m=n and $\beta_m = \beta_n$).

When modes m and n are identically the same mode, the integrand

of the expression (7.303) has no nett spatial variation, which

leads to the result that

$$\int_{S_1} (-\underset{\approx}{T}_m \cdot \underset{\sim}{v}_n^* - \underset{\approx}{T}_n^* \cdot \underset{\sim}{v}_m) \cdot d\underset{\sim}{S}_1 = \underset{m=n}{\overset{+}{-}4P} \qquad (7.304)$$

where the positive sign is chosen for waves propagating with a

positive x wave vector component. Here, as in the electro-

acoustic waveguide analysis, P can be interpreted as the total

acoustic power carried normal to S_1 by a unit amplitude, ($C_n=1$),

n^{th} normal surface mode provided that the stress fields, $\underset{\approx}{T}$,

and velocity fields, $\underset{\sim}{v}$, are peak value quantities.

Case 2: Modes m and n differ in both wave vector

components, (resolved parallel to the periodic

boundaries), by non-zero multiples of $2\pi/L$.

Observe, from Figure 7.3, that the integral over surface S_1

can be split into two separate contributions, namely those over

planes S_a and S_b, which pass through adjacent sides of the

periodicity square. Because both components of the wave vectors

of modes m and n differ by non-zero multiples of $2\pi/L$, the

structure of the integrand of expression (7.303) forces the

integrals over S_a and S_b to each be zero. Hence, for the

conditions of case 2, which includes the possibility that modes

m and n may be the same, but oppositely propagating, normal

surface mode,

$$\int_{S_1} (-\underset{\approx}{T}_m \cdot \underset{\sim}{v}_n^* - \underset{\approx}{T}_n^* \cdot \underset{\sim}{v}_m) \cdot d\underset{\sim}{S}_1 = \underset{m \neq n}{0} \qquad (7.305)$$

Case 3: Modes m and n differ in only one wave vector

component, (resolved parallel to the periodic

boundaries), by a non-zero multiple of $2\pi/L$.

Restricting consideration to surface acoustic waves travelling on isotropic materials, this case can arise only in the circumstances described by Figure 7.5. One pair of wave vector components, namely those that differ by $n2\pi/L$, $(n \neq 0)$, are of equal magnitude, but are oppositely directed. On the plane parallel to these components, designated S_b, the structure of the integrand of (7.303) is sufficient to guarantee that the contribution to the integral over S_1 from S_b is zero. Elastic isotropy requires that $|\beta_m| = |\beta_n|$, so that the other wave vector component pair, resolved parallel to S_a, must be of equal magnitude and similarly directed. Therefore the integrand of expression (7.303) displays no nett spatial variation on the surface S_a and must be examined carefully in order to derive the necessary orthogonality relation. The detailed analysis of Appendix III furnishes the desired result that the integral over S_a is also zero, which completes the proof that

$$\int_{S_1} (-\underset{\approx}{T}_m \cdot \underset{\sim}{v}_n^* - \underset{\approx}{T}_n^* \cdot \underset{\sim}{v}_m) \cdot d\underset{\sim}{S}_1 = 0 \qquad m \neq n \qquad (7.306)$$

for this final mode wave vector combination.

The surface normal mode orthogonality relation, obtained by combining the studies of cases 1, 2 and 3 above, is;

$$\int_{S_1} (-\underset{\approx}{T}_m \cdot \underset{\sim}{v}_n^* - \underset{\approx}{T}_n^* \cdot \underset{\sim}{v}_m) \cdot d\underset{\sim}{S}_1 = \pm 4P \qquad m = n \qquad (7.307)$$
$$= 0 \qquad m \neq n$$

where, as has been noted already, the positive sign is chosen for transducer input modes. A further relationship, involving an integral over S_2 (refer Figure 7.3) may be deduced from equation (7.302), which expresses the fact that the integral over the total perimeter surface of the periodic boundary is zero, and equation (7.307). This second result is
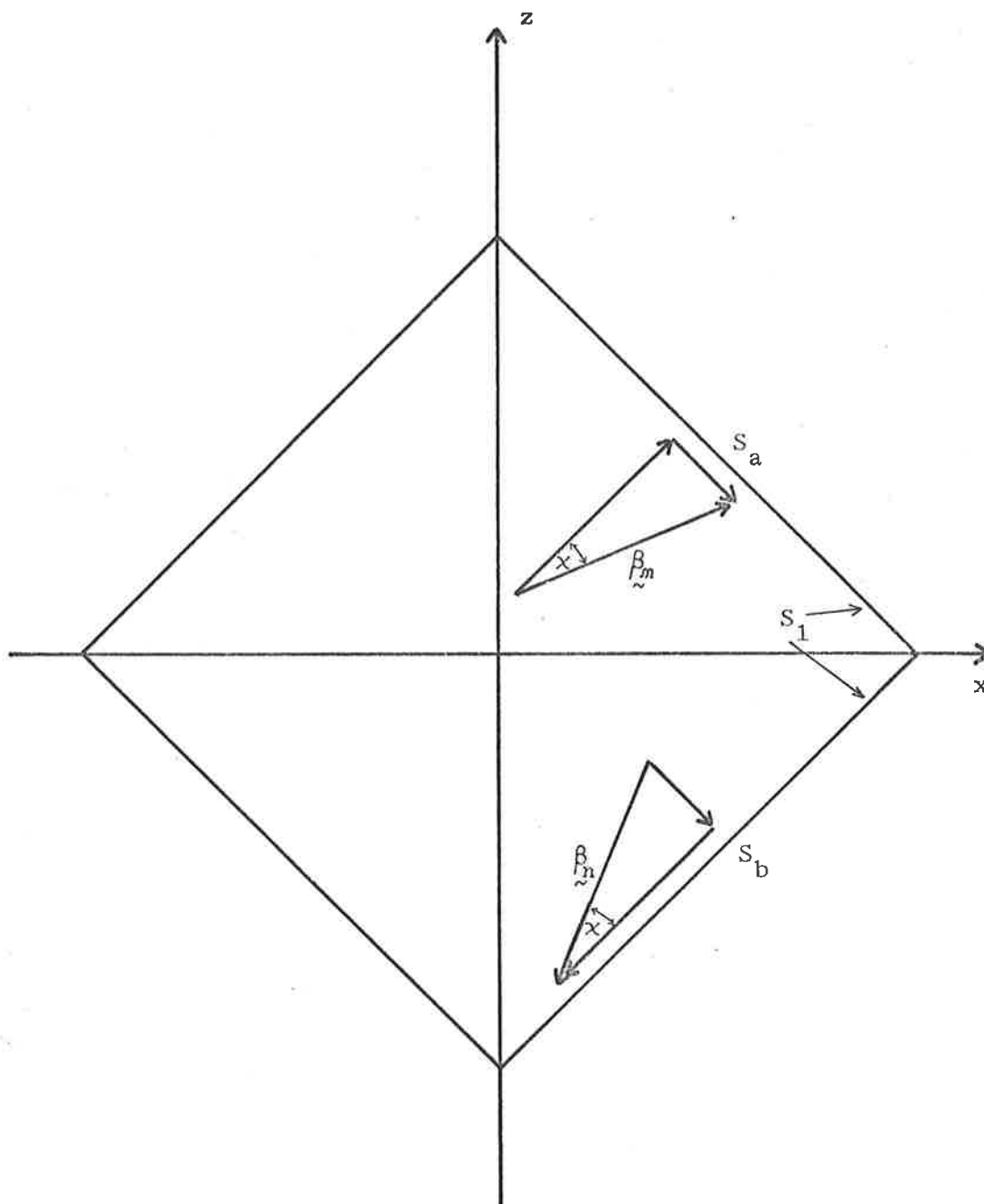
Figure 7.5

Wave vectors of normal surface modes in orthogonality derivations.

Case 3: Modes m and n differ in only one wave vector component

by a non-zero multiple of $2\pi/L$

(Isotropic medium assumed).

$$\int_{S_2} (-T_m \cdot v_n^* - T_n^* \cdot v_m).dS_2 = \begin{matrix} + \\ -4P \end{matrix} \quad m=n \qquad (7.308)$$
$$= 0 \quad m \neq n$$

where now the positive sign applies to transducer output modes.

A comparison of equations (6.337) and (7.307) shows the similar form taken by the normal mode orthogonality conditions in both an electroacoustic waveguide and an acoustic surface situation.

7.4 An Expression for the Amplitude of a Normal Surface Mode Excited by a Known Source Distribution.

In keeping with the corresponding segment of the waveguide analysis, section 6.4, this calculation starts from the complex reciprocity relation, equation (6.201), in which fields T_i and v_i are those excited by the acoustic body force density source, F_i, and field solution "j" is replaced by normal mode n (n positive or negative).

Hence equation (6.201) may be written as

$$\oint_S (-T_i \cdot v_n^* - T_n^* \cdot v_i).dS = \int_V (v_n^{*T} \cdot F_i)dv \qquad (7.401)$$

where v is the volume enclosed by surface S, as defined in Figure 7.3, and the source, F_i, is contained within this volume of the substrate. The argument developed in the preceding section allows no contribution to the surface integral of equation (7.401) from either the upper or lower closing surface, so that this relationship becomes

$$\int_{S_0} (-T_i \cdot v_n^* - T_n^* \cdot v_i).dS = \int_V (v_n^{*T} \cdot F_i)dv \qquad (7.402)$$

in which S_0 is, as established in Figure 7.3, the perimeter surface of the periodic boundary.

Adhering to the analytical approach used in the electroacoustic waveguide study, and reintroduced in the derivation of the surface

normal mode orthogonality relation, the integral over S_0 may be separated into integrals over the regions S_1 and S_2 (refer Figure 7.3). Recall, too, from section 6.42, that it is necessary to adopt separate expansions for the excited fields, in terms of normal mode amplitude coefficients, on these two surfaces. Thus put

$$\underset{\approx}{T}_i = \sum_{m=1}^{\infty} C_m \underset{\approx}{T}_m$$

$$\underset{\sim}{v}_i = \sum_{m=1}^{\infty} C_m \underset{\sim}{v}_m \qquad \text{on } S_1 \qquad (7.403)$$

and

$$\underset{\approx}{T}_i = \sum_{m=-1}^{-\infty} C_m \underset{\approx}{T}_m$$

$$\underset{\sim}{v}_i = \sum_{m=-1}^{-\infty} C_m \underset{\sim}{v}_m \qquad \text{on } S_2 \qquad (7.404)$$

wherein the spatial variation, with respect to x and z, of the normal mode n is as $e^{j\underset{\sim}{\beta}_n \cdot \underset{\sim}{r}}$.

Continuing the now well-known procedure (103), (112), (113), an expression for the coupled normal mode amplitude coefficients can be obtained by substituting from equations (7.403) and (7.404) into the integral relation (7.402), and by using the orthogonality conditions (7.307) and (7.308) to simplify the integrands. The result, which is true for both positive and negative mode numbers, is

$$C_n = \frac{1}{4P} \int_V (\underset{\sim}{v}_n^{*T} \cdot \underset{\sim}{F}_i) dv \qquad (7.405)$$

Here P retains the interpretation established in relation to equation (7.304).

A comparison of equations (6.427) and (7.405) emphasises the similarities between the coupled mode amplitude expressions in the

acoustic waveguide and surface interaction contexts.

7.5 Determination of the Output from the Detection Transducer.

To show how the very many normal surface modes, scattered from an interaction region, relate to the signal output in the electrical port of a detection transducer, the scattering matrix formalism introduced in section 7.2 is employed. Through this approach the output signal, C_{out}, from the transducer can be determined to be

$$C_{out} = \sum_{n=1}^{\infty} C_n S_{On} \qquad (7.501)$$

the sum being over all input modes to the transducer. Expressions for the amplitudes (C_n, n=1,2,... ∞) of the coupled normal modes are available from equation (7.405), so that

$$C_{out} = \frac{1}{4P} \int_V \left[\sum_{n=1}^{\infty} S_{On} (v_n^{*T} . F_i) \right] dv \qquad (7.502)$$

In order to proceed further advantage is taken of the property of forward and reverse propagating surface acoustic waves, of mode numbers n and -n, respectively, (and of the same frequency), namely that

$$v_n^{*} = -v_{-n} \qquad (7.503)$$

When the wave motion is in isotropic media, this result is evident from the very nature of the Rayleigh wave particle displacements:- 2 dimensional, confined to the sagittal plane and describing a retrograde ellipse at the free surface, as detailed in section 3.15. If the substrate is anisotropic, the same velocity field relation obtains, but the proof is more difficult. Because an iterative computerised calculation is required to analyse anisotropic surface acoustic wave propagation (67), (78), (79), (refer sections 3.25, 3.35) it is convenient to allow the machine to verify the above relationship. Appendix I

provides a specific example of the surface wave displacement coefficients
and decay constants for forward and reverse travelling waves in an
anisotropic material; from these results it is clear that equation
(7.503) is still valid.

This enables the expression (7.502) to be modified to show that

$$C_{out} = -\frac{1}{4P} \int_V \left[(\sum_{n=1}^{\infty} S_{-n0} \, v_{-n}^T).F_i \right] dv \qquad (7.504)$$

where the symmetry property of the scattering matrix has been utilized
also. It is now possible to interpret the inner-bracketed term of
equation (7.504) as the actual velocity field of a unit amplitude,
($C_n = 1$), acoustic wave radiated towards the scattering region by a
power P signal applied to the detection transducer. In view of the
experimental device design described in section 5.1, in which all
transducers operate in the near field region, it is reasonable to assume,
in the present approximation, that an IDT of aperture W launches,
towards the scattering region, a uniform, but limited-width, surface
acoustic wave. Hence the field amplitudes within the square brackets
can be evaluated so as to ensure that power P is carried.

Because interest centres on calculating the fraction of the
incident energy scattered in a particular direction, the further assump-
tion, namely that the perturbed area of the substrate surface is illumin-
ated by another limited-width surface wave signal of power P, is appro-
priate. This determines clearly defined amplitudes for the body force
densities, F_i, induced by the incident wave interacting with the surface
perturbation. The properties of the symmetric scattering matrix
establish that the output power at the detection transducer is $P|C_{out}|^2$,
so that the ratio of output to incident power is

$$\cdot \quad \left[\int_V \underset{\sim}{v}_s \cdot \underset{\sim}{F}_i \, dv \right]^2 \Big/ 16P^2$$

where $\underset{\sim}{v}_s$ is the velocity field of the power P signal launched from the detection transducer towards the scattering region, and $\underset{\sim}{F}_i$ is the body force density created at the scattering region by an incident wave of power P.

Now this result can be related to the general surface scattering situation illustrated in Figure 7.1. The ratio of the output signal amplitude (measured at transducer T_r) to the input signal amplitude (applied to transducer T_p) is

$$\frac{\text{Scattered Amplitude}}{\text{Incident Amplitude}} = \frac{1}{4P} \left[\int_V \underset{\sim}{v}_r \cdot \underset{\sim}{F}_p \, dv \right] \qquad (7.505)$$

Here $\underset{\sim}{v}_r$ is the velocity field of the uniform, but limited-width surface wave which propagates from the receiving transducer, T_r, towards the scattering region, a power P. $\underset{\sim}{F}_p$ is the acoustic body force density created by the interaction of an identical surface wave, launched from transducer T_p, with the perturbed area of the propagation surface. In applying the formula of equation (7.505) it is important to note that the phasors $\underset{\sim}{v}_r$ and $\underset{\sim}{F}_p$ are the usual peak value quantities.

Equation (7.505) forms the basis for the theoretical predictions of surface acoustic wave crossbar coupler performance presented in Chapters IX and X.

CHAPTER VIII

THE CALCULATION OF SOURCE DISTRIBUTIONS BY PERTURBATION THEORY.

8.0 Introduction.

Chapters VI and VII have described techniques for calculating the amplitudes of normal modes excited by a known distribution of sources, for interactions in an electroacoustic waveguide and on an acoustic propagation surface. Two pre-requisites for this undertaking are a description of the normal (source-free) propagating modes of the system and the availability of an explicitly calculable expression for the source distributions. This chapter outlines a general method for calculating the source distributions using a perturbation theory. The method is of widespread applicability and is, in fact, the only approach to a solution in a large number of wide-ranging problems. Brief discussions are presented in relation to both an electromagnetic and an acoustic propagation structure. A specific example, formulated in the latter context, examines the coupling interaction from two distinct viewpoints; these lead to two different, but equally viable, interpretations of the perturbation expressions. The detailed calculations of Chapter IX further amplify the acoustic applications.

8.1 Notation for Field Quantities.

In order to obtain the most general results, the notation normally reserved for descriptions of linear relations in vector spaces in expositions of the quantum theory (117) is introduced. The electric, magnetic, acoustic stress and acoustic velocity fields are regarded as field quantities; the values of all of these at all points of the system under study form the field vector $|X\rangle$. Similarly, the sources of electromagnetic and acoustic fields, i.e. the current density and the

mechanical body force density, at all points, are combined into the single multi-dimensional vector $|Z\rangle$. The linearity of the field equations allows the assertion that the source vector is derivable from the field vector through a relationship of the form

$$|Z\rangle \quad = \quad B \ |X\rangle \tag{8.101}$$

where B is a linear operator depending in detail upon the boundaries of the system and upon the properties of the medium at all points of space.

8.2 The Perturbation Expansion.

The immediate aim is to derive relations, which are correct to first order, between the new fields and sources which are created when the boundaries or the material properties are subject to some small perturbation. An unperturbed operator, B_0, perturbing operator, B_1, and perturbed operator, B, can be defined such that

$$B = B_0 + \lambda B_1 \tag{8.201}$$

and the perturbation is small when λ tends to zero. Following the usual perturbation theory approach (117), it is assumed that both the perturbed field, $|X\rangle$, and the perturbed source, $|Z\rangle$, can be expressed as a power series in λ ; viz,

$$|X\rangle \quad = |X_0\rangle + \lambda |X_1\rangle + \lambda^2 |X_2\rangle + \text{----} \tag{8.202}$$

$$|Z\rangle \quad = |Z_0\rangle + \lambda |Z_1\rangle + \lambda^2 |Z_2\rangle + \text{----} \tag{8.203}$$

Here $|X_0\rangle$ and $|Z_0\rangle$ are the unperturbed fields and sources, while $|X_1\rangle$ and $|Z_1\rangle$ are the first order perturbation corrections. These expansions can be substituted into equation (8.101) to show, after the collection of like powers in λ, that

$$|Z_0\rangle \quad = B_0 \ |X_0\rangle \tag{8.204}$$

$$\lambda |z_1\rangle \quad = \quad \lambda B_1 \ |x_0\rangle \quad + \quad B_0 \lambda |x_1\rangle \qquad (8.205)$$

$$\text{Term a} \qquad\qquad \text{Term b}$$

Equation (8.205) is the desired expression for the additional sources introduced by perturbing the propagation structure.

8.3 Derivation and Interpretation of Expressions for the Sources in terms of the Perturbation Expansion.

The interpretation of equation (8.205), and its application to the search for explicitly calculable expressions for the sources of a perturbed system are illustrated now in both an electromagnetic and an acoustic context.

8.31 Sources in a Perturbed Electromagnetic Propagation Structure.

A suitable example is afforded by the electromagnetic waveguide into the cross-section of which is placed a rod of conductivity, σ. Sources of electromagnetic fields are the conduction current density, $\underset{\sim}{J}$, and the charge density, q. For a.c. fields the time-varying component of charge density is not independent of $\underset{\sim}{J}$, but the two quantities are related through the continuity equation

$$\underset{\sim}{\nabla} \cdot \underset{\sim}{J} \quad + \quad (\partial q / \partial t) = 0 \qquad\qquad (8.311)$$

Currents flowing in the conducting rod provide additional sources, the distribution of which is described by equation (8.205), for the excitation of electromagnetic fields. A more detailed examination of equation (8.205) is needed to determine the meaning of each of the terms a and b on the right hand side, how they can be evaluated, and which of them contribute to the coupling integrals by which one calculates the amplitudes of the normal modes excited.

Term a is the result of the perturbation, λB_1, acting upon the unperturbed field, $|X_0\rangle$. These two quantities are known — indeed

they are assumed known in the statement of the problem — so this term

can be calculated readily. In the present example of a perturbed

electromagnetic waveguide

$$\lambda B_1 \, |X_0\rangle = \sigma \, |E_0\rangle \tag{8.312}$$

where $|E_0\rangle$ is the unperturbed electric field-vector. Term b arises

from the action of the unperturbed operator, B_0, upon the perturbation

component, $\lambda|X_1\rangle$, of the field. This latter component is, in general,

unknown, so that the term $B_0 \, \lambda \, |X_1\rangle$ cannot be calculated simply. But

fortunately it usually makes no contribution to the coupling integral,

as described by equations (6.427) and (7.405), for any normal mode.

The vanishing of this term in the case of a conducting rod located

within an electromagnetic waveguide can be demonstrated easily; the

only source currents which can flow under the unperturbed operator, B_0,

are confined to the waveguide walls where the normal mode electric

fields are zero.

The preceding discussion indicates that the success of the pertur-

bation treatment in the present context rests upon the fact that, of

the two source terms on the right hand side of equation (8.205), the

first provides coupling to the normal modes and is explicitly calculable,

while the second, although not explicitly calculable, is uncoupled from

the normal modes.

8.32 Sources on a Perturbed Acoustic Propagation Surface.

In the acoustic context attention is focussed upon the interaction

which is of primary interest in the study of the microsonic crossbar

coupler. Coupling between an incident and an emergent surface wave is

provided by the addition, to the propagation surface, of a region of

uniform periodic mass-loading. Depending upon the precise manner in

which the surface perturbation is introduced into the analytical model,
two different interpretations of equation (8.205) are possible.   These
two separate viewpoints, and the interpretations to which they lead,
are discussed as cases 1 and 2 below.   In both instances the sources
of acoustic fields are defined to be those force densities which can-
not be expressed as the mass acceleration product of the unperturbed
medium, or alternatively, from equation (3.213), as the divergence of
the unperturbed stress tensor.

Case 1. One convenient model, illustrated in Figure 8.1(a), takes

account of the periodic mass-loading by incorporating

atoms of a slightly greater mass than those of the substrate

material into regions of the stress-free propagation surface

in a manner which correctly represents the spatial period-

icity of the deposited overlay in the actual device.

Using this model, and the above definition of acoustic

sources, it is obvious that no additional sources are

created by the mass-loading; indeed none are present in

the problem.   The perturbation equation (8.205) therefore

becomes

$$0 \; = \; \lambda \, B_1 \; |X_0\rangle \quad + \quad B_0 \, \lambda \, |X_1\rangle \tag{8.321}$$

Although, as in the electromagnetic example, term a is

explicitly calculable and term b is not, equation (8.321)

can be rearranged as

$$\lambda \, |Z_e\rangle \quad = -B_0 \, \lambda \, |X_1\rangle \tag{8.322}$$

$$\text{where} \quad \lambda \, |Z_e\rangle \quad = \lambda \, B_1 \; |X_0\rangle \tag{8.323}$$

in which form a suitable interpretation can be made.

Stress-free Propagation
Surface

Periodic Surface Mass Loading Region

Surface
Acoustic Wave
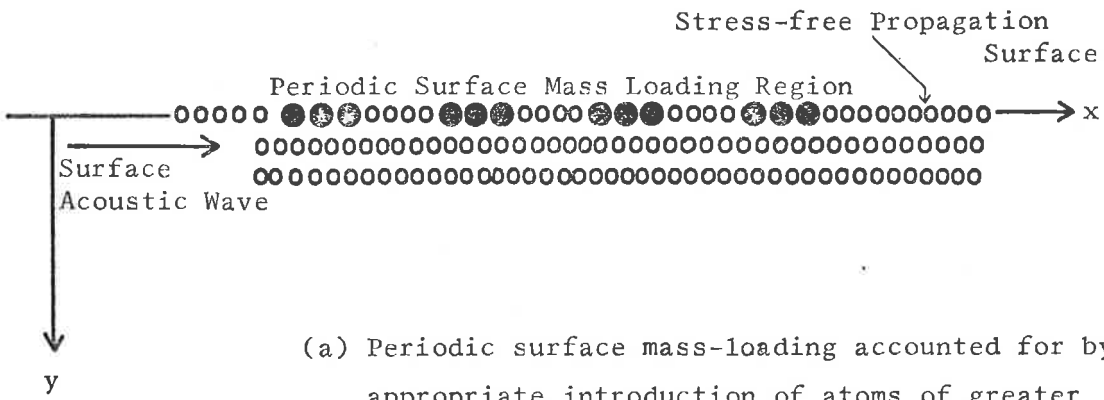
(a) Periodic surface mass-loading accounted for by
    appropriate introduction of atoms of greater
    mass into the substrate surface.

$$W(\rho', c_{ijkl}, x, z)$$

Surface Acoustic
Wave
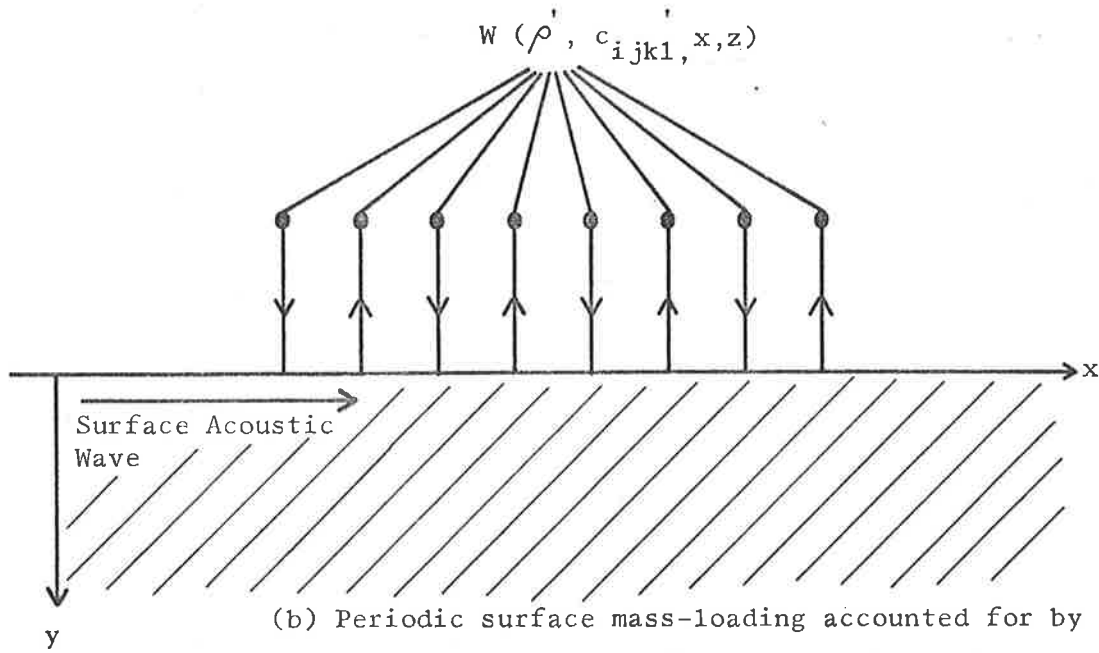
(b) Periodic surface mass-loading accounted for by
    an external system of levers which applies an
    appropriate periodic stress distribution to the
    propagation surface.

Figure 8.1

Analytical models of the periodic surface mass-loading used
to interpret perturbation expressions for the sources.

The right hand side of equation (8.322) results from the action of the perturbed field upon the unperturbed boundary. Thus equations (8.322) and (8.323) lead to the conclusion that the perturbed fields launched by the scattering mechanism can be considered as having been excited by an actual source distribution, $\lambda | z_e \rangle$, applied to the unperturbed boundary. In this way the effect of the surface perturbation can be replaced by that of an equivalent source distribution, $\lambda | z_e \rangle$, which acts on the unperturbed system and which is explicitly calculable through equation (8.323).

Case 2. Figure 8.1 (b) shows an alternative analytical model in which a system of external levers, the ends of which are bonded to the substrate surface, creates, on that surface, a stress pattern identical to that resulting from the interaction of an incident surface wave and the periodic mass-loading. The function $W(\rho', c'_{ijkl}, x, z)$, (which is a function not only of position on the xz propagation surface, but also of the mass density, ρ' , and the elastic constants, c'_{ijkl}, of the overlay) is used to describe the spatial and material property dependences of the mass-loading interaction, and hence also of the acoustic stress pattern on the model surface.

An interpretation of the source equation (8.205), as it applies in this situation, is now sought. Once again term a is explicitly calculable, and can be written in the form

$$\lambda B_1 | X_0 \rangle \; = \; W(\rho', c'_{ijkl}, x, z) \frac{\partial}{\partial t} |v_0\rangle \qquad (8.324)$$

where $|v_0\rangle$ is the unperturbed surface acoustic wave velocity evaluated at the free surface, $y = 0$. Term b must be zero because under the unperturbed operator, B_0, the propagation surface is stress-free for all fields; thus

$$B_0 \; \lambda | X_1 \rangle \; = \; 0 \qquad (8.325)$$

The utility of this treatment rests upon the fact that of the two source terms on the right hand side of equation (8.205) the first provides coupling to the normal modes, and is explicitly calculable, while the second, individual components of which are unknown, makes no contribution to the coupled fields.

8.4 Additional and Equivalent Source Distributions.

The studies of sections 8.31 and 8.32 illustrate the two different situations in which changing the propagation conditions within a system can be viewed either as an additional-source or as a source-free perturbation. An important result, common to all three interpretations discussed previously, is that the only source distribution, either additional or equivalent, coupling to the normal modes through the interaction integral is

$$\lambda | z_1 \rangle \; = \; \lambda B_1 | X_0 \rangle \qquad (8.401)$$

It is clear, from the example in section 8.32, that the precise form of the λB_1 depends upon the manner in which the perturbation is incorporated into the analytical model. Because the elements of $\lambda B_1 | X_0 \rangle$ are explicitly calculable, the above expression provides a result which

can be used directly in equations (6.427), (7.405) and (7.505) to determine the amplitudes of the normal modes excited by this source distribution.

In section 9.2 the sources described by equation (8.401) are derived in detail for the particular perturbation caused by the addition of periodic mass-loading to a surface acoustic wave propagation surface. Later sections of Chapter IX utilize these expressions for the sources to calculate the amplitudes of the normal modes which they launch. The viewpoint of section 8.32, case 2, is adopted in all of these subsequent calculations. As is emphasised by equation (8.324), and as will become apparent in section 9.2, this approach allows consideration not only of the predominant effect due to the mass of the perturbing layer, but also of the less significant effect due to the "elastic stiffness" of the overlay material.

CHAPTER IX

A DETERMINATION OF THE THEORETICAL PERFORMANCE OF THE SURFACE ACOUSTIC WAVE CROSSBAR COUPLER.

9.0 Introduction.

By drawing directly upon the results of many of the preceding chapters it is now possible to derive detailed and explicitly calcul-able expressions for those parameters which allow a theoretical assess-ment of the microsonic crossbar directional coupler.   The ultimate goals of the following analytical procedures are to obtain descriptions of the strength and frequency dependence of the coupled and directivity signals.

9.1 A Procedure for Analysis of Directional Coupler Performance.

Theoretical predictions of crossbar coupler behaviour rest upon the general coupled amplitude ratio expression of equation (7.505). The particular scattering situation to which this result is now to be applied is depicted in the metal overlay patterns of Figure 5.1. Essential features of the coupler, common to both styles A and B, are illustrated in Figure 9.1.   The device is, of course, reciprocal in that a wave launched at transducer 1 is coupled to transducers 2 and 3, but not to 4, while a signal applied to transducer 4 is coupled to transducers 2 and 3, but not to 1, etc.   To avoid confusion the con-vention is adopted, throughout this chapter, that the input signal is launched always from transducer 1; this means that the coupled wave is detected at transducer 3, the transmitted signal at transducer 2, and the unwanted directivity or back-scattered signal at transducer 4.

From equation (7.505) the coupled to incident surface wave amplitude ratio is
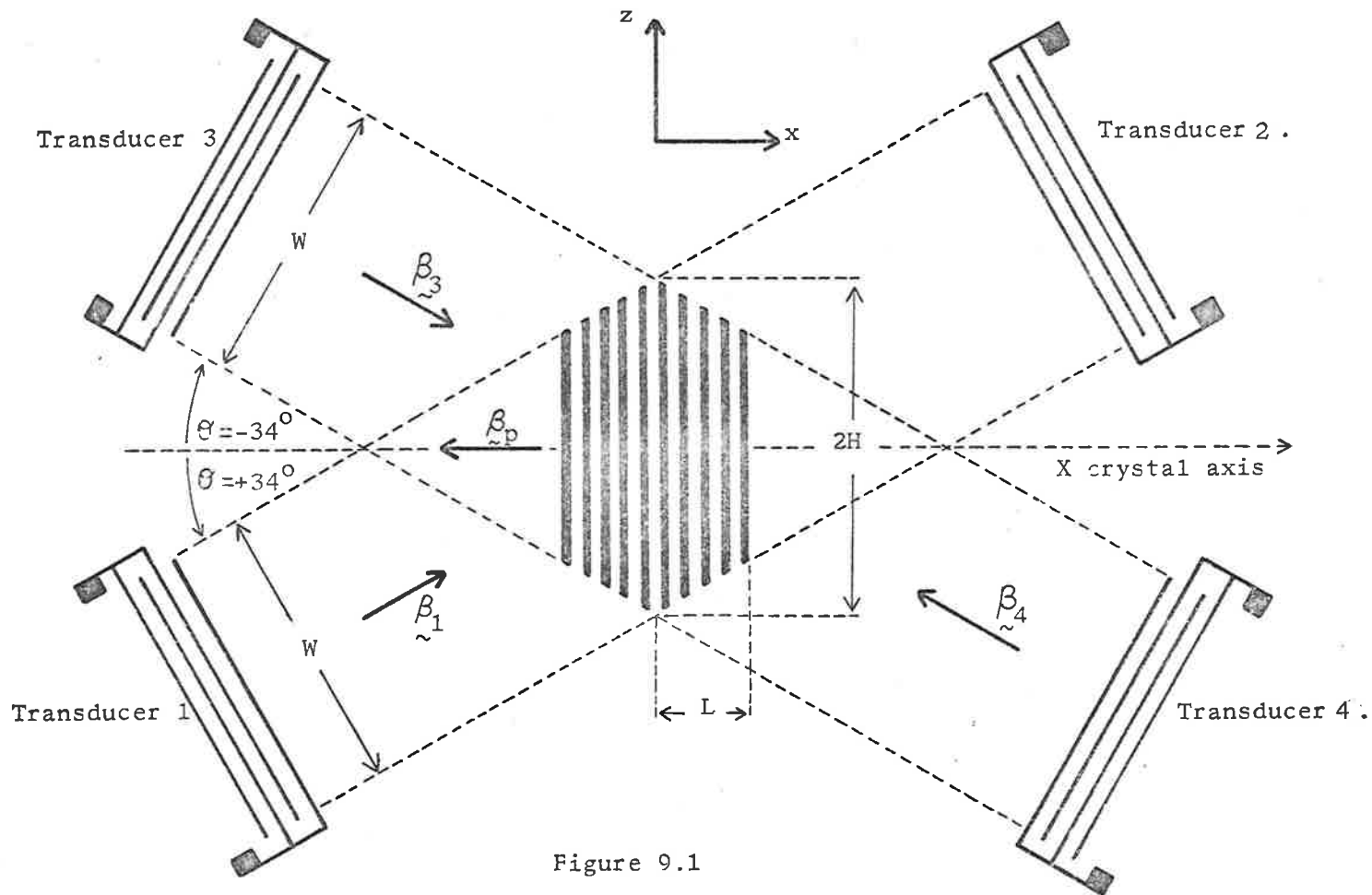
Figure 9.1

Surface acoustic wave crossbar directional
coupler configuration.

$$C = \left[\int v_3 \cdot F_1 \, dv \right] / 4P \qquad (9.101)$$

and the directivity to incident surface wave amplitude ratio is

$$D = \left[\int v_4 \cdot F_1 \, dv \right] / 4P \qquad (9.102)$$

All of the field variables in these two expressions retain the meanings established in section 7.5. F_1 is the peak value of the body force density produced by the interaction of an input surface acoustic wave, of beam-width W and of power P radiated from transducer 1 towards the scattering region, with the surface perturbation. The quantities v_3 and v_4 are the peak acoustic velocity fields of similar surface waves launched, again towards the interaction area, from transducers 3 and 4, respectively.

Further examination of the expressions for the coupled and directivity signal amplitude ratios is warranted. Significantly the general description of the scattered to incident amplitude ratios, equation (7.505), implies that some energy is scattered in all directions and at all frequencies. The crossbar coupler design procedure of section 5.1 selects an orientation and a periodicity for the surface mass-loading perturbation such that of the small amount of forward-launched surface wave energy not transmitted directly from transducer 1 to transducer 2, almost all is coupled to transducer 3. In theory, only surface wave signals of very small amplitudes are radiated in all other directions, the directivity signal detected at transducer 4 being a particular example of these.

Detailed consideration is given, in the following section, to the development of a procedure which facilitates calculations of the coupled to incident signal amplitude ratio, using equation (9.101). The

structures of equations (9.101) and (9.102), which at first sight seem
essentially identical, suggest that a corresponding calculation procedure
for the directivity signal amplitude ratio can be deduced; this is under-
taken in section 9.12, which also indicates the greater complexity of
the directivity signal analysis.

9.11 Coupled Signal Analysis Procedure.

For a fixed incident wave direction, the coupled wave amplitude
varies with output wave vector orientation in a manner which depends
upon three factors associated with the integral of equation (9.101).
The first of these is the term $\underset{\sim}{v_3} \cdot \underset{\sim}{F_1}$, which depends upon the directions
taken by the input and exit waves, and upon their angular separation, γ.
A second factor arises from the properties of the integral itself.
The discussion of section 8.32 indicates, and the calculations of section
9.23 show in detail, that the acoustic body force density, $\underset{\sim}{F_1}$, can be
replaced, at least for the present surface mass-loading interaction,
by an acoustic surface force density, $\underset{\sim}{F_1}$ dy, acting on the unperturbed
propagation boundary, y = 0.   This allows the volume integral of equation
(9.101) to reduce to an integral over the area, A, of the scattering
region which is illuminated by both transducers 1 and 3.   The term
$\left[\underset{\sim}{v_3} \cdot (\underset{\sim}{F_1} \, dy) \right]$ adds an $e^{j \underset{\sim}{\beta} \cdot \underset{\sim}{r}}$ spatial dependence within the surface,
where

$$\underset{\sim}{\beta} = \underset{\sim}{\beta_1} + \underset{\sim}{\beta_3} + \underset{\sim}{\beta_p} \qquad (9.111)$$

Here $\underset{\sim}{\beta_1}$ is the wave vector of the input signal launched from
transducer 1,

$\underset{\sim}{\beta_3}$ is the wave vector of the signal scattered towards trans-
ducer 3,

. β_p is the wave vector of the surface perturbation,

and r is a position vector in the plane of the surface.

It is clear, from Figure 5.2 and the accompanying discussion of section

5.12, that $\beta = 0$ and hence $e^{j\beta \cdot r} = 1$ at the centre frequency. In

as much as β_1 and β_3 are frequency dependent, this term also describes

the frequency response of the coupled wave amplitude. These two

properties of $e^{j\beta \cdot r}$ are exploited in the ensuing calculation procedure.

The third source of scattered amplitude dependence upon output

wave direction is more subtle and requires a closer study of the

expression (9.101). C_{ω_0}, the coupled to incident surface wave ampli-

tude at the centre frequency, ω_0, can be expressed now in the form

$$C_{\omega_0} = \left[\int (v_3^0 \cdot F_1 \, dy) \, dx \, dz \right] / 4WP_u$$

$$= (v_3^0 \cdot F_1 \, dy) \, A / 4WP_u \qquad (9.112)$$

where the superscript "0" denotes a term evaluated at the propagation

surface, $y = 0$. Here also, from equation (7.304),

$$P_u = -\tfrac{1}{2} \int_0^\infty \text{Real Part} \left[T_{xj} \, \dot{u}_j^* \right] \, dy \qquad (9.113)$$
$$j = x, y, z.$$

is the component of acoustic power flow, per unit beam-width of the

scattered wave, in the direction of the coupled wave vector (nominally

assumed to be the x coordinate direction in the above expression).

W, as shown in Figure 9.1, is the aperture of the IDTs. The same

figure introduces the additional quantities H and L which are the half-

width and half-length, respectively, of the mass-loading grid; with

these, equation (9.112) can be further modified to obtain

$$C_{\omega_0} = (v_3^0 \cdot F_1 \, dy) \, 4LH\Delta \, / \, 4 \, WP_u$$

i.e. $C_{\omega_0} = (v_3^0 \cdot F_1 \, dy) \, 2L \, \Delta \, / \, 4P_u \cos \theta$ (9.114)

In this expression

$$\Delta = A \, / \, 4LH \qquad (9.115)$$

is an area correction factor which relates the actual area of the

scattering region, A, to that of a rectangle of sides 2L and 2H. As

defined in Figures 5.2 and 9.1, θ is the angle between the incident

and perturbation wave vectors; the device configurations pictured in

Figure 5.1 set $\theta = 34^0$. Equation (5.124) states that the periodicity,

λ_p, of the surface perturbation is related to the centre frequency

wavelength, λ_0, of the input surface wave signal, through the require-

ment that

$$\lambda_p = \lambda_0 \, / \, 2 \cos \theta \qquad (9.116)$$

This result can be used in equation (9.114) to determine

$$C_{\omega_0} = N \lambda_0 \; (v_3^0 \cdot F_1 \, dy) \, \Delta \, / \, 8P_u \cos^2 \theta \qquad (9.117)$$

where N is the number of mass-loading elements in the scattering region.

When written in this form, it is obvious that the coupled wave amplitude

ratio is increased according to $\sec^2 \theta$, as the angle of separation,

$\tau = 2\theta$, between input and output waves is increased. Equation (9.117)

serves not only to highlight the third source of scattered amplitude

dependence upon the direction of the output wave but also to present

the expression for the coupled wave amplitude ratio in a form well

suited to calculation.

The prior discussion suggests that an analysis of the magnitude

and frequency response of the coupled signal proceeds most simply by

following the three separate steps outlined below.

•1. From the perturbation approach of equation (8.401), determine the surface force density sources created by the application of periodic mass-loading to the propagation surface:- this provides the $(F_{\sim 1} \, dy)$ factor of equation (9.117).

2. Use equation (9.117) to calculate C_{ω_0}, the coupled to incident surface wave amplitude ratio at the device centre frequency.

3. Separately explore the coupled signal frequency response as described by

$$F(\omega) = \iint e^{j \beta_{\sim} \cdot x_{\sim}} \, dA \qquad (9.118)$$

in which $\beta_{\sim}$ is given by equation (9.111).

Note that step 2 requires, as assumed already in section 5.1, that a single wave vector, $\beta_{\sim p}$, be assigned to the periodic surface perturbation. The coupled mode function, $F(\omega)$, takes account of the finite extent of the scattering region. In section 9.6 an argument justifying this treatment, which neglects contributions from higher harmonics of the scattering perturbation, is presented.

9.12 Directivity Signal Analysis Procedure.

A comparison of equations (9.101) and (9.102) emphasises the basic fact that the coupled and directivity signals are scattered by the same distribution, $(F_{\sim 1} \, dy)$, of acoustic surface force density. But an analysis of the strength and frequency response of the directivity wave is considerably more complicated because the wave vector diagram for this scattered signal does not close, even at band centre; this property is inferred in Figure 9.1, and is enlarged upon in section 9.5. Nevertheless the calculation can proceed in similar steps to those described previously for the coupled signal.

.1. Calculate, by analogy with equation (9.117), the quantity

$$D'_{\omega_0} = N \lambda_0 \, (v_4^0 \cdot F_1 \, dy) \, \Delta \, / \, 8P_u \, \cos^2\theta \qquad (9.121)$$

which contributes to the directivity signal amplitude ratio at the centre frequency.

2. By analogy with equation (9.118), separately evaluate the function

$$G(\omega) = \iint e^{j \, \beta \cdot r} \, dA \qquad (9.122)$$

where now

$$\beta = \beta_1 + \beta_4 + \beta_p \qquad (9.123)$$

Since $\beta \neq 0$, $e^{j \, \beta \cdot r} \neq 1$ at band centre, so that the centre frequency directivity to incident signal amplitude ratio, D_{ω_0}, must be evaluated by utilizing the results of steps 1 and 2;

$$D_{\omega_0} = D'_{\omega_0} \, G(\omega_0) \, / \, A \qquad (9.124)$$

A is, as usual, the area of the surface perturbation illuminated by both transducers 1 and 4; - i.e. the entire scattering region shown in Figures 5.1 and 9.1. The frequency response of the directivity signal amplitude ratio is determined solely by the coupled mode integral of equation (9.122).

Normally the directivity of a directional coupler is expressed as a coupled to directivity signal amplitude ratio (in dB). This quantity and its frequency variation can be calculated by combining the above result, equation (9.124), with those of section 9.11, equations (9.117) and (9.118), to show that

$$\text{Directivity} = \frac{\text{Coupled Signal Amplitude}}{\text{Directivity Signal Amplitude}}$$

$$= C_{\omega_0} \, F(\omega) \, / \, D'_{\omega_0} \, G(\omega) \qquad (9.125)$$

9.2 Derivation of the Source Distribution Produced by Periodic Mass Loading on a Surface Acoustic Propagation Surface.

The effect, on surface acoustic wave motion, of mechanically loading the boundary has been examined in connection with studies of propagation (108), (122), microsonic waveguide structures (48) - (50), scattering (108), (110), (111), and IDT performance (108), (110). The derivation of acoustic source distributions undertaken here is based directly upon Skeie's perturbation treatment (110) of the mass-loaded propagation surface. His results are reproduced only in the detail required for an understanding of the analytical procedures and for the correct interpretations to be placed upon variables in subsequent calculations. As later sections of this chapter show, the utilization of these source terms in deriving explicit expressions for the scattered wave amplitudes differs considerably from Skeie's method; sections 7.5 and 9.1 have developed an integral technique suited to the investigation of scattering on a surface in preference to the scattering matrix formulation established by Skeie to explore a one-dimensional situation.

9.21 Surface Acoustic Wave Propagation on a Free Surface.

Consider, in the notation of Chapter III, a surface acoustic wave travelling in the +x direction on the surface $y = 0$ of a substrate which is non (or weakly) piezoelectric, but which may or may not be elastically anisotropic. The surface density of the elastic energy carried by this wave motion is

$$ W_e = \tfrac{1}{2} \int_0^\infty T_{ik} \, S_{ik}{}^* \, dy \qquad (9.211) $$
$$ i,k = x,y,z $$

and the surface density of the kinetic energy is

$$W_k = \tfrac{1}{2}\rho\omega^2 \int_0^\infty u_i\, u_i^* \; dy \qquad (9.212)$$
$$i,k = x,y,z$$

When a uniform surface acoustic wave propagates through a lossless medium the phase velocity and particle displacement components adjust themselves in a way such that

$$\Delta W = W_e - W_k$$
$$= 0 \qquad (9.213)$$

9.22 Surface Acoustic Wave Propagation on a Uniformly Mass-Loaded Surface.

Suppose now that the wave motion is perturbed by depositing onto the substrate surface a thin layer, of height h, of a material with different elastic properties. This situation is illustrated in Figure 9.2. Providing that the overlay is sufficiently thin it is reasonable to assume, in the first approximation, that the particle displacements are of a constant amplitude throughout the total thickness of the film and that they are described by the displacement components for propagation on the free substrate surface. Under these conditions, equations (9.211) and (9.212) show that

$$\Delta W = \tfrac{1}{2}h\,(c'_{iklm}\, S_{ik}^{\;0}\, S_{lm}^{\;0*} - \rho'\omega^2\, u_i^{\;0}\, u_i^{\;0*}) \qquad (9.221)$$

where the stresses, T_{ik}, have been expanded, through equation (3.211), in terms of the fourth order elastic constant tensor, c'_{iklm}, and the strains, S_{lm}. In this relationship the primed quantities are properties of the overlay material, while the superscript "0" denotes acoustic field quantities to be evaluated at the free surface of the unloaded substrate.

Equation (9.221) describes a ficticious energy unbalance between
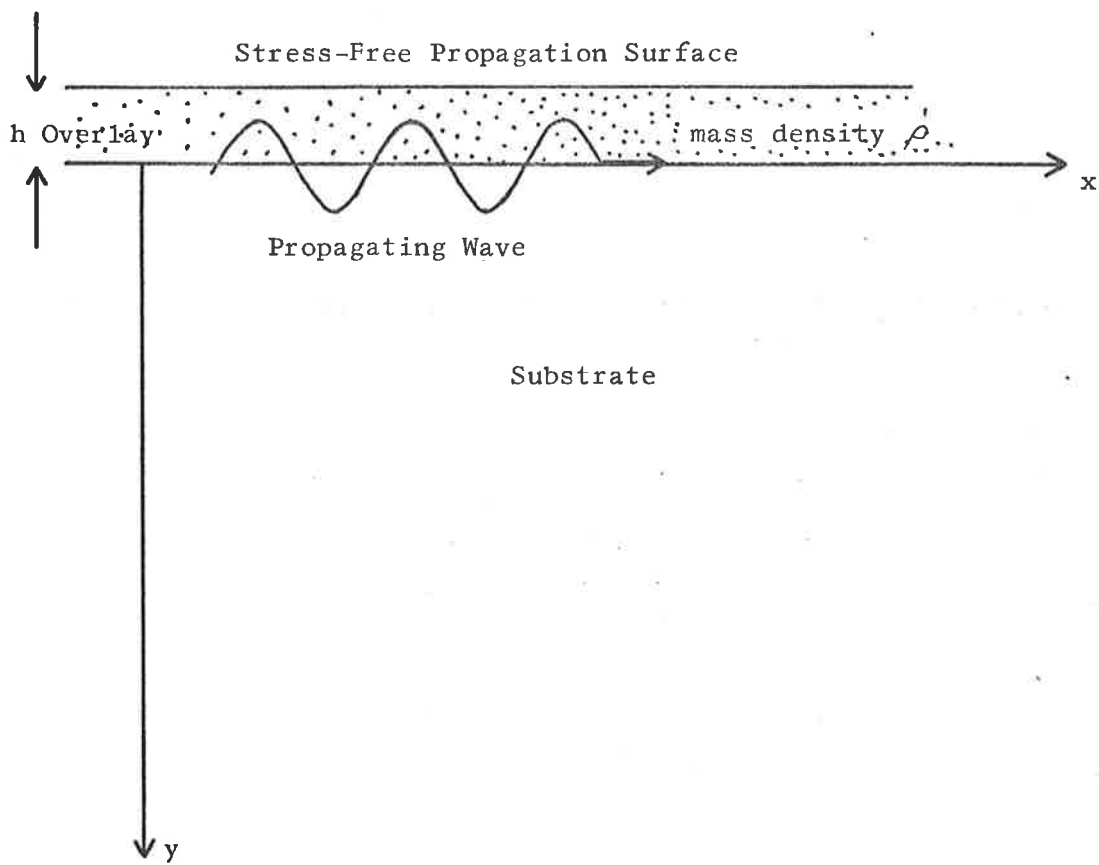
Figure 9.2

Surface acoustic wave propagation on a uniformly
mass-loaded surface.

the kinetic and stored elastic surface energy densities associated with

the wave motion in the layered medium.   In practice this energy

difference does not arise because the surface wave phase velocity and

particle displacements are readjusted, on addition of the overlay, to

maintain $\Delta W = 0$.   But the above expression for ΔW offers a conven-

ient method for deriving, correct to first order, two important results.

The first of these is the phase velocity perturbation, which may

be an increase, if the overlay stiffens the substrate, or a decrease,

if the overlay provides mass-loading.   A precise knowledge of this

velocity perturbation is the key to the design of thin film guides for

surface acoustic waves (30), (48) - (50), (123) and of laminated media

surface wave dispersive delay lines (2), (4), (124):- it is also an

important parameter in Skeie's derivation of a reflection coefficient

for an individual finger of an IDT (110).   But in the present study

the phase velocity perturbation plays only a secondary role.   In

analyses of microsonic crossbar coupler performance the scattered wave

amplitudes must be predicted by a perturbation treatment of the surface

mass-loading interaction.   Thus, as stated in section 5.2, and as

detailed for individual devices in sections 10.3 and 10.8, practical

couplers are fabricated from comparatively thin surface mass-loading

overlays (of height less than 1% of a surface acoustic wavelength)

for which the velocity slowing is quite small, (typically less than 3%).

But should it be desirable to know the velocity perturbation in a

particular situation — e.g., to facilitate the design of a scattering

grid functioning at a precise centre frequency — approximate results

for certain substrate and overlay material combinations are plotted by

Skeie (110), and more accurate values are calculated by other workers

(49); (50) exploring modes of propagation in surface acoustic waveguides.

The second important result which can be derived from the ficticious energy unbalance of equation (9.221) is the distribution of surface force densities due to the presence of the overlay.   A calculable expression for these sources is, of course, of vital importance to a theoretical investigation of crossbar directional coupler performance.

9.23 Source Distributions on a Uniformly Mass-Loaded Surface.

At this juncture the overlay is assumed to be elastically isotropic; this is in harmony with the device fabrication procedure described in section 5.2, where the deposited mass-loading film is gold.   Now the elastic constant matrix, c'_{iklm}, of the overlay material can be replaced by its isotropic counterpart, which involves only Lamés's elastic constants, λ' and μ'.   Skeie uses the stress-free propagation surface boundary conditions to show that the energy unbalance of equation (9.221) can be manipulated (112) into the form

$$\Delta W = \frac{h}{2} \beta^2 \left[\frac{4\mu' (\lambda' + \mu')}{(\lambda' + 2\mu')} u_x^0 u_x^{0*} + \mu' u_z^0 u_z^{0*} - \rho' v_s^2 u_i^0 u_i^{0*} \right] \qquad i = x,y,z \qquad (9.231)$$

in which β $(= \omega/v_s)$ is the surface acoustic wave vector on the unperturbed substrate.   Differentiation of ΔW with respect to the components of particle displacements yields the components of reaction surface force density,

$$\Delta F_i = - \left[\partial(\Delta W) / \partial u_i \right] \qquad i = x,y,z \qquad (9.232)$$

which, from equation (9.231), are

$$\Delta F_x = h\omega^2 \left[\rho' - \frac{4\mu'(\lambda' + \mu')}{v_s^2(\lambda' + 2\mu')} \right] u_x^0$$

$$\Delta F_y = h\omega^2 \rho' u_y^0 \qquad\qquad (9.233)$$

$$\Delta F_z = h\omega^2 \left[\rho' - \frac{\mu'}{v_s^2} \right] u_z^0$$

Reference to equations (8.324) and (8.401) shows that the above expressions for the reaction surface force densities have the structure predicted by the general perturbation theory of Chapter VIII:- the sources, ΔF_i, are calculable in terms of the unperturbed field quantities, u_i^0, which are the displacement components on the free (unplated) surface, and the properties of the boundary perturbation, namely the material constants, λ', μ' and ρ', of the overlay. As mentioned briefly in section 8.4, the analysis presented here allows the sources described by equation (9.233) to contain both mass loading terms, (in ρ'), and stiffness loading terms (in μ') (108), (110). Because the substrate is, in general, anisotropic, the transverse component of particle displacement is usually non-zero, which leads, in turn, to a non-zero value of ΔF_z.

The elastic isotropy of the overlay permits the surface force densities of equation (9.233) to be written in a manner more suited to numerical evaluation. In isotropic media the shear wave phase velocity, v_t', and the longitudinal wave phase velocity, v_1', are determined by

$$v_t' = (\mu'/\rho')^{\frac{1}{2}} \qquad\qquad (9.234)$$

$$\text{and} \quad v_1' = \left[(\lambda' + 2\mu')/\rho' \right]^{\frac{1}{2}} \qquad\qquad (9.235)$$

The ratio of the two volume wave velocities is fixed by the Poisson's

ratio, σ', of the material to be

$$q' = (v_t' / v_1')^2 = (0.5 - \sigma') / (1 - \sigma') \qquad (9.236)$$

With these three relationships the sources of equation (9.233) can be re-expressed as

$$\Delta F_x = h\omega^2\rho' \left[1 - 4(1 - q')(v_t'/v_s)^2 \right] u_x^0$$

$$\Delta F_y = h\omega^2\rho' u_y^0 \qquad (9.237)$$

$$\Delta F_z = h\omega^2\rho' \left[1 - (v_t'/v_s)^2 \right] u_z^0$$

in which form they are more amenable to calculation.

9.24 Source Distributions on a Periodically Mass-Loaded Surface.

The surface force densities of equation (9.237) are those caused by the addition to the propagation surface of a continuous, uniform mass-loading film of thickness, h. But the practical crossbar couplers illustrated in Figures 5.1 and 5.3 have a mass-loading provided by a periodic array of metal strips, etched from a continuous overlay, so that their profile, in a cross-sectional plane containing the X crystal axis, is rectangular, as sketched in Figure 9.3. The function $\varsigma(x,y)$ which describes this profile can be decomposed by Fourier theory into its harmonic components;

$$\varsigma(x,y) = \frac{2h}{\pi} \left[\cos \beta_p x - \frac{1}{3} \cos 3\beta_p x + \frac{1}{5} \cos 5\beta_p x - \quad\ldots\ldots \right]$$

$$= \frac{h}{\pi} \left[(e^{j\beta_p x} + e^{-j\beta_p x}) - \frac{1}{3}(e^{j3\beta_p x} + e^{-j3\beta_p x}) \right.$$

$$\left. + \frac{1}{5}(e^{j5\beta_p x} + e^{-j5\beta_p x}) - \quad\ldots\ldots \right] \qquad (9.241)$$

In this expression β_p $(= 2\pi/\lambda_p)$ is the magnitude of the perturbation wave vector. Later calculations of the coupled signal amplitude consider only the contribution arising from $\underset{\sim}{\beta}_p = -\beta_p$, while derivations
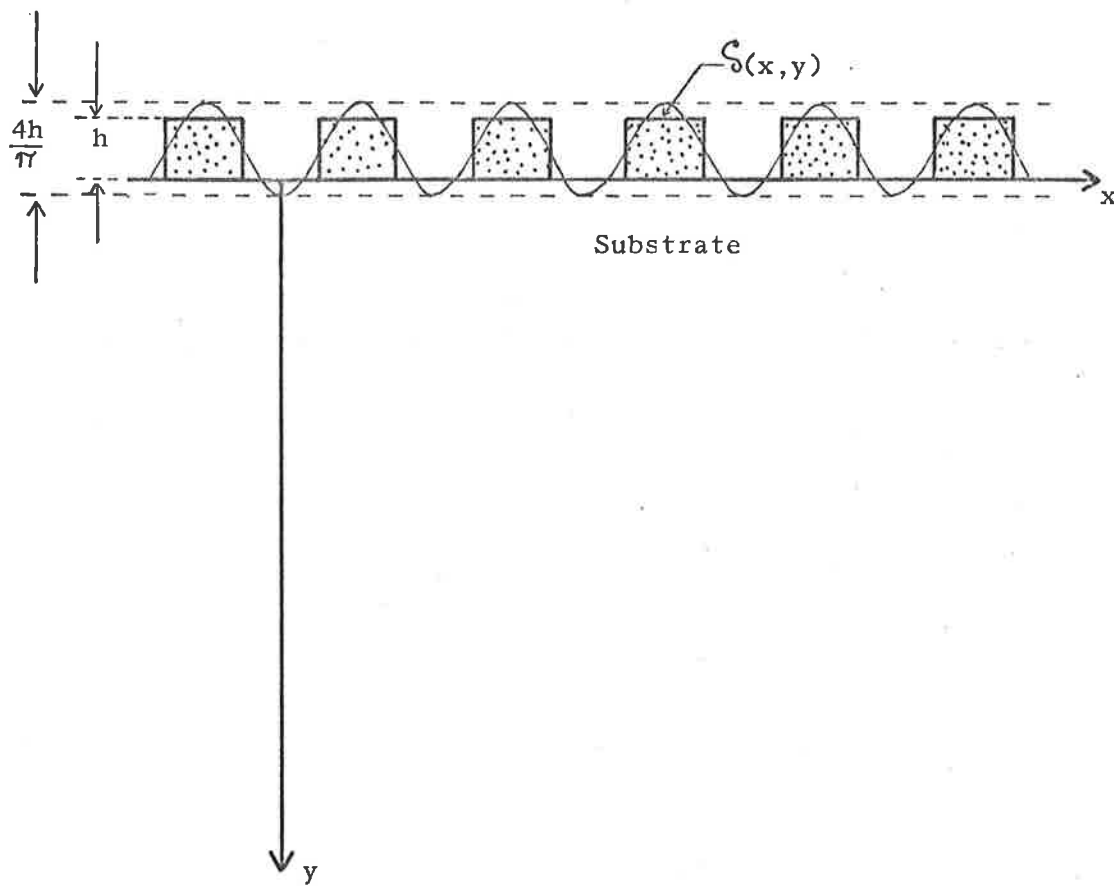
Figure 9.3

Periodic mass-loading of an acoustic propagation
surface.

of the directivity signal amplitude consider contributions from $\beta_{\sim p} = \pm \beta_p$. As noted in section 9.11, this approach neglects the higher harmonic components of the periodic surface mass loading, (i.e. $\beta_{\sim p} = \pm 3 \beta_p$, $\pm 5 \beta_p$ etc. in equation (9.241)) and its validity must be established carefully; this task is undertaken in section 9.6.

It can be seen from the expansion, (9.241), that the surface force densities for periodic mass-loading of a surface acoustic wave propagation surface are determined by equation (9.237) with h replaced by h/π ; i.e.

$$\Delta F_x = (h/\pi) \omega^2 \rho' \left[1 - 4(1 - q') (v_t'/v_s)^2 \right] u_x^0$$

$$\Delta F_y = (h/\pi) \omega^2 \rho' u_y^0 \qquad\qquad (9.242)$$

$$\Delta F_z = (h/\pi) \omega^2 \rho' \left[1 - (v_t'/v_s)^2 \right] u_z^0$$

The ΔF_i have an obvious time and spatial dependence of the form $\exp\left\{ j \left[\omega_i t - (\beta_{\sim i} + \beta_{\sim p}).\underset{\sim}{r} \right] \right\}$ which has been omitted from, but is implied within, the above expressions.

9.3 Derivation of the Centre Frequency Coupled Wave Amplitude Ratio.

Armed with the above calculable expressions for the surface force densities, equation (9.117) can be expanded into a form which allows an evaluation of the centre frequency coupled wave amplitude ratio, C_{ω_0}, in a specified situation. This expansion procedure is handled most easily in three stages, as detailed in the following three sections.

9.31 The Mass-Loading Interaction Power.

The singly most difficult factor to manipulate in equation (9.117) is the "interaction power" term, $(v_{\sim 3}^0 . F_{\sim 1} dy)$. Equation (3.224) recalls that the components of surface acoustic wave particle displacement in

anisotropic media are of the form

$$u_i = \sum_{j=1}^{3} C_i{}^{(j)} e^{-\alpha^{(j)} \omega y/v_s} e^{j\omega(t-x/v_s)} \qquad i = x,y,z$$

while equation (3.323) shows that the corresponding result in piezo-
electric materials differs only in the respect that summation is over
j=1 to 4. Thus the free surface particle displacement components are

$$u_i{}^0 = \sum_j C_i{}^{(j)} \qquad i = x,y,z \qquad (9.311)$$

the summation being over j=1 to 3 when piezoelectricity is absent or
neglected, and over j=1 to 4 when piezoelectric properties are included
in the analysis. A comparison of the results presented in Appendices
I and II reveals that when the substrate is weakly piezoelectric, the
total surface wave particle displacement components are essentially
the same whether the computational process considers the medium to
be non-piezoelectric, piezoelectric, or piezoelectric with an ideal
metal overlay. The ensuing calculations are based upon the data
outputs of computer program "Anisom", (Appendix I); the discussion of
section 10.31 demonstrates that this neglect of piezoelectric contribu-
tions does not reduce the accuracy of theoretical predictions of the
coupled wave amplitudes.

Figures 5.1 and 9.1 indicate that the incident wave radiated by
the IDT in port 1 of the experimental crossbar coupler travels at $+34^{\circ}$
to the X crystal axis, on the AT cut quartz surface, and has, in the
coordinate notation of Figure 9.1, a positive x wave vector component.
Hence the free surface particle displacements for this wave are

$$\left[u_i{}^0\right]_1 = \sum_j C_i{}^{(j)} = K_i \qquad i = x,y,z \qquad (9.312)$$

the $C_i^{(j)}$ being those listed in Appendix I (page 4), and the "$[\ ]_1$",

denoting a field quantity associated with a wave launched by the IDT

in port 1.   The above expression allows numerical values for the u_i^0

to be substituted into equation (9.242) to obtain the surface force

densities, $(F_1\ dy)$.

The second factor that must be known in order to compute the

interaction power is v_3^0, which is defined, in section 9.1, to be the

peak velocity field of a "similar" surface acoustic wave launched from

transducer 3 towards the scattering region.   This wave is "similar"

in the sense that it carries the same power per unit beamwidth as the

input wave radiated from transducer 1.   Figure 9.1 discloses that the

wave whose velocity field is v_3 propagates along the path angled at

-34^0 to the X crystal axis and has a positive x wave vector component.

The free surface velocity field components of this signal are

$$\left[v_i^0 \right]_3 = j\omega \sum_j C_i^{(j)} = j\omega M_i \qquad i = x,y,z \qquad (9.313)$$

where the $C_i^{(j)}$ are to be found in Appendix I (page 8).   As recorded

in section 3.52, and as evidenced by the analytical curves of Figure

3.5, the AT cut quartz crystal exhibits elastic symmetry about the X

crystal axis.   One result of this symmetry property, which may be

deduced from the numerical data in Appendix I, is that in equations

(9.312) and (9.313),

$$K_x = M_x^{*}$$

$$K_y = -M_y^{*} \qquad\qquad (9.314)$$

$$K_z = -M_z^{*}$$

The same relationships hold for the displacement amplitude coefficients

of all pairs of surface waves which differ only in the sign of their

wave vector component resolved normal to an axis of elastic symmetry, on an anisotropic substrate.

Equations (9.242) and (9.312) provide expressions for the components of the surface force density, $(F_1 \, dy)$, as formulated in a coordinate system determined by the wave vector of the signal launched from transducer 1 (now labelled the x' coordinate direction) and the free surface normal (y'). But equation (9.313) describes the components of the velocity field v_3^0 in a system whose orientation is governed by the wave vector of the signal launched from transducer 3 $(x''$ coordinate direction) and the surface normal (y''). This coordinate notation is illustrated in Figure 9.4, which shows that the x'' coordinate system is rotated an angle $\tau = 2\theta$ about the y' axis from the x' coordinate system; clearly τ is the angular separation of the input and coupled wave vectors. Before attempting to calculate the interaction power, $(v_3^0 \cdot F_1 \, dy)$, the usual tensor transformation

$$v_i' = a_{ki} v_k''$$

(9.315)

in which $a_{ki} = \cos(x_k'', x_i')$ must be employed to obtain expressions for the components of v_3^0 in the x' coordinate system. These are established to be

$$\left[v_x^0 \right]_3 = j\omega \left[M_x \cos\tau + M_z \sin\tau \right]$$

$$\left[v_y^0 \right]_3 = j\omega M_y$$

(9.316)

$$\left[v_z^0 \right]_3 = j\omega \left[-M_x \sin\tau + M_z \cos\tau \right]$$

Now the interaction power can be expanded as the sum of component products through the relation

(9.317)

$$(v_3^0 \cdot F_1 \, dy) = \left[v_x^0 \right]_3 \left[\Delta F_x \right]_1 + \left[v_y^0 \right]_3 \left[\Delta F_y \right]_1 + \left[v_z^0 \right]_3 \left[\Delta F_z \right]_1$$
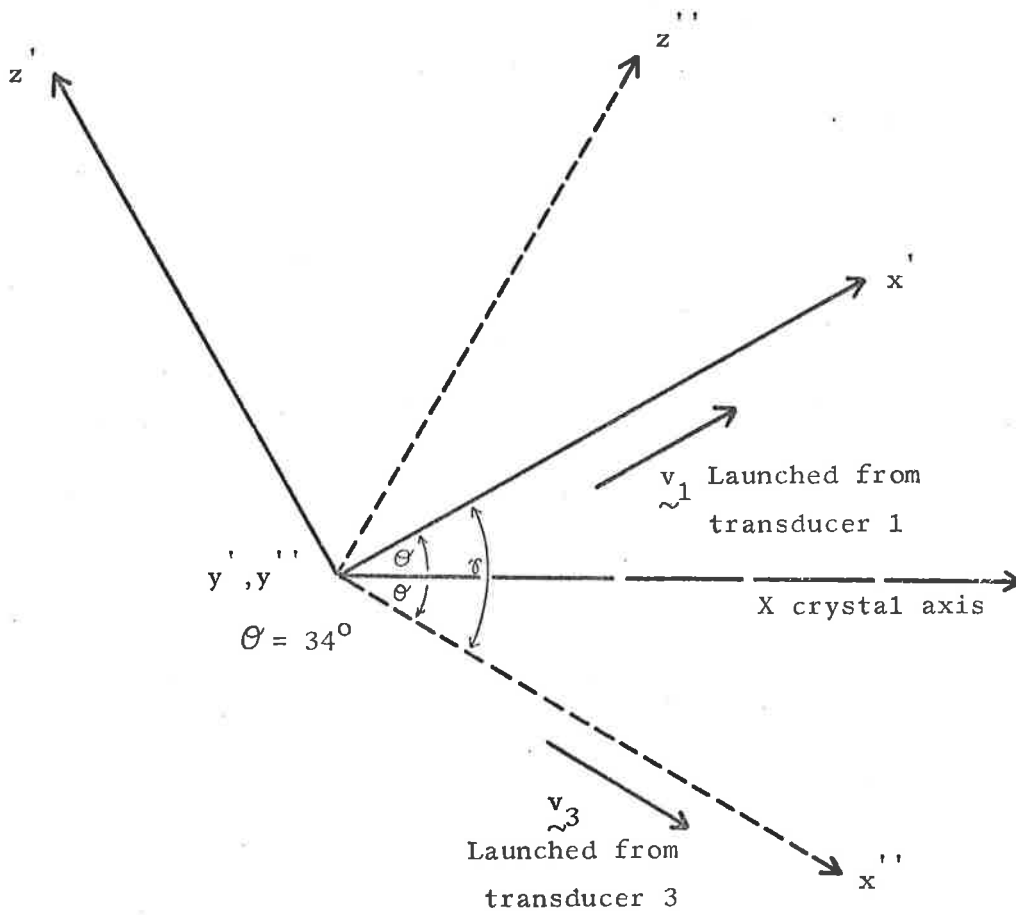
Figure 9.4

Coordinate notation used to determine the acoustic

interaction power.

Equations (9.242), (9.312) and (9.316) allow these contributions to

$(v_3^0 \cdot F_1 \, dy)$ to be expressed as

$$\left[v_x^0\right]_3 \left[\Delta F_x\right]_1 = j\omega^3 \frac{h}{\pi} \rho' \left[1 - 4(1-q') \left(\frac{v_t'}{v_s}\right)^2\right] K_x \left[M_x \cos\gamma + M_z \sin\gamma\right]$$

$$\left[v_y^0\right]_3 \left[\Delta F_y\right]_1 = j\omega^3 \frac{h}{\pi} \rho' \, K_y \, M_y \qquad\qquad (9.318)$$

$$\left[v_z^0\right]_3 \left[\Delta F_z\right]_1 = j\omega^3 \frac{h}{\pi} \rho' \left[1 - \left(\frac{v_t'}{v_s}\right)^2\right] K_z \left[-M_x \sin\gamma + M_z \cos\gamma\right]$$

in which form they are calculable from a knowledge of the elastic

properties of the overlay and the surface wave propagation character-

istics on the substrate.

9.32 The Power Per Unit Beamwidth of a Surface Acoustic Wave.

The final quantity which must be expressed in a calculable form

to permit an evaluation of the centre frequency coupled amplitude ratio

from equation (9.117), is P_u, the component, in the direction of the

wave vector, of acoustic power flow per unit beam-width of the surface

wave. Equation (3.241) shows that the components of acoustic power

flow per unit beamwidth of a surface wave are

$$P_i = -\frac{1}{2} \int_0^\infty \text{Real Part } (T_{ij} \, \dot{u}_j^*) \, dy \qquad\qquad (9.321)$$

$$i = x, z \qquad\qquad j = x, y, z$$

where P_y, the component normal to the free surface, is zero. The two

non-zero contributions, P_x and P_z, can be written in the form

$$P_i = \frac{1}{2} \omega \left[\text{Real Part } (R_i)\right] \qquad\qquad (9.322)$$

where it is clear, from the structure of the integrand of equation

(9.321) and from the analysis of section 3.2, that the R_i can be

expressed in terms of the surface wave particle displacement amplitude

coefficients, $C_i^{(j)}$, the decay constants, $\alpha^{(j)}$, and the elastic constants of the medium. Computer programs "Anisom" and "Pianm" calculate the complex quantities R_x and R_z which, in the data outputs contained in Appendices I and II, are loosely labelled as the longitudinal and transverse "power flow components", respectively. For the chosen propagation paths of the crossbar coupler, (i.e. at $\pm 34^o$ to the X crystal axis on AT cut quartz),

$$\text{Real Part } (R_z) \ll \text{Real Part } (R_x)$$

which ensures that the misalignment angle

$$\phi = \arctan \left[\text{Real } (P_z) / \text{Real } (P_x) \right]$$
$$= \arctan \left[\text{Real } (R_z) / \text{Real } (R_x) \right] \qquad (9.323)$$

between wave and power flow vectors is essentially zero.

In section 9.11 and, in particular through equation (9.113), P_u is defined to be the component of acoustic power flow, per unit beamwidth of the scattered wave, in the direction of the coupled wave vector; i.e. of the wave travelling towards transducer 3 from the perturbed surface region. Figure 9.1 indicates that this wave propagates at an angle of -34° to the X crystal axis; hence

$$P_u = \tfrac{1}{2} \omega \left[\text{Real Part } (R_x) \right] \qquad (9.324)$$

where R_x is the "longitudinal" power flow component whose numerical value is listed in Appendix I (page **8**).

9.33 An Explicitly Calculable Expression for the Coupled to Incident Wave Amplitude Ratio at the Device Centre Frequency.

The results of the two preceding sections can be used now to derive an explicitly calculable expression for the centre frequency coupled to incident amplitude ratio, C_{ω_0}. Substitution from equations (9.318) and (9.324) into (9.117) yields

$$C_{\omega_0} = j\pi v_s^2 \frac{h}{\lambda_0} \rho' \frac{1}{[\text{Real}(R_x)]} \frac{N\Delta\Gamma}{\cos^2\theta} \tag{9.331}$$

wherein

$$\Gamma = \left[1 - 4(1 - q')\left(\frac{v_t'}{v_s}\right)^2\right] K_x \left[M_x \cos\gamma + M_z \sin\gamma\right]$$

$$+ K_y M_y$$

$$+ \left[1 - \left(\frac{v_t'}{v_s}\right)^2\right] K_z \left[-M_x \sin\gamma + M_z \cos\gamma\right] \tag{9.332}$$

The individual terms of these two relationships fall into three separate categories; those determined by the device geometry, those describing the elastic properties of the overlay material and those depending upon the characteristics of a surface acoustic wave propagating on the free substrate surface. For the particular directional coupler configurations of Figure 5.1, each term of equations (9.331) and (9.332) can be given, through the results derived in sections 9.1, 9.2 and 9.3, a definite numerical value.

Equation (9.331) shows that the centre frequency coupled amplitude ratio depends linearly upon three factors;

1. the number of mass-loading strips, N,

2. the overlay height relative to the centre frequency surface acoustic wavelength, (h/λ_0),

and 3. the mass density, ρ', of the overlay.

All of these features are in accord with those which might be deduced from an intuitive study of the device designs pictured in Figure 5.1.

9.4 The Coupled Signal Frequency Response.

Recall, from the discussion of section 9.1 and, in particular,

from.equations (9.111) and (9.118), that the frequency response of the coupled to incident signal amplitude ratio is described by the coupled mode function

$$F(\omega) = \iint e^{j\underset{\sim}{\beta}\cdot\underset{\sim}{r}} \, dA$$

in which

$$\underset{\sim}{\beta} = \underset{\sim}{\beta}_1 + \underset{\sim}{\beta}_p + \underset{\sim}{\beta}_3$$

and the integration is over the finite area, A, of the scattering region illuminated by both transducers 1 and 3. The coordinate notation chosen for the process of evaluating $F(\omega)$ is established in Figure 9.5. Also shown in the same figure is the centre frequency wave vector diagram for the coupled signal; because this closes, $\underset{\sim}{\beta} = 0$ at band centre, and $F(\omega_0) = A$.

For the selected coordinate notation,

$$F(\omega) = \iint e^{j(\beta_{1x} + \beta_{px} + \beta_{3x})x} \, dz \, dx \qquad (9.401)$$

where β_{1x} denotes the x component of $\underset{\sim}{\beta}_1$, and similar definitions apply to β_{px} and β_{3x}. Equation (9.401) makes use of the fact that neither $\underset{\sim}{\beta}_p$ nor ($\underset{\sim}{\beta}_1 + \underset{\sim}{\beta}_3$) has a z component, even when $\omega \neq \omega_0$. Thus put

$$\beta = \beta_{1x} + \beta_{px} + \beta_{3x} \qquad (9.402)$$

so that the integral of equation (9.401) reduces to

$$F(\omega) = \iint e^{j\beta x} \, dz \, dx \qquad (9.403)$$

If integration is carried out first with respect to z the contribution, $F_R(\omega)$, from mass-loading bars to the right of the origin in Figure 9.5, is
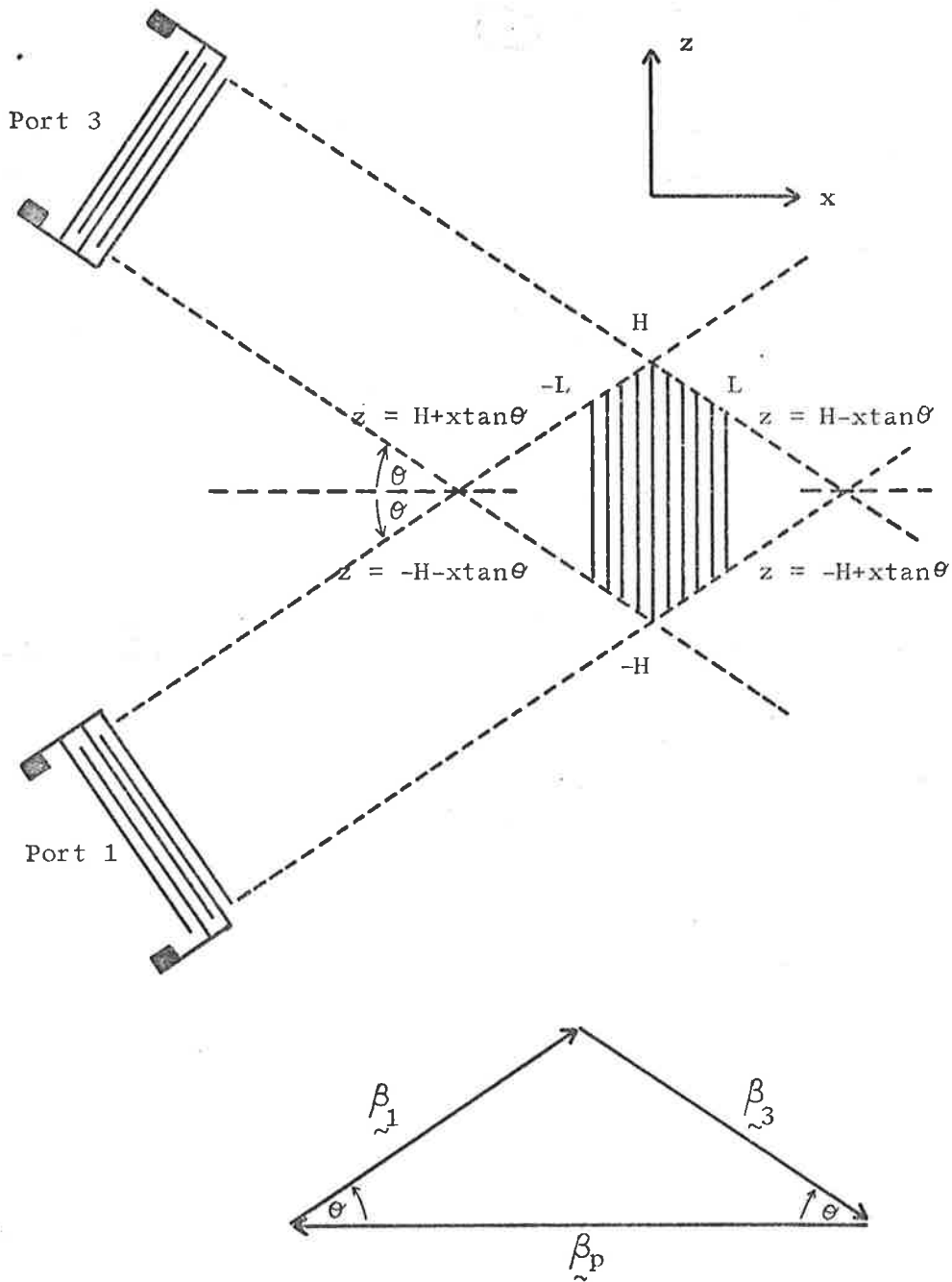
Figure 9.5

Coordinate notation for analysing the coupled signal
frequency response.

$$F_R(\omega) = \int_0^L \int_{(-H+x\tan\theta)}^{(H-x\tan\theta)} e^{j\beta x} \, dz \, dx$$

$$= 2 \int_0^L (H-x\tan\theta) \, e^{j\beta x} \, dx$$

This expression can be integrated by parts to show that

$$F_R(\omega) = 2\left[\frac{H(e^{j\beta L} - 1)}{j\beta} - \frac{L\tan\theta \; e^{j\beta L}}{j\beta} - \frac{\tan\theta \; (e^{j\beta L} - 1)}{\beta^2} \right] \tag{9.404}$$

In an identical manner the contribution, $F_L(\omega)$, from bars to the left of the origin can be calculated from first principles. Alternatively this factor can be deduced from the expression for $F_R(\omega)$ by substituting

$$-L \quad \text{for} \quad L$$

and $\quad -\tan\theta \quad$ for $\tan\theta$

in equation (9.404), and multiplying the result by -1 to account for the changed direction of integration; this procedure provides that

$$F_L(\omega) = 2\left[\frac{H(1-e^{-j\beta L})}{j\beta} + \frac{L\tan\theta \, e^{-j\beta L}}{j\beta} + \frac{\tan\theta(1-e^{-j\beta L})}{\beta^2} \right] \tag{9.405}$$

Adding equations (9.404) and (9.405), and performing simple algebraic manipulations determines that the overall frequency response of the coupled signal is governed by the function

$$F'(\omega) = 2\left(\frac{L}{\lambda_0}\right)^2 \tan\theta \left[c \, \frac{\sin\beta L}{\beta L} + \frac{\sin^2\left(\frac{\beta L}{2}\right)}{\left(\frac{\beta L}{2}\right)^2} \right] \tag{9.406}$$

where $\quad c = 2\left[\frac{H}{L\tan\theta} - 1 \right]$ $\tag{9.407}$

and both sides of $F(\omega)$ have been divided by $\lambda_0{}^2$ to obtain the dimensionless function $F'(\omega)$.

9.41 <u>Calculation of the Coupled Signal Frequency Response</u>.

Although the function $F'(\omega)$ furnishes the desired description of the coupled signal frequency response for the device whose geometry is illustrated in Figure 5.1, it is of use only if a further result, formulating β in terms of the fractional off-centre frequency, can be derived. The difference, $\Delta\omega$, between the device centre frequency, ω_0, and the actual operating frequency, ω, at any instant of time, is

$$\Delta\omega = \omega - \omega_0 \qquad (9.411)$$

By reference to Figure 9.5 this difference frequency can be expressed in the alternative form

$$\Delta\omega = v_s \,(\beta_{1x} - \beta_{1x_0}) \sec\theta \qquad (9.412)$$

in which β_{1x_0} is the x wave vector component of the signal, of frequency ω_0, launched from transducer 1. Provided that operation takes place at frequencies near band centre the coupled signal, of frequency $\omega \neq \omega_0$, can be regarded still as a surface wave directed towards transducer 3; hence the relation

$$\Delta\omega = v_s(\beta_{3x} - \beta_{1x_0}) \sec\theta \qquad (9.413)$$

is equally valid. Summing equations (9.412) and (9.413) produces the expression

$$\Delta\omega = v_s \,(\beta_{1x} + \beta_{3x} - 2\beta_{1x_0}) \sec\theta$$

$$= v_s \,(\beta_{1x} + \beta_{3x} + \beta_p) \sec\theta$$

$$= \frac{v_s}{2} \,\beta \sec\theta \qquad (9.414)$$

where the latter results emerge from equation (5.123), used in conjunction with Figure 5.2, and from equation (9.402). The above relationship can be rearranged into the more convenient form

$$\frac{\beta L}{2} = \frac{\Delta \omega}{\omega_0} \frac{2 \pi L}{\lambda_0} \cos \theta \qquad (9.415)$$

which, when used in conjunction with equation (9.406), allows calculation of the coupled signal frequency response for a microsonic cross-bar coupler of specified geometry.

9.42 The Nature of the Coupled Signal Frequency Response.

On intuitive grounds alone, the configuration of the metal overlay patterns pictured in Figure 5.1 suggests that the coupled signal would exhibit a frequency behaviour of basically $\sin x/x$ dependence, where $x = N \pi (\Delta \omega / \omega_0)$ and N is, as usual, the number of mass-loading elements. This establishes an approximate 3dB fractional bandwidth of $(7/8N)$. But the occurrence of an additional factor, to take account of the varying length of these scattering bars which, as is indicated in Figure 9.1, do not all intercept the full width of the incident acoustic beam, could be predicted as well.

These expectations are realized in the analytical expressions describing the coupled signal frequency response. The dimensions of the scattering regions in both coupler styles are such that c, defined by equation (9.407), is greater than unity; this fact is evidenced by the photographs of Figure 5.1. This means that the function, $F'(\omega)$, of equation (9.406), is dominated by the $(\sin \beta L/\beta L)$ term; L, being the half-length of the interaction grid, is proportional to N, and equation (9.415) shows that β is proportional to $(\Delta \omega/\omega_0)$. The second term of equation (9.406), $\sin^2(\beta L/2)/(\beta L/2)^2$, introduces a small

correction to the basic response and determines a 3dB bandwidth slightly greater than that provided by the $(\sin \beta L / \beta L)$ factor alone. All of these features are demonstrated more clearly in the theoretical coupled signal response curves, calculated by combining the results of equations (9.331), (9.332), (9.406) and (9.415), and plotted in section 10.3.

9.5 The Magnitude and Frequency Response of the Directivity Signal.

The procedure to be followed in a derivation of the relative magnitude and frequency behaviour of the directivity signal is outlined in section 9.12. By analogy with the corresponding expressions for the coupled wave amplitude ratio, i.e. equations (9.331) and (9.332), the quantity D'_{ω_0} introduced in equation (9.121) can be deduced to be

$$D'_{\omega_0} = j\pi v_s^2 \frac{h}{\lambda_0} \rho' \frac{1}{[\text{Real } (R_x)]} \frac{N\Delta \Gamma}{\cos^2 \theta} \qquad (9.501)$$

where now

$$\Gamma = \left[1 - 4(1-q') \left(\frac{v_t'}{v_s} \right)^2 \right] K_x \left[M_x^* \cos \gamma + M_z^* \sin \gamma \right]$$

$$+ K_y M_y^*$$

$$+ \left[1 - \left(\frac{v_t'}{v_s} \right)^2 \right] K_z \left[-M_x^* \sin \gamma + M_z^* \cos \gamma \right] \qquad (9.502)$$

Here the complex conjugates of the M_i arise through the property of forward and reverse propagating surface acoustic waves which is formulated in equation (7.503); it may be recalled, from the discussion of section 9.1 and from Figure 9.1, that the velocity field, $\underset{\sim}{v_4}$, associated with the directivity signal analysis is that of a wave travelling in the opposite direction to the one whose velocity field, $\underset{\sim}{v_3}$, appears in the expressions for the coupled signal amplitude ratio. The values of

the M_i are determined still by equation (9.313), in which the $C_i^{(j)}$

are taken from Appendix I, (page 8).   But as noted in section 9.12,

the wave vector diagram for the directivity signal does not close at

the centre frequency, so that D'_{ω_0} alone does not described the

directivity to incident wave amplitude ratio at ω_0.

The remaining task, therefore, is to calculate the coupled mode

function

$$G(\omega) = \iint e^{j\underset{\sim}{\beta} \cdot \underset{\sim}{r}} \, dA$$

wherein

$$\underset{\sim}{\beta} = \underset{\sim}{\beta_1} + \underset{\sim}{\beta_p} + \underset{\sim}{\beta_4}$$

and integration is over the area of the interaction region illuminated

by both transducers 1 and 4; i.e. the whole scattering grid.   Figure

9.6, which retains the coordinate notation established for the calcula-

tion of the coupled signal frequency response, clearly indicates that

both the positively (+x) and negatively (-x) directed perturbation

wave vectors arising from the fundamental Fourier component of the

mass-loading periodicity (refer equation (9.241)) can contribute to the

directivity signal.   Because these wave vector diagrams do not close

$\underset{\sim}{\beta}$, as defined above, is non-zero, and can be resolved into its x and

z components, $\underset{\sim}{\beta_x}$ and $\underset{\sim}{\beta_z}$.   It can be seen that the only difference

between the resultant $\underset{\sim}{\beta}$'s in diagrams (a) and (b) of Figure 9.6, is that

$\underset{\sim}{\beta_x}$ changes sign.   Initially the calculation of $G(\omega)$ presented below

considers only the contribution from the (+x) term of $\underset{\sim}{\beta_p}$; i.e. from

the situation depicted in Figure 9.6(a).

From the preceding discussion the coupled mode function can be

written as
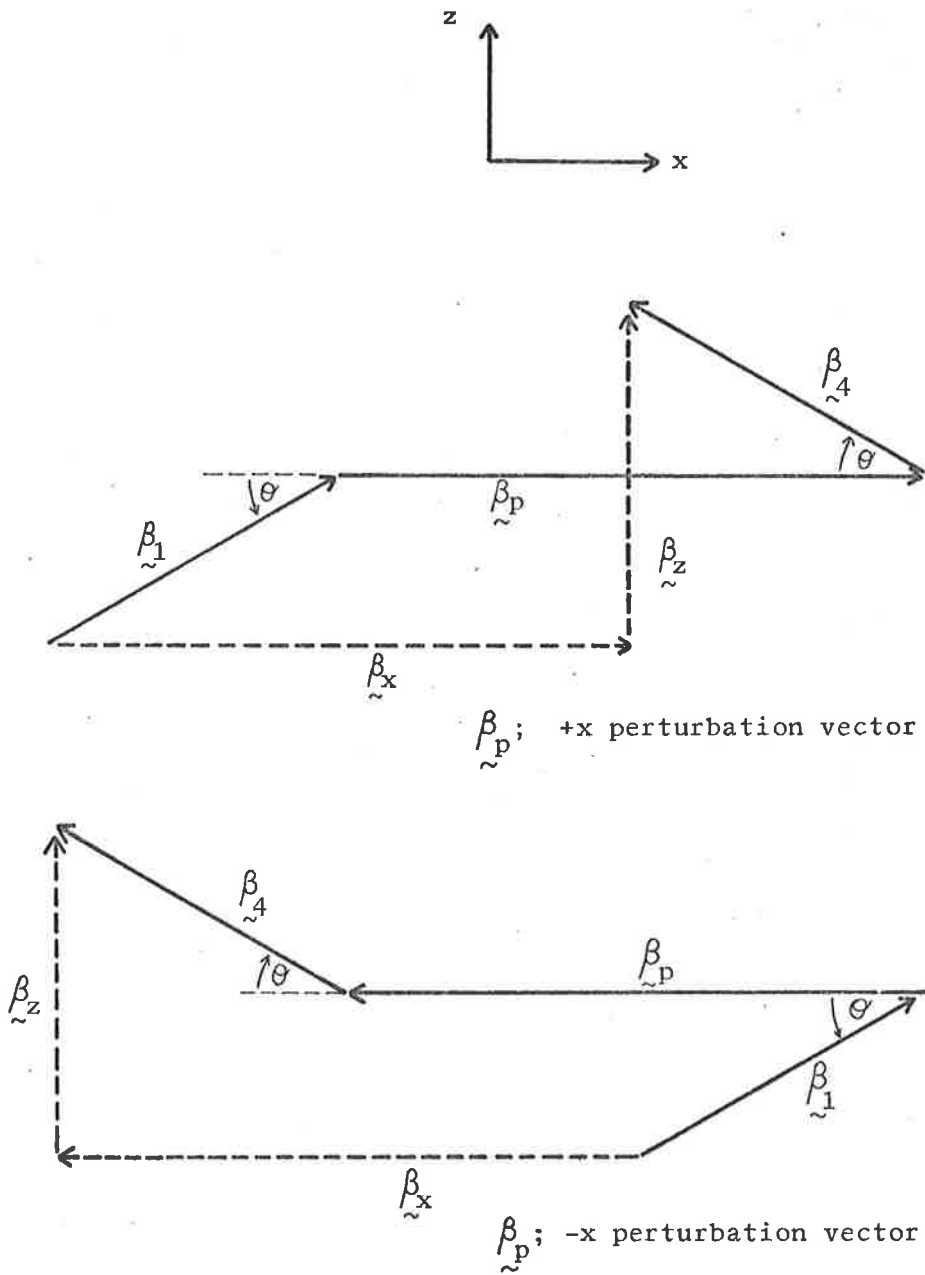
Figure 9.6

Wave vector diagrams for the directivity signal.

$$G(\omega) = \iint e^{j\beta_x x} \, e^{j\beta_z z} \, dx \, dz \qquad (9.503)$$

the components of the resultant $\underset{\sim}{\beta}$ being

$$\beta_x = \beta_{1x} + \beta_{px} + \beta_{4x} \qquad (9.504)$$

$$\text{and} \quad \beta_z = \beta_{1z} + \beta_{pz} + \beta_{4z}$$

Pursuing the approach used in the coupled signal response analysis, the contribution to $G(\omega)$ from mass-loading bars to the right of the origin in Figure 9.5 is

$$G_R(\omega) = \int_0^L \int_{(-H+x\tan\Theta)}^{(H-x\tan\Theta)} e^{j\beta_x x} \, e^{j\beta_z z} \, dz \, dx$$

Performing this integration leads to the rather unwieldy result that

$$G_R(\omega) = -\frac{1}{\beta_z} \left[\frac{e^{j\eta} - e^{j\beta_z H}}{(\beta_x - \beta_z \tan\Theta)} + \frac{e^{-j\beta_z H} - e^{j\nu}}{(\beta_x + \beta_z \tan\Theta)} \right] (9.505)$$

where
$$\eta = \beta_z H + \beta_x L - \beta_z L \tan\Theta$$
$$\qquad (9.506)$$

$$\text{and} \quad \nu = \beta_x L + \beta_z L \tan\Theta - \beta_z H$$

The variable interchanges detailed in section 9.4 allow the deduction, from equation (9.505), of the corresponding expression for $G_L(\omega)$, the contribution to the directivity response from scattering bars to the left of the origin. These two functions, $G_R(\omega)$ and $G_L(\omega)$, can then be summed to obtain the total response. Following considerable algebraic manipulation the emerging result is

$$G'(\omega) = \frac{4}{\beta_z^2} \left(\frac{1}{\lambda_0}\right)^2 \frac{\left[\chi \sin\beta_x L \sin\delta + \tan\Theta (\cos\beta_z H - \cos\beta_x L \cos\delta) \right]}{(\chi^2 - \tan^2\Theta)} \qquad (9.507)$$

in which $\qquad \chi = \beta_x / \beta_z$

$\qquad\qquad\qquad\qquad\qquad\qquad\qquad\qquad\qquad\qquad$ (9.508)

and $\qquad \delta = \beta_z (H-L \tan\theta)$

In accordance with the treatment of the coupled signal frequency response function, $G(\omega)$ has been divided by the square of the centre frequency surface wavelength, λ_0, to yield the dimensionless function, $G'(\omega)$, of equation (9.507). It may be noted, from the above expressions, that $G'(\omega)$ is unaffected by a change in sign of β_x. This means that the (-x) fundamental perturbation wave vector, as illustrated in Figure 9.6(b), makes a contribution to the directivity signal which equals that due to the (+x) perturbation wave vector component; hence the overall directivity signal response is governed by

$$G''(\omega) = 2 G'(\omega) \qquad\qquad (9.509)$$

9.51 Calculation of the Directivity Signal Frequency Response.

As discovered in the investigation of the coupled wave response, relationships such as (9.507) and (9.509) are only useful in characterizations of practical devices when the variables can be formulated in terms of an actual operating frequency, ω, and the device centre frequency, ω_0. This information is available from the wave vector diagrams of Figure 9.6 which show that

$$\beta_x = \frac{4\pi}{\lambda_0} \cos\theta$$

$$\qquad\qquad\qquad\qquad\qquad\qquad\qquad (9.511)$$

and $\qquad \beta_z = \frac{4\pi}{\lambda_0} \frac{\omega}{\omega_0} \sin\theta$

The results of equations (9.501), (9.507) and (9.509) can be combined to obtain the centre frequency directivity to incident signal amplitude ratio;

$$D_{\omega_0} = D'_{\omega_0} G''(\omega_0) \qquad\qquad (9.512)$$

Equation (9.125) indicates the technique which can be used to express the directivity of the crossbar directional coupler in the usual manner; i.e. as a coupled to directivity signal amplitude ratio. The directivity amplitude ratio, as a function of frequency, is

$$\frac{\text{Coupled Amplitude}}{\text{Directivity Amplitude}} = C_{\omega_0} F'(\omega) / D'_{\omega_0} G''(\omega) \qquad (9.513)$$

where the contributing functions are described by equations (9.331), (9.406), (9.501), (9.507) and (9.509). This relationship is the basis from which the theoretical directivity curves of section 10.3 are calculated and plotted.

9.6 The Importance of Contributions from the Higher Harmonic Components of the Surface Perturbation.

Equation (9.241) highlights the fact that the preceding analyses have neglected the harmonic wave vector components, ($\pm 3 \beta_p$, $\pm 5 \beta_p$, etc), of the periodic surface mass-loading perturbation. The validity of this procedure, in relation to both the coupled and directivity responses, must now be established.

9.61 Contributions to the Coupled Signal.

Wave vector diagrams for the higher harmonic components, unlike that shown in Figure 9.5 for the fundamental (+x) perturbation wave vector, fail to close. Their contributions to the coupled signal amplitude must be evaluated, therefore, by the techniques described in section 9.5. The directivity plots of Figures 10.1 and 10.6 indicate that such contributions are typically more than 40dB below that provided by the fundamental perturbation component for which the wave vector diagram closes. Thus, in the coupled signal analysis, the neglect of harmonic components of the surface perturbation is clearly justified.

9.62 Contribution to the Directivity Signal.

From Figure 9.6 it can be seen that the wave vector diagram for the nth harmonic component of the periodic surface mass-loading perturbation is similar to that of the fundamental, except that β_x is increased in magnitude by a factor of n.   Equation (9.507) reveals that the magnitude of the contribution to $G'(\omega)$, i.e. to the directivity signal amplitude ratio, from the nth harmonic component must be inversely proportional to n.   The manner in which the harmonic components sum to provide the complete response is stated in equation (9.241); this relationship provides two more important features.   Firstly, each contribution is reduced by the further factor of n contained within the coefficients of the Fourier series expansion of the perturbation profile. The overall variation of the directivity signal amplitude contribution from the harmonic terms is as $1/n^2$.   Secondly the harmonic contributions alternate in sign, tending to cancel each other.   Hence the consideration of only the fundamental component of the periodic surface perturbation is also valid in an analysis of the directivity signal.

CHAPTER X

A COMPARISON OF THE THEORETICAL AND EXPERIMENTAL

PERFORMANCE OF THE MICROSONIC CROSSBAR DIRECTIONAL COUPLER

10.0 Introduction.

Before the analytical results of the previous chapter can be used

to predict the performance of the crossbar directional coupler, several

further quantities must be calculated. The first section of this

chapter presents sufficient details of the metal overlay patterns,

shown in Figure 5.1, to permit an evaluation of the area correction

factor, $\triangle$, for each coupler style. Numerical data for the elastic

constants of the mass-loading overlay material, and a description of a

technique for precisely measuring the height of the scattering bars

are contained in the same section. The experimental methods which

enable the behaviour of both coupler styles to be recorded, and the

procedure by which these results are processed, are discussed. Theoret-

ical and practical response curves are plotted side-by-side and are

compared in the following section. The two sets of results are examined

firstly on an individual basis, for each device fabricated, and then

features common to this type of surface acoustic wave directional coupler

are reviewed. Possible sources of the relatively small discrepancies

between theoretical and experimental behaviour are considered in the

concluding remarks of this chapter.

10.1 Additional Data Required for Theoretical Performance Assessment.

Predictions of crossbar coupler response, based upon the analytical

expressions of sections 9.3 to 9.5, require numerical values for the

dimensions of the interaction region, (from which the area correction

factor can be calculated), the elastic properties of the overlay and

the height of the mass-loading bars.

10.11 Dimensions of the Scattering Surface Perturbation.

The functions $F'(\omega)$ and $G'(\omega)$, which describe the frequency dependence of the coupled and directivity signal amplitudes, respectively, are, as shown by equations (9.406) and (9.507), dimensionless. For this reason the parameters H, L and λ_0 can, in calculations of these functions, take their numerical values as measured directly from the original rubylith device pattern. (But note that in evaluating the magnitudes of the coupled and directivity waves, using equations (9.331) and (9.501), λ_0 ($= v_s / f_0$) must be the actual centre frequency surface acoustic wavelength).

Coupler Style A.

The rubylith mask for this coupler style, a photograph of which appears in Figure 5.1(a), was cut to a scale which allowed the width of each electrode in the IDTs to be 2mm. This determines that

$$\lambda_0 = 8mm$$

while measurement records the half-width of the interaction grid as

$$H = 45.84mm.$$

A scattering region comprising N mass-loading elements has a half-length

$$L = (2N - 1) \ d/2$$

where d is the width of each element. Through equation (5.124), the above expression can be presented in the calculable form

$$L = (2N - 1) \lambda_0 / 8 \cos\theta \tag{10.111}$$

where, for coupler style A, N = 10 and, as usual, $\theta = 34°$. Figure 9.1 shows that the area correction factor, defined by equation (9.115), is

$$\Delta = \left[1 - \frac{L \tan\theta}{2H} \right] \tag{10.112}$$

which, on substitution of the above numerical values, returns

$$\triangle \ = \ 0.83 \tag{10.113}$$

for couplers of style A (with N = 10).

Coupler Style B

The rubylith pattern for this coupler style was scaled so that each IDT electrode could be cut to a width of one sixteenth of an inch. Hence

$$\lambda_0 \ = \ 4.0$$

and, by measurement,

$$H \ = \ 30.46$$

both dimensions being in sixteenths of an inch. Once again L can be calculated from equation (10.111), but now there are 20 mass-loading bars in the scattering region. These values provide an area correction factor

$$\triangle = \ 0.74 \tag{10.114}$$

for couplers of style B (with N = 20).

10.12 The Elastic Properties of the Overlay.

The gold film from which the mass-loading bars are etched is assumed to have the elastic properties of the bulk material (97); i.e.,

$$\text{mass density,} \quad \rho' \ = \ 19.3$$

$$\text{Poisson's ratio,} \quad \sigma' \ = \ 0.421$$

and shear wave velocity,

$$v_t' \ = \ 1.239 \ \text{Km/sec.}$$

Section 10.74 discusses further the accuracy of this step, in view of the somewhat uncertain elastic properties of vacuum-deposited films, and of the dependence of these properties upon film thickness.

10.13 Film Thickness Measurements.

During the process of etching the desired crossbar coupler patterns
from the deposited metal films, sharp steps are created in the overlay
profile. Thus the most convenient method, from the viewpoints of
simplicity and avoidance of damage to the completed device, for measuring
the film thickness is optical interference. This task is made even
simpler by the availability of a Wild M-20 microscope fitted with an
interference attachment (125). The two sets of fringes, i.e. those
appearing on the gold and the quartz surface, are observed initially
under white light, to establish the order of the fringes. By inserting
a 0.540 micron narrow-band optical filter, the relative fringe shift
can be measured to within one tenth of a fringe, and hence the film
thickness can be determined to within ·027 micron. In all practical
crossbar couplers fabricated during this study, the IDTs are etched
from gold overlays whose heights, as recorded by the above procedure,
lie within the range 0.1 to 0.15 microns. The measured heights of
the much thicker surface mass-loading films are quoted in section 10.3,
when the theoretical and practical performance of each individual
coupler is discussed.

10.2 Procedure for Experimental Studies of Coupler Response.

Figures 4.5 and 4.6 illustrate the essential details of the equip-
ment and experimental arrangement employed in studies of the crossbar
coupler. Because of the slightly different construction of coupler
styles A and B, as indicated in Figures 5.1(a) and (b), the precise
experimental procedure varies a little in each case, and is discussed
separately below.

Coupler Style A.

The jig in which couplers of this style are mounted is pictured in Figure 5.4(a). A single input and a single output transformer, designed by the approach of section 5.34 to tune and impedance match an IDT, are provided. In the style A pattern the transducers on the main transmission paths are separated by approximately 1.2cms; this propagation distance allows surface wave pulses of up to 3.5μsecs duration to be transmitted and received without interference from the signal which is coupled electromagnetically from the input to the output transducer. At a specified frequency the amplitude, C, of the coupled signal (detected at transducer 3), and the amplitude, T, of the transmitted signal (detected at transducer 2) are recorded by connecting the same receiving circuit, in turn, to each transducer. On the assumption that the coupling mechanism is lossless, the coupled wave amplitude is expressed in terms of the incident wave amplitude to determine the

$$\text{Coupling Factor (dB)} = 10\log_{10}\left[1 + (T/C)^2\right] \qquad (10.201)$$

A similar measurement of the directivity signal amplitude, D, is made and the quantity

$$\text{Directivity (dB)} = 20\log_{10} (C/D) \qquad (10.202)$$

calculated. The whole procedure is repeated at selected intervals over the frequency range of interest.

Coupler Style B.

Crystals upon which metal patterns of coupler style B are fabricated are placed in the more elabourate test unit pictured in Figure 5.4(b). An increased transducer separation of approximately 4cms.

permits the propagation of pulse lengths up to 12.5μsecs without encountering interference; measurements on style B couplers therefore can represent more closely the CW behaviour. Again only single input and output transducer tuning circuits are provided. Following the experimental method outlined above the amplitudes C, T and M of the coupled, transmitted and monitored surface wave signals (the latter being measured at transducer 5 in Figure 5.1(b)) are recorded, at the same frequency, by connecting the same receiver circuit, in turn, to each IDT. Note that the much shorter path length (approx. 1cm.) between the launching and monitoring IDTs forces the measurement of M to be made with a reduced pulse length of about 3μsecs. The quantity

$$P_L \text{ (dB)} = 10\log_{10}\left[M^2/(T^2 + C^2)\right] \tag{10.203}$$

which is a measure of the acoustic energy lost - i.e. not received at either transducer 2 or 3 — through the coupling mechanism, is cal-culated. Providing that P_L is sufficiently small the lossless coupling assumption remains valid and the coupling factor can be computed from equation (10.201). The amplitude of the back-scattered wave is noted, and the directivity evaluated using equation (10.202). As for couplers of style A, this procedure is repeated at other frequencies.

10.3 Experimental and Theoretical Results for Individual Devices.

This section presents and compares the theoretical and practical response curves for individual crossbar couplers; the same results are discussed from an integrated viewpoint in section 10.6. At this junc-ture it is appropriate to summarise the analytical expressions of Chapter IX from which the theoretical curves of this and the following sections are calculated.

Coupled to Incident Signal Amplitude Ratio, (C/I).

Magnitude at centre frequency

- equations (9.331) and (9.332).

Frequency dependence

-equation (9.406) in conjunction with equations (9.407)

and (9.415).

Coupling factor

- reciprocal of above amplitude ratio expressed in dB.

i.e. Coupling Factor (dB) = $20 \log_{10}$ (I/C)   (10.301)

Coupled to Directivity Signal Amplitude Ratio, (C/D).

Magnitude and frequency dependence

- equation (9.513), constituent functions of which can be

obtained from equations (9.501), (9.502), (9.507), (9.508),

(9.509) and (9.511).

Directivity

- above amplitude ratio expressed in dB.

i.e. Directivity (dB) = $20 \log_{10}$ (C/D).   (10.302)

10.31 <u>Coupler Model A.1</u>   (Style A, Model 1)

This, the first surface acoustic wave crossbar directional coupler

to be tested in the study (126), verifies the assertion of section 2.32,

that coupling between an input and an output wave can be achieved by

the application of periodic mass-loading to the propagation surface.

The ten mass-loading bars in this device are etched from a gold film

of height h = 2.09microns and provide, as shown in Figure 10.1, an

experimental coupling factor of 12.1 dB over a 3 dB fractional band-

width of 0.093, centred on 10 MHz. This practical centre frequency
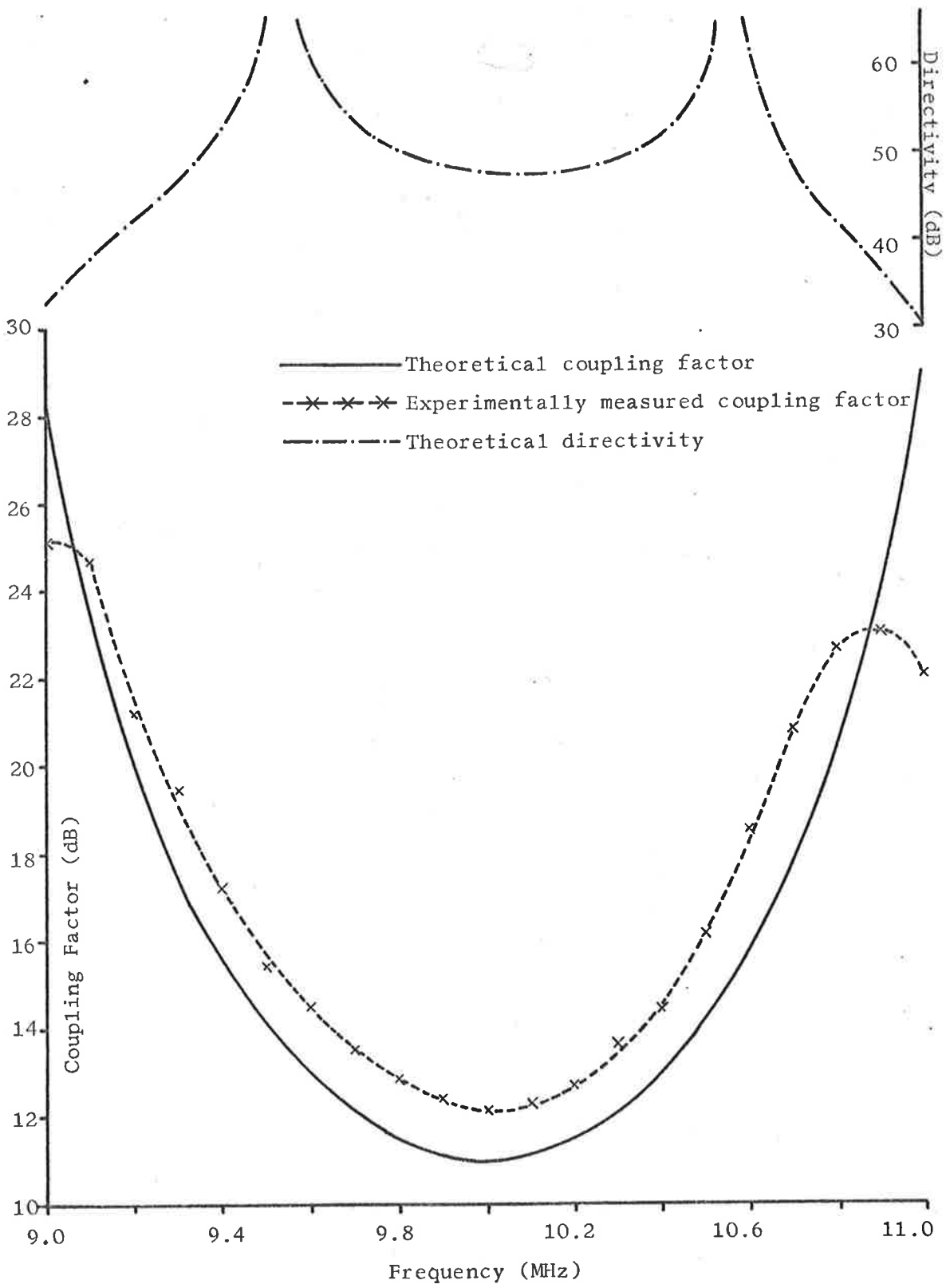
Figure 10.1

Practical and theoretical response of coupler model A.1

is 3% lower than the design value of 10.3 MHz, due to the velocity

slowing (108), (110), (122) of the surface wave as it passes through

the region of surface mass-loading.   (The "design" centre frequency

is that determined by the acoustic wave velocity on the free substrate

surface and the periodicity of the mass-loading elements; it neglects

the inevitable reduction in phase velocity as the wave traverses the

perturbed area of the substrate surface.)   Also drawn in Figure 10.1

is the theoretical coupled signal frequency response, which predicts

a centre frequency coupling factor of 11.0 dB, or 1.1 dB greater than

obtained in practice.   An alternative value for the theoretical centre

frequency coupling factor can be determined by using the results of

computer program "Pianm" rather than "Anisom" to calculate the free

surface particle displacement components — i.e. the K_i and M_i of

equation (9.332).   As stated in section 3.26, the surface wave particle

displacements computed by a procedure which incorporates the piezo-

electric properties of the medium are, in materials possessing weak

electroacoustic coupling, almost identical to those determined by

neglecting piezoelectricity.   The coupling factor should be essentially

the same, therefore, whether the data of Appendix I or Appendix II is

used in the calculation of the theoretical coupling factor.   Indeed

drawing upon the results of "Pianm" leads to an analytical centre

frequency coupling factor of 10.9 dB, only 0.1 dB stronger than deduced

earlier.   Because this difference is so small, all subsequent calcula-

tions utilize the simpler propagation data supplied by "Anisom" and

listed in Appendix I.   The two curves of Figure 10.1 indicate a close

similarity between the practical and theoretical frequency dependence

for the main lobe of the coupled signal response.

.No "back-scattered" directivity signal can be detected over the entire frequency range explored. The receiver sensitivity and the noise level in the experimental system allows signals of amplitude 4 millivolts p.-p. to be observed on the CRO. Hence the measured coupled pulse amplitude of approximately 160 millivolts p.-p. at 10 MHz means that the centre frequency directivity must, in practice, be in excess of 32 dB. This is supported by the analytically calculated directivity response plotted in Figure 10.1; the curve shows that a crossbar coupler of style A (with 10 elements in the mass-loading grid), has a predicted directivity in excess of 47 dB over the device bandwidth.

Transmitted and coupled surface wave signals for two input pulses of different lengths are pictured in Figure 10.2. Section 10.4 discusses the origin and the significance of the two distinct pulse envelope shapes observed for the propagated surface waves.

10.32 Coupler Model B.1   (Style B, Model 1)

Figure 10.3 discloses that this device, whose twenty mass-loading strips are formed from an overlay of height h = 0.749 microns, affords an experimental centre-frequency coupling factor of 15.3 dB. The practical 3 dB fractional bandwidth of 0.050 is slightly more than half that of coupler model A.1, which has only half the number of mass-loading elements. This bandwidth is centred on 10.48 MHz, a frequency 0.7% lower than the design value of 10.55 MHz. The theoretical coupled signal response for this device is also plotted in Figure 10.3, and indicates a centre frequency coupling factor of 14.4 dB, or 0.9 dB larger than measured by experiment. General harmony exists between the theoretical and practical curves describing the frequency variation of the coupled signal amplitude; the only region over which
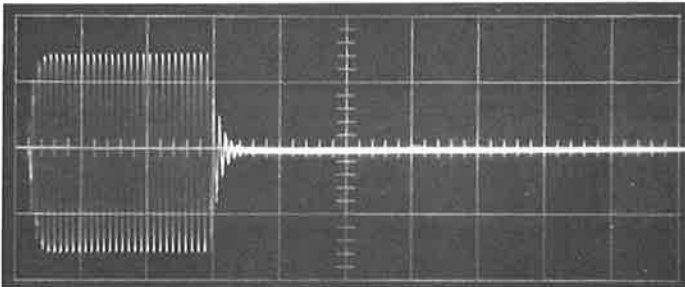
Vertical scale
20 volts/cm.
Horizontal scale.
1 μ sec/cm.

(a) Input signal applied to transducer 1.
($\tau \doteq 3\mu$ secs)

Vertical scale
.05 volts/cm.
Horizontal scale
1 μ sec/cm.
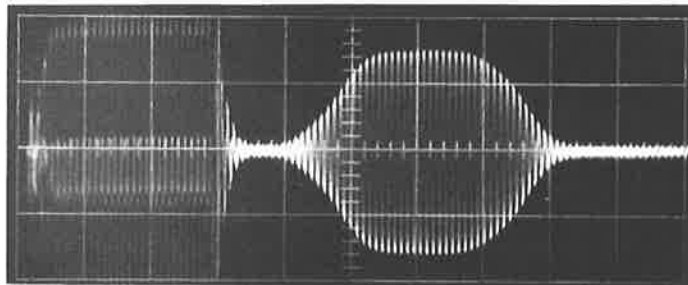
(b) Coupled pulse received at transducer 3
for input of (a).
(30dB receiver gain).

Vertical scale
0.2 volts/cm.
Horizontal scale
1 μ sec/cm.

(c) Transmitted pulse received at trans-
ducer 2 for input of (a).
(30dB receiver gain)

Figure 10.2
Surface acoustic wave pulse shapes in crossbar coupler model A.1.
All signals at f = 10.19 MHz.
[Left hand pulse in photographs (b), (c), (e) and (f) is an electro-
magnetically coupled signal .]

Vertical scale
20 volts/cm.
Horizontal scale
0.5 μ sec/cm.

(d) Input signal applied to transducer 1.
($\tau \doteqdot 1\mu$ sec).
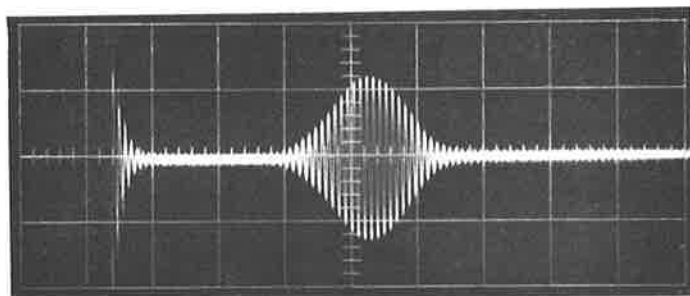
Vertical scale
.05 volts/cm.
Horizontal scale
1 μ sec/cm.

(e) Coupled pulse received at transducer 3
for input of (d).
(30dB receiver gain).

Vertical scale
0.2 volts/cm.
Horizontal scale
1 μ sec/cm.
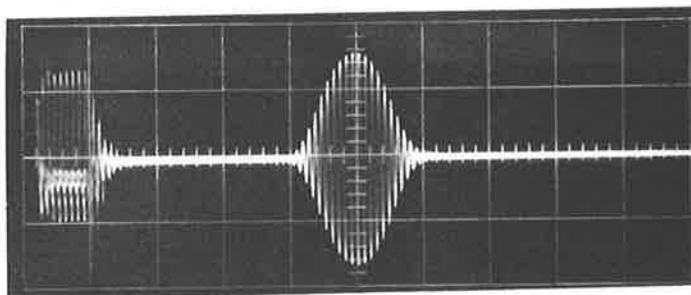
(f) Transmitted pulse received at trans-
ducer 2 for input of (d).
(30dB receiver gain).

Figure 10.2 (cont.)
Surface acoustic wave pulse shapes in crossbar coupler model A.1.
All signals at f = 10.19 MHz.
[Left hand pulse in photographs (b), (c), (e) and (f) is an electro-
magnetically coupled signal.]

Figure 10.3
Practical and theoretical coupled
signal response of coupler model B.1

———————Theoretical coupling factor
x—x—x—Experimentally measured coup-
ling factor.
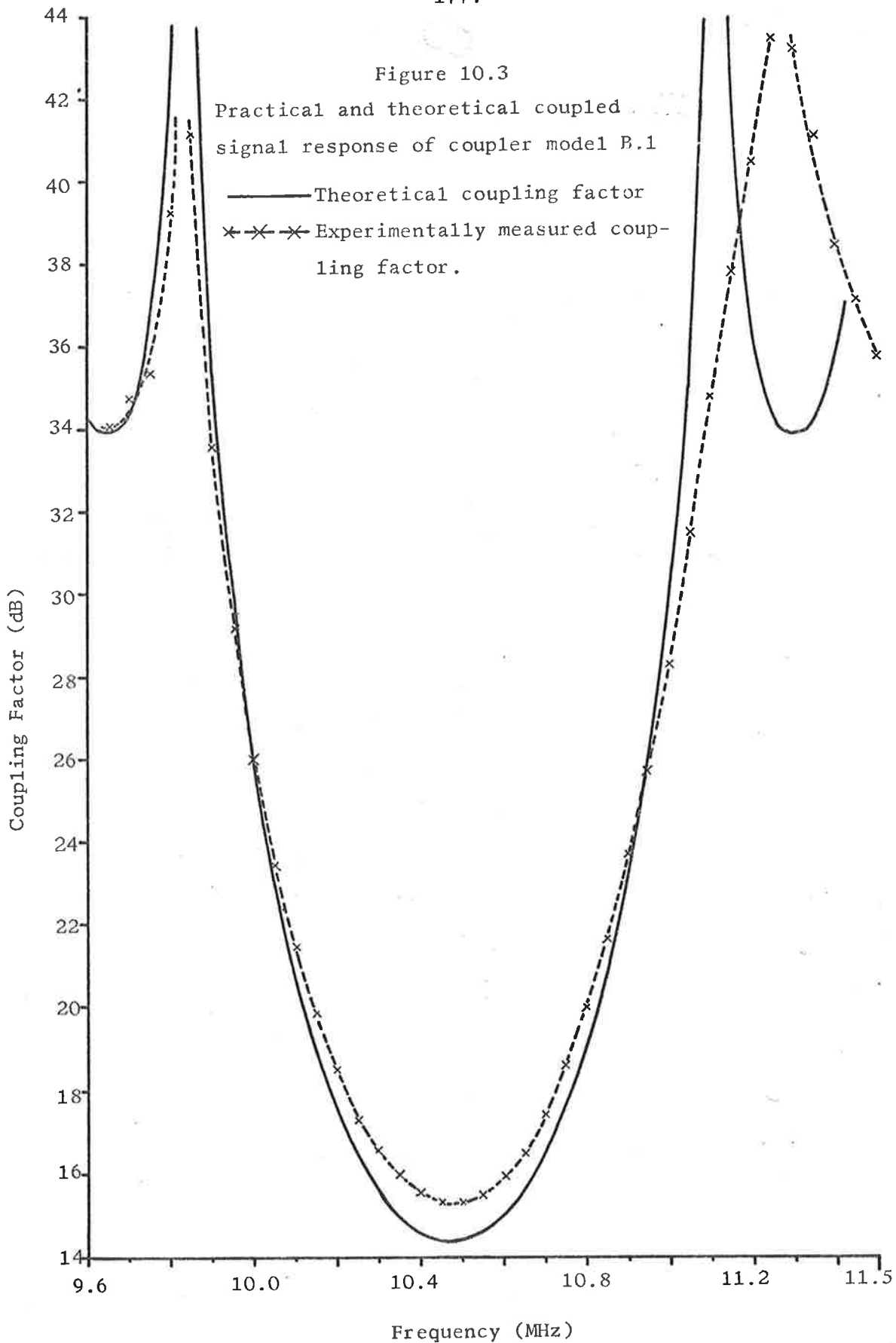
the two sets of results differ substantially is the higher frequency side-lobe.

The experimentally determined coupling loss, P_L, defined by equation (10.203), is presented as a function of frequency in Figure 10.4. P_L is less than 1 dB at band centre, and less than 1.2 dB over the 3 dB bandwidth of the coupled signal response. These values, in themselves, are sufficiently small to justify the lossless coupling assumption, and to permit the processing of experimental results through equation (10.201). But the practical measurements described in section 10.33, and the discussion of section 10.65, lead to the conclusion that only a small fraction of these losses are directly attributable to the periodic mass-loading coupling mechanism.

Pictured in Figure 10.5 are the monitored, transmitted and coupled surface wave signals for two input pulses of different durations. A comparison of these photographs with those of Figure 10.2, for coupler style A, indicates, by the reduced amplitudes of the electromagnetically coupled signals, the improved shielding afforded by the jig illustrated in Figure 5.4(b). These pulse shapes are typical of the waveforms observed in experiments with the five directional couplers of this style; their general form is examined further in section 10.4.

Of considerable interest is the oscillogram of Figure 10.5(h), which shows the signal received at the directivity transducer (IDT 4), for near mid-band operation. Bearing in mind the geometrical and spatial symmetry of the coupler, a comparison of photographs (d) and (h) reveals that the directivity pulse should appear in the $10-20\,\mu$sec time slot of (h); in practice only background noise is observed at the greatest receiver sensitivity. The small pulses to the right of the
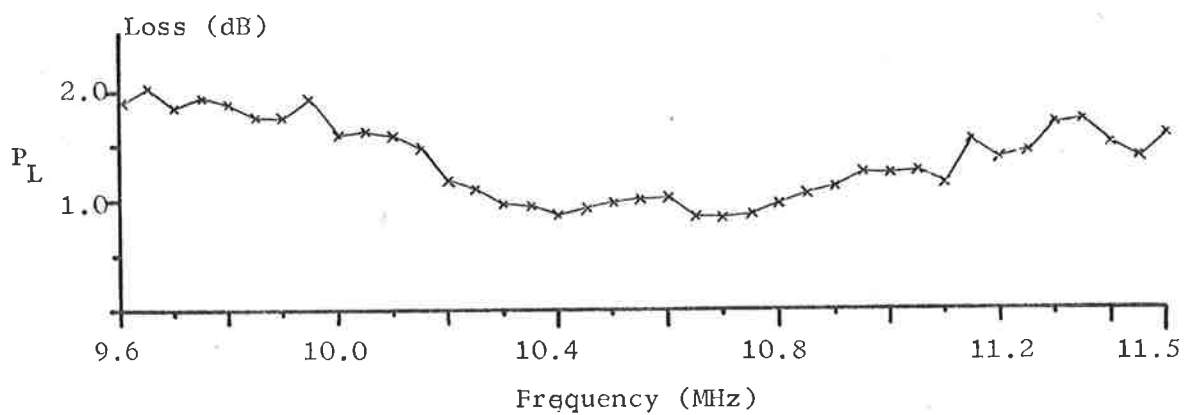
Figure 10.4

Experimentally measured coupling loss for coupler model B.1.
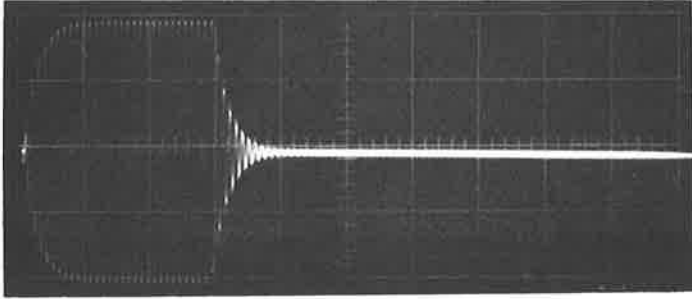
Vertical scale
20 volts/cm.
Horizontal scale
1μ sec/cm.

(a) Input signal applied to transducer 1.

($\tau \doteqdot 3\mu$secs).

Vertical scale
2 volts/cm.
Horizontal scale
1μsec/cm.
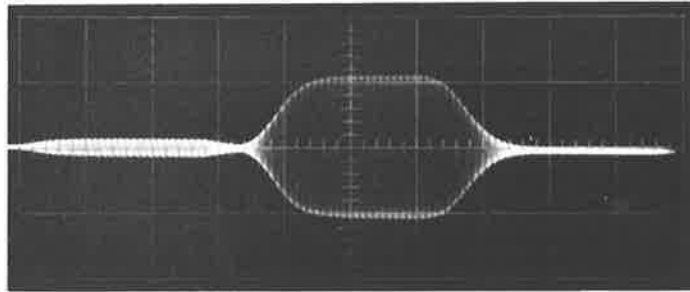
(b) Received pulse at monitor transducer 5
for input of (a).
(40dB receiver gain).

Figure 10.5
Surface acoustic wave pulse shapes in crossbar coupler model B.1.
All signals at f = 10.55 MHz.
[Left hand pulse in photographs (b), (d) – (h), (j) and (k) is an
electromagnetically coupled signal.]

Vertical scale
20 volts/cm.
Horizontal scale
5μ sec/cm.
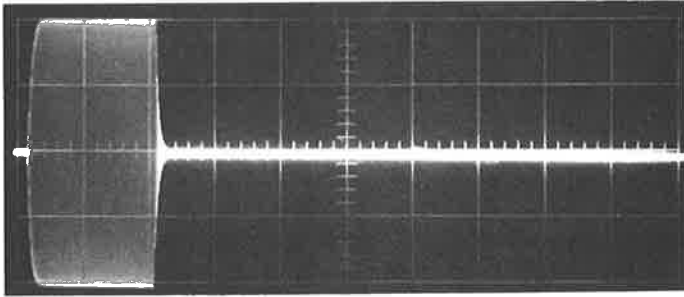
(c)   Input signal applied to transducer 1.

($\tau \doteqdot 10\mu$ secs).

Vertical scale
0.2 volts/cm.
Horizontal scale
5μ sec/cm.
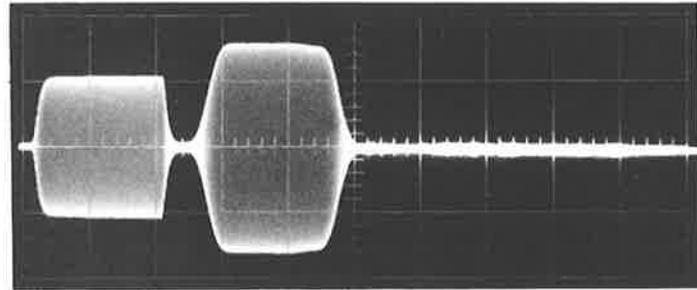
(d) Coupled pulse received at transducer 3

for input of (c).

(40dB receiver gain).

Vertical scale
0.2 volts/cm.
Horizontal scale
2μ sec/cm.

(e) Coupled pulse received at transducer 3

for input of (c).

(40dB receiver gain - time origin shifted
to left).

Figure 10.5 (cont.)

Surface acoustic wave pulse shapes in crossbar coupler model B.1.

All signals at f = 10.55 MHz.

[Left hand pulse in photographs (b), (d) - (h), (j) and (k) is an

electromagnetically coupled signal]

182.

Vertical scale
1 volt/cm.
Horizontal scale
5 μsec/cm.
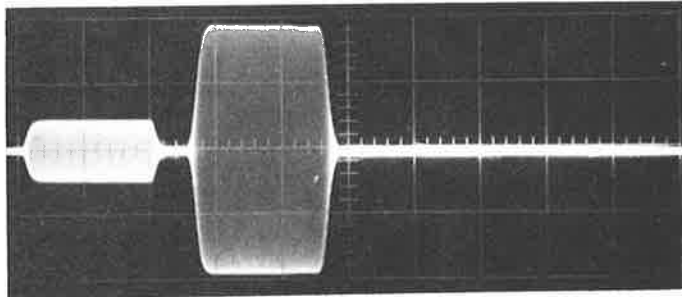
(f) Transmitted pulse received at transducer
2 for input of (d).
(40dB receiver gain).

Vertical scale
1 volt/cm.
Horizontal scale
2 μsec/cm.
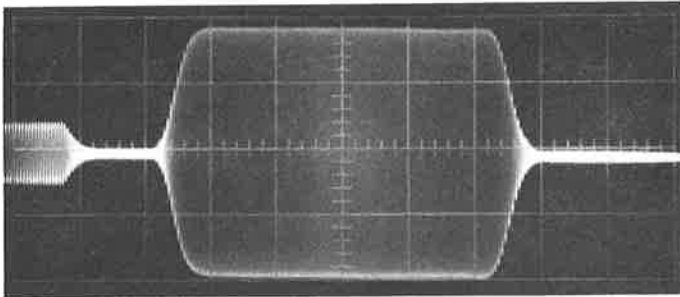
(g) Transmitted pulse received at trans-
ducer 2 for input of (d).
(40dB receiver gain - time origin shifted
to left.

Vertical scale
.01 volt/cm.
Horizontal scale
5 μsec/cm.
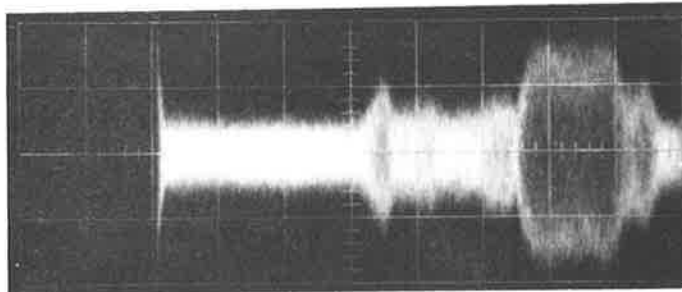
(h) Directivity signal received at transducer
4 for input of (d). Directivity pulse
should appear in 10-20 μsec time slot.
(40dB receiver gain).

Figure 10.5 (cont.)
Surface acoustic wave pulse shapes in crossbar coupler model B.1.
All signals at f = 10.55 MHz.
[Left hand pulse in photographs (b), (d) - (h), (j) and (k) is an
electromagnetically coupled signal.]
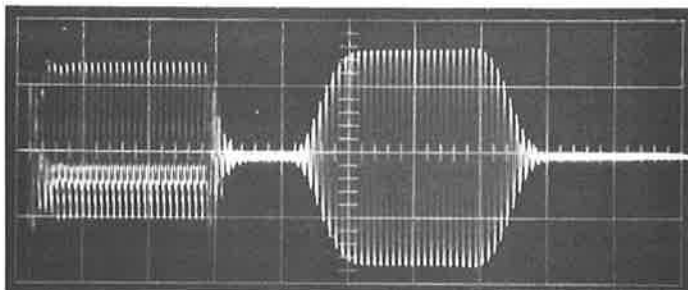
Vertical scale
20 volts/cm.
Horizontal scale
2μ sec/cm.
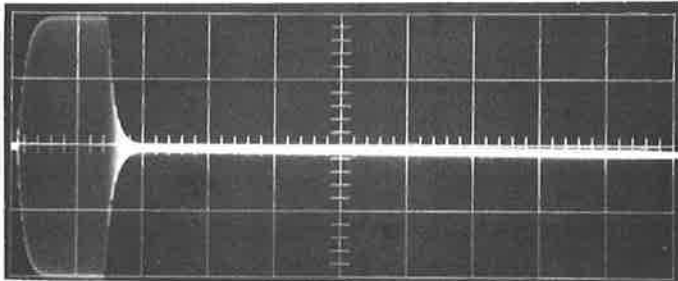
(i) Input signal applied to transducer 1.
($\tau \doteq 3\mu$ secs).

Vertical scale
0.2 volts/cm.
Horizontal scale
2μ sec/cm.
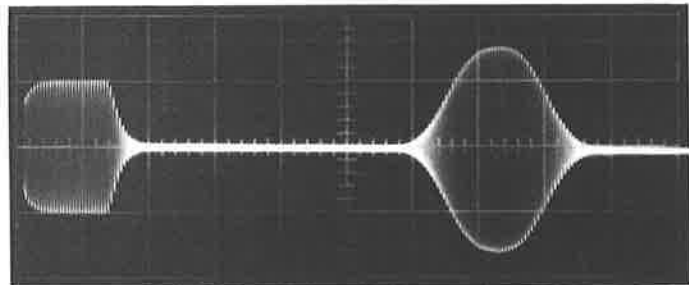
(j) Coupled pulse received at transducer 3
for input of (i).
(40dB receiver gain).

Vertical scale
1 volt/cm.
Horizontal scale
2μ sec/cm.
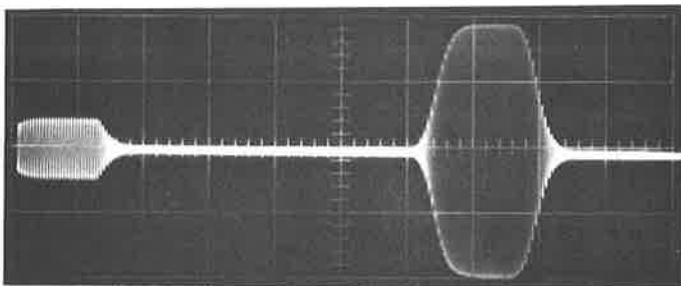
(k) Transmitted pulse received at trans-
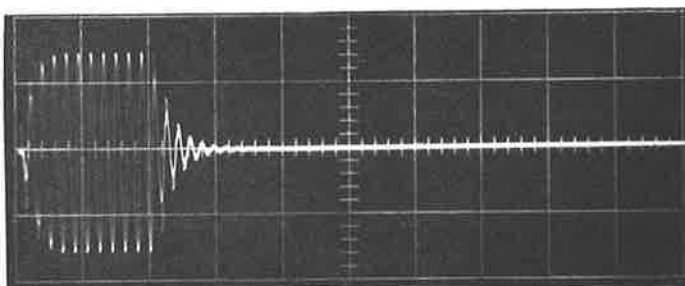ducer 2 for input of (i).
(40dB receiver gain).

Figure 10.5 (cont.)
Surface acoustic wave pulse shapes in crossbar coupler model B.1.
All signals at f = 10.55 MHz.
[Left hand pulse in photographs (b), (d) - (h), (j), and (k) is an
electromagnetically coupled signal.]

directivity signal time slot (i.e. delayed further in time) arise from the reflection of the coupled signal at the crystal edges behind trans-ducer 3. Figure 5.3(b) recalls that acoustically absorbing "black wax" is placed on the substrate surface behind the IDTs to damp these reflections; although this procedure reduces the unwanted signals by about 30 dB, they are not removed entirely. The failure to observe a directivity wave at any frequency within the range 9.6 to 11.5 MHz is a feature common to all the crossbar couplers tested experimentally and it allows a lower bound to be placed on the directivity of each device. For model B.1, the coupler presently under discussion, the directivity must be greater than 41 dB at band centre. This value is supported by the theoretical directivity response for style B couplers, with twenty mass-loading bars in the scattering region; this curve is plotted in Figure 10.6 and predicts a directivity in excess of 55 dB over the 3 dB coupling bandwidth.

10.33 Coupler Model B.2   (Style B, Model 2)

A gold film of thickness h = 0.506 microns provides the surface mass-loading in this model. As in all couplers of style B, twenty scattering bars are etched from this overlay. The experimental response curve, Figure 10.7, shows that a coupling factor of 18.55 dB is achieved at a centre frequency of 10.50 MHz, the 3 dB fractional bandwidth being 0.049. Drawn in the same figure is the corresponding analytically-calculated response which determines a centre frequency coupling factor of 17.7 dB, 0.85 dB larger than recorded by experiment. As for coupler model B.1, the theoretical and practical frequency dependences of the coupled signal amplitude are very similar, the greatest discrepancies occurring in the high frequency side lobe.
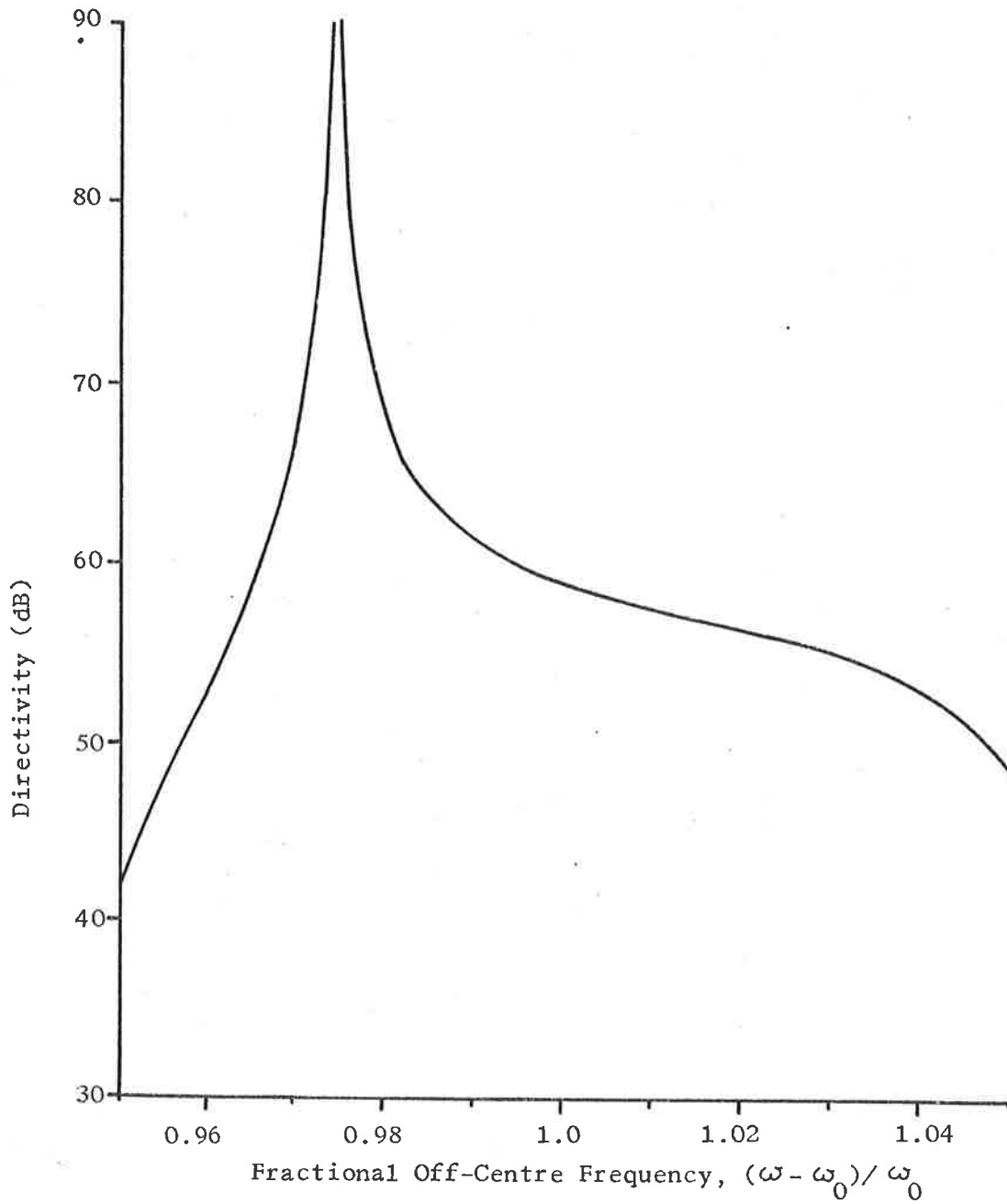
Figure 10.6

Theoretical directivity for crossbar couplers of style B
(with 20 mass-loading elements).

Figure 10.7

Practical and theoretical coupled

signal response of coupler model B.2.

———————— Theoretical coupling
factor.

✕-✕-✕ Experimentally measured
coupling factor.
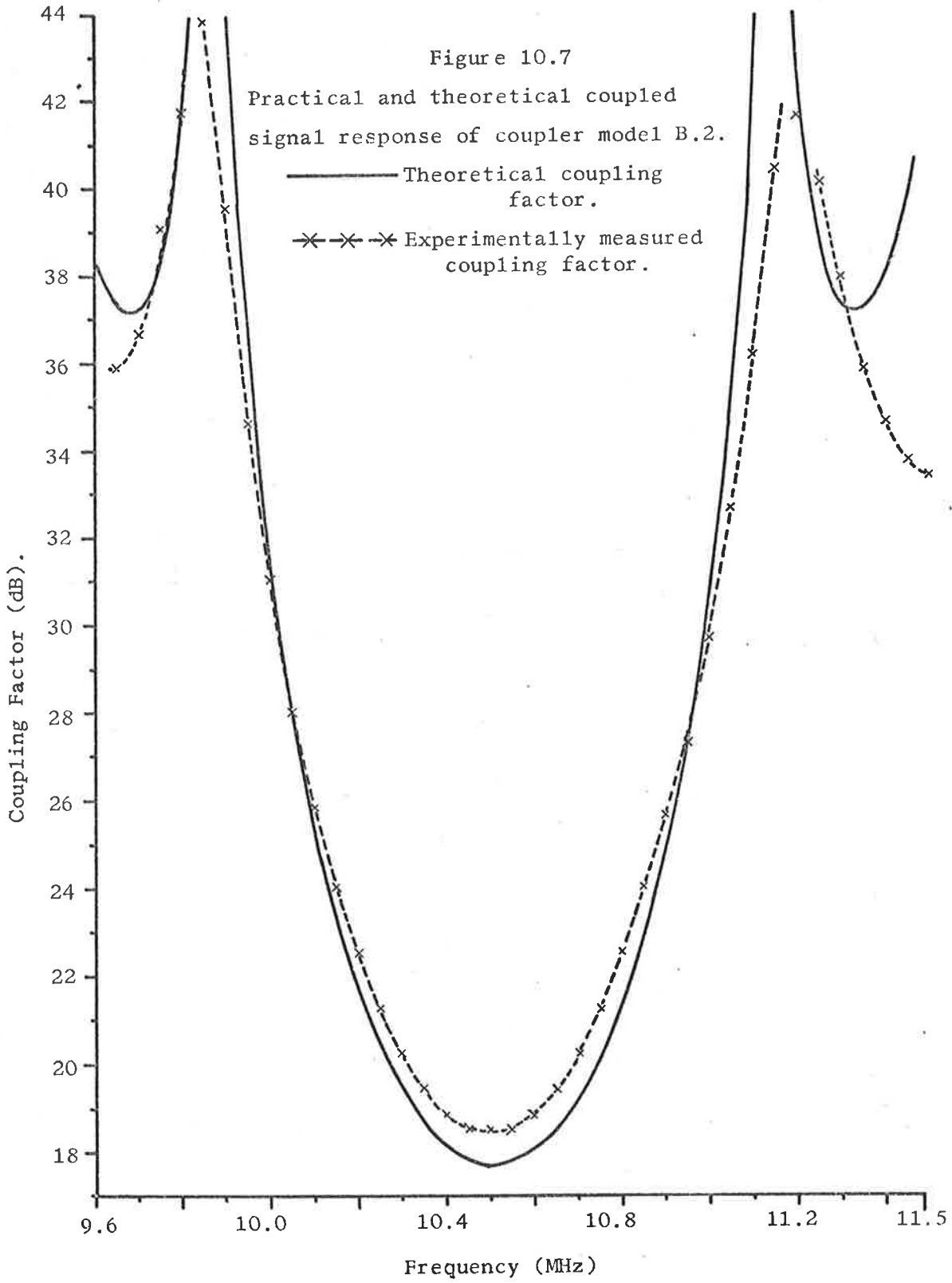
•Figure 10.8 depicts the experimentally measured coupling loss as a function of frequency; P_L is less than 1.4 dB over the 3 dB coupling bandwidth, and is only 0.8 dB at the centre frequency. After all practical studies of this directional coupler have been completed, the mass-loading surface perturbation is removed by etching, without damaging the IDTs. This allows a second series of measurements to obtain the propagation loss, P_α , calculable from equation (10.203) as

$$P_\alpha \ \text{(dB)} \ = 20 \ \log_{10} \ \text{(M/T)}$$

which is the acoustic loss as the surface wave travels from transducer 5 to transducer 2. The results of this investigation are also plotted in Figure 10.8; the two experimental curves in this figure disclose that the quantity $(P_L - P_\alpha)$, which is the true coupling loss, (i.e. that due directly to the coupling mechanism), is only 0.15 dB at the centre frequency. This provides verification of the lossless scattering postulation put forward in section 2.2. In keeping with the one-dimensional scattering situation described by Figures 2.1 and 2.2, $(P_L - P_\alpha)$ is larger for frequencies above band centre. A more detailed examination of the practically measured propagation loss is undertaken in section 10.65.

Although no back-scattered surface wave signal can be detected, a lower practical limit of 38 dB can be placed on the centre frequency directivity of this model.

10.34 Coupler Model B.3   (Style B, Model 3)

The experimental response curve of Figure 10.9 reveals that this device provides a coupling factor of 18.69 dB from mass-loading bars of height h = 0.492 microns, and achieves a 3 dB fractional bandwidth of 0.049 centred on 10.50 MHz. Drawn in the same figure is the corres-
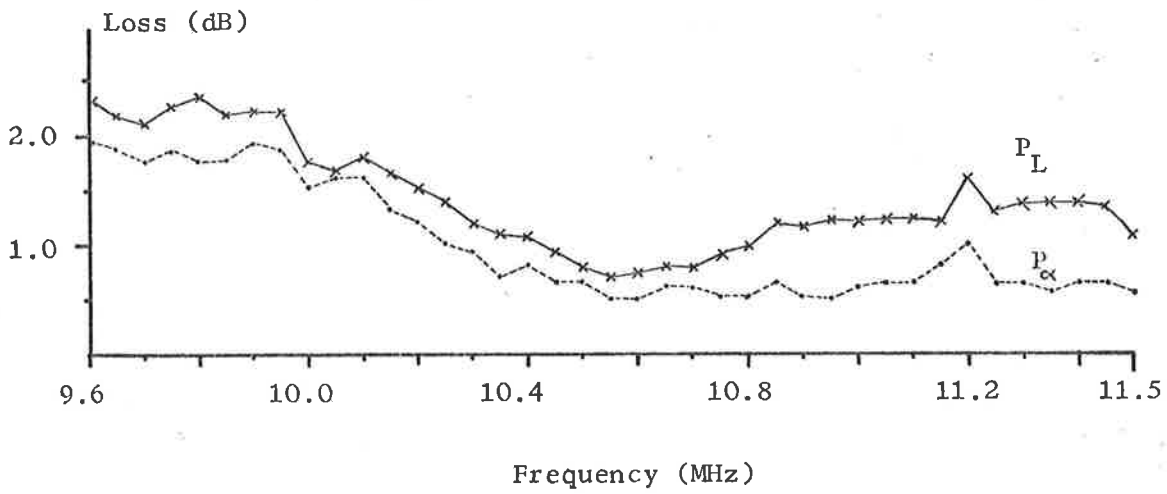
Figure 10.8

Experimentally measured coupling and propagation loss for coupler

model B.2.

×—×—× Experimentally measured coupling loss.

·—·—·. Experimentally measured propagation loss in
absence of scattering grid.

Figure 10.9

Practical and theoretical coupled

signal response of coupler model B.3

————— Theoretical coupling factor.

—x—x—x— Experimentally measured coupling factor.
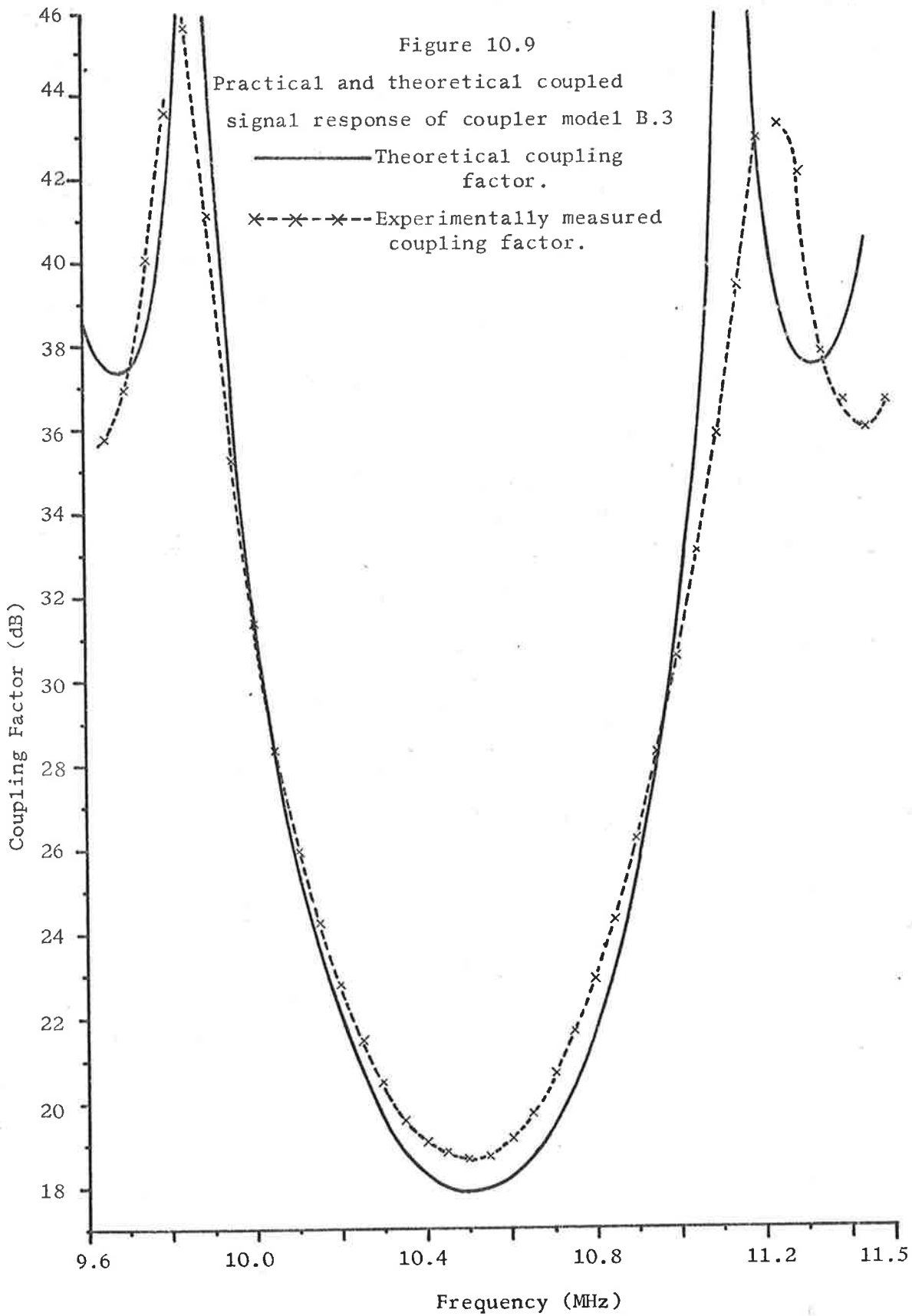
ponding theoretical response, which predicts a centre frequency
coupling factor of 17.9 dB — 0.79 dB larger than obtained in practice
— and which shows the usual harmony with the experimental frequency
dependence.   A plot of coupling loss (P_L) versus frequency, presented
in Figure 10.10, exhibits a loss of only 0.7 dB at mid-band, and less
than 1.2 dB over the 3 dB bandwidth of the coupled signal response.
The experimentally determined lower bound for the centre frequency
directivity of this crossbar coupler is 38 dB.

10.35 Coupler Model B.4.   (Style B, Model 4)

An interaction grid of twenty mass loading bars, each of height
h = 0.446 microns, leads to a practical peak coupling factor of 19.89 dB
in this model.   The graph of the experimental coupled signal response
is contained in Figure 10.11, and records a fractional 3 dB bandwidth
of 0.050 at a centre frequency of 10.52 MHz.   A calculation of the
theoretical coupling factor determines a peak value of 18.8 dB, which
is 1.09 dB stronger than measured experimentally.   The practical and
analytical response curves of Figure 10.11 display the now familiar
close agreement which is noted in the frequency behaviour of the three
previous models.   A coupling loss of 0.6 dB at 10.52 MHz, and of less
than 1.1 dB over the coupling bandwidth, is evidenced by the experimental
results plotted in Figure 10.12.   For this coupler a practical lower
limit of 37 dB can be placed on the centre frequency directivity.

10.36 Coupler Model B.5.   (Style B, Model 5)

The final crossbar directional coupler of this style to be tested
has a region of periodic surface mass-loading formed from a gold overlay
of height h = 0.304 microns.   This produces, as plotted in Figure 10.13
a practical coupling factor of 24.1 dB at a centre frequency of 10.52 MHz,
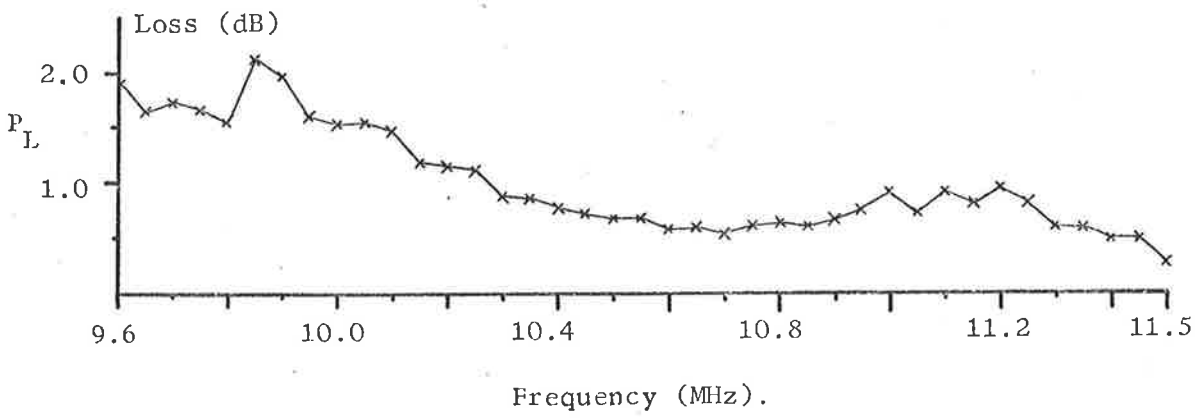
Figure 10.10

Experimentally measured coupling loss for coupler model B.3.

Figure 10.11

Practical and theoretical coupled
signal response of coupler model B.4.

——————Theoretical coupling
factor.

✻-✻-✻ Experimentally measured
coupling factor.
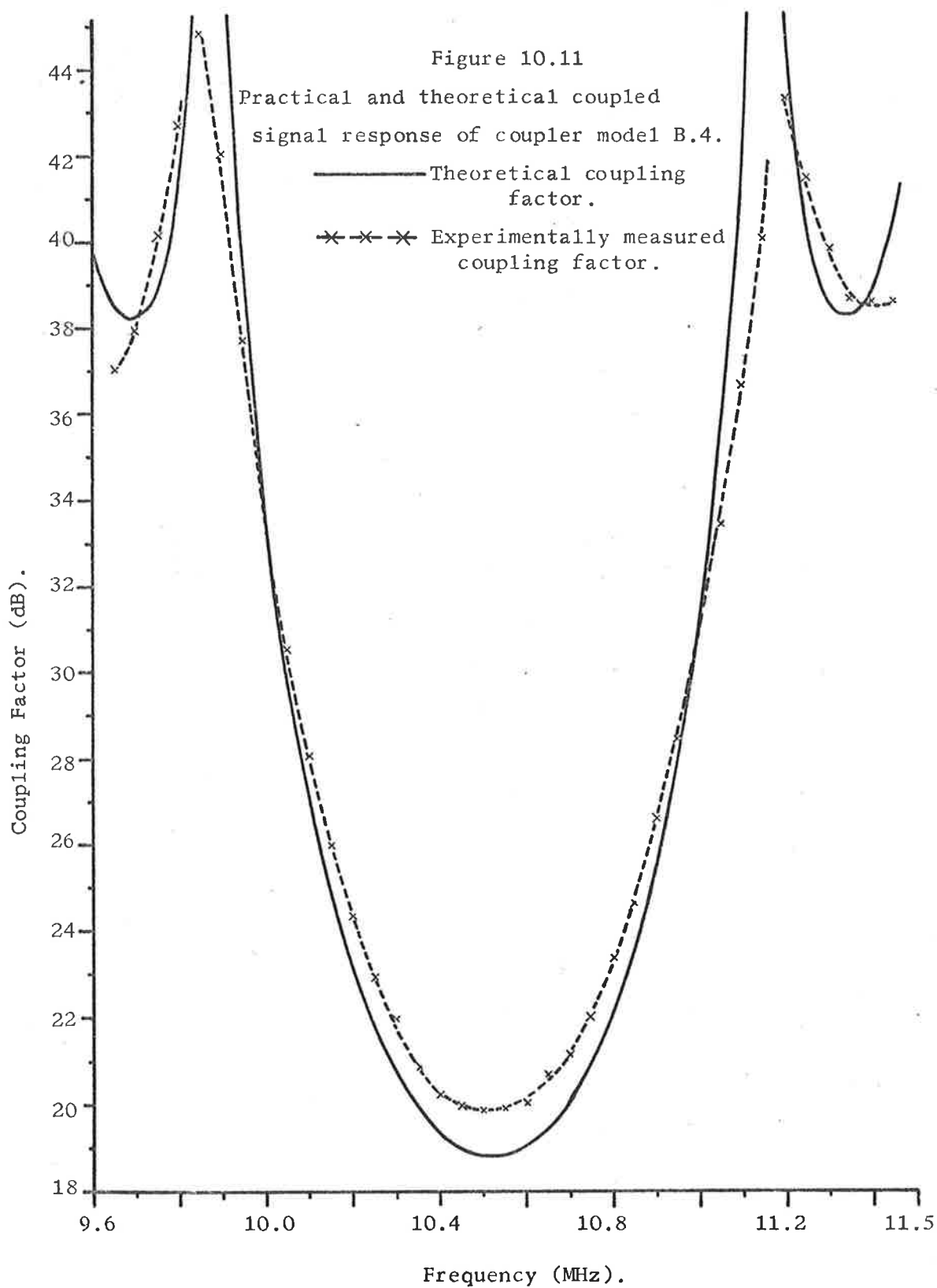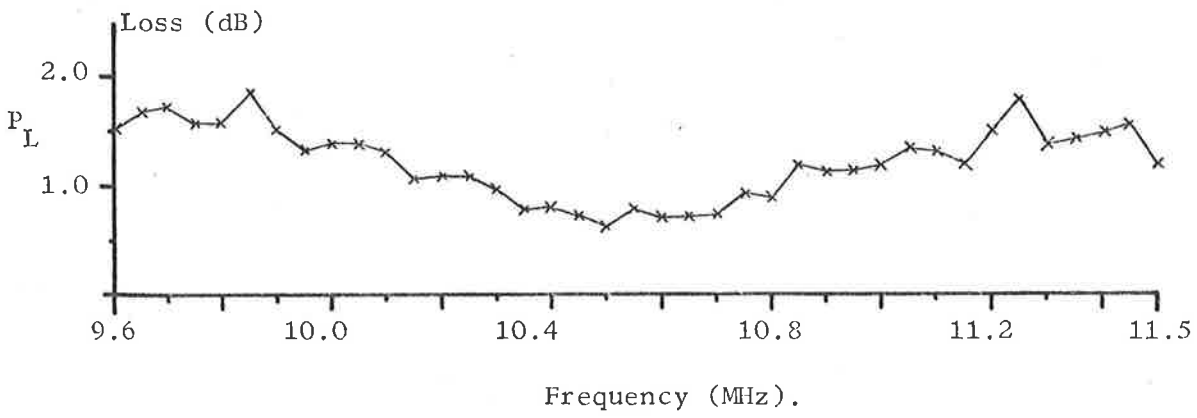
Figure 10.12

Experimentally measured coupling loss for coupler model

B.4.
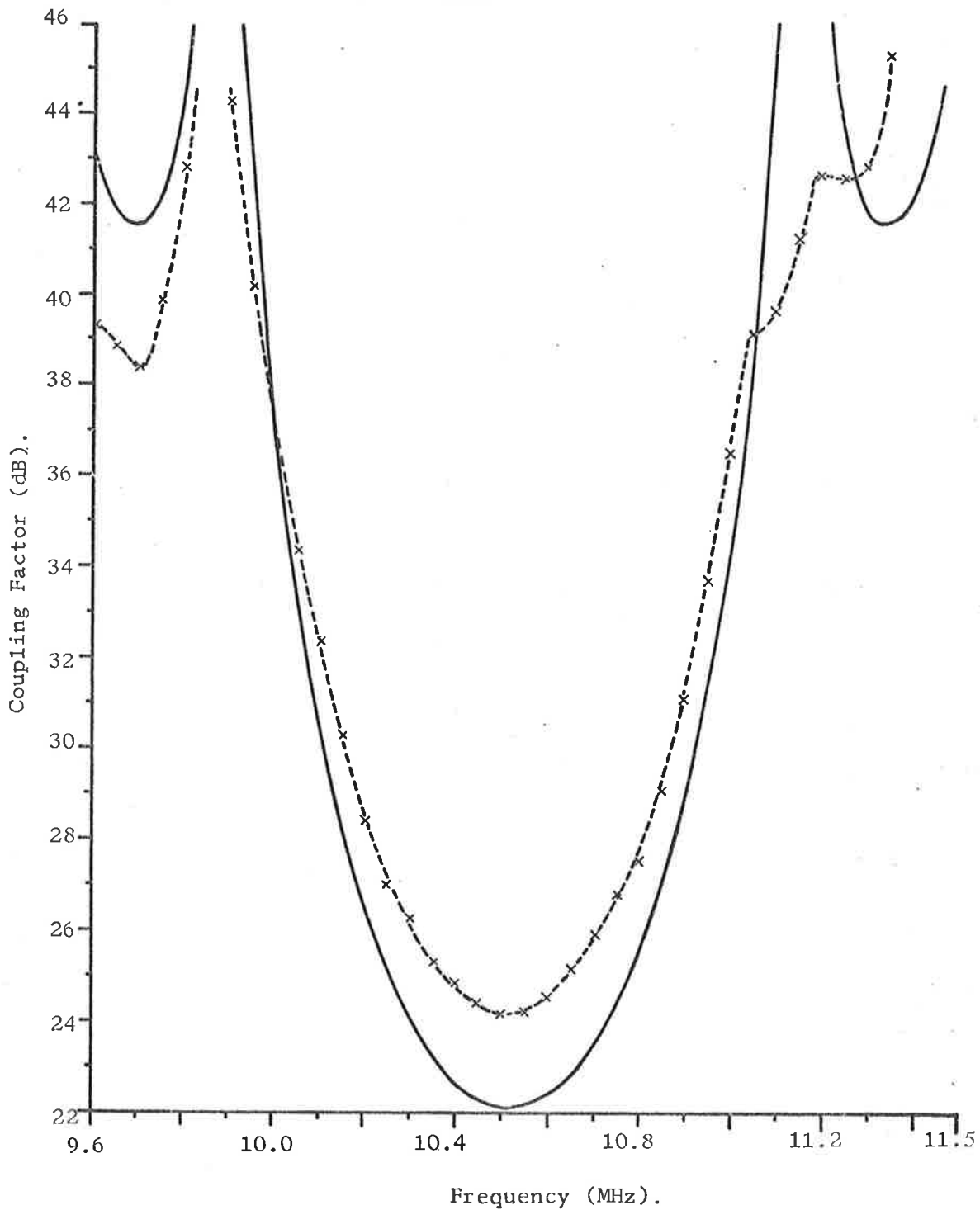
Figure 10.13.

Practical and theoretical coupled signal response of coupler

model B.5.

——————— Theoretical coupling factor.

—×—×—× Experimentally measured coupling factor.

and with a fractional 3 dB bandwidth of 0.049.   Calculations of the
theoretical coupled signal response predict a peak coupling factor of
22.1 dB.   The discrepancy of 2.0 dB between the experimentally and
analytically determined centre frequency coupling factors is consider-
ably greater than found in other models.   As shown by the graphs of
Figure 10.13, the experimental frequency response also displays,
particularly at the high-frequency side-lobe, a larger departure from
the theoretical dependence than noted in the preceding investigations.

A measurement of the coupling loss for this device cannot be
made due to a broken electrode finger in the monitor transducer.   The
absence of an observable directivity wave allows the conclusion that
the practical centre frequency directivity is more than 33 dB for this
model of the microsonic crossbar coupler.

10.4 Transmitted and Coupled Surface Wave Pulse Shapes.

It is clear from the photographs of Figures 10.2 and 10.5 that
the transmitted and coupled surface wave signals have pulse envelopes
of a somewhat different shape.   The origin of this variation is illus-
trated in Figures 10.14 and 10.15 for the case of an input pulse of
10 μ secs duration, (the carrier frequency being 10 MHz), applied to the
input IDT of a surface acoustic wave crossbar directional coupler having
twenty periodic mass-loading bars in the interaction region.   This is
precisely the situation to which photographs (c) - (g) of Figure 10.5,
taken during tests of coupler model B.1, relate.   A comparison of the
waveforms sketched in Figures 10.14 and 10.15 shows that the coupled
surface wave pulse, detected at transducer 3, is 20 cycles longer over-
all, and has a central flat region of the envelope 20 cycles shorter,
than the transmitted pulse received at transducer 2.   Experimentally

Input pulse of duration

$\tau = 10\,\mu$ secs, $\omega = 10$ MHz.

Impulse response
of 5 electrode
pair transmitting
IDT

Envelope of launched surface
acoustic wave pulse.

Envelope of launched surface
acoustic wave pulse.

Impulse response
of 5 electrode
pair receiving IDT

Envelope of received (transmitted)
surface acoustic wave pulse.
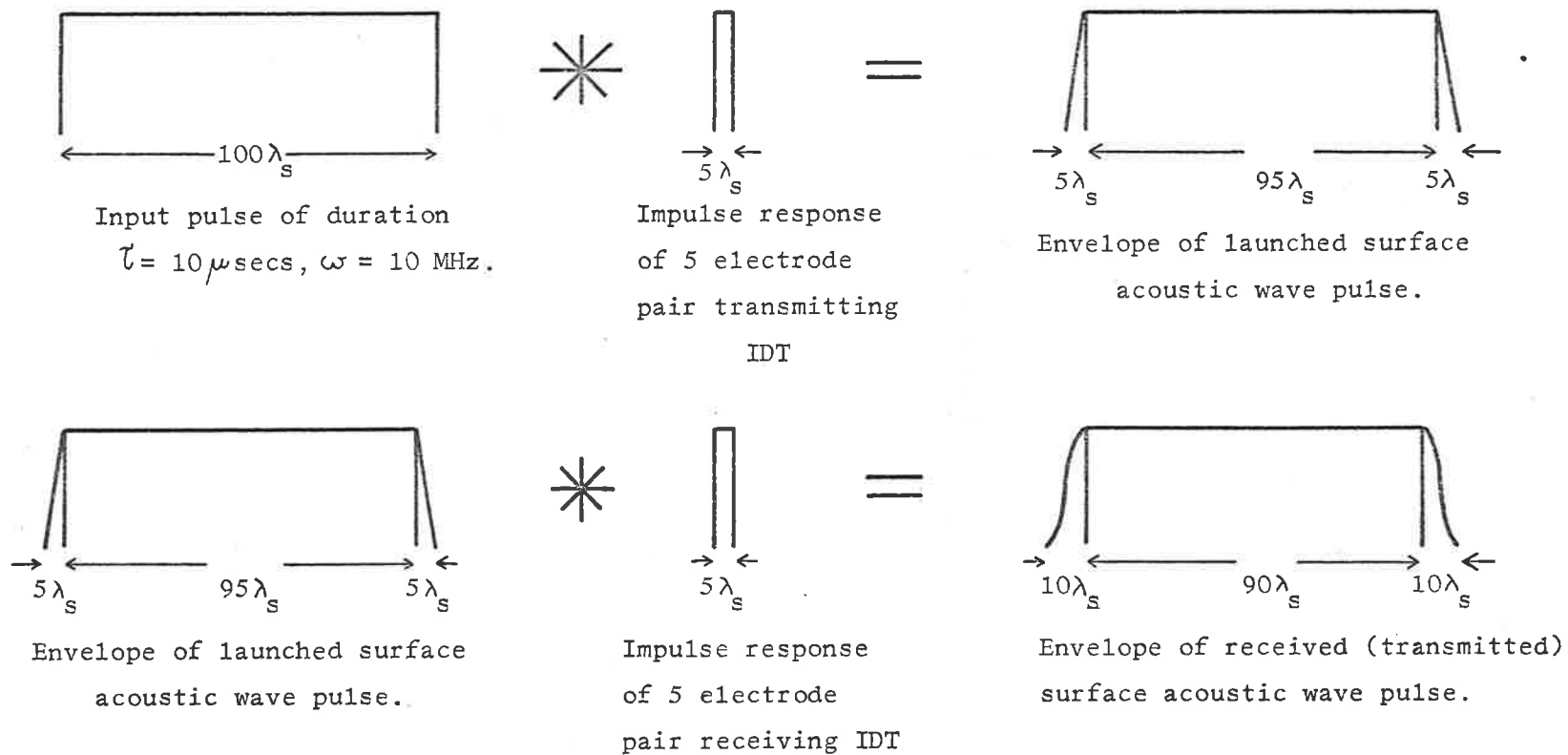
Figure 10.14.

Envelope of the transmitted surface acoustic wave pulse.

(✳ implies convolution).
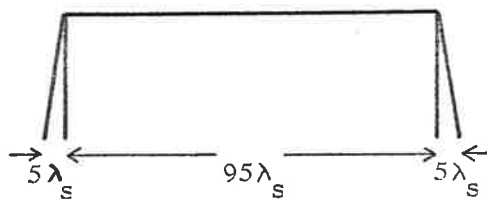
Envelope of launched surface
acoustic wave pulse.
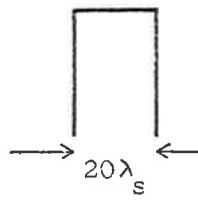
Impulse response
of a 20 element
scattering grid.
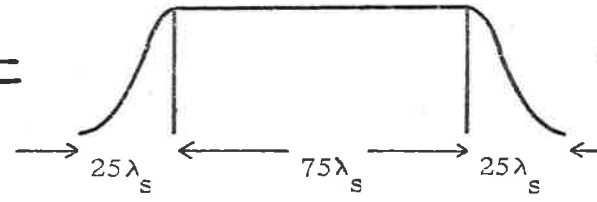
Envelope of coupled surface acoustic
wave pulse.
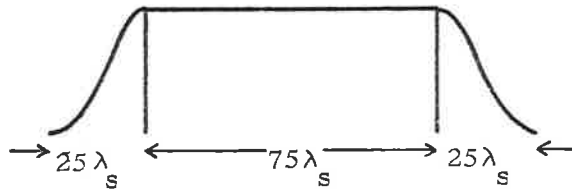
Envelope of coupled surface
acoustic wave pulse.
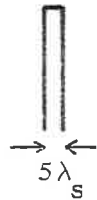
Impulse response
of 5 electrode pair
receiving IDT.
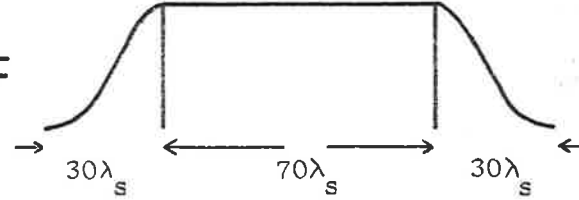
Envelope of detected coupled surface
acoustic wave pulse.

Figure 10.15.

Envelope of the coupled surface acoustic
wave pulse.

($*$ implies convolution)

observed pulse envelopes, and in particular those pictured in the

oscillograms of Figure 10.5 (e) and (g), are of the shape predicted

by analysis. The differences between the coupled and transmitted

surface wave signal envelopes are accentuated in Figures 10.2 (e), (f)

and 10.5 (j), (k) which illustrate waveforms resulting from input pulses

of short duration.

10.5 Strong Coupling of Surface Acoustic Waves

-Coupler Model A.2.

The experimental results of section 10.3 suggest that a region of

heavy periodic surface mass-loading, which permits very strong coupling,

offers one technique for reflecting surface acoustic waves with compar-

atively little loss. To investigate this possibility a coupler of

style A, but with twenty mass-loading elements etched from a very thick

gold film of height h = 9.63 microns, is fabricated and tested. The

coupled signal response of this device, as measured by experiment, is

plotted in Figure 10.16. This discloses a minimum coupling factor of

0.43 dB — i.e. the coupled wave amplitude is three times larger than

the transmitted wave amplitude, which means a coupled to transmitted

power ratio of 9:1 — at 9.70 MHz. Because of the large degree of

velocity slowing as the wave passes through the area of the substrate

surface which is covered by the very thick mass loading bars, this centre

frequency is 6% lower than the design value of 10.3 MHz. For obvious

reasons the perturbation analysis of Chapter IX cannot be used to cal-

culate the amplitudes of the scattered surface waves in this strongly

coupled situation. It is evident, too, from Figure 10.16, that the

experimentally recorded coupling factor no longer exhibits the $\sin(x)/x$

frequency dependence noted in studies of devices providing much weaker

Figure 10.16.
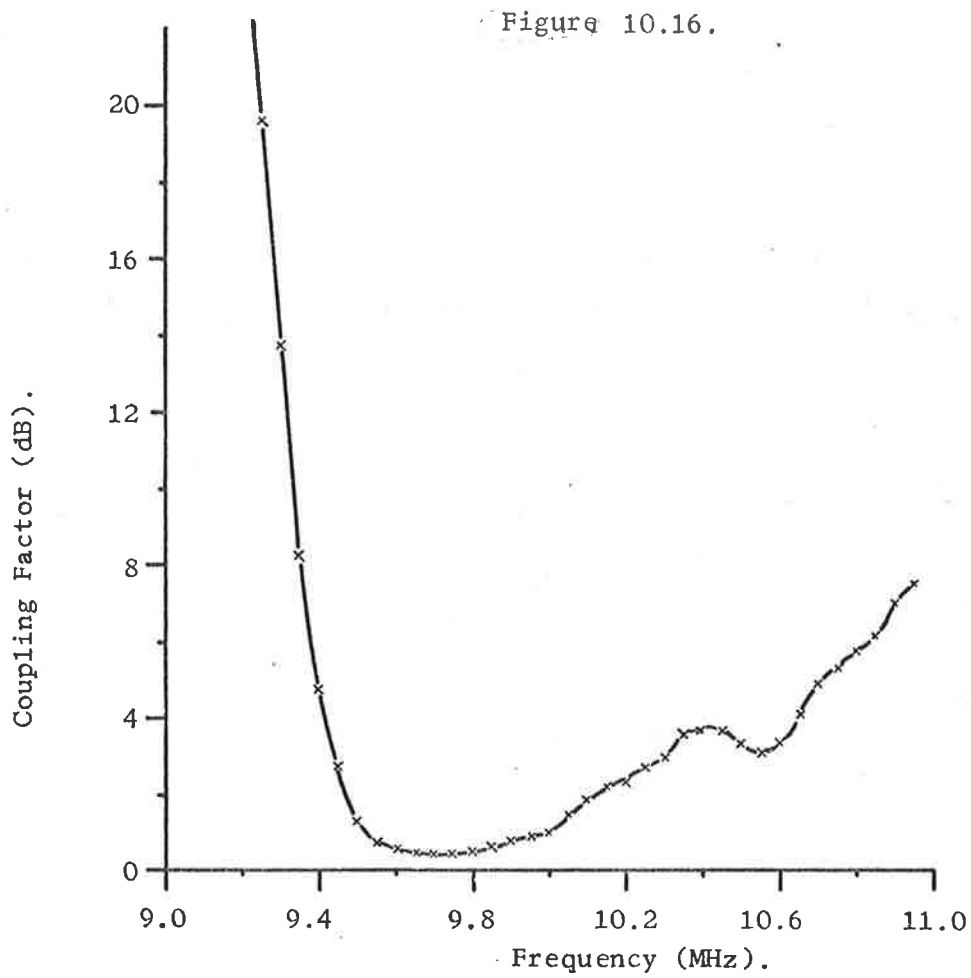
Experimental observation of strong coupling of surface acoustic waves by periodically mass-loading the propagation surface.

Coupler model A.2.

coupling.

Perhaps the most useful result emerging from this investigation
is the indication that a strongly coupled crossbar coupler (of which
a surface wave reflector is the limiting case) should be fabricated,
if possible with regard to bandwidth requirements, from a large number
of moderately thick mass-loading elements in preference to a small
number of very thick bars.   Designs based upon the latter approach,
although affording a wider bandwidth, suffer from two intrinsic prob-
lems.   Firstly, a perturbation analysis cannot be used to predict the
amplitude of the coupled signal; a guide to the performance of a many-
element mass-loading grid formed from a moderately thick overlay can
be obtained from an analysis of the device whose mass-loading bars are
of the same height, but are much smaller in number.   Secondly, unless
specific allowance is made for the phase velocity perturbation intro-
duced by the presence of the surface mass-loading, the centre frequencies
of the scattering interaction and of the IDTs which provide communica-
tion at the ports become separated by significant amounts.

10.6 Experimental and Theoretical Results in Summary.

Table 10.1 summarises the coupled signal behaviour, both experi-
mental and theoretical, of the surface acoustic wave directional couplers
whose performance is discussed individually in section 10.3.   The
features which emerge from an integrated examination of the results for
all models of the crossbar coupler can now be described.

10.61 Bandwidths and Centre Frequencies.

The theoretical or design centre frequencies quoted in Table 10.1
neglect the phase velocity perturbation caused by the application of
the mass-loading overlay to the propagation surface.   In the light of

Coupler Model	N	h (microns)	Centre Frequency (MHz)		3dB Fractional Bandwidth		Centre Frequency Coupling			
							(dB)		A.R.	
			Theor.	Prac.	Theor.	Prac.	Theor.	Prac.	Theor.	Prac.
A.1	10	2.09	10.3	10.0	0.1	.093	11.0	12.1	0.283	0.248
B.1	20	0.749	10.55	10.48	.05	.05	14.4	15.3	0.191	0.172
B.2	20	0.506	10.55	10.50	.05	.049	17.7	18.55	0.130	0.118
B.3	20	0.492	10.55	10.50	.05	.049	17.9	18.69	0.127	0.116
B.4	20	0.446	10.55	10.52	.05	.05	18.8	19.89	0.115	0.101
B.5	20	0.304	10.55	10.52	.05	.05	22.1	24.1	.078	.062
A.2	20	9.63	10.3	9.70	.05			0.43		0.952

Table 10.1

Summary of Theoretical and Experimental Coupled Signal Responses.

N = number of elements in mass loading region.

h = overlay height (microns).

A.R. = centre frequency coupled to incident sur-

face wave amplitude ratio.

the discussion of section 9.22 it is not surprising that couplers whose
interaction region is fabricated from a comparatively thick film have
a practical centre frequency considerably lower than the design value.
But the table indicates, as expected, that the experimental and the
design centre frequencies approach coincidence as the thickness of the
mass-loading layer tends to zero. The fractional 3 dB coupling band-
widths of all devices tested, with the obvious exception of the surface
wave "reflector", model A.2, follow closely the predictions of coupled
mode theory.

10.62 Centre Frequency Coupling Factor.

For the first five models listed in Table 10.1, the analytically
calculated centre frequency coupling factors are stronger than those
measured in practice by relatively small amounts ranging between 0.8
and 1.1 dB. A larger discrepancy occurs for the weakest coupler,
model B.5, whose peak experimental coupling factor of 24.1 dB is 2.0 dB
less than provided by theory. The scattering bars of this crossbar
coupler are etched from a gold overlay only 0.304 microns thick — the
thinnest of all the mass-loading films deposited in the present study.
That the elastic constants of the bulk material, as used in the theoret-
ical calculations, might not adequately represent the properties of
this thin film is the subject of further discussion in section 10.74.

10.63 Centre Frequency Coupled to Incident Amplitude Ratio.

Equations (9.331) and (9.332), derived from the perturbation
analysis of Chapter IX, state that the coupled to incident surface
wave amplitude ratio is linearly proportional to the height of the
periodic surface mass-loading bars, for a coupler of specified config-
uration (i.e. N, ω_0, substrate and overlay material combination, and

device geometry all being fixed).   Points representing the coupled

signal amplitude ratios and overlay heights as measured experimentally

for the five crossbar couplers of style B are marked in Figure 10.17.

A sixth point, marked thus ⊗, represents the practical performance

of coupler model A.1.   Because Figure 10.17 refers exclusively to

style B couplers, this last result is plotted as the experimentally

recorded coupled signal amplitude ratio for coupler model A.1 with an

ordinate given by an "effective" mass-loading film thickness of h =1.14

microns (c.f. actual height of 2.09 microns).   (By taking account of

the different area correction factors, centre frequencies and number of

mass-loading bars in the two device styles, this effective height is

calculated to be the film thickness needed in a style B coupler to pro-

duce the same peak coupled signal amplitude ratio as measured experi-

mentally in model A.1).

As shown in Figure 10.17, these practical results suggest that a

linear relationship between the coupled wave amplitude ratio and the

film thickness exists, for the particular circumstances of the present

investigation, in the region h < 0.9 microns — i.e. for coupled to

incident surface wave amplitude ratios of less than 0.2.   For overlays

of greater height, which provide stronger coupling, the slope of the

relationship steadily decreases.   It is interesting to note that this

limit of linear behaviour is reached when the height of the mass-loading

bars is less than 0.3% of a surface acoustic wavelength at the operating

frequency.   But the high mass density of gold, which is more than seven

times the mass density of the substrate material, quartz, introduces an

"amplification factor" into the calculation of the surface force densities

created by periodically mass-loading the propagation surface.
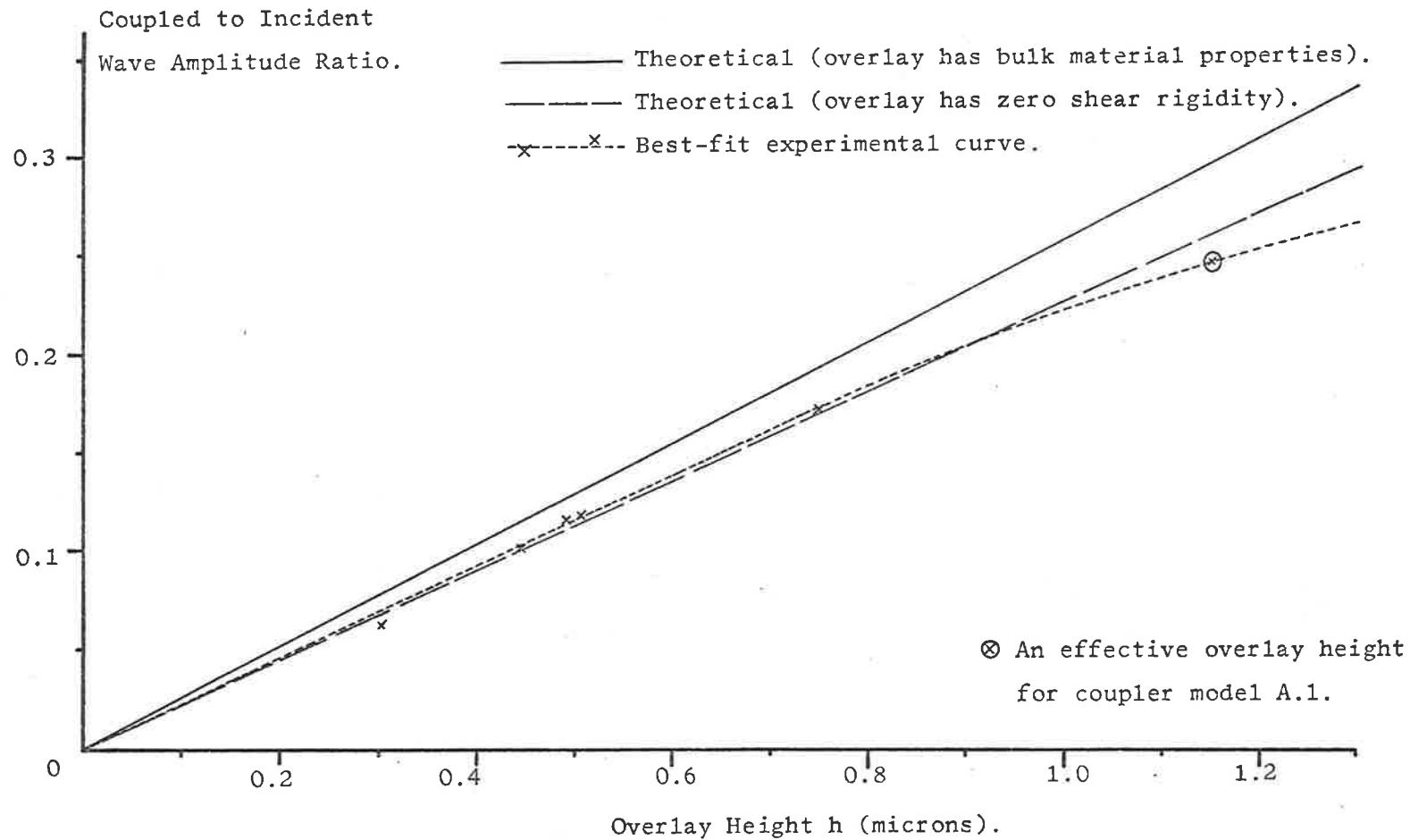
Figure 10.17.

Coupled to incident surface acoustic wave amplitude ratio as a function of overlay height, h.

(h small).

˙Figure 10.17 presents also the theoretical linear relationship,
between the coupled signal amplitude ratio and the mass-loading film
thickness, as calculated from equation (9.331), using the bulk material
constants to describe the elastic properties of the gold overlay; this
determines a straight line whose equation is

$$\frac{\text{Coupled Amplitude}}{\text{Incident Amplitude}} \;=\; 0.259\ h \qquad\qquad (10.631)$$

where h is the height, measured in microns, of the scattering bars.
The third graph in this figure is a further theoretical result calcu-
lated from equation (9.331); on this occasion the overlay is assumed
to have the elastic properties of bulk gold, except that it is of zero
shear rigidity (i.e. $\mu' = 0$ and hence $v_t' = 0$ in equation (9.332)).
This provides a relationship of the form

$$\frac{\text{Coupled Amplitude}}{\text{Incident Amplitude}} \;=\; 0.228\ h \qquad\qquad (10.632)$$

which is, as shown in Figure 10.17, almost coincident with the linear
segment of the "best-fit" curve drawn through the experimental points.
The significance of the above two analytical relationships is considered
in greater depth in section 10.74.

Figure 10.18 extends the graphs of the previous figure to accomo-
date mass loading films of greater thickness and so allows the plotting
of a point to represent the practical performance of each coupler listed
in Table 10.1.   Once again the result for model A.1, marked ⊗, has
been processed to indicate the performance of a similar style B coupler.
But on this occasion the result is plotted as an "effective coupled
amplitude ratio", calculated to be that provided by a style B coupler
whose mass-loading bars are of height h = 2.09 microns (i.e. the actual
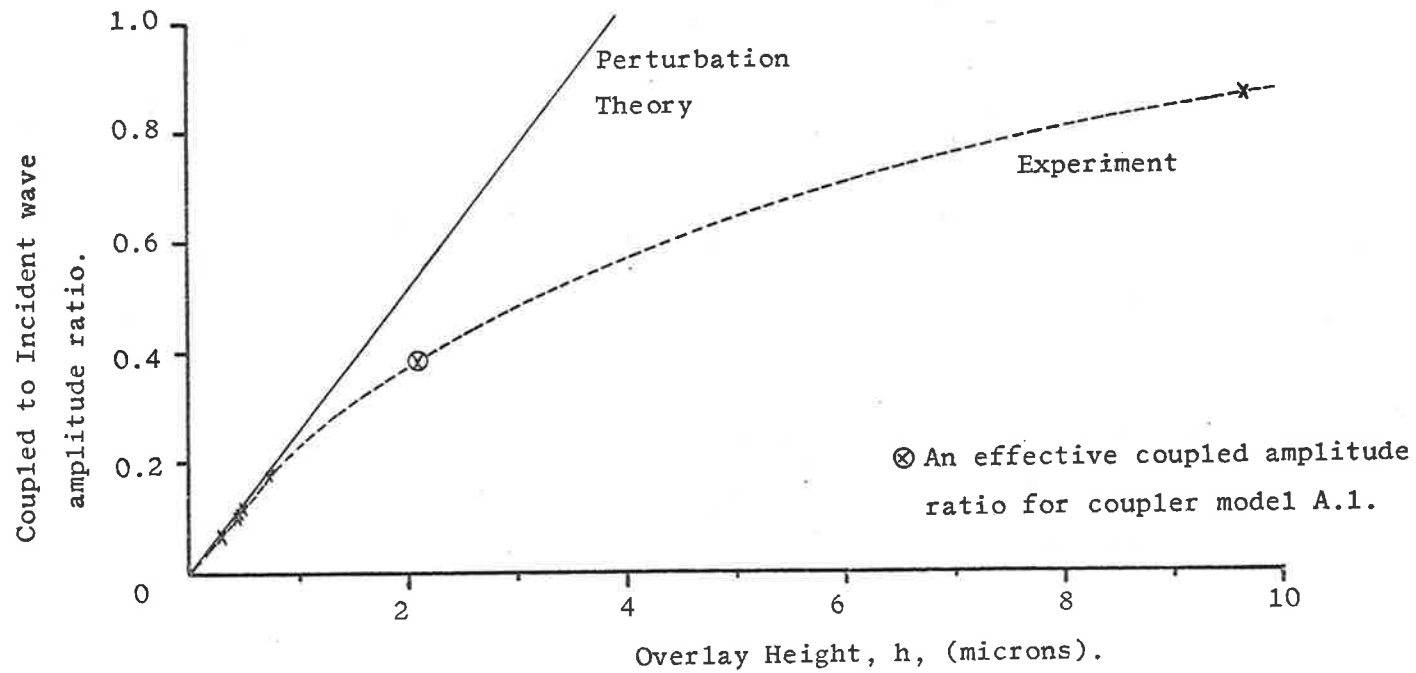
Figure 10.18.

Coupled to incident surface acoustic wave amplitude ratio as a function of overlay height, h.

(h large).

thickness of the overlay in model A.1). As anticipated, Figure 10.18 discloses an increasing discrepancy between the experimental and theoretical behaviour, (the latter being determined from the perturbation analysis of Chapter IX), with increasing overlay thickness.

10.64 Directivity.

Sections 10.31 to 10.36 report that, over the entire frequency range of experimental interest, no "back-scattered" surface wave could be detected at transducer 4, in any of the crossbar couplers. The absence of such a signal allows the establishment of a lower limit to the practical directivity. For coupler model A.1 this bound is 32 dB at the centre frequency, which compares with the theoretical value, taken from Figure 10.1, of a directivity in excess of 47 dB over the 3 dB bandwidth of the coupled signal response. Through equation (9.513) the coupled mode analysis predicts a directivity of 59 dB at the centre frequency and of more than 55 dB over the 3 dB coupling bandwidth for style B crossbar couplers (with N = 20). The experimentally determined lower limits for the centre frequency directivity of the five style B couplers tested in this study lie between 33 and 41 dB.

10.65 Coupling Loss.

Practical measurements of coupling loss for four models of coupler style B, (model B.5 excluded), return values between 0.6 and 1.0 dB at the centre frequency, and between 1.1 and 1.4 dB over the 3 dB bandwidth of the coupled signal response. These losses, per se, are sufficiently small to justify the lossless coupling assumption by which the experimental results are processed and plotted. But the curves of Figure 10.8, representing measurements taken with model B.2, reveal that only a small proportion of the observed loss is due to the coupling

mechanism.   As described in section 10.33, a propagation loss of

0.65 dB is recorded, in the absence of the surface perturbation, over

the path length of approximately 3 cms between transducers 5 and 2,

at the device centre frequency of 10.50 MHz.   This leaves a contribu-

tion of only 0.15 dB loss introduced by the coupling process.

But the observed propagation loss of approximately 0.22 dB/cm is

an order of magnitude greater than that which could be due to elastic

losses alone at 10 MHz (17), (18), (45), (61), (127). The analytical

results of section 3.52 and, more specifically, of Table 3.1, recall

that the main transmission paths of the crossbar couplers are oriented

along a direction for which ϕ, the misalignment angle between the nett

acoustic power flow and wave vectors, is zero and $\partial\phi/\partial\theta$ is - 0.45

(θ being an angle which defines the wave vector orientation on the

propagation surface).   A simple calculation shows that the total

propagation loss of 0.65 dB can be accounted for by an angular displace-

ment of the metal overlay pattern, from the ideal position on the sub-

strate surface, of $\pm 1.5^{o}$.   The discussion contained in section 5.22

establishes that the overall tolerance in siting the main coupler paths

at $\pm 34^{o}$ to the X crystal axis is $\pm 1.5^{o}$, with the fabrication techniques

employed in this study.

10.7 <u>Sources of Discrepancies Between the Theoretical and Practical</u>

   <u>Coupled Signal Responses.</u>

Although the preceding sections clearly demonstrate that there is

general agreement between the experimental and the analytically-cal-

culated performances of the surface acoustic wave crossbar directional

coupler, it is instructive to explore the possible sources of the small

discrepancies which do arise, primarily in the centre frequency coupling

factor.

10.71 Pattern Misalignment During the Photofabrication Process.

The most likely source of error is that considered in section

10.65, namely an angular displacement of the device mask from the

optimum design position, (as determined by the substrate orientation),

during the photofabrication process.   Using the wider results computed

by program "Anisom" — i.e. data describing surface wave propagation

on paths in the vicinity of $\pm34^{o}$ to the X crystal axis on AT cut quartz

— the theoretical effect, upon centre frequency coupling, of such a

misorientation of the metal overlay pattern can be calculated.   This

undertaking, which rests upon equations (9.331) and (9.332), yields the

results shown in Figure 10.19; the curve indicates a coupling factor

dependence of ±0.3 dB per degree of misorientation for small departures

from the design position.   Hence the rotational location tolerance of

$\pm1.5^{o}$, noted in section 5.22, introduces an uncertainty of ±0.45 dB

into the centre frequency coupling factor.

10.72 Errors in Preparing the Original Device Mask.

Two different errors, each of which modifies the theoretical centre

frequency coupling factor, must be considered under this heading.   The

first is an angular misalignment of the periodic mass-loading elements

(i.e. of the perturbation wave vector) in relation to correctly aligned

input and output paths as defined by the IDTs in each port.   Because

the original rubylith pattern is twenty-five times larger than the

final photographic mask, such errors should be less than $\pm0.5^{o}$.   A mis-

orientation of the scattering elements means that the coupled signal

wave vector diagram, Figure 5.2, no longer closes at band centre; its

effect can be calculated, therefore, from the directivity function of
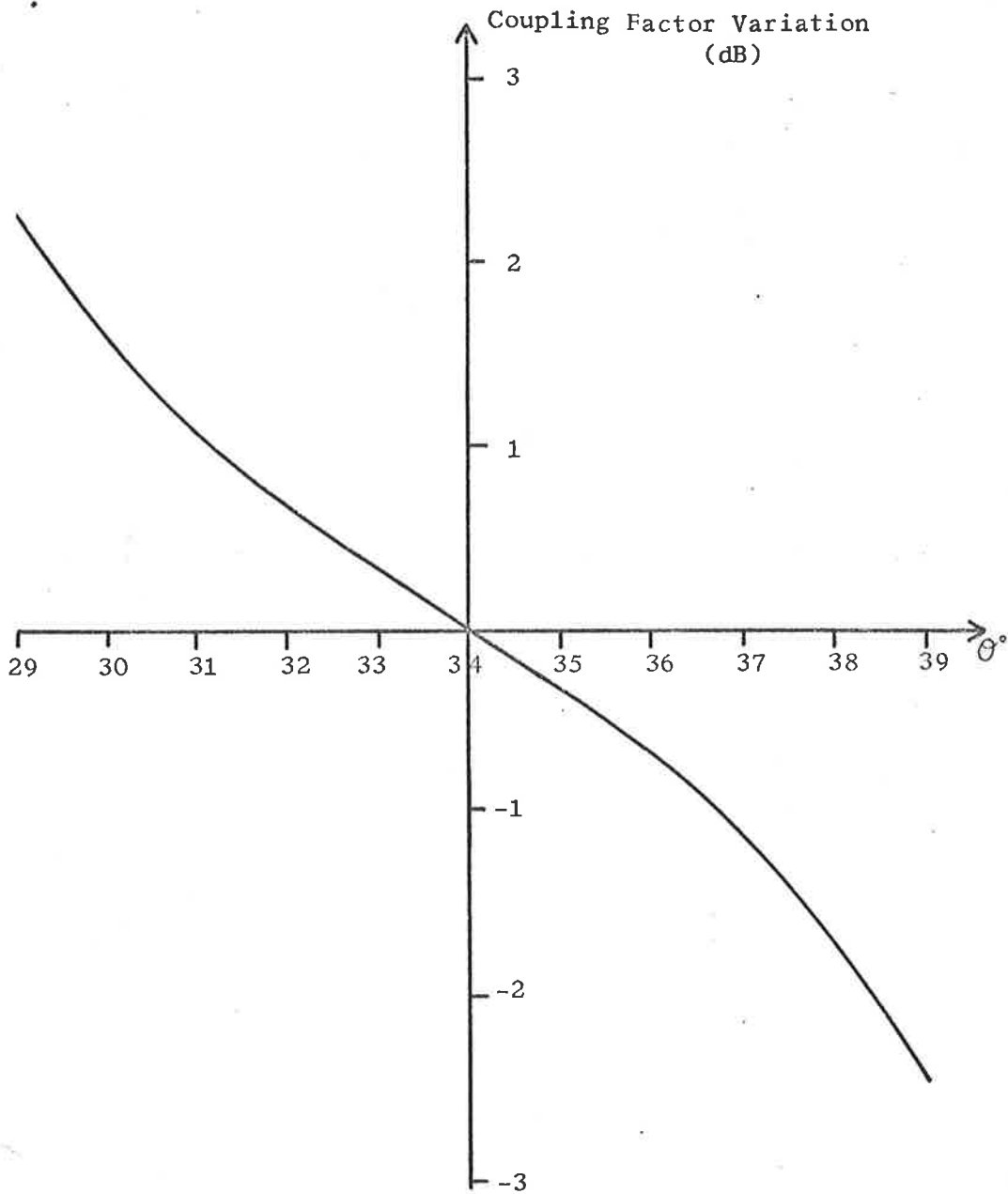
Figure 10.19.

Dependence of centre frequency coupling factor upon pattern misorientation.

(i.e. Rotation of the photographic mask from the ideal position relative to the substrate orientation).

θ is angle between wave vector of incident wave and X crystal axis.

equation (9.507), which returns the results shown in Figure 10.20. This curve predicts, for the possible mis-orientation of $\pm 0.5°$, a reduction in centre frequency coupling factor of 0.43 dB.

The second source of error which can arise in cutting the rubylith pattern is an incorrectly located output (coupled) wave path, for correctly aligned input and surface perturbation wave vectors. A calculation of the manner in which the centre frequency coupling factor deteriorates due to such a non-ideal design is complicated by the need to consider two separate factors. The first of these is a non-closing wave vector diagram, the contribution from which is provided once more by equation (9.507). A second arises on account of substrate anisotropy, which causes the particle displacement components of the coupled surface wave to be dependent upon the output wave direction. The contribution from this factor can be evaluated from equation (9.331) and from details, supplied by program "Anisom", of surface wave propagation in the vicinity of the paths at $\pm 34°$ to the X crystal axis on AT cut quartz.

Figure 10.21 describes the overall dependence of the centre frequency coupling factor upon output wave vector orientation as determined by combining the results of calculations of the two aforementioned factors. Again an error of this nature should not exceed ± 0.5 degrees; this limit allows for a reduction in centre frequency coupling factor of up to 0.3 dB. A further observation which can be made from Figure 10.21 is that the 3 dB coupled beamwidth is approximately $5°$; this lends additional support to the design contention that almost all of the scattered acoustic energy is detected as a coupled surface wave at transducer 3.

Angular Rotation of Scattering Grid (degrees).
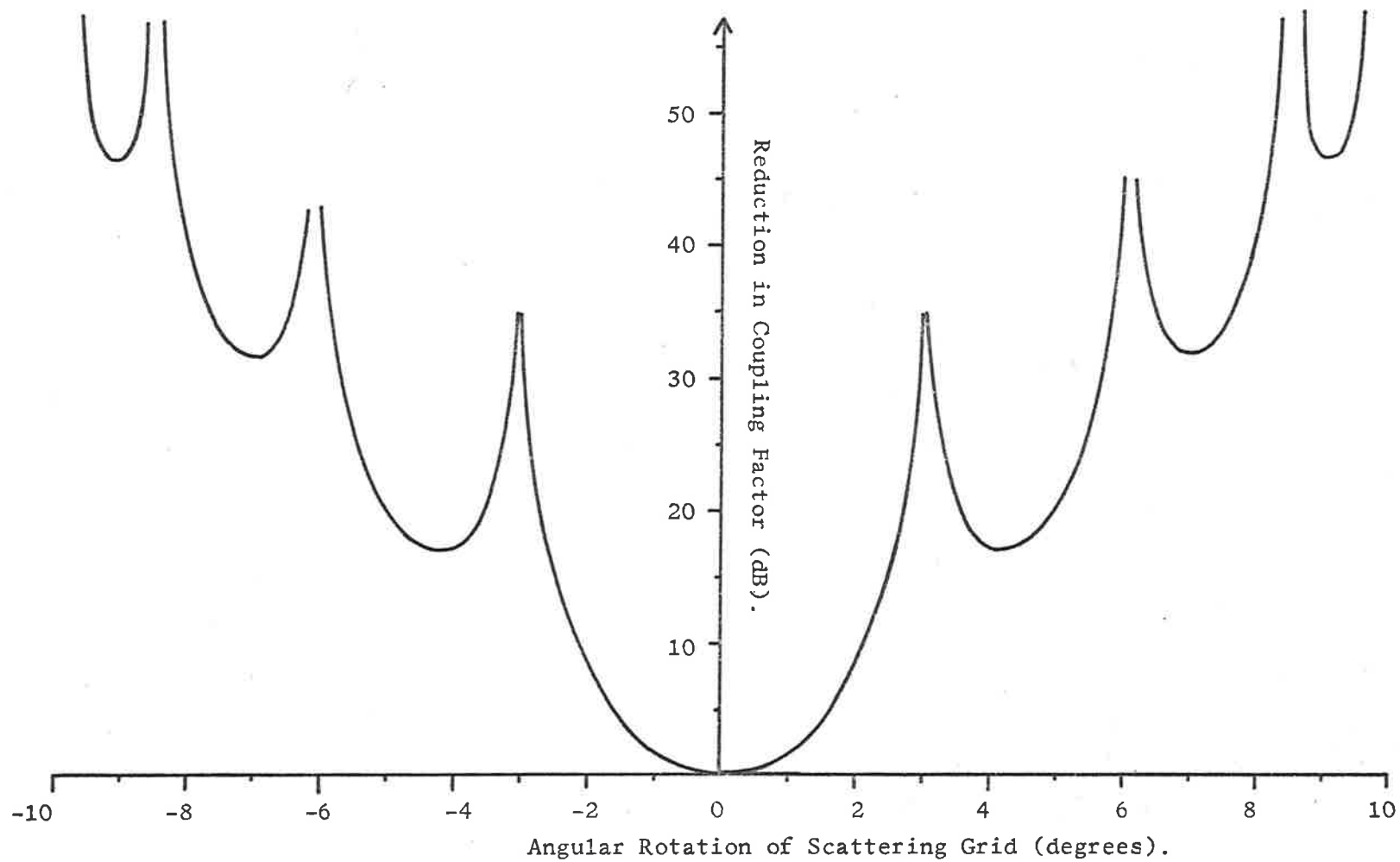
Figure 10.20.

Effect, upon centre frequency coupling factor, of rotating the scattering grid.

(input and output wave vectors fixed).

Angle between exit wave and X crystal axis (degrees).
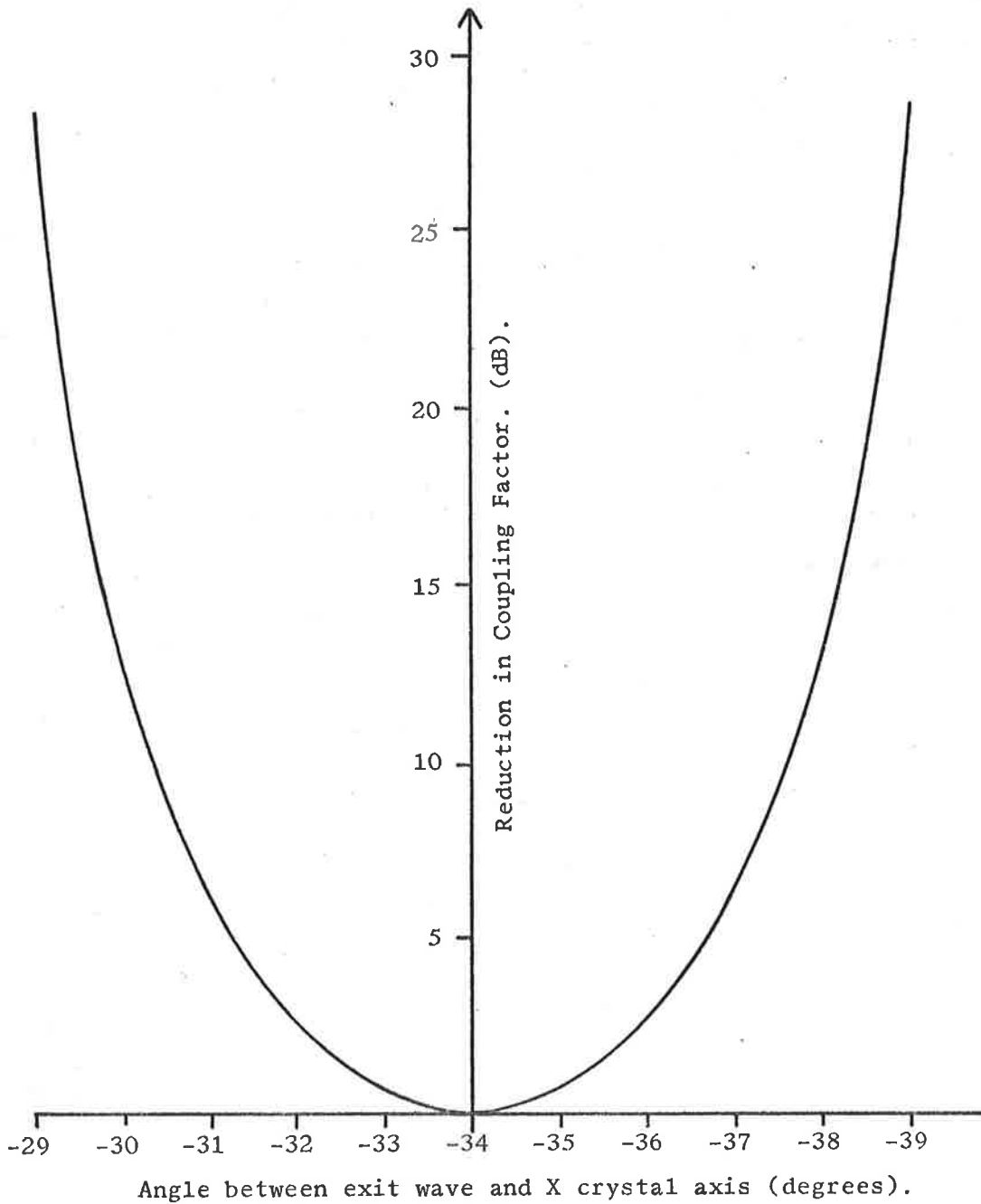
Figure 10.21.

Effect, upon centre frequency coupling factor, of varying the

orientation of the output wave.

(input and perturbation wave vectors fixed).

10.73 The Accuracy of A Perturbation Analysis.

Section 9.2 presents a perturbation treatment of surface acoustic wave propagation on a mass-loaded surface; upon this all subsequent calculations of the coupled wave amplitude ratios depend. The perturbation analysis makes two fundamental assumptions. One is that the surface wave particle displacements on the mass-loaded surface can be replaced by those of the wave motion on the free substrate surface. Obviously this step is only accurate when the perturbing film is sufficiently thin to ensure that no significant modification to the particle displacements of an incident wave occurs. The other important assumption is that the input wave is unattenuated as it travels through the region of periodic mass-loading. This can only be true of a thin overlay which provides weak coupling.

The practical couplers whose performance is discussed in section 10.3 are designed, in general, to have relatively weak coupling and should, therefore, be amenable to analysis by a perturbation approach. Two possible exceptions are coupler models A.1 and B.1, both of which exhibit moderate coupling, and for which a perturbation calculation may be somewhat less accurate. Figures 10.17 and 10.18 illustrate the greater discrepancies which arise between experimental and theoretical results (the latter being determined from the first order perturbation analysis) with increasing strength of coupling.

10.74 The Uncertain Elastic Properties of the Thin Film Overlay.

In the light of the discussion in the preceding section, it is surprising to note, from Table 10.1, that the largest difference between practical and theoretical centre frequency coupling factors occurs, as shown by the response curves of Figure 10.13, for coupler model B.5

which possesses the lowest coupling of all the devices tested. The argument of section 10.73 suggests that this is the very coupler for which a perturbation calculation should be most accurate.

Of the sources of discrepancies described above the only error which can alter the centre frequency coupling factor of one device without modifying the performance of other models fabricated from the same photographic mask, is that described in section 10.71; i.e., rotation of the mask with respect to the substrate. But model B.5 has a theoretical-practical centre frequency coupling factor difference which is 1 dB more than recorded for other style B couplers. A discrepancy of this magnitude can be caused only by a rotational misalignment 3° greater than introduced in the fabrication of any other device.

As reported in sections 4.3 and 5.22, the overall tolerance on pattern alignment is $\pm 1.5^{\circ}$, of which $\pm 1.0^{\circ}$ is contributed during the process of substrate machining. The five crystals upon which style B couplers are fabricated were prepared simultaneously in a single batch and all should possess the same misalignment of substrate edges from crystal axes. Thus it would seem highly improbable that the metal overlay pattern of one crossbar coupler is rotated an additional 3° from the design alignment, compared to the patterns of its companion models.

One plausible explanation resides in the fact that coupler model B.5 is formed from the thinnest metal film, (h = 0.304 microns) of all the mass-loading layers deposited in this study. Very little quantitative information concerning the elastic properties of thin metal films is available from the litterature; most practical data relates to tensile strength measurements (128) - (131). The results of one such

experiment (128), (129) suggest that, at least in regard to tensile strength, gold and silver films thicker than 0.25 microns behave like the bulk material, while thinner films have considerably different characteristics — notably a much higher tensile strength. Such a variation of elastic properties with film thickness could account for the experimental behaviour of coupler model B.5 as compared with the performance of the other devices. Unfortunately the experimental observation of the dependence of tensile strength upon film thickness is not conclusive; later, but less complete, measurements of the same parameter do not seem to indicate the same behaviour (130).

In investigations of the input admittance of IDTs on lithium niobate Skeie (110) sometimes notes (in particular, when the aluminium electrode fingers are deliberately mass-loaded by a further layer of gold) closer agreement between theoretical and experimental values by assuming that the metal films are of zero shear rigidity. Figure 10.17 shows that the same assumption leads to a linear relationship, between the coupled wave amplitude ratio and the mass-loading film thickness, which is almost identical to that suggested by the practical results. Once more, unfortunately, there is no evidence of either an experimental or a theoretical nature to support the zero shear rigidity assumption. But the two analytically calculated relationships drawn in Figure 10.17 indicate the extent of the possible variation in the theoretical results due to uncertainties regarding the elastic properties of the mass-loading layer.

10.8 The Electroacoustic Contribution to the Scattering Mechanism.

The analyses of Skeie (110) and Auld (108) show that the reflection coefficient of a surface acoustic wave normally incident upon a metal

strip, of finite height h, deposited upon the surface of a piezoelectric medium, is linearly proportional to

$$\xi \;=\; -A_m \left|\Delta v/v\right|_{mass} \;+\; A_s \left|\Delta v/v\right|_{stiffness} \;+\; \left|\Delta v/v\right|_{sc} \qquad (10.801)$$

Here A_m and A_s are constants determined by the properties of the substrate, while the other variables are interpreted as follows;

$\left|\Delta v/v\right|_{sc}$ is, as defined by equation (3.001), the phase velocity perturbation caused solely by the combined effects of the substrate piezoelectricity and the overlay conductivity.

$\left|\Delta v/v\right|_{mass}$ is the phase velocity perturbation due solely to the mass-loading provided by the overlay. Clearly this parameter is a function of the height and mass density of the deposited film.

$\left|\Delta v/v\right|_{stiffness}$ is the surface wave phase velocity perturbation introduced solely by the elastic stiffness of the overlay. This term is a function of the shear rigidity of the deposited film.

Definitions similar to equation (3.001) can be formulated for $\left|\Delta v/v\right|_{mass}$ and $\left|\Delta v/v\right|_{stiffness}$ if so desired.

In IDT design the mass-loading effect is minimised by using thin aluminium fingers, and the $\left|\Delta v/v\right|_{sc}$ term of equation (10.801) may dominate (71), (132). Calculation shows that this type of interaction, resulting from the short-circuiting of the piezoelectric fields at the metallised surface, virtually alone is responsible for the experimental observation, by Tseng (23), of the Bragg reflection of surface acoustic waves from a grid of aluminium strips deposited on a strongly piezo-

electric (PZT-4) substrate. However in the present study the mass-loading effect has been reinforced deliberately, and the analytical calculations of the coupled wave amplitude ratios, as detailed in Chapter IX, have considered only the first two terms of equation (10.801). The curves of Figure 10.17 show that the elastic stiffness of the overlay makes a small contribution to the coupling in comparison with that provided by the mass-loading, but the relative importance of a contribution arising from the $\left|\Delta v/v\right|_{sc}$ term of equation (10.801) has not been established.

For gold films on a fused quartz substrate (which, in regard to phase velocity perturbation, should provide a reasonable indication of the behaviour of a surface wave propagating on gold-coated crystalline quartz, as used in the experimental versions of the crossbar coupler) Skeie (110) determines that

$$\left|\Delta v/v\right|_{mass} \doteqdot 2\beta h$$
$$\text{for} \quad \left|\Delta v/v\right|_{mass} < 20\% \qquad (10.802)$$

where, as usual, h is the mass-loading film height and β $(= \omega/v_s)$ is the magnitude of the surface acoustic wave vector. The crossbar coupler fabricated from the thinnest overlay is model B.5 for which

$$h = 0.304 \text{ microns},$$
$$v_s = 3.264 \text{ Km/sec} \quad \text{(Appendix II)},$$
$$f = 10.52 \text{ MHz} \quad \text{(centre frequency, Table 10.1)},$$

and $\omega = 2\pi f$.

Substituting these values into equation (10.802) discloses that

$$\left|\Delta v/v\right|_{mass} \doteqdot 1.2\% \qquad (10.803)$$

For the main transmission paths of the couplers, Table 3.1 states that

$$\left|\Delta v/v\right|_{sc} = 0.074\% \qquad\qquad (10.804)$$

while the data of Appendix I can be used in Auld's formula (108) to

obtain

$$\left|A_m\right| \doteqdot 0.73 \qquad\qquad (10.805)$$

The results presented in equations (10.803) - (10.805), show,

when inserted into equation (10.801), that for even the crossbar coupler

providing the weakest coupling, the mass-loading contribution to the

scattered wave amplitudes is more than an order of magnitude greater

than that arising from the "electroacoustic fields — conducting

electrodes" type interaction. Hence the neglect of this latter mech-

anism in theoretical calculations of coupler performance is justified.

In view of the aim of section 10.7, it is worthwhile to note one

further feature of the scattering process which can be deduced from

the foregoing discussion. Auld (108) demonstrates that when the sub-

strate is elastically isotropic A_m is real; equations (3.151) and

(3.152) can be used in Auld's formula to obtain the additional result

that for practical isotropic materials this coefficient is negative.

This allows the conclusion, based on the structure of equation (10.801),

that the $\left|\Delta v/v\right|_{mass}$ and the $\left|\Delta v/v\right|_{sc}$ contributions to the reflected

wave reinforce each other under such circumstances. Although A_m

becomes complex when the medium is anisotropic detailed calculation

(which, for the particular conditions applying to the practical cross-

bar couplers, can be undertaken using the description of surface wave

characteristics supplied in Appendix I) shows that these two contribu-

tions still tend to enhance each other. The incorporation of the

electroacoustic component of the scattering mechanism into the crossbar

coupler analysis would lead to very slightly stronger theoretical

coupling factors.   Therefore this factor acts to widen the gap between
practical and analytical results, and does not offer an explanation for
the existing discrepancies.

0.9   Sources of Discrepancies in Relation to the Theoretical and

Practical Results.

Table 10.1 and the discussion of section 10.6 highlight the general
close agreement between the theoretical and practical behaviour of the
microsonic crossbar directional coupler.   In particular they emphasize
that the most significant discrepancies between the two sets of results
occur in determinations of the centre frequency coupling factor; values
measured by experiments with five devices are between 0.8 and 1.1 dB
weaker than predicted by theory, while a further device, which provides
the lowest coupling, shows a departure of 2.0 dB.   But the arguments
of sections 10.71 and 10.72 reveal that angular tolerances on pattern
preparation and alignment can modify the centre frequency coupling
factor, as calculated for the ideal device, by amounts ranging from
+0.45 dB to -1.2 dB.   Hence the general agreement between experimental
and theoretical centre frequency coupling factors, as for the other
device parameters discussed in sections 10.3 to 10.6, is quite sound.

CHAPTER XI

THE APPLICATION OF PERIODIC MASS LOADING OF A SURFACE ACOUSTIC WAVE PROPAGATION SURFACE TO MICROSONIC COMPONENT DESIGN.

11.0 Introduction.

This study of the periodic surface mass-loading interaction has been conducted, as stated in the aims of the thesis, section 1.4, in the context of a surface acoustic wave directional coupler design. But the potential device applications of this coupling mechanism extend much further than this; some of the more significant of these, in the light of the experimental and theoretical results of Chapter X, are now discussed.

11.1 Surface Acoustic Wave Directional Couplers.

In this category, which includes devices more correctly describable as power dividers and acoustic beam splitters, a wide variety of component designs has been proposed and tested (23), (47), (49), (51), (55), (121), (126), (133) - (140); space limitations permit a consideration of only the more promising and the more versatile.

Directional couplers formed by two adjacent thin film strip surface acoustic waveguides are studied initially in the weak coupling situation through a perturbation analysis developed by Tiersten (49). As a consequence of the weak coupling the devices require a large coupling length, (i.e. the distance needed for energy to be transferred completely from one guide to the adjacent guide), and provide only a narrow bandwidth. The work of Adkins and Hughes (51) extends Tiersten's analysis to accomodate both strong and weak coupling. Their investigations include experimentation with the three directional coupler designs sketched in Figure 11.1. By using much stronger coupling, their sep-
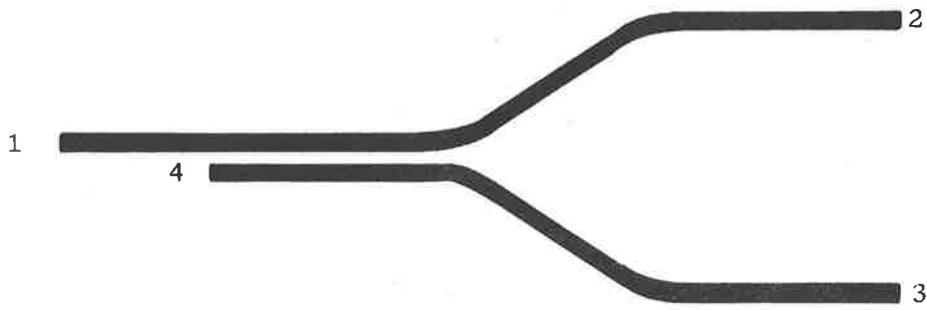
(a) Separated double guide directional coupler.
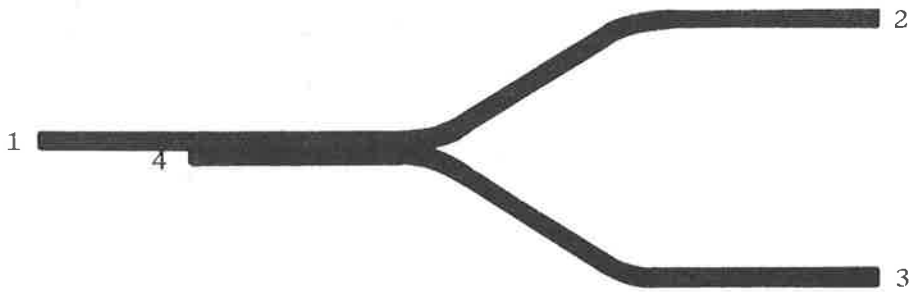
(b) Contiguous double guide directional coupler.
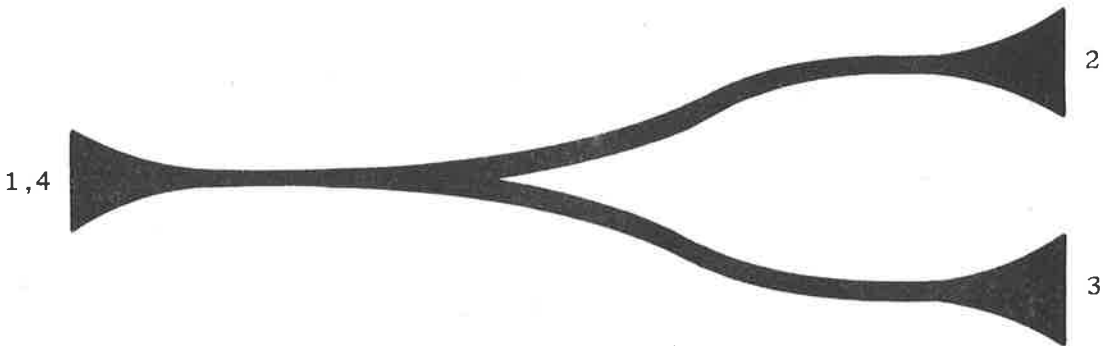
(c) Y junction directional coupler.

Figure 11.1

Thin film strip guide surface acoustic wave directional couplers.

[after Adkins & Hughes (51).]

arated double guide coupler, Figure 11.1(a), achieves a wider band-
width than Tiersten's device.   But this style of coupler is still
inherently narrow-band due to the exponential transverse decay of energy
outside the confines of the strip guide (49), (50).   Estimations of
performance capabilities based upon detailed theoretical and practical
studies (51) suggest bandwidths of from 1% to 20% for coupling factors
within the range of 18-25 dB.

The contiguous directional coupler, illustrated in Figure 11.1(b),
is the limiting case of the separated double guide coupler, as the
separation approaches zero.   This device has not received the same
intensive study afforded the separated double guide coupler, but both
theory and experiment suggest an improved performance over the latter
style.   Coupling lengths five to ten times shorter, and bandwidths
five times flatter may be possible with the contiguous coupler, but the
range of available coupling factors is reduced to 0-10 dB (51).   Figure
11.1(c) shows the final arrangement to be examined by Adkins and Hughes;
experiments verify the obvious properties of this Y junction coupler,
namely that it provides 3 dB coupling over broad bandwidths.

From the investigations undertaken by Tiersten (49) and Adkins and
Hughes (51) it seems reasonable to conclude that surface acoustic wave
directional couplers fabricated from various configurations of thin
film strip guides suffer from the four disadvantages listed below.

1. The components are inherently frequency dispersive due
    to the laminated surface wave propagation structure.

2. Unless epitaxial growth is used to create single crystal
    thin film overlays, the surface acoustic waveguides may
    have a large propagation loss at high frequencies.

3. If the surface waves are to be launched by IDTs, which currently provide the most convenient method of transduction, tapered waveguide sections or "horns" must be employed to collect all the acoustic energy radiated from the transducer aperture, typically 100 surface wavelengths in width, and to direct this into the guiding path, whose width usually is of the order of a surface wavelength. Inevitably some acoustic losses occur in these waveguide transition regions; one set of experimental measurements (51) report a per horn loss of 5 dB at 25 MHz.

4. In certain configurations difficulty in confining the propagating acoustic modes to the guides may be encountered (51).

In proposing the above factors as the major problems associated with the successful implementation of strip guide couplers, it is assumed that the contiguous coupler overcomes the narrow bandwidth restriction inherent in the separated double guide coupler. The first two problems stated above might be surmounted by the utilization of very thin metal overlays, which achieve surface guidance through the velocity slowing introduced by the short-circuiting of the electroacoustic fields at the surface of a piezoelectric substrate (25), (141). These guides promise a much lower propagation loss and a frequency dispersion reduced by three orders of magnitude (51) in comparison with polycrystalline mass-loading overlays (49), (50).

The surface acoustic wave crossbar directional coupler suffers from none of the four defects listed above. But it shares, with the

separated double guide coupler, the problem of narrow bandwidth.   This

becomes particularly apparent when the performances of the devices

described in section 10.3 are reviewed in terms of the usual specifica-

tions placed upon electromagnetic microwave directional couplers — e.g.

coupling factors of 3.0 $\pm$0.15 dB or 20.0 $\pm$1.0 dB over the required

bandwidth.   The response curves of Figures 10.7, 10.9 and 10.11 imply

that the present crossbar coupler design can meet the latter specifica-

tion over a fractional bandwidth of only slightly more than 4%.   This

available bandwidth could be increased by using a mass-loading region

of graded periodicity, but this necessitates that careful attention be

paid to the overall device geometry to avoid frequency dispersion —

e.g. "chirped" IDTs of tapered periodicity (142), (143) could be employed

to off-set the frequency dispersion introduced by the non-uniform

spacing of the mass-loading elements.

A most interesting recent development is the acoustic surface

wave multi-strip coupler, (MSC), designed and tested by Marshall and

Paige (121), (136) - (140).   The structure of the MSC is shown in

Figure 11.2; its coupling interaction results from an array of thin

parallel metallic strips deposited on a strongly piezoelectric substrate.

A surface acoustic wave, with wave vector normal to the strips, is

launched into one half of the device, (along track A for example), and

establishes, through the electroacoustic fields which accompany the

wave motion, an alternating potential between adjacent metal strips.

These potentials must also appear in track B, where they excite a new

surface wave.   Power fed into one track thus couples periodically

back and forth between the two tracks as the wave travels along the

substrate.   The MSC operates over an extremely broad fractional band-

Piezoelectric Substrate.

IDT 1   Track A

IDT 2

IDT 4   Track B

IDT 3

MSC

(multi-strip-coupler)
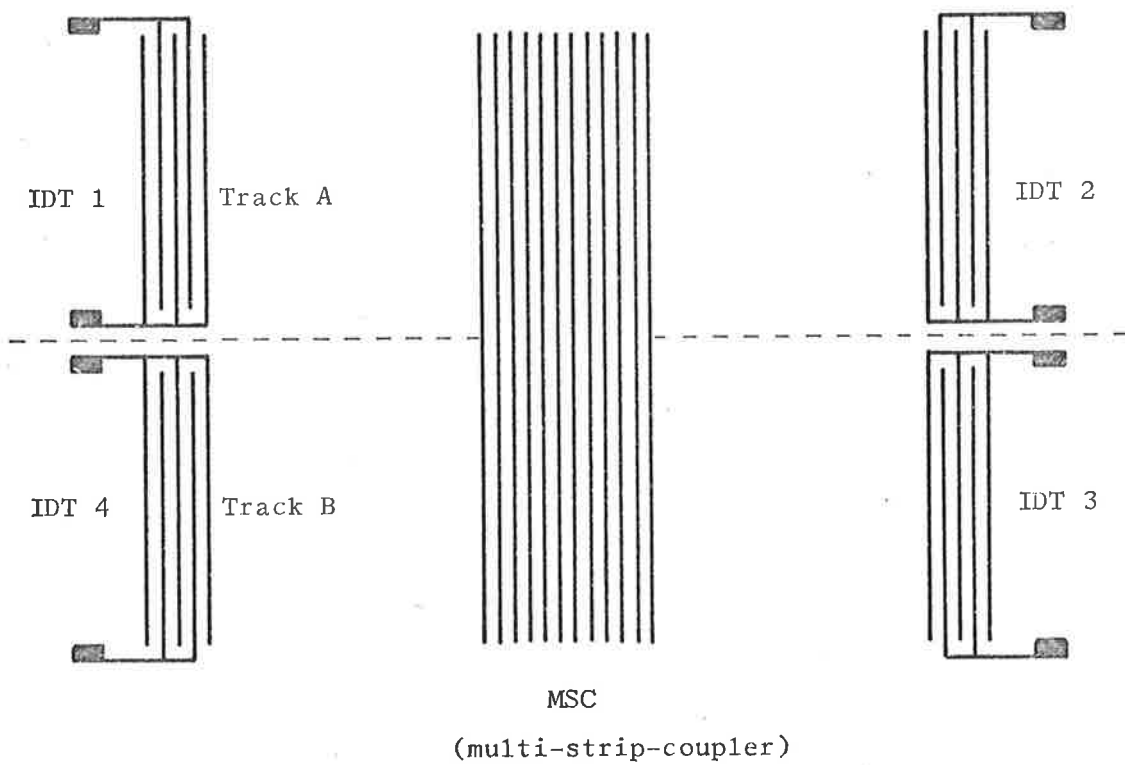
Figure 11.2.

Schematic diagram of the multi-strip directional coupler (MSC) with

IDTs at input and output ports.

[After Marshall & Paige (136)]

width of between 100% and 120%. Strip widths can be selected to be of a comparable dimension to that of the IDT electrodes, so that no more stringent resolution requirements are demanded of the photolithographic processes. A fundamental limitation of this device is that it must be fabricated on a strongly piezoelectric medium. The coupling length of the MSC is inversely proportional to the electromechanical coupling constant of the substrate material (136); the most optimistic calculation determines a coupling length of 20 surface wavelengths on strongly piezoelectric YZ lithium niobate (67), (71), which is pleasingly short, but the corresponding length on weakly piezoelectric YX quartz (67), (71), (78) is greater than 500 surface wavelengths.

Hence the MSC performs efficiently only on single crystal cuts, such as YZ lithium niobate, and polycrystalline ceramics which possess high electroacoustic coupling; the former materials are generally quite expensive, (at least one order of magnitude more costly than quartz), while the latter are limited by acoustic propagation loss to frequencies of approximately 50 MHz or less (144). Obviously the advantage which the crossbar coupler offers over this device is that the periodic mass-loading coupling mechanism does not place any special demands upon the properties of the substrate; in practice, as in the present research programme, a weakly piezoelectric single crystal material, e.g. quartz, proves convenient from the viewpoints of low cost and surface wave excitation using IDTs. However the microsonic crossbar coupler cannot approach the wide bandwidths available with the MSC. The two coupler designs share the desirable features that coupling can be obtained through an interaction which is independent of external circuit elements,

that the surface wave signals are in the form of broad uniform beams
and that the components are fabricated by the same photolithographic
processes used to form IDTs; all of these qualities are required of
devices which are to be compatible with existing surface acoustic wave
technology (134).   Following sections show that the MSC and the cross-
bar coupler share, in addition, a diversity of other possible applica-
tions.

Sections 2.32 and 10.8 note that the coherent scattering of surface
acoustic waves can be observed with coupling mechanisms other than that
supplied by periodically mass-loading the surface (23), (59), (71),
(108), (110), (145).   Of these, the most attractive and potentially
most useful interaction is provided by a periodic array of thin metal
fingers deposited upon a piezoelectric propagation surface (23).
Since the phase velocity of a surface acoustic wave decreases as it
enters a metal-plated area of the substrate from an uncoated region (25),
(141), partial reflection of an incident wave occurs at such a junc-
tion (108), (110), (114), (146).   In a given situation, where the
materials of the substrate and the overlay are specified, the coupled
to incident surface wave amplitude ratio in the surface mass-loading
crossbar coupler is determined primarily by two factors (refer section
9.33);

       1.   the number, N, of elements in the interaction grid,

  and   2.   the thickness of the mass-loading film.

This behaviour may be contrasted with that of a coupler exploiting the
"piezoelectric stiffness" scattering mechanism described above (23);
the latter type of device has a bandwidth inversely proportional to N,
and a coupling factor proportional to N, where N is the number of thin

conducting strips in the scattering area. The crossbar coupler design

based upon a periodic surface mass-loading interaction has a greater

flexibility introduced by the selection of the parameter 2 above, and

affords, within limits imposed mainly by fabrication problems and the

range of validity of theoretical performance predictions calculated by

perturbation analyses, independent control of strength of coupling and

bandwidth.

11.2 Launching Surface Acoustic Waves Along Paths of Low or Zero

Acoustoelectric Coupling.

One experimental method for characterising surface acoustic wave

motion on an insulating medium requires the deposition of a narrow

conducting stripe onto the surface, normal to the direction of pro-

pagation. The surface motion is measured by recording the electro-

motive force generated across this metal stripe in the presence of

a static magnetic field (147), (148). Components of the surface wave

particle displacements perpendicular to the stripe can be resolved in

both magnitude and phase by rotating the applied magnetic field about

the axis of the stripe. But when the substrate is piezoelectric a

voltage, (of the same frequency as that generated by the effect described

above), is detected across the stripe in the absence of a magnetic

field; this voltage is due to the electroacoustic fields which accompany

the propagating surface wave. Although compensation for this electro-

acoustically induced e.m.f. can be made in experiments to explore the

free surface particle displacements of a surface acoustic wave (148),

in related device applications (149) of this measurement phenomenon it

is advantageous if the excitation of this unwanted field can be avoided.

An obvious solution is to use a non-piezoelectric substrate, but

the problem of transduction arises. The hybrid transducer (150) - (155), four configurations of which are illustrated in Figure 11.3, is one method whereby surface acoustic waves can be launched onto a piezo-electrically inert substrate. Coupling to the wave is achieved through a conventional IDT and a thin piezoelectric film deposited on the sub-strate surface. Experimentally measured two-way electroacoustic con-version losses as low as 12 dB, obtained with ZnO overlays on fused silica (153) and on isopaustic glass (152) at frequencies as high as 90 MHz, are reported in the litterature. The price which must be paid for this convenience of launching surface waves onto non-piezo-electrics with IDTs, is a more complex fabrication procedure, which requires the deposition of thin piezoelectric films. Further problems associated with these transducers are frequency dispersion, if the over-lay extends over the whole propagation path, or acoustic reflections, if the piezoelectric film is placed only in the vicinity of the trans-ducers.

Figure 11.4(a) shows an alternative scheme which allows surface waves to be excited in non-piezoelectric media; this method relies upon the scattering, into the surface mode, of a volume acoustic wave incident upon a periodically roughened surface (60), (62), (63). Because the surface perturbation must have a periodicity of the order of one surface wavelength, the scheme imposes comparatively stringent requirements upon the procedures needed to etch or to machine grooves of specified width, depth and shape. A more convenient technique, requiring a structure which can be fabricated by conventional photo-lithographic processes, is sketched in Figure 11.4(b) and depends upon the scattering, into a surface wave, of a volume acoustic wave incident
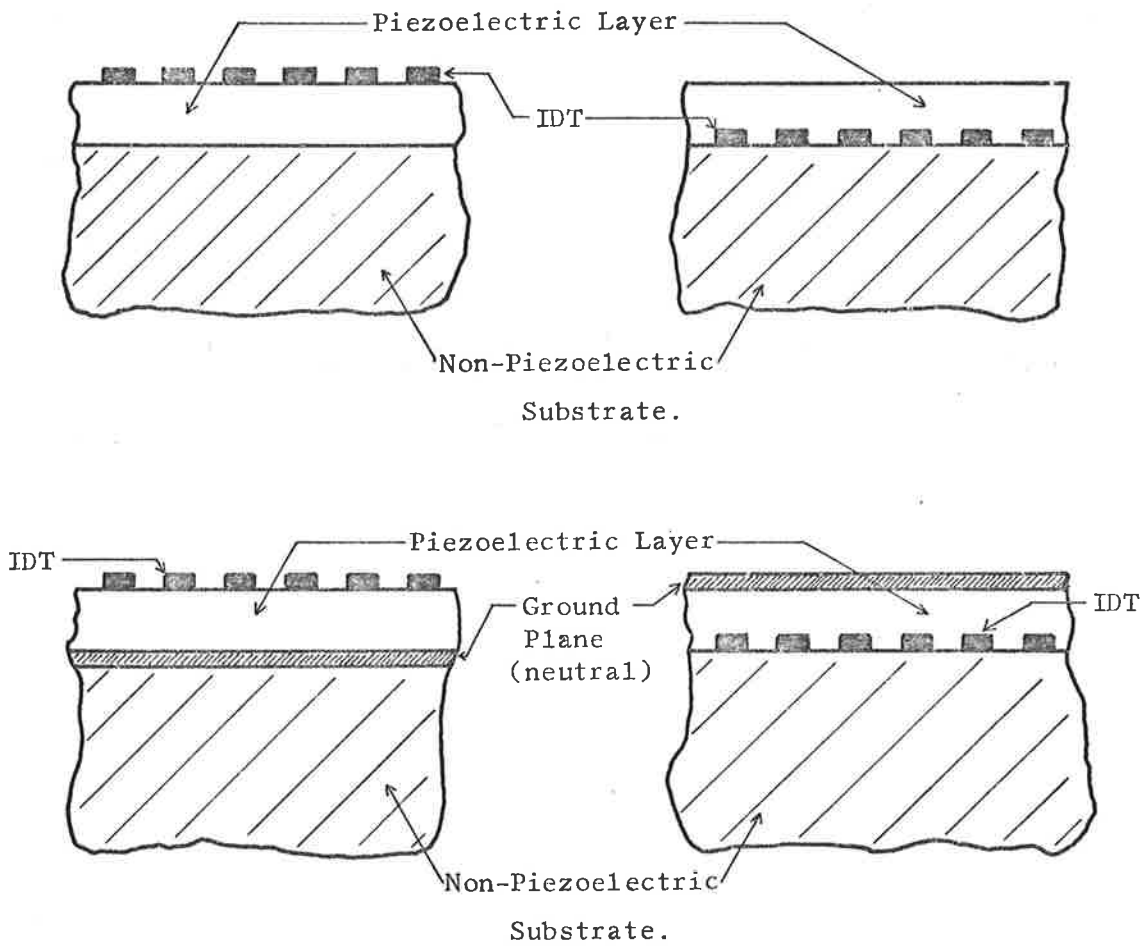
Figure 11.3

Four hybrid transducer configurations for generating surface acoustic
waves on non-piezoelectric substrates using IDTs.

[after Smith (154)]
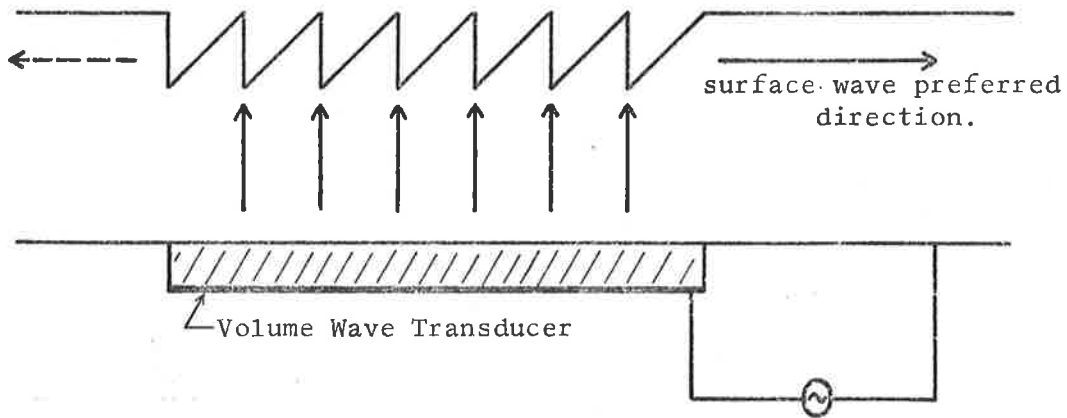
(a) By volume wave scattering at a region of
periodic surface roughness.
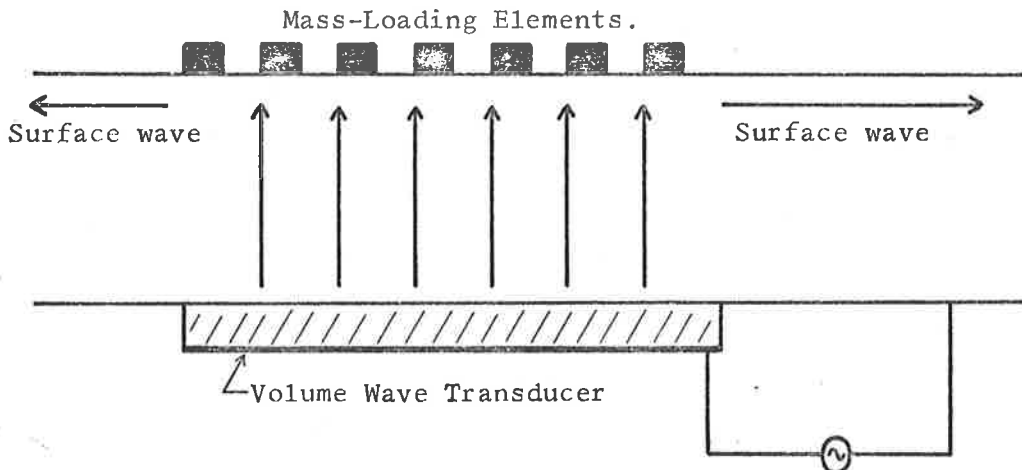
(b) By volume wave scattering at a region of
periodic surface mass loading.

Figure 11.4

Surface acoustic wave excitation in non-piezoelectric media through
mode conversion.

[(a) after Humphryes and Ash (62)]

upon a region of periodic mass-loading applied to the substrate surface. The performance of this transduction scheme is analysed by Bertoni (111), and can be calculated by the analytical steps described in Chapters VII, VIII and IX of this thesis.

A final method, which in some situations may provide the most attractive solution to the problem outlined at the beginning of this section, is illustrated in Figure 11.5. This approach, which exploits the elastic and electroacoustic anisotropy of a single crystal piezo-electric substrate, is discussed, by way of specific example, in terms of a Y cut quartz propagation surface. A surface wave is launched from an IDT aligned along the X crystal axis, which has one of the highest electroacoustic coupling factors available in a quartz crystal (refer Figure 3.4 and section 3.524). The region of heavy periodic surface mass-loading, which provides a perturbation wave vector of the desired magnitude and orientation, coherently scatters almost all of the incident acoustic energy through an angle of ninety degrees into a surface wave propagating along the Z crystal axis. (Note that in calculating the periodicity and orientation of the mass-loading grid needed to achieve this scattering, account must be taken of the differ-ent phase velocities of surface waves directed along the X and Z axes of the Y cut crystal — refer Figure 3.4).

Detailed analysis proves, as indicated by Figure 3.4(c), that there are no electroacoustic field components coupled to the surface wave motion whose wave vector lies along the Z crystal axis of a Y cut quartz substrate. Hence the arrangement of Figure 11.5 allows, in studies of the surface wave particle motion and in related microsonic device applications (149) of this "vibrated conducting stripe — static
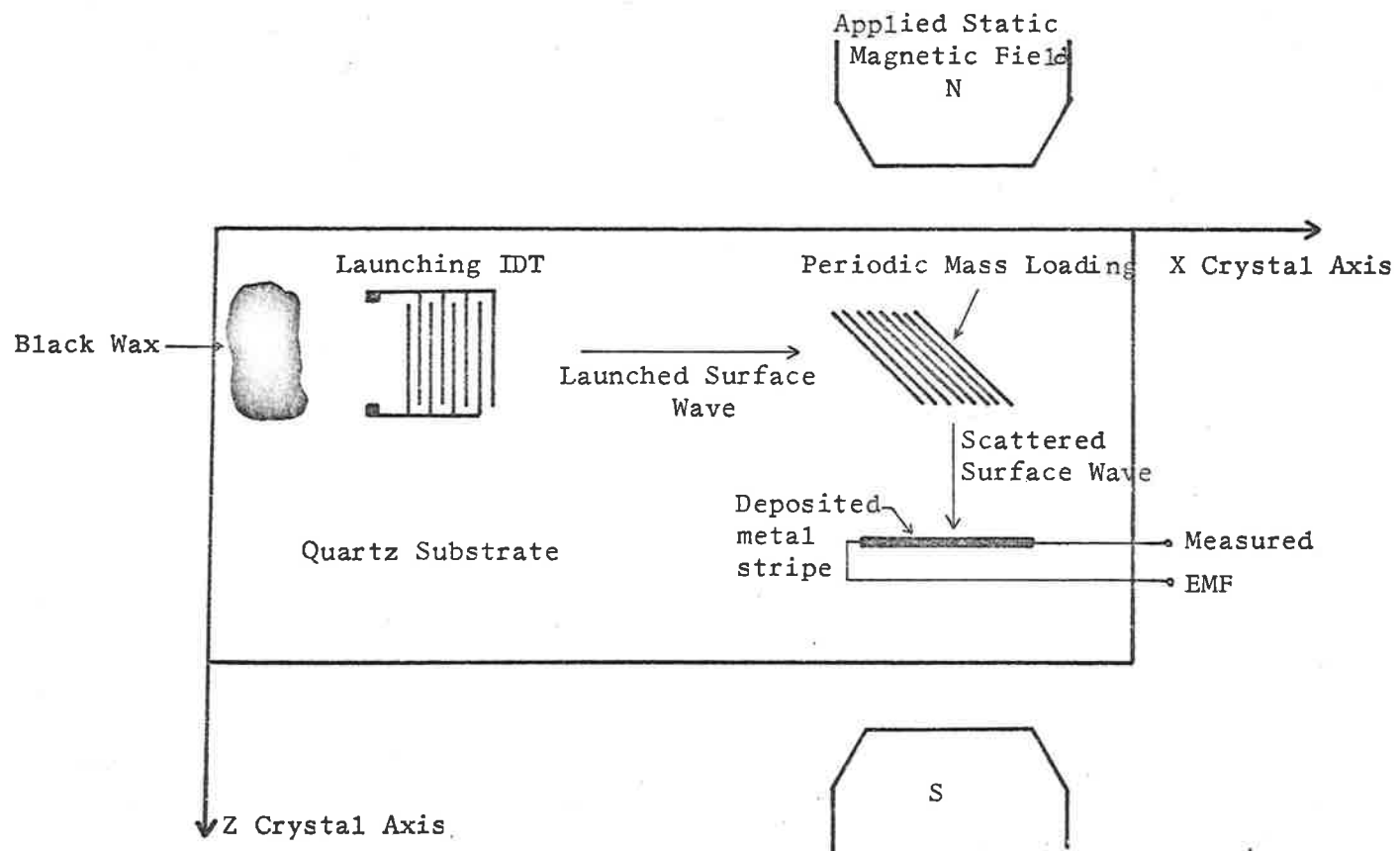
Figure 11.5

(Device application of) The characterisation of surface acoustic wave propagation using a static magnetic field.

"magnetic field" interaction, the measurement of generated e.m.f.s without the need of precompensation to account for the electroacoustic fields. This proposal requires the selection of a piezoelectric substrate which has, on a single plane surface, directions of both high and low electroacoustic coupling, these two path-types being separated by an angle sufficiently large to permit individual access to the launched and scattered beams. But fortunately quite a number of common piezoelectric single crystal cuts possess these properties (24), (25), (67) (78), (80). To off-set this restriction, the scheme offers a method for launching surface waves onto paths of low or zero electroacoustic coupling using a structure which can be fabricated entirely in the single photolithographic process required to form an IDT.

11.3 Surface Acoustic Wave Delay Line Taps.

The most commonly used tap in a surface acoustic wave delay line (28), (29), (156) is the simple uniform bidirectional IDT sketched in Figure 1.1. This transducer is analysed by Smith et al. (70), (71), whose results are replotted in Figure 4.2, on the basis of lossless three-port microwave junction theory. Two important sources of aberration in these tapped delay lines are acoustic reflections at the individual taps, and regeneration, the process whereby a signal received at one tap is reradiated by all other receiving transducers to which it is electrically connected in parallel. One solution to this problem is the development of tap patterns which contrive to produce cancellation of these unwanted signals. The design of "low-noise" tapped surface wave delay lines using this strategy can follow two courses. Carr (157) has shown experimentally that careful attention to the spacing of the interdigital electrodes within a tap can reduce

substantially the amplitudes of the reflected signals. A similar regard for the inter-tap spacings should allow significant cancellation of both reflected and regenerated waves.

An alternative approach, illustrated in Figure 11.6, employs weakly coupled periodic surface mass-loading bars as energy sampling elements. These grids, suitably angled to the delay line axis, scatter a small proportion of the incident surface wave energy towards a nearby receiving IDT. Being essentially a four-port structure, and therefore capable of lossless operation while matched in every port, the surface mass-loading grids offer one method of breaking the nexus between electromechanical conversion loss and acoustic reflection loss inherent in the simple bidirectional (three-port) IDT tap (70).

The lossless three-port analysis of Smith et al. (70) predicts zero acoustic reflection from a short-circuited IDT. As emphasised by Auld (108) and Skeie (110), this analysis neglects the reflection of an incident surface wave due to the presence, on the propagation surface, of the metal fingers which introduce periodic mass and "elastic stiffness" loading, and "short-circuiting" of the electroacoustic fields. All of these effects contribute to a velocity retardation and partial reflection of an incident surface wave. The discussion of section 10.8 indicates that the reflection coefficient at a single finger can be made quite small by operating on a weakly piezoelectric substrate and by etching the transducer from a thin overlay of a material whose acoustic impedance matches that of the substrate — e.g. aluminium has an acoustic impedance very similar to that of quartz (73), (144). But the quarter-wavelength electrode spacing of a
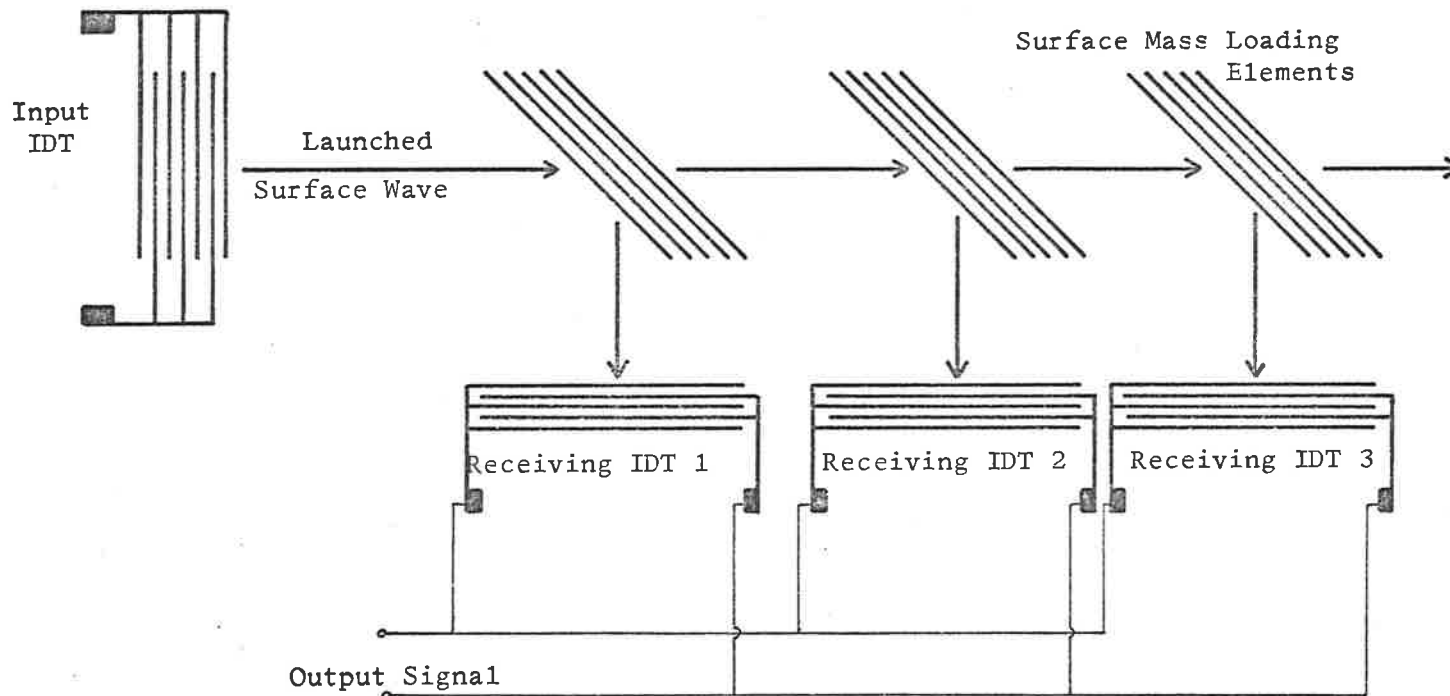
Figure 11.6

Surface acoustic wave delay line with tapping provided by periodic surface

mass-loading grids.

conventional IDT is such that a normally incident surface wave at the synchronous (centre) frequency satisfies the fundamental Bragg condition stated in equation (2.203). This means that the small amounts of acoustic energy reflected at each finger sum coherently. In devices employing transducers with many electrode pairs or in certain filter designs (as discussed briefly in the following section) requiring long interdigital electrode structures, a reflected surface wave of considerable amplitude can result.

In order to determine the deterioration of IDT performance or the aberrations in frequency response of an "apodized comb" surface wave filter (26) caused by this unwanted reflected signal, its amplitude must be calculated. When the dominant contribution to the reflected surface wave arises from the mass-loading effect of the fingers, as may be the case on a substrate possessing low piezoelectric coupling, the analytical expressions derived in Chapter IX can be used to calculate the reflected to incident wave amplitude ratio. On strongly piezoelectric materials, where the periodic "short-circuiting" of the electroacoustic fields by the conducting electrodes provides a comparable or greater contribution to the reflected wave amplitude than does the mass-loading interaction, computations must be based upon the more general results of Auld (108) and Skeie (110).

11.4 Surface Acoustic Wave Filters.

A realm in which commercial applications for surface acoustic wave devices seem certain to be realised is filter synthesis. Surface wave interdigital transducer structures afford a simple and convenient technique whereby a wide variety of frequency response characteristics including, for example, general band-pass filters (158) - (160), tele-

vision intermediate frequency band-pass filters (27), (134), (161),

(162) and matched filters for "chirped" radar signals (26), (34), (142)

or for coded pulse trains (28), (29), (34), (156), can be synthesised.

In these and similar applications the small surface acoustic wavelengths

ensure economy of occupied space, which in turn means small substrate

sizes and low cost.   Although the most general frequency response can,

theoretically, be synthesised by carefully designed apodized IDTs (26),

(163), (164), it may well be that certain types of response — e.g.

strong band absorption or band rejection — can be provided more effic-

iently by applying a prescribed roughness profile (55), (56), (59),

(60), (63) or mass-loading perturbation (165) to the propagation surface.

The behaviour of surface acoustic wave filters constructed using a

surface roughness interaction can be assessed from the one-dimensional

results plotted in Figures 2.1 and 2.2 (59), (60), (63).   At the

roughened surface an incident surface wave is scattered, over a selected

frequency range, into volume modes, which can be absorbed at some dis-

tance from the free surface.   Surface wave filters synthesised by the

addition, to the propagation surface, of a prescribed mass-loading dis-

tribution, whether the frequency selectivity be due to reflection of

an incident wave, or to scattering into volume modes, can be designed

to meet specified responses through the analytical techniques of Chap-

ters VI to IX.   Sittig and Coquin (165) have conducted preliminary

theoretical and experimental studies of a surface wave delay line which

achieves a linear frequency dispersion relation through the reflection

of an input wave at mass loading elements deposited at selected points

on the substrate surface.   But the possibility of developing surface

acoustic wave filters, with specified frequency responses of a more general form, using one of the aforementioned mechanisms which entail perturbing, by surface roughness or mass-loading, the propagation surface, remains to be explored.

11.5 Surface Acoustic Wave Reflectors.

The reflection of acoustic surface waves at periodic structures, which leads to spurious signals and a departure from ideal performance in IDTs, "apodized comb" filters and tapped delay lines, may be encouraged in other microsonic device applications (71), (119), (121), (166).

Until recently the two effective techniques by which a surface acoustic wave could be reflected with tolerable loss were from an IDT, inductively tuned to provide a high quality factor (71), when the substrate is moderately to strongly piezoelectric, or from a carefully machined slot or crystal edge (99) - (101), (167), (168); both of these methods yield strong reflection over only narrow bandwidths. The reflection of surface waves at single boundaries in layered media had also been observed (169), (170), but this approach did not offer any significant practical advantages. A new version of the multi-strip coupler tested by Marshall et al. (121), (138) proves a most convenient method for reflecting surface waves over broad bandwidths. But like the MSC, this component functions effectively only on substrate materials with high electroacoustic coupling constants.

That surface acoustic waves can be strongly reflected, over useful bandwidths, from regions of periodic surface mass-loading is demonstrated adequately by the experimental results plotted in Figure 10.16.

Such a reflector has many applications to microsonic component designs, the more significant of which are discussed below.

11.51 Unidirectional Surface Acoustic Wave Transducers.

Most unidirectional IDT designs require either a tuned interdigital array to redirect the backward-launched surface wave (71), or a bi-phase (119) or a tri-phase (120) driving circuit and/or an electrode pattern considerably more complex than the simple bidirectional array for their operation (70), (71), (119), (120); in these schemes unidirectional transduction is achieved usually at the price of a reduced bandwidth. The MSC reflector (121), (138) allows the design of a unidirectional transducer with a bandwidth only marginally less than that of a bidirectional array (70), (71) but which is suitable only for strongly piezoelectric substrates.

Figure 11.7(a) illustrates how a normal-incidence surface wave reflector, formed from a grid of surface mass-loading bars spaced at one quarter wavelength, can redirect the reverse-propagating wave launched from a bidirectional IDT to create a unidirectional transducer. In this role the mass-loading interaction offers an advantage over the commonly employed high Q interdigital transducer, in that it requires no external circuit elements, and over the MSC reflector, in that it is not limited to operation on materials exhibiting high electroacoustic coupling.

11.52 Long Surface Acoustic Wave Delay Lines.

At present four techniques are available for obtaining long signal delay times using surface acoustic waves propagating on a single substrate of finite dimensions. The first allows a wave to travel around

(a) Unidirectional Transducers

(c) Resonators

Output

IDT

Input IDT

(b) Folded delay line paths.

R_2 Input/Output R_1 R_3

Input pulse
time

Output pulse
train
time

(d) One-port network identification
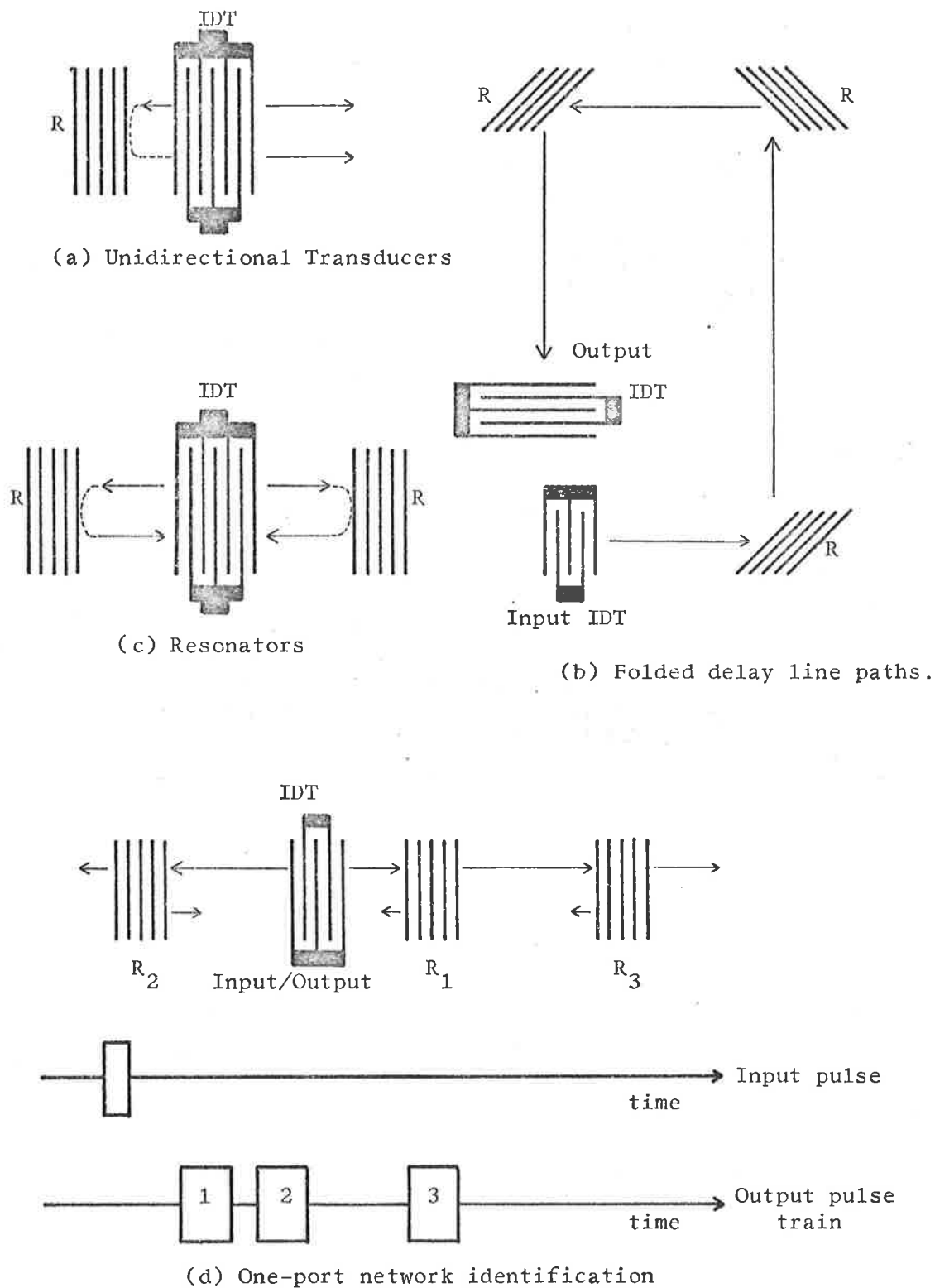
Figure 11.7

Device applications for surface acoustic wave reflectors formed
from periodic surface mass-loading grids (marked R in above diagrams)

the perimeter surface of a suitably shaped single crystal (31) - (33)
(the single crystal material being necessary to provide low acoustic
propagation loss). Problems associated with this arrangement include
the continually changing effects of anisotropy on the propagating wave
as it travels around the curved ends of the crystal, the stringent
requirements of machining the block profile to avoid end reflections,
and the fact that this structure does not adhere to the concept of a
planar surface wave device technology. A second method employs a
coiled surface wave thin film strip guide (30), (48) - (50); prototypes,
fabricated from a thin gold overlay deposited upon a fused quartz sub-
strate, have been tested in the 10-20 MHz frequency range (30).
Although difficulties with spurious signal interference and high pro-
pagation loss did not arise in these low frequency experiments, there
is no guarantee that they, coupled with frequency dispersion, will not
introduce serious design problems at higher frequencies.

The third approach depends upon multiple reflections of the launched
surface wave at the edges of the crystal or from slots formed in the
propagation surface (99) - (101), (166) - (168). Here the primary
limitations are the demands placed upon machining or etching of the
single crystal material, and the fact that operation must be restricted
to a narrow bandwidth to avoid losses due to mode conversion or to the
propagation of the incident wave around the crystal edge or slot (167).
A fourth technique is offered by the "reflecting track-changer" studied
recently by Marshall (138). This device combines the properties of
the MSC and its associated reflector to enable the reflection of an
incident surface wave onto a path adjacent to the input path. The

disadvantages of the "track-changer" are that it occupies a compara-
tively large length of the propagation path and, in common with other
members of this family of devices (121), (136) - (140), it requires a
substrate with a large electromechanical coupling constant for practical
implementation.   A further undesirable feature of this design is that
the experimentally recorded loss of approximately 2-3 dB (138) (over
a 50% bandwidth centred on 80 MHz) for each change of track is quite
high when long delay lines, involving several such manoeuvres, are
sought.

Figure 11.7(b) shows how periodic surface mass-loading grids might
be used to reflect an incident surface acoustic wave and thus to fold
a delay line path so that full advantage can be taken of the available
substrate surface area.   The experimental results presented in Figure
10.16 indicate a loss of only 0.43 dB, but this value has been calcul-
ated from the practical measurements in a manner which assumes a loss-
less coupling mechanism.   It may be that the acoustic losses, due to
scattering of the incident surface wave into volume modes, which the
results of section 10.3 demonstrate are small for weak coupling situa-
tions, become more significant for interactions at regions of very
heavy periodic surface mass-loading; this would increase the calculated
loss of 0.43 dB per reflection.   The most serious disadvantage of the
system sketched in Figure 11.7(b), is that for signals in the form of
carrier frequency pulses, the pulse is lengthened by (N - 1) cycles
on reflection from an N-element grid (refer section 10.4).   This
unwanted property, which is shared by the MSC "track-changer", places
an upper limit upon the bit-rate which can be achieved in a given

situation — i.e. for a specified carrier frequency pulse length, number of reflections and number of mass-loading bars in each reflector.

11.53 Surface Acoustic Wave Resonators.

Because steps towards the development of high efficiency surface wave reflectors, independent of external circuit elements, have been reported only recently (112), (121), (126), the few surface wave resonator designs which have been proposed (32), (33), (52) depart from the usual concept of a "cavity" defined by two end reflectors. Knox and van den Heuvel (52) describe experimental measurements made with a thin film "ring guide" resonator, which operates in a similar fashion to the separated double guide coupler (49), (51) illustrated in Figure 11.1(a). Energy is coupled from a main surface acoustic waveguide into an adjacent closed-loop guide at those frequencies for which the circumference of the latter is an integral number of surface wavelengths. An unattractive feature of this design is that the ring guide must be many (e.g., ninety) wavelengths long to ensure a sufficiently large radius of curvature and hence low-loss propagation. In addition it poses the problem, noted earlier in relation to the thin film strip guide directional couplers, that if IDTs are to be used for transduction, an effective means of focussing the broad launched acoustic beam onto the narrow guiding structure must be found. Recirculating surface wave delay lines, of the type in which the signal propagates around the perimeter surface of a specially shaped crystal (32), (33), provide an alternative technique for resonator fabrication. But in this role the three disadvantages, listed in section 11.52, which limit their appeal in the development of long delay lines still

apply.

Figure 11.7(c) shows how two surface wave reflectors, which may be of a periodic mass-loading or an MSC style (121), can be arranged to form a resonator. Once more the mass-loading grid offers the advantage that it operates on a wider variety of substrate materials.

11.54 Position Encoding in a One-Port Surface Acoustic Wave Device.

A multi-tap surface acoustic wave delay line, (the taps being identical bidirectional IDTs), in which all taps, including the array which launches the input wave in a conventional tapped delay line (28), (29), (156), are connected in parallel forms a one-port network (171). When excited by a carrier frequency pulse of short duration this device responds, a few microseconds later, by inducing a voltage pulse train across the source resistance. The position, in time, of each reply pulse is determined by the relative spatial location of the transducers in the one-port delay line; detection of the response pulse train provides an unambiguous method for identifying the activated line. In practice the "basic" reply pulse train is complicated by unwanted signals resulting from the processes of acoustic reflection and regeneration which occur, as discussed in section 11.3, at each bidirectional IDT tap.

An alternative design for such a one-port surface wave device is sketched in Figure 11.7(d), which shows that input/output access is obtained through a bidirectional IDT, and the reply sequence is generated by partial reflection of the launched wave from suitably placed regions of periodic surface mass-loading. Secondary reflections are the major source of spurious pulses in this structure, but these are

fewer in number than the aberrations encountered in the one-port tapped
delay line described above; this improved behaviour can be expected
because there is no effect analagous to "regeneration" with surface
mass-loading taps.

11.6 Summary and Conclusions.

This thesis has been concerned principally with a theoretical
and experimental study of some important aspects of the behaviour of
a surface acoustic wave incident upon a region of periodic surface
mass-loading deposited upon the propagation surface. In particular
attention has been focussed upon that range of frequencies for which
the wave vector of the incident signal and of the surface perturbation
satisfy, or nearly satisfy, the first order Bragg relation; under these
conditions a strong interaction occurs, and a surface acoustic wave of
large amplitude is coherently scattered from the perturbed area of the
substrate surface. But in investigating this topic, contributions to
several other facets of surface wave technology have been made.

The results plotted in Figures 2.1 and 2.2 provide, for the first
time (60), (63), theoretical verification of previously published
experimental measurements (59) of surface wave attenuation, due to
scattering into volume modes, at a periodically roughened surface.
An analysis of surface acoustic wave propagation in anisotropic and
piezoelectric single crystals, as presented in Chapter III, has allowed
two computer programmes, of widespread utility, to be developed.
Program "Anisom" is able to compute numerical data which completely
characterises surface wave motion in any direction on a surface of any
orientation cut from any non- (or weakly-) piezoelectric single crystal

material; program "Pianm" returns similar information describing sur-
face wave propagation on the paths of a piezoelectric single crystal
medium. These computer programs are of considerable value in assessing
the utility of a substrate for a particular microsonic device applica-
tion. The analytical curves of Figure 3.5, plotted from data output
by "Anisom" and "Pianm" summarise the properties of surface acoustic
waves propagating on an AT cut quartz crystal. This particular cut,
which has been widely employed in volume mode oscillators and trans-
ducers (89), has been overlooked generally in surface wave studies
until now. Analysis, and the experimental results contained in sec-
tion 4.4 which provide partial confirmation of the theoretically cal-
culated behaviour, disclose that the AT cut crystal offers some
attractive features, with regard to surface wave component design, not
found in other cuts of quartz more frequently used in microsonic devices
(24), (67).

These properties of AT cut quartz have been exploited, in Chapter
V, to design a surface acoustic wave crossbar directional coupler, in
which the coupling mechanism is obtained by periodically mass-loading
the substrate surface. Methods of electromagnetic microwave analysis
and their application to electroacoustic propagation structures have
received considerable attention in the litterature (106) - (114). But
it is hoped that the presentation of this topic in Chapter VI has
contributed to an improved understanding by placing the work of other
authors (106) - (111), (114) in perspective with each other and with
the approach of the current investigation (112), (113). The following
chapter has adapted these analytical techniques, derived in the context
of an electroacoustic waveguide, to a study of a surface situation.

A novel viewpoint, developed jointly at an earlier stage of the research programme (112), (113), invokes quantum mechanical and scattering matrix concepts to simplify calculations of the coupled wave amplitudes launched by the interaction of a surface acoustic wave and the mass loading perturbation upon which it is incident.

Chapters IX and X have described detailed original investigations, both theoretical and experimental, of the surface acoustic wave cross-bar directional coupler. A comparison of the two sets of results has indicated close agreement between the behaviour of the coupler as predicted from an analytical model, and as measured in practice. Consideration has been given, in the final chapter, to the many potential surface acoustic wave device applications of the periodic surface mass-loading interaction. The discussion, which has compared the projected device performance with that of existing designs, has included surface wave directional couplers, delay line taps, filters, and reflectors; it has been noted that the latter lead to new techniques for fabricating unidirectional transducers, folded delay line paths, resonators and one-port networks, and to a method whereby surface waves of large amplitude can be steered into paths of low electroacoustic coupling.

It is felt that this work represents a significant step towards the realization of an integrated surface acoustic wave technology, principally because it demonstrates a technique for signal processing operations, such as coupling, power splitting and filtering, which can be implemented by means of suitably designed thin film overlay structures deposited upon piezoelectric or non-piezoelectric materials. In this way these functions can be performed by microsonic devices whose con-

struction requires only the normal photolithographic procedures used in IDT fabrication, and in no case does the interaction mechanism need external circuit elements.

APPENDIX I.

COMPUTER PROGRAM "ANISOM"

<u>Contents of Appendix.</u>

Introduction

    "Anisom" is a general purpose computer program developed to analyse

surface acoustic wave propagation on any non- (or weakly-) piezo-

electric single crystal surface. The program, which neglects piezo-

electricity, can characterise the wave motion in any direction on a

surface of any orientation cut from a crystal belonging to any elastic

symmetry class. Typical data outputs are illustrated in later pages

of this appendix by focussing attention upon the particular case of a

surface wave propagating at $\pm34^\circ$ to the X crystal axis on AT cut quartz.

The (X,Y,Z) coordinate system referred to in these print-outs is the

propagation coordinate system, (i.e. <u>not</u> the crystal axes), which is

chosen so that the wave travels in the X direction on the surface

Y = 0, and the medium occupies the region Y > 0. Hence the particle

displacement amplitude coefficients, (refer section 3.22, equation

(3.224)), are listed in the order $C_x^{(1)}$, $C_x^{(2)}$, $C_x^{(3)}$, $C_y^{(1)}$,--------

$C_z^{(3)}$. Only the output format has been changed from the listing of

"Anisom" supplied previously (79).

Flow Chart of Program Anisom.

Insert elastic constants of material.

↓

Transform elastic constants from crystal axes coordinate system to propagation coordinate system.

↓

Select a trial value of surface wave phase velocity.

↓

Set up, via the equations of motion, the sixth order polynomial in the decay constants, $\alpha^{(j)}$.

↓

Solve the polynomial for $\alpha^{(j)}$, j=1,2, ---6.

↓

Test if three $\alpha^{(j)}$ have positive real parts.

Yes ↓

Select three $\alpha^{(j)}$ with positive real parts and determine, from equations of motion, the amplitude ratios, $\beta_i^{(j)}$, corresponding to each $\alpha^{(j)}$.

↓

Calculate the value of the boundary condition determinant.

↓

Test if this value is zero.

Yes ↓

Have correct velocity. Calculate amplitude coefficients, $B^{(j)}$, and hence the $C_i^{(j)}$ from boundary condition equations.

↓

Calculate components of power flow.

↓

Calculate misalignment angle between wave and power flow vectors.

↓

End

Select new trial value of surface wave phase velocity

No

No

PROGRAM ANISOM-RESULTS FOR FREE AT CUT QUARTZ SURFACE

ANGLE BETWEEN WAVE VECTOR AND X CRYSTAL AXIS= 34DEGREES

SURFACE WAVE PHASE VELOCITY= 3251.0M/SEC.

SURFACE WAVE DECAY CONSTANTS

	REAL	IMAG
J=1	1.235E-01	-2.620E-02
J=2	4.750E-01	-1.138E-01
J=3	1.670E+00	-5.821E-02

PARTICLE DISPLACEMENT AMPLITUDE COEFFICIENTS

X COMPONENT

J=1	1.000E+00	0.
J=2	-6.432E-01	2.967E-02
J=3	-2.852E+00	-6.232E+00

Y COMPONENT

J=1	1.097E+01	-5.846E+00
J=2	3.769E-01	2.494E-01
J=3	-6.332E-01	4.362E-01

Z COMPONENT

J=1	-6.016E+00	2.519E+00
J=2	3.630E+00	4.799E-01
J=3	-3.541E-01	-3.001E-02

FREE SURFACE PARTICLE DISPLACEMENT AMPLITUDES

X COMPONENT =-2.496E+00   -6.202E+00
Y COMPONENT = 1.072E+01   -5.160E+00
Z COMPONENT =-2.739E+00   2.969E+00

FREE SURFACE PARTICLE DISPLACEMENT AMPLITUDES
                ABSOLUTE VALUES
X COMPONENT = 6.685E+00
Y COMPONENT = 1.190E+01
Z COMPONENT = 4.040E+00

COMPLEX POWER FLOW COMPONENTS
LONGITUDINAL= 2.137E+13   -2.068E+11
   TRANSVERSE= 4.811E+09   -3.400E+11

MISALIGNMENT ANGLE=   .0129DEGREES

PROGRAM ANISOM-RESULTS FOR FREE AT CUT QUARTZ SURFACE

PROGRAM MODIFIED TO EXAMINE THE REVERSE PROPAGATING WAVE

ANGLE BETWEEN WAVE VECTOR AND X CRYSTAL AXIS= 34DEGREES

SURFACE WAVE PHASE VELOCITY= 3251.0M/SEC.

SURFACE WAVE DECAY CONSTANTS

	REAL	IMAG
J=1	1.235E-01	2.620E-02
J=2	4.750E-01	1.138E-01
J=3	1.670E+00	5.821E-02

PARTICLE DISPLACEMENT AMPLITUDE COEFFICIENTS

X COMPONENT

J=1	1.000E+00	0.
J=2	-6.432E-01	-2.967E-02
J=3	-2.852E+00	6.232E+00

Y COMPONENT

J=1	1.097E+01	5.846E+00
J=2	3.769E-01	-2.494E-01
J=3	-6.332E-01	-4.362E-01

Z COMPONENT

J=1	-6.016E+00	-2.519E+00
J=2	3.630E+00	-4.799E-01
J=3	-3.541E-01	3.001E-02

FREE SURFACE PARTICLE DISPLACEMENT AMPLITUDES
X COMPONENT =-2.496E+00   6.202E+00
Y COMPONENT = 1.072E+01   5.160E+00
Z COMPONENT =-2.739E+00 -2.969E+00

FREE SURFACE PARTICLE DISPLACEMENT AMPLITUDES
            ABSOLUTE VALUES
X COMPONENT = 6.685E+00
Y COMPONENT = 1.190E+01
Z COMPONENT = 4.040E+00

COMPLEX POWER FLOW COMPONENTS
LONGITUDINAL= 2.137E+13   2.068E+11
   TRANSVERSE= 4.811E+09   3.400E+11

MISALIGNMENT ANGLE=   .0129DEGREES

PROGRAM ANISOM-RESULTS FOR FREE AT CUT QUARTZ SURFACE

ANGLE BETWEEN WAVE VECTOR AND X CRYSTAL AXIS=-34DEGREES

SURFACE WAVE PHASE VELOCITY= 3251.0M/SEC.

SURFACE WAVE DECAY CONSTANTS

	REAL	IMAG
J=1	1.235E-01	2.620E-02
J=2	4.750E-01	1.138E-01
J=3	1.670E+00	5.821E-02

PARTICLE DISPLACEMENT AMPLITUDE COEFFICIENTS

X COMPONENT

J=1	1.000E+00	0.
J=2	-6.432E-01	-2.967E-02
J=3	-2.852E+00	6.232E+00

Y COMPONENT

J=1	-1.097E+01	-5.846E+00
J=2	-3.769E-01	2.494E-01
J=3	6.332E-01	4.362E-01

Z COMPONENT

J=1	6.016E+00	2.519E+00
J=2	-3.630E+00	4.799E-01
J=3	3.541E-01	-3.001E-02

FREE SURFACE PARTICLE DISPLACEMENT AMPLITUDES

X COMPONENT =-2.496E+00   6.202E+00
Y COMPONENT =-1.072E+01   -5.160E+00
Z COMPONENT = 2.739E+00   2.969E+00

FREE SURFACE PARTICLE DISPLACEMENT AMPLITUDES
                ABSOLUTE VALUES
X COMPONENT = 6.685E+00
Y COMPONENT = 1.190E+01
Z COMPONENT = 4.040E+00

COMPLEX POWER FLOW COMPONENTS
LONGITUDINAL= 2.137E+13   2.068E+11
   TRANSVERSE=-4.811E+09   -3.400E+11

MISALIGNMENT ANGLE= -.0129DEGREES

APPENDIX II

COMPUTER PROGRAM "PIANM"

Contents of Appendix
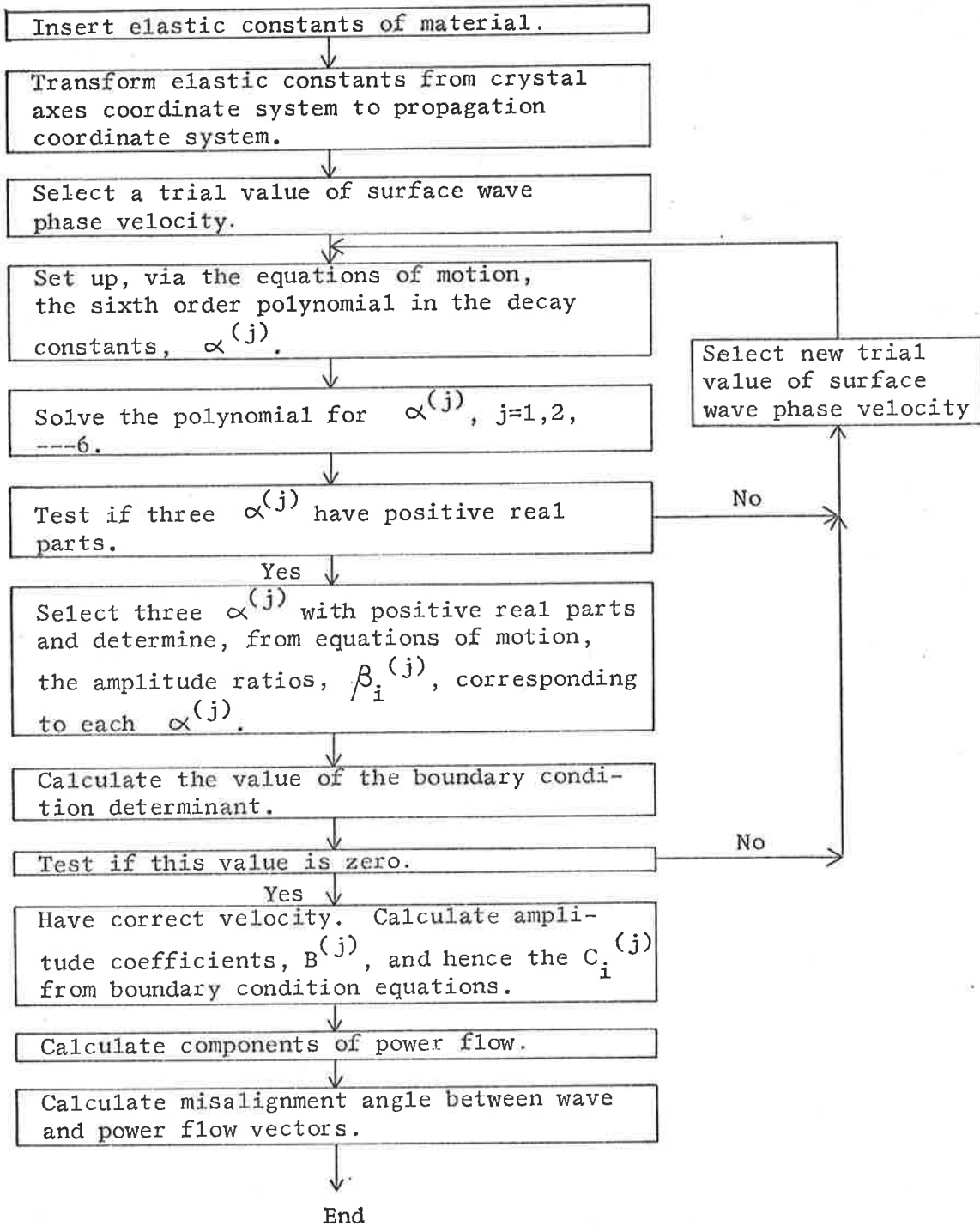
Introduction.

"Pianm" is a general purpose computer program developed to analyse surface acoustic wave propagation on any piezoelectric single crystal surface. This program, which takes account of the piezoelectric and dielectric properties of the medium, can characterise the wave motion in any direction on a surface of any orientation cut from a crystal belonging to any elastic symmetry class. Typical data outputs are illustrated in later pages of this appendix by using "Pianm" to examine a surface wave travelling at $+34^{o}$ to the X crystal axis on AT cut quartz; the wave vector has a positively directed component resolved parallel to the X crystal axis. Section 3.4 and the original program listing (79) indicate the minor modification which must be made to the computational procedure to allow "Pianm" to analyse propagation on the "ideally metallised" piezoelectric surface. Details of surface wave motion on both the "free" and the "coated" surface, in the above situation, are provided in this appendix. The coordinate and amplitude coefficient notation is as established in Appendix I, except that in this piezoelectric analysis four decay constants, $\alpha^{(j)}$, and four amplitude coefficients, $C_i^{(j)}$, are found for each component of the particle displacements; in addition there are four coefficients, $C_4^{(j)}$, which describe the scalar electric potential, ψ (equation 3.323). The only changes in the version of "Pianm" which produced the outputs on the following pages and that for which listings have been presented previously (79) are that the computational procedures have been extended, in the style of "Anisom", to calculate the misalignment angle between the wave and power flow vectors and the output format has been improved.

Flow Chart of Program Pianm

Insert elastic, piezoelectric and
dielectric constants of material.

Transform elastic, piezoelectric,
and dielectric constants from
crystal axes coordinate system to
propagation coordinate system.

Select a trial value of surface
wave phase velocity.

Set up, via the equations of motion,
the eighth order polynomial in the
decay constants, $\alpha^{(j)}$.

Solve the polynomial for $\alpha^{(j)}$,
j=1,2,--------8.

Test if four $\alpha^{(j)}$ have positive
real parts.

Yes

Select four $\alpha^{(j)}$ with positive
real parts and determine, from
equations of motion, the amplitude
ratios, $\beta_i^{(j)}$, corresponding to
each $\alpha^{(j)}$.

Calculate the value of the boundary
condition determinant.

Test if this value is zero.

Yes

Have correct velocity. Calculate
amplitude coefficients, $B^{(j)}$, and
hence the $C_i^{(j)}$ from boundary
condition equations.

Calculate components of power flow.

Calculate misalignment angle between
wave and power flow vectors.

Select new trial
value of surface
wave phase velocity.

No

No

End

PROGRAM PIANM-RESULTS FOR FREE AT CUT QUARTZ SURFACE

ANGLE BETWEEN WAVE VECTOR AND X CRYSTAL AXIS= 34DEGREES

SURFACE WAVE PHASE VELOCITY= 3264.4M/SEC.

SURFACE WAVE DECAY CONSTANTS

	REAL	IMAG
J=1	1.245E-01	-2.021E-02
J=2	4.788E-01	-1.163E-01
J=3	9.885E-01	-2.871E-02
J=4	1.667E+00	-3.657E-02

PARTICLE DISPLACEMENT AMPLITUDE COEFFICIENTS

X COMPONENT

J=1	1.000E+00	0.
J=2	-6.172E-01	5.373E-02
J=3	1.848E-01	-9.458E-02
J=4	-3.679E+00	-6.647E+00

Y COMPONENT

J=1	1.182E+01	-6.775E+00
J=2	3.455E-01	1.523E-01
J=3	2.317E-03	-1.566E-01
J=4	-6.639E-01	5.925E-01

Z COMPONENT

J=1	-6.131E+00	2.934E+00
J=2	3.600E+00	2.289E-01
J=3	3.424E-01	1.463E-01
J=4	-5.196E-01	-5.953E-02

ELECTRIC POTENTIAL

J=1	4.074E+10	-1.001E+10
J=2	-1.263E+10	1.199E+09
J=3	-5.653E+10	-2.946E+10
J=4	4.114E+10	1.393E+10

FREE SURFACE PARTICLE DISPLACEMENT AMPLITUDES
X COMPONENT =-3.111E+00 -6.688E+00
Y COMPONENT = 1.150E+01 -6.187E+00
Z COMPONENT =-2.709E+00   3.250E+00
ELECTRIC POT= 1.272E+10 -2.434E+10

PARTICLE DISPLACEMENT AMPLITUDES AT SURFACE
ABSOLUTE VALUES
X COMPONENT = 7.376E+00
Y COMPONENT = 1.306E+01
Z COMPONENT = 4.231E+00
ELECTRIC POT= 2.747E+10

COMPLEX POWER FLOW COMPONENTS
LONGITUDINAL= 2.530E+13   -2.232E+11
   TRANSVERSE= 1.855E+11   -4.230E+11

MISALIGNMENT ANGLE=   .4201DEGREES

PROGRAM PIANM-RESULTS FOR IDEALLY METALLISED
             AT CUT QUARTZ SURFACE

ANGLE BETWEEN WAVE VECTOR AND X CRYSTAL AXIS= 34DEGREES

SURFACE WAVE PHASE VELOCITY= 3261.9M/SEC.

SURFACE WAVE DECAY CONSTANTS

	REAL	IMAG
J=1	1.262E-01	-2.017E-02
J=2	4.801E-01	-1.164E-01
J=3	9.885E-01	-2.870E-02
J=4	1.667E+00	-3.657E-02

PARTICLE DISPLACEMENT AMPLITUDE COEFFICIENTS

X COMPONENT

J=1	1.000E+00	0.
J=2	-6.025E-01	1.830E-02
J=3	1.387E-01	-1.765E-01
J=4	-3.694E+00	-6.472E+00

Y COMPONENT

J=1	1.179E+01	-6.881E+00
J=2	3.257E-01	1.654E-01
J=3	-6.861E-02	-1.551E-01
J=4	-6.433E-01	5.897E-01

Z COMPONENT

J=1	-6.095E+00	2.971E+00
J=2	3.487E+00	4.203E-01
J=3	4.036E-01	-1.124E-02
J=4	-5.101E-01	-5.120E-02

ELECTRIC POTENTIAL

J=1	4.077E+10	-1.020E+10
J=2	-1.237E+10	4.695E+08
J=3	-6.893E+10	-3.375E+09
J=4	4.051E+10	1.313E+10

PARTICLE DISPLACEMENT AMPLITUDES AT SURFACE

X COMPONENT =-3.158E+00   -6.630E+00
Y COMPONENT = 1.140E+01   -6.281E+00
Z COMPONENT =-2.715E+00   3.329E+00
ELECTRIC POT=-1.144E+07   2.692E+07

PARTICLE DISPLACEMENT AMPLITUDES AT SURFACE
                ABSOLUTE VALUES
X COMPONENT = 7.344E+00
Y COMPONENT = 1.302E+01
Z COMPONENT = 4.296E+00
ELECTRIC POT= 2.925E+07

APPENDIX III.

THE ORTHOGONALITY OF SURFACE NORMAL MODES

Problem Statement

The context in which this problem arises is detailed in section 7.3, case 3. Figure A3.1 establishes the coordinate notation to be used in this derivation - it should be noted that the present notation differs from that shown in Figures 7.2, 7.3 and 7.5 of the main text.

Two surface acoustic modes, m and n, whose wave vectors are $\underset{\sim}{\beta}_m$ and $\underset{\sim}{\beta}_n$, are propagating on an elastically isotropic medium, so that $|\underset{\sim}{\beta}_m| = |\underset{\sim}{\beta}_n|$. The components of these wave vectors, resolved parallel to the periodic boundaries, must be integral multiples of $2\pi/L$, where L is the length of a side of the periodicity square. In the particular case under consideration, the components of the wave vectors of modes m and n, resolved parallel to x_1, differ by a non-zero multiple of $2\pi/L$;

i.e. $\qquad (\beta_{mx_1} - \beta_{nx_1}) = n2\pi/L \qquad n \neq 0$

The wave vector components of these modes resolved parallel to x_3, do not so differ. When the medium is isotropic, the only way in which this situation can arise is that depicted in Figure A3.1 - β_{mx_1} and β_{nx_1} are equal in magnitude, but oppositely directed, while β_{mx_3} and β_{nx_3} are identical in both magnitude and direction.

In order to establish an orthogonality relation for modes m and n it is necessary to prove that

$$\int_{S_1} (-T_m \cdot v_n^* - T_n^* \cdot v_m) \cdot dS_1 = 0 \qquad (A3.001)$$

where the surface S_1 consists of S_a and S_b, the periodic boundary surfaces parallel to x_3 and x_1, respectively, and normal to the propagation surface.
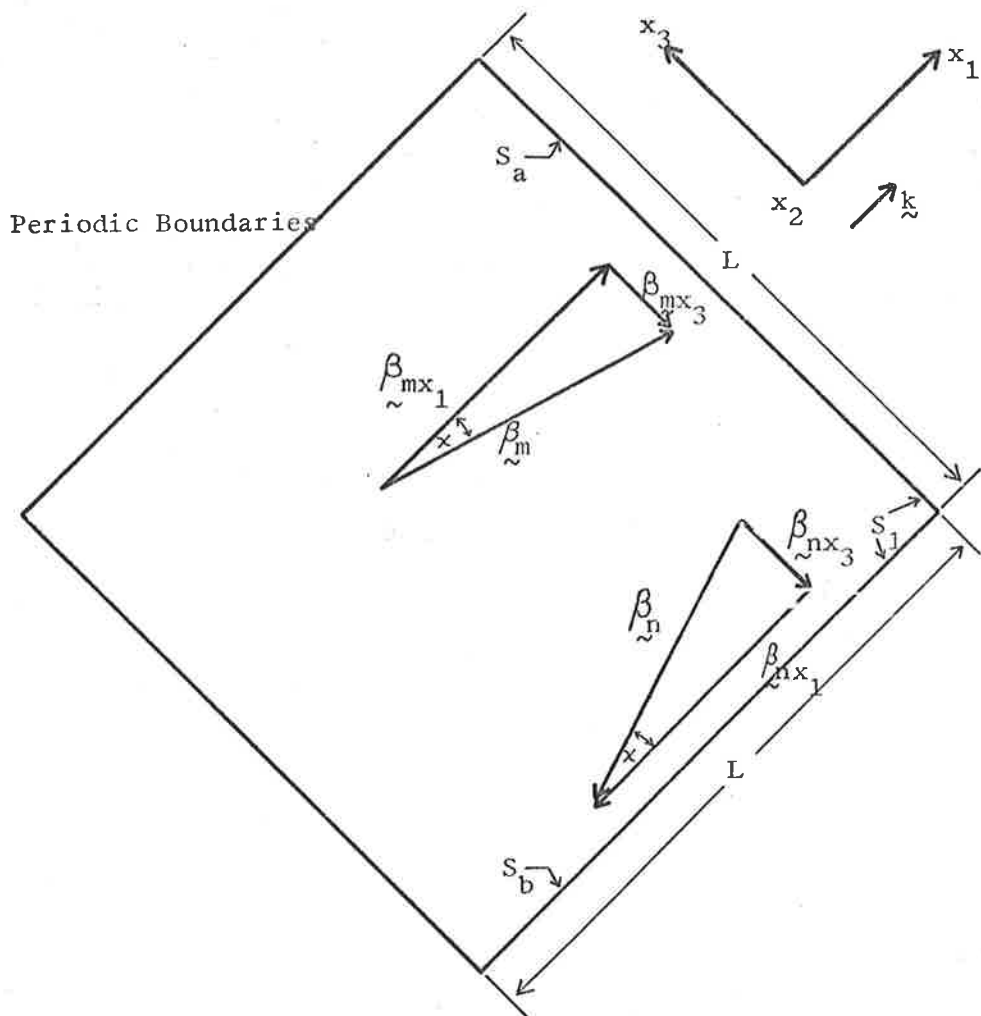
Figure A3.1

Wave vectors of normal surface modes in orthogonality

derivations.

Case 3: Modes m and n differ in only one wave vector

component by a non-zero multiple of $2\pi/L$.

(Isotropic medium assumed).

Proof.

Terms of the integrand of the expression (A3.001) have an

$\exp\left[j(\beta_{nx_1} - \beta_{mx_1})x_1\right]$ variation, which provides a spatial dependence

of the form $\exp\left[j\,2\pi\,nx_1/L\right]$, and thus determines that

$$\int_{S_b} (-\underset{\approx}{T}_m \cdot \underset{\sim}{v}_n^* - \underset{\approx}{T}_n^* \cdot \underset{\sim}{v}_m) \cdot dS_b = 0 \qquad\qquad \text{(A3.002)}$$

But the same terms also have an $\exp\left[j\,(\beta_{nx_3} - \beta_{mx_3})x_3\right]$ variation,

which exhibits no spatial dependence upon the x_3 coordinate, so that

no correspondingly simple deduction of the result for $\int_{S_a}$ can be made.

To complete a proof of the orthogonality relation for modes m and n,

it remains to show that

$$\int_{S_a} (-\underset{\approx}{T}_m \cdot \underset{\sim}{v}_n^* - \underset{\approx}{T}_n^* \cdot \underset{\sim}{v}_m) \cdot \underset{\sim}{k}\, dS_a = 0$$

where $\underset{\sim}{k}$ is a unit vector along the x_1 coordinate axis.

The first term of the integrand can be expanded as $\qquad$ (A3.003)

$$\underset{\sim}{k}^T \underset{\approx}{T}_m \underset{\sim}{v}_n^* = \left[T_{11}\right]_m \left[v_1^*\right]_n + \left[T_{12}\right]_m \left[v_2^*\right]_n + \left[T_{13}\right]_m \left[v_3^*\right]_n$$

where the stress components, T_{ij}, and velocity components, v_i, are those

of modes m and n referred to the x_i coordinate system; i.e. not to the

propagation coordinate system for each mode. Once again the square

brackets and mode number subscripts are used to denote field quantities

due to the various modes.

The first task then is to determine expressions for the stress

components, T_{11}, T_{12}, T_{13}, and the velocity components v_1, v_2, v_3, in

the x_i coordinate system, of a surface acoustic wave propagating at

an angle χ to the x_1 coordinate axis, on the surface $x_2 = 0$ (refer

Figure A3.1).

. A propagation coordinate system $x_i{}'$, in which the stress components, $T_{ij}{}'$, and velocity components, $v_i{}'$, are known through the equations of section 3.1, is introduced. As sketched in Figure A3.2, the $x_i{}'$ coordinate system is rotated an angle X, about the x_2 axis, from the x_i coordinate system. The required stress and velocity components can be calculated through the usual tensor transformations

$$T_{ij} = a_{ki} \, a_{1j} \, T_{kl}{}'$$

and

$$v_i = a_{ki} \, v_k{}'$$

(A3.004)

where

$$a_{ki} = \begin{bmatrix} \cos X & 0 & -\sin X \\ 0 & 1 & 0 \\ \sin X & 0 & \cos X \end{bmatrix}$$

These transformations determine that

$$T_{11} = T_{11}{}' \cos^2 X + 2T_{13}{}' \cos X \sin X + T_{33}{}' \sin^2 X$$

$$T_{12} = T_{12}{}' \cos X + T_{32}{}' \sin X$$

(A3.005)

$$T_{13} = -T_{11}{}' \cos X \sin X + T_{13}{}' (\cos^2 X - \sin^2 X) + T_{33}{}' \sin X \cos X$$

and

$$v_1 = v_1{}' \cos X - v_3{}' \sin X$$

$$v_2 = v_2{}'$$

(A3.006)

$$v_3 = v_1{}' \sin X + v_3{}' \cos X$$

By simple direct substitution from equations (3.151) and (3.152) into (3.122) and finally into (3.121), it can be shown that a surface acoustic wave propagating in the $x_1{}'$ direction on the isotropic surface $x_2{}' = 0$ has the following properties;
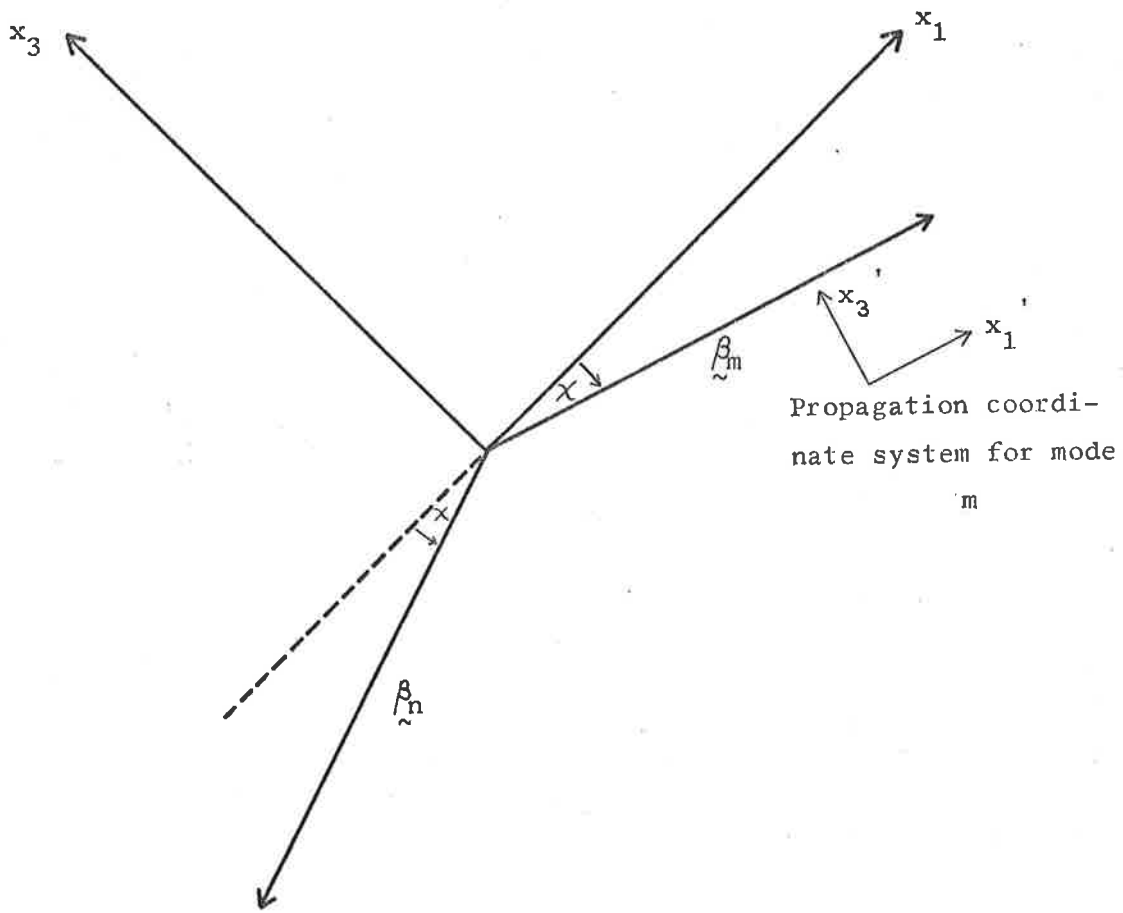
Figure A3.2

Coordinate notation for surface normal mode ortho-
gonality derivation (case 3).

$$. 1. \quad v_3{}' = T_{13}{}' = T_{23}{}' = 0$$

$$2. \quad T_{11}{}' \text{ and } T_{33}{}' \text{ are in phase with } v_1{}'. \qquad (A3.007)$$

$$3. \quad T_{12}{}' \text{ is in phase with } v_2{}'.$$

When coupled with property 1 above, the field expansions (A3.005) and

(A3.006) allow (A3.003) to be written in the form

$$
\underset{\sim}{k}^T \underset{\approx}{T}_m \underset{\sim}{v}_n^* = \left[v_1^* \cos \chi \right]_n \left[T_{11} \cos^2\chi + T_{33} \sin^2\chi \right]_m
$$

$$
+ \left[v_2^* \right]_n \left[T_{12} \cos \chi \right]_m
$$

$$
\qquad\qquad\qquad (A3.008)
$$

$$
+ \left[v_1^* \sin \chi \right]_n \left[-T_{11} \cos\chi \sin\chi + T_{33} \cos\chi \sin\chi \right]_m
$$

where the primes have been removed from the field quantities on the

right hand side of the relationship, but these are assumed to be

calculated in the $x_i{}'$ propagation coordinate system.

Figure A3.1 indicates that

$$
\left[\chi \right]_n = 180° - \left[\chi \right]_m
$$

so that

$$
\left[\cos\chi \right]_n = - \left[\cos\chi \right]_m = -\cos\chi
$$

$$
\qquad\qquad\qquad (A3.009)
$$

$$
\text{and} \quad \left[\sin\chi \right]_n = \left[\sin\chi \right]_m = \sin\chi
$$

These results allow equation (A3.008) to be rearranged as

$$
\underset{\sim}{k}^T \underset{\approx}{T}_m \underset{\sim}{v}_n^* = - \left[v_1^* \right]_n \cos\chi \left\{ \left[T_{11} \right]_m \cos^2\chi + \left[T_{33} \right]_m \sin^2\chi \right\}
$$

$$
+ \left[v_2^* \right]_n \left[T_{12} \right]_m \cos\chi
$$

$$
+ \left[v_1^* \right]_n \sin^2\chi \cos\chi \left\{ - \left[T_{11} \right]_m + \left[T_{33} \right]_m \right\} \qquad (A3.010)
$$

Through equations (A3.005), (A3.006) and (A3.007) the second term

in the integrand of equation (A3.002) can be expanded to obtain

$$\underset{\sim}{k}^T \underset{\approx}{T}_n^* \underset{\sim}{v}_m = \left[v_1\right]_m \cos\chi \left\{\left[T_{11}^*\right]_n \cos^2\chi + \left[T_{33}^*\right]_n \sin^2\chi\right\}$$

$$- \left[v_2\right]_m \left[T_{12}^*\right]_n \cos\chi$$

$$+ \left[v_1\right]_m \sin^2\chi\cos\chi \left\{\left[T_{11}^*\right]_n - \left[T_{33}^*\right]_n\right\} \quad \text{(A3.011)}$$

where the results of (A3.009) have been used to simplify the expression.

Modes m and n have identical acoustic fields when the medium

is elastically isotropic, so that

$$\left[T_{pq}\right]_m = \left[T_{pq}\right]_n$$

and

$$\left[v_p\right]_m = \left[v_p\right]_n$$

In particular, mode numbers m and n can be interchanged in equation

(A3.011). Furthermore, because of the phase relationships, outlined

in (A3.007), which pertain in isotropic surface acoustic wave propaga-

tion, the right hand side of equation (A3.011) is real, and therefore

its complex conjugate can be taken without invalidating the equation.

Hence interchanging mode numbers m and n in equation (A3.011),

and taking the complex conjugate of the right hand side shows, when

coupled with equation (A3.010), that

$$\underset{\sim}{k}^T \underset{\approx}{T}_m \underset{\sim}{v}_n^* + \underset{\sim}{k}^T \underset{\approx}{T}_n^* \underset{\sim}{v}_m = 0 \quad \text{(A3.012)}$$

from which can be deduced the required result that

$$\int_{S_a} \left(-\underset{\approx}{T}_m \cdot \underset{\sim}{v}_n^* - \underset{\approx}{T}_n^* \cdot \underset{\sim}{v}_m\right).d\underset{\sim}{S}_a = 0$$

Q.E.D.

REFERENCES

1. RAYLEIGH, LORD, "On Waves Propagated along the Plane Surface of
        an Elastic Solid", Proc. London Math. Soc., vol. 17,
        1885, pp. 4-11.

2. SEZAWA, K., "Dispersion of Elastic Waves Propagated on the Sur-
        face of Stratified Bodies and on Curved Surfaces",
        Bull. Earthquake Res. Inst. Tokyo, vol. 3, 1927, pp.1-18.

3. BREKHOVSKIKH, L.M., "Surface Waves Confined to the Curvature of
        the Boundary in Solids", Soviet Physics - Acoustics,
        vol. 13, no. 4, April-June 1968, pp. 462-472.

4. EWING, W.M., JARDETZKY, W.S. and PRESS, F., "Elastic Waves in
        Layered Media", McGraw-Hill, New York, 1957, Chapts. 1,
        2,4,5,7.

5. COOK, E.G. and van VALKENBURG, H.E., "Surface Waves at Ultrasonic
        Frequencies", A.S.T.M. Bulletin, May 1954, pp. 81-84.

6. CARLIN, B., "Ultrasonics", McGraw-Hill, 1960, 2nd Edition,
        Chapt. 8.

7. VIKTOROV, I.A., "Investigation of Methods for Exciting Rayleigh
        Waves", Soviet Physics - Acoustics, vol. 7, no. 3, Jan.-
        March 1962, pp. 236-244.

8. STONELEY, R., "The Propagation of Surface Elastic Waves in a
        Cubic Crystal", Proc. Roy. Soc. (London), vol. A232,
        1955, pp. 447-458.

9. GOLD, L., "Rayleigh Wave Propagation on Anisotropic (Cubic)
        Media", Phys. Rev., vol. 104, no. 6, Dec. 1956, pp. 1532
        -1536.

10. GAZIS, D.C., HERMAN, R. and WALLIS, R.F., "Surface Elastic Waves
        in Cubic Crystals", Phys. Rev., vol. 119, no.2, July
        1960, pp. 533-544.

11. BUCHWALD, V.T., "Rayleigh Waves in Anisotropic Media", Quart.
        Jrnl. Mech. Appl. Math., vol. 14, pt. 4, 1961, pp. 461-
        469.

12. BUCHWALD, V.T. and DAVIS, A., "Surface Waves in Elastic Media
        with Cubic Symmetry", Quart. Jrnl. Mech. Appl. Math.,
        vol. 16, pt. 3, Aug. 1963, pp. 283-294.

13.. WHITE, D.L., "The Depletion Layer Transducer", I.R.E. Trans. Ultrasonics Eng., vol. UE-9, July 1962, pp. 21-27.

14. FOSTER, N.F., "Cadmium Sulphide Diffusion-Layer Transducers", I.E.E.E. Trans. Ultrasonics Eng., vol UE-10, July 1963, pp. 39-44.

15. FOSTER, N.F., "Ultra-High Frequency Cadmium Sulphide Transducers", I.E.E.E. Trans. Sonics and Ultrasonics, vol. SU-11, Nov. 1964, pp. 63-68.

16. BROCKELSBY, C.F., PALFREEMAN, J.S. and GIBSON, R.W., "Ultrasonic Delay Lines", London: Iliffe, 1963.

17. OLSON, F.A., YAEGER, J.R. and WILSON, R.A., "Generation and Attenuation of Microwave Phonons in Lowest-Loss Dielectric Crystals", Proc. 5th Intl. Conf. Acoustics, Liege 1965, paper D67.

18. LAMB, J., REDWOOD, M. and SHTEINSHLEIFER, Z., "Absorption of Compressional Waves in Solids from 100 to 1000 Mc/s", Phys. Rev. Lett., vol. 3, no. 1, July 1959, pp. 28-29.

19. SPENCER, E.G. et al., "Microwave Elastic Properties of Non-magnetic Garnets", Jrnl. Appl. Phys., vol. 34, no. 10, Oct. 1963, pp. 3059-3060.

20. SPENCER, E.G., LENZO, P.V. and NASSAU, K., "Elastic Wave Propagation in Lithium Niobate", Appl. Phys. Lett., vol. 7, no. 3, Aug. 1965, pp. 67-69.

21. WHITE, R.M. and VOLTMER, F.W., "Direct Piezoelectric Coupling to Surface Elastic Waves", Appl. Phys. Lett., vol. 7, no. 12, Dec. 1965, pp. 314-316.

22. TSENG, C.C., "Propagation and Amplification of Surface Elastic Waves on Hexagonal Piezoelectric Crystals", Ph. D. Dissertation, University of California, Berkeley, 1966.

23. TSENG, C.C., "Elastic Surface Waves on Free and Metallised Surface of CdS, ZnO and PZT-4", Jrnl. Appl. Phys., vol. 38, no. 11, Oct. 1967, pp. 4281-4284.

24. COQUIN, G.A. and TIERSTEN, H.F., "Analysis of the Excitation and Detection of Piezoelectric Surface Waves on Quartz by means of Surface Electrodes", J.A.S.A., vol. 41, no. 4, pt. 2, 1967, pp. 921-939.

25. CAMPBELL, J.J. and JONES, W.R., "A Method for Estimating Optimal Crystal Cuts and Propagation Directions for Excitation of Piezoelectric Surface Waves", I.E.E.E. Trans. Sonics and Ultrasonics, vol. SU-15, no. 4, Oct. 1968, pp. 209-217.

26. TANCRELL, R.H. and HOLLAND, M.G., "Acoustic Surface Wave Filters", Proc. I.E.E.E., vol. 59, no. 3, March 1971, pp. 393-401.

27. MITCHELL, R.F., PRATT, R.G., SINGLETON, J.S. and WILLIS, W., "Surface Wave Filters", Mullard Tech. Communication, vol.11, no. 108, Nov. 1970, pp. 179-180.

28. COSTANZA, S.T., HAGON, P.J. and MacNEVIN, L.A., "Analog Matched Filter using Tapped Acoustic Surface Wave Delay Line", I.E.E.E. Trans. Microwave Theory Tech. (Correspondence), vol. MTT-17, no. 11, Nov. 1969, pp. 1042-1043.

29. SQUIRE, W.D., WHITEHOUSE, H.J. and ALSUP, J.M., "Linear Signal Processing and Ultrasonic Transversal Filters", I.E.E.E. Trans. Microwave Theory Tech., vol. MTT-17, no. 11, Nov. 1969, pp. 1020-1040.

30. ADKINS, L.R. and HUGHES, A.J., "Long Delay Lines employing Surface Acoustic Wave Guidance", Jrnl. Appl. Phys., vol. 42, no. 5, April 1971, pp. 1819-1822.

31. LEWIS, M.F. and PATTERSON, E., "Novel Helical-Path Surface Wave Delay Line", Appl. Phys. Lett., vol. 18, no. 4, Feb. 1971, pp. 143-145.

32. BOND, W.L., REEDER, T.M. and SHAW, H.J., "Wrap-Around Surface-Wave Delay Lines", Electronics Lett., vol. 7, no. 3, Feb. 1971, pp. 79-80.

33. CHO, F.Y., HUNSINGER, W.J. and LAWSON, R.L., "Surface Waves Circulating on Piezoelectric Substrates", Appl. Phys. Lett., vol. 18, no. 7, April 1971, pp. 298-301.

34. • SABINE, H. and COLE, P.H., "Acoustic Surface Wave Devices: A Survey", Proc. I.R.E.E. (Aust), vol. 32, no. 12, Dec. 1971, pp. 445-458.

35. LAKIN, K.M. and COLLINS, J.H., "100 MHz Surface Acousto-electric Amplifier Exhibiting Stable Terminal Gain with DC Drift Field", Proc. I.E.E.E., vol. 57, no. 4, April 1969, pp. 740-742.

36. LAKIN, K.M. and SHAW, H.J., "Surface Wave Delay Line Amplifiers", I.E.E.E. Trans. Microwave Theory and Tech., vol. MTT-17, no. 11, Nov. 1969, pp. 912-920.

37. REEDER, T.M., SHAW, H.J. and WESTBROOK, E.M., "Noise and Saturation Characteristics of the Separated Medium Rayleigh Wave Amplifier", Paper H-8, I.E.E.E. Ultrasonics Symposium, San Francisco, Oct. 1970.

38. COLDREN, L.A. and KINO, G.S., "Monolithic Acoustic Surface-Wave Amplifier", Appl. Phys. Lett., vol. 18, no. 8, April 1971, pp. 317-319.

39. LEAN, E.G.H., POWELL, C.G. and KUHN, L., "Acoustic Surface Wave Mixing on $\propto$-Quartz", Appl. Phys. Lett., vol. 15, no. 1, July 1969, pp.10-12.

40. SLOBODNIK, A.J., "Nonlinear Effects in Microwave Acoustic $LiNbO_3$ Surface-Wave Delay Lines", J.A.S.A., vol. 48, no. 1, pt. 2, July 1970, pp. 203-210.

41. LUUKKALA, M. and KINO, G.S., "Convolution and Time Inversion using Parametric Interactions of Acoustic Surface Waves", Appl. Phys. Lett., vol. 18, no. 9, May 1971, pp. 393-394.

42. WHITE, R.M., "Surface Elastic Wave Propagation and Amplification", I.E.E.E. Trans. on Electron Devices, vol. ED-14, no. 4, April 1967, pp. 181-189.

43. BROERS, A.N., LEAN, E.G. and HATZAKIS, M., "1.75 GHz Acoustic-Surface-Wave Transducer Fabrication by an Electron Beam", Appl. Phys. Lett., vol. 15, no. 3, Aug. 1969, pp. 98-101.

44. • LEAN, E.G. and BROERS, A.N., "2·5GHz Interdigital Wave Trans-
ducers Fabricated by an Electron Beam", I.E.E.E.
Ultrasonics Symposium, St. Louis, Sept. 1969.

45. CARR, P.H., "The Generation and Propagation of Acoustic Surface
Waves at Microwave Frequencies", I.E.E.E. Trans. Micro-
wave Theory Tech., vol. MTT-17, no. 11, Nov. 1969,
pp. 845-855.

46. ARMSTRONG, D.B., "Solid State Surface Acoustic Delay Lines",
Litton Industries Research Dept., Technical Note
TN70-1, Jan. 1970.

47. ASH, E.A. and MORGAN, D.P., "Realization of Microwave Circuit
Functions using Acoustic Surface Waves", Electronics
Lett., vol. 3, no. 10, Oct. 1967, pp. 462-463.

48. ASH, E.A., De La RUE, R.M. and HUMPHRYES, R.F., "Microsound
Surface Waveguides", I.E.E.E. Trans. Microwave Theory
Tech., vol. MTT-17, no. 11, Nov. 1969, pp. 882-892.

49. TIERSTEN, H.F., "Elastic Surface Waves Guided by Thin Films",
Jrnl. Appl. Phys., vol. 40, no. 2, Feb. 1969, pp. 770-
789.

50. ADKINS, L.R. and HUGHES, A.J., "Elastic Surface Waves Guided by
Thin Films: Gold on Fused Quartz", I.E.E.E. Trans.
Microwave Theory Tech., vol. MTT-17, no. 11, Nov. 1969,
pp. 904-911.

51. ADKINS, L.R. and HUGHES, A.J., "Investigations of Surface Acoustic
Wave Directional Couplers", I.E.E.E. Trans. Sonics and
Ultrasonics, vol. SU-19, no. 1, Jan. 1972, pp.45-58.

52. KNOX, R.M. and van den HEUVEL, A.P., "Elastic Surface Wave
Circuits at Microwave Frequencies", Paper presented at
I.E.E. and I.E.E.E. European Microwave Conference,
London, England, Sept. 1969.

53. BURKE, B.E., "An Electronically Variable Surface Acoustic Wave
Phase Shifter", Paper IV-4, 1971 I.E.E.E. International
Microwave Symposium, Washington, May 1971.

54. . VIKTOROV, I.A. and KAEKINA, T.M., "The Scattering of Ultrasonic
        Rayleigh Waves at Models of Surface Defects", Soviet
        Physics-Acoustics, vol. 10, no. 1, July-Sept. 1964,
        pp. 25-27.

55. ASH, E.A., "Realization of Microwave Circuit Functions Using
        Acoustic Waves", Paper 8-1, 1967 G-MTT Intl. Microwave
        Symposium, Boston, Mass., May 1967.

56. BREKHOVSKIKH, L.M., "Propagation of Surface Rayleigh Waves along
        the Uneven Boundary of an Elastic Body", Soviet Physics-
        Acoustics, vol. 5, no. 3, 1959, pp. 288-295.

57. BYKOV, N.S. and SHNEIDER, Y.G., "Experimental Study of the Effect
        of Surface Quality on the Damping of Surface Waves",
        Soviet Physics - Acoustics, vol. 6, no. 4, Oct.-Dec.,
        1960, pp. 500-502.

58. BYKOV, N.S. and SHNEIDER, Y.G., "Burnishing of the Surface of
        an Acoustic Line and its Effect on Surface Wave Attenua-
        tion", Soviet Physics - Acoustics, vol. 8, no. 2, April-
        June, 1962, p. 186.

59. RISCHBIETER, F., "Messungen an Oberflächenwellen in Festen
        Körpern ", Acustica, vol. 16, no. 2, 1965/66, pp. 75-83.

60. SABINE, H., "Communication Applications of Surface Acoustic Waves.
        Scattering from Surface Roughness", Tech. Report 2-69,
        Dept. Elect. Eng., University of Adelaide, June 1969.

61. SABINE, H. and COLE, P.H., "Communications Applications of
        Surface Acoustic Waves", Tech. Report 1-68, Dept. Elect.
        Eng., University of Adelaide, Nov. 1968.

62. HUMPHRYES, R.F. and ASH, E.A., "Acoustic-Bulk-Surface-Wave Trans-
        ducer", Electronics Lett., vol. 5, no. 9, May 1969,
        pp. 175-176.

63. SABINE, P.V.H., "Rayleigh Wave Propagation on a Periodically
        Roughened Surface", Electronics Lett., vol. 6, no. 6,
        March 1970, pp. 149-151.

64. BRAGG, W.H. and BRAGG, W.L., "X-rays and Crystal Structure",
        Bell & Sons, 1915, pp. 15-17.

65. • LIM, T.C. and FARNELL, G.W., "Search for Forbidden Directions of Elastic Surface Wave Propagation in Anisotropic Crystals", Jrnl. Appl. Phys., vol. 39, no. 9, Aug.1968, pp. 4319-4325.

66. FARNELL, G.W. and LIM, T.C., "Character of Pseudo Surface Waves on Anisotropic Crystals", J.A.S.A., vol. 45, no. 4, April 1969, pp. 845-851.

67. SLOBODNIK, A.J. and CONWAY, E.D., "Microwave Acoustics Handbook, Volume I: Surface Wave Velocities", Physical Sciences Research Paper No. 414, USAF Cambridge Res. Labs., Bedford, Mass., March 1970.

68. SLOBODNIK, A.J. and SZABO, T.L., "Design Data for Microwave Acoustic Surface Wave Devices", Paper presented at I.E.E.E-GMTT Intl. Microwave Symposium, Washington, May 1971.

69. SLOBODNIK, A.J., "A Laser Probe for Microwave Acoustic Surface Wave Investigations", Report no. AFCRL-70-0404, Air Force Cambridge Research Labs., Bedford, Mass., July 1970.

70. SMITH, W.R. et al., "Analysis of Interdigital Surface Wave Transducers by use of an Equivalent Circuit Model", I.E.E.E. Trans. Microwave Theory Tech., vol. MTT-17, no. 11, Nov. 1969, pp. 856-864.

71. SMITH, W.R. et al., "Design of Surface Wave Delay Lines with Interdigital Transducers", I.E.E.E. Trans. Microwave Theory Tech., vol. MTT-17, no. 11, Nov. 1969, pp. 865-873.

72. AULD, B.A. and KINO, G.S., "Normal Mode Theory for Acoustic Waves and its Application to the Interdigital Transducer", I.E.E.E. Trans. Electron Devices, vol. ED-18, no. 10, Oct. 1971, pp. 898-908.

73. DE KLERK, J., "Ultrasonic Transducers - Surface Wave Transducers" Ultrasonics, vol. 9, no. 1, Jan. 1971, pp. 35-48.

74. SOKOLNIKOFF, I.S., "Mathematical Theory of Elasticity", McGraw-Hill, (2nd Edn), New York, 1956, Chapts. I, III.

75. • REDWOOD, M., "Mechanical Waveguides", Pergamon, Oxford, 1960.

76. BERGMANN, L., "Der Ultraschall", Zurich, Hirzel, 5th Ed., 1949, p. 405.

77. "Standards on Piezoelectric Crystals, 1949", Proc. I.R.E, vol. 37, Dec. 1949, pp. 1378-1395.

78. SABINE, H., "Communication Applications of Surface Acoustic Waves. Microsonic Components on Anisotropic, Piezoelectric Surfaces", Tech. Report 2-70, Dept. Elect. Eng., University of Adelaide, Nov. 1970.

79. SABINE, H., "Surface Wave Propagation in Anisotropic Media. Program Listings for Numerical Solution", Supplement to Tech. Report 2-70, Dept. Elect. Eng., University of Adelaide, Nov. 1970.

80. SABINE, H. and COLE, P.H., "Design Data for Anisotropic Surface Acoustic Wave Devices", Paper presented at Conference of Institution of Engineers, Aust., on "Materials for the Electrical and Electronics Industries", Perth, W.A., Aug. 1971.

81. ENGAN H., INGEBRIGTSEN, K.A. and TONNING, A., "Elastic Surface Waves in α - Quartz: Observation of Leaky Surface Waves", Appl. Phys. Lett., vol. 10, no. 11, June 1967, pp. 311-313.

82. DERESIEWICZ, H. and MINDLIN, R.D., "Waves on the Surface of a Crystal", Jrnl. Appl. Phys., vol. 28, no. 6, June 1957, pp. 669-671.

83. SCHULZ, M.B., MATSINGER, B.J. and HOLLAND, M.G., "Temperature Dependence of Surface Acoustic Wave Velocity on α - Quartz" Jrnl. Appl. Phys., vol. 41, no. 7, June 1970, pp. 2755-2765.

84. WEGLEIN, R.D., PEDINOFF, M.E., and WINSTON, H., "Diffraction Spreading of Surface Waves on $LiNbO_3$", Electronics Lett., vol. 6, no. 20, Oct. 1970, pp. 654-656.

85. BOND, W.L., "Notes on Solution of Problems in Odd Job Vapor Coating", Jrnl. Optical Soc. Am., vol. 44, no. 6, June 1954, pp. 429-438.

86. COLLINS, J.H. and HAGON, P.J., "Applying Surface Wave Acoustics", Electronics, vol. 42, no. 23, Nov. 1969, pp. 97-103.

87. BODE, H.W., "Network Analysis and Feedback Amplifier Design", Van Nostrand, New York, 1945, sect. 16.3.

88. FANO, R.M., "Theoretical Limitations on the Broadband Matching of Arbitrary Impedances", Jrnl. Franklin Institute, vol. 249, Jan.-Feb. 1950, pp. 51-84 and 139-154.

89. MASON, W.P., "Physical Acoustics", Academic Press, New York, vol. 1, pt. A, 1964, Chapts. 3,5.

90. THURSTON, R.N., "Effect of Electrical and Mechanical Terminating Resistances on Loss and Bandwidth according to the Conventional Equivalent Circuit of a Piezoelectric Transducer", I.R.E. Trans. Ultrasonic Eng., vol. UE-7, no. 1, Feb. 1960, pp. 16-25.

91. CROFUT, W., "Broadband Microwave Acoustic Delay Lines", Microwave Jnl., vol. 10, no. 2, Jan. 1967, pp. 65-72.

92. REEDER, T.M. and WINSLOW,D., "Characteristics of Microwave Acoustic Transducers for Volume Wave Excitation", I.E.E.E. Trans. Microwave Theory Tech., vol. MTT-17, no. 11, Nov. 1969. pp. 927-941.

93. JONES, W.S., HARTMANN, C.S. and HARRIS, J.L., "Matching Optimisation to Interdigital Surface Wave Devices", Electronics Lett., vol. 6, no. 11, May 1970, pp. 333-335.

94. ENGAN, H., "Interdigital Electrode Transducers for the Excitation of Elastic Surface Waves in Piezoelectric Media", Electronics Research Lab., Norwegian Institute of Technology, Trondheim, Norway, Elab Report TE-91, Sept. 1967.

95. EASTMAN, D.E., "An Ultrasonic Study of Magnetoelastic and Anelastic Properties of Yttrium Iron Garnet", Ph. D. Dissertation, Mass. Inst. Technology, Aug. 1965.

96. SCHULZ, M.B. and HOLLAND, M.G., "Surface Acoustic Wave Delay Lines with Small Temperature Coefficient", Proc. I.E.E.E., vol. 58, no. 9, Sept. 1970, pp. 1361-1362.

97. MASON, W.P., "Physical Acoustics", Academic Press, New York,
        vol. 3, pt. B, 1965, pp. 77-90.

98. KINO, G.S., Microwave Laboratory, W.W. Hansen Laboratories of
        Physics, Stanford University, Stanford, California. -
        Private Communication.

99. VIKTOROV, I.A., "Reflection of Ultrasonic Lamb and Rayleigh
        Waves by a Rectangular End Section of a Plate", Soviet
        Physics - Acoustics, vol. 13, no. 1, July-Sept. 1967,
        pp. 107-108.

100. VIKTOROV, I.A., "Rayleigh and Lamb Waves", Plenum, New York,
        1967.

101. GLOERSEN, P.G., "Guiding and Reflection of Surface Elastic Waves",
        M.Sc. Thesis, University of California, Berkeley, 1969.

102. DAVIES, L.W., A.W.A. Physical Laboratory, Rydalmere, N.S.W.,
        Aust. - Private Communication.

103. COLLIN, R.E., "Foundations for Microwave Engineering", McGraw-
        Hill, New York, 1966, pps. 56-59, 121-124, 170-176,
        183-185.

104. FANO, R.M., CHU, L.J. and ADLER, R.B., "Electromagnetic Fields,
        Energy and Forces", Wiley, New York, 1960, pp. 365-373.

105. RAMO, S., WHINNERY, J.R. and van DUZER, T., "Fields and Waves
        in Communication Electronics", Wiley, New York, 1960,
        pp. 589-590.

106. AULD, B.A., "Application of Microwave Concepts to the Theory of
        Acoustic Fields and Waves in Solids", I.E.E.E. Trans.
        Microwave Theory Tech., vol. MTT-17, no. 11, Nov. 1969,
        pp. 800-811.

107. WALDRON, R.A., "Perturbation Formulas for Elastic Resonators and
        Waveguides", I.E.E.E. Trans. Sonics and Ultrasonics,
        vol. SU-18, no. 1, Jan. 1971, pp. 16-20.

108. AULD, B.A., "Surface Wave Theory", Invited Proceedings of 1970
        I.E.E.E. Ultrasonics Symposium, (L.W. Kessler Ed.),
        I.E.E.E., New York, 1971, pp. 1-15.

109. KINO, G.S. and REEDER, T.M., "A Normal Mode Theory for the Rayleigh Wave Amplifier", I.E.E.E. Trans. Electron Devices, vol. ED-18, no. 10, Oct. 1971, pp. 909-920.

110. SKEIE, H., "Electrical and Mechanical Loading of a Piezoelectric Surface Supporting Surface Waves", J.A.S.A., vol. 48, no. 5, pt. 2, May 1970, pp. 1098-1109. Comments and Corrections: J.A.S.A., vol. 50, no. 1, pt. 2, July 1971, pp. 383-384.

111. BERTONI, H.L., "Piezoelectric Rayleigh Wave Excitation by Bulk Wave Scattering", I.E.E.E. Trans. Microwave Theory Tech., vol. MTT-17, no. 11, Nov. 1969, pp. 873-882.

112. SABINE, H. and COLE, P.H., "Communication Applications of Surface Acoustic Waves. Analysis and Design of the Microsonic Crossbar Coupler", Tech. Report 1-72, Dept. Elect. Eng., University of Adelaide, Jan. 1972.

113. SABINE, H. and COLE, P.H., "Reciprocity Relations and Coupled Mode Theory Applied to Guided Microsonic Waves", Paper 20, R.R.B. Symposium on Microwaves, Adelaide, Feb. 1972.

114. OLINER, A.A., BERTONI, H.L. and LI, R.C.M., "Transmission Line Formalism for Guided Acoustic Waves and Variational Expressions for Acoustic Wave Discontinuities", Polytech. Inst. Brooklyn, Report No. R-452.

115. WYLIE, C.R., "Advanced Engineering Mathematics", McGraw-Hill, New York, 1960, pp. 502-505.

116. HAVLICE, J.F., BOND, W.L. and WIGTON, L.B., "Elastic Poynting Vector in a Piezoelectric Medium", I.E.E.E. Trans. Sonics and Ultrasonics, vol. SU-17, no. 4, Oct. 1970, pp. 246-249.

117. MESSIAH, A., "Quantum Mechanics", North Holland Publishing Co., Amsterdam, vol. 1, 1965, pp. 193, 243-292, vol. 2, 1966, pp. 685-689.

118. EISBERG, R.M., "Fundamentals of Modern Physics", Wiley, New York, 1961, pp. 220, 525-526.

119. COLLINS, J.H., GERARD, H.M., REEDER, T.M., and SHAW, H.J., "Unidirectional Surface Wave Transducer", Proc. I.E.E.E., vol. 57, no. 5, May 1969, pp. 833-835.

120. HARTMANN, C.S., JONES, W.S. and VOLLERS, H. "Wideband Unidirectional Interdigital Surface Wave Transducers", Technical Report TR-08-71-19, Texas Instruments, Dallas, Texas, March 1971.

121. MARSHALL, F.G., PAIGE, E.G.S. and YOUNG, A.S., "New Unidirectional Transducer and Broadband Reflector of Acoustic Surface Waves", Electronics Lett., vol. 7, no. 21, Oct. 1971, pp. 638-640.

122. ALSOP, L.E., GOODMAN, A.S. and ASH, E.A., "Surface Wave Dispersion in a Mass-Loaded Half-Space", J.A.S.A., vol. 50, no. 1, pt. 2, 1971, pp. 176-180.

123. van DUZER, T., "Lenses and Graded Films for Focussing and Guiding Acoustic Surface Waves", Proc. I.E.E.E., vol. 58, no. 8, Aug. 1970, pp. 1230-1237.

124. MORGAN, D.P. and ASH, E.A., "Acoustic -Surface-Wave Dispersive Delay Line", Proc. I.E.E., vol. 116, no. 7, July 1969, pp. 1125-1134.

125. TOLANSKY, S., "Surface Microtopography", Interscience Publishers, London, 1960.

126. SABINE, P.V.H., "Surface-Acoustic-Wave Reflectors", Electronics Lett., vol. 7, no. 22, Nov. 1971, pp. 653-654.

127. BUDREAU, A.J. and CARR, P.H., "Temperature Dependence of the Attenuation of Microwave Frequency Elastic Surface Waves in Quartz", Appl. Phys. Lett., vol. 18, no. 6, March 1971, pp. 239-241.

128. BEAMS, J.W., "Mechanical Properties of Thin Films of Gold and Silver", in 'Structure and Properties of Thin Films' C.A. Neugebauer, J.B. Newkirk and D.A. Vermilyen, Eds., Wiley, 1959.

129. BEAMS, J.W., BREAZEALE, J.B. and BART, W.L., "Mechanical Strength of Thin Films of Metals", Phys. Rev., vol. 100, no. 6, Dec. 1955, pp. 1657-1661.

130. NEUGEBAUER, C.A., "Tensile Properties of Thin, Evaporated Gold Films", Jrnl. Appl. Phys., vol. 31, no. 6, June 1960, pp. 1096-1101.

131. MAISSEL, L.I. and GLANG, R. (Eds.), "Handbook of Thin Film Technology", McGraw-Hill, New York, 1970, Chapts.11,12.

132. SKEIE, H., "Development and Evaluation of an Equivalent Circuit Model for Acoustic Surface Wave Transducers", Paper C6/4:1, Proc. 1971 European Microwave Conference, vol. 2, Stockholm, Aug. 1971.

133. KRIMHOLTZ, R. and MATTHAEI, G.L., "Amplification of Acoustic Surface Waves by means of a Broadband Hybrid-Junction Transducer and Negative-Resistance Circuits", Electronics Lett., vol. 7, no. 9, May 1971, pp. 233-235.

134. WHITE, R.M., "Surface Elastic Waves", Proc. I.E.E.E., vol. 58, no. 8, Aug. 1970, pp. 1238-1276.

135. MORGAN, D.P., "Directional Coupler Using Acoustic Surface Waves", Electronics Lett., vol. 7, no. 14, July 1971, pp. 412-413.

136. MARSHALL, F.G. and PAIGE, E.G.S., "Novel Acoustic-Surface-Wave Directional Coupler with Diverse Applications", Electronics Lett., vol. 7, no. 16, Aug. 1971, pp. 460-462.

137. MARSHALL, F.G. and PAIGE, E.G.S., "Observed Properties of an Acoustic-Surface-Wave Multistrip Coupler", Electronics Lett., vol. 7, no. 16, Aug. 1971, pp. 463-464.

138. MARSHALL, F.G., "Reflecting Trackchanger: New Acoustic-Surface-Wave Component for Folding Long Delay Lines onto Small Substrates", Electronics Lett., vol. 8, no. 1, Jan. 1972, pp. 8-9.

139. MAINES, J.D., MARSHALL, F.G., OLIVER, J.F.C. and PAIGE, E.G.S., "Frequency-Dependent Behaviour of an Acoustic-Surface-Wave Multistrip Coupler", Electronics Lett., vol. 8, no. 4, Feb. 1972, pp. 81-82.

140. MARSHALL, F.G., "New Technique for the Suppression of Triple-Transit Signals in Surface-Acoustic-Wave Delay Lines", Electronics Lett., vol. 8, no. 12, June 1972, pp. 311-312.

141. SCHULZ, M.B. and MATSINGER, J.H., "Rayleigh Wave Electromechan - ical Coupling Constants", Technical Memorandum T-908, Raytheon Company, Research Division, Jan. 1972.

142. TANCRELL, R.H., SCHULZ, M.B., BARRETT, H.H., DAVIS, L. and HOLLAND M.G., "Dispersive Delay Lines Using Ultrasonic Waves", Proc. I.E.E.E., vol. 57, no. 6, June 1969, pp. 1211-1213.

143. MORGAN, D.P., "Log-Periodic Transducers for Acoustic Surface Waves", Proc. I.E.E., vol. 119, no. 1, Jan. 1972, pp. 55-60.

144. MITCHELL, R.F., "Some New Materials for Ultrasonic Transducers", Ultrasonics, vol. 6, no. 2, April 1968, pp. 112-116.

145. AULD, B.A., WILSON, D.A., WINSLOW, D.K., and YOUNG, E., "Control of Acoustic Surface Waves with Photoconductive CdS Film", Appl. Phys. Lett., vol. 18, no. 8, April 1971, pp. 339-341.

146. OLINER, A.A., "Microwave Network Methods for Guided Elastic Waves", I.E.E.E. Trans. Microwave Theory and Tech., vol. MTT-17, no. 11, Nov. 1969, pp. 812-826.

147. KAJIMURA, K., INABA, R. and MIKOSHIBA, N., "Experimental Evi- dence for Elliptic Particle Motion Accompanied by Elastic Surface Waves", Appl. Phys. Lett., vol. 19, no. 6, Sept. 1971, pp. 182-184.

148. LAWRENCE, M.W. and DAVIES, L.W., "Surface Motion Measurements on Surface Elastic Waves", Appl. Phys. Lett., vol. 20, no. 8, April 1972, pp. 328-329.

149. DAVIES, L.W., A.W.A. Physical Laboratory, Rydalmere, N.S.W., Aust. - Private Communication.

150. van den HEUVEL, A.P., OWEN, D.B. and JOSHI, S.G., "The Hybrid Transducer", Paper C-8, I.E.E.E. Ultrasonics Symposium, St. Louis, Missouri, Sept. 1969.

151. HICKERNELL, F.S., SHULDA, G.F. and BREWER, J.W., "Zinc Oxide and Cadmium Sulphide Overlay Surface Wave Transducers", Paper G-11, I.E.E.E. Ultrasonics Symposium, San Fran- cisco, California, Oct. 1970.

152. SANDBANK, C.P. and BUTLER, M.B.N., "Acoustic Surface Waves on Isopaustic Glass", Electronics Lett., vol. 7, no. 17, Aug. 1971, pp. 499-501.

153. EVANS, D.R., LEWIS, M.F. and PATTERSON, E., "Sputtered ZnO Surface-Wave Transducers", Electronics Lett., vol. 7, no. 18, Sept. 1971, pp. 557-558.

154. SMITH, W.R., "Coupling Efficiency Estimates for Acoustic Surface Wave Excitation with Piezoelectric Film Overlays", Jrnl. Appl. Phys., vol. 42, no. 7, 1971, pp. 3016-3018.

155. SOLIE, L.P., "Piezoelectric Acoustic Surface Waves for a Film on Substrate", Appl. Phys. Lett., vol. 18, no. 4, Feb. 1971, pp. 111-112.

156. "Surface Acoustic Wave Tapped Delay Lines", Preliminary Data Sheet, Research and Technology Marketing Dept., Autonetics, Anaheim, California, Aug. 1971.

157. CARR, P.H., "Reduction of Reflections in Surface Wave Devices with Quarter-Wave Taps", Paper presented at I.E.E.E.-GMTT International Microwave Symposium, Chicago, Illinois, May 1972.

158. HARTEMANN, P. and DIEULESAINT, E., "Acoustic-Surface-Wave Filters", Electronics Lett., vol. 5, no. 25, Dec. 1969, pp. 657-658.

159. "Surface Acoustic Wave Bandpass Filters", Preliminary Data Sheet, Research and Technology Marketing Dept., Autonetics, Anaheim, California, Aug. 1971.

160. HARTEMANN, P., "Narrow-Bandwidth Rayleigh-Wave Filters", Electronics Lett., vol. 7, no. 22, Nov. 1971, pp. 674-675.

161. DeVRIES, A.J., ADLER, R., DIAS, J.F. and WOJCIK, T.J., "Realization of a 40MHz Colour Television IF Response using Surface Wave Transducers on Lead Zirconate Titanate", Paper G-5, I.E.E.E. Ultrasonics Symposium, St. Louis, Missouri, Sept. 1969.

162. CHAUVIN, D., COUSSOT, G. and DIEULESAINT, E., "Acoustic-Surface-Wave Television Filters", Electronics Letters, vol. 7, no. 17, Aug. 1971, pp. 491-492.

163., KHARUSI, M.S., TANCRELL, R.H. and WILLIAMSON, R.C., "Acoustic-Beam Profiles in Surface-Wave Filters", Electronics Lett., vol. 8, no. 9, May 1972, pp. 238-240.

164. GERARD, H.M., JUDD, G.W. and PEDINOFF, M.E., "Phase Corrections for Weighted Acoustic Surface-Wave Dispersive Filters", I.E.E.E. Trans. Microwave Theory Tech., vol. MTT-20, no. 2, Feb. 1972, pp. 188-192.

165. SITTIG, E.K. and COQUIN, G.A., "Filters and Dispersive Delay Lines Using Repetitively Mismatched Ultrasonic Transmission Lines", I.E.E.E. Trans. Sonics and Ultrasonics, vol. SU-15, no. 2, April 1968, pp. 111-119.

166. STERN, E., "Microsound Components, Circuits and Applications", I.E.E.E. Trans. Microwave Theory Tech., vol. MTT-17, no. 11, Nov. 1969, pp. 835-844.

167. VIKTOROV, I.A., "Rayleigh Waves in the Ultrasonic Range", Soviet Physics - Acoustics, vol. 8, no. 2, Oct.-Dec. 1962, pp. 118-129.

168. ADLER, R., KORPEL, A. and DESMARES, P., "An Instrument for Making Surface Waves Visible", I.E.E.E. Trans. Sonics and Ultrasonics, vol. SU-15, no. 3, July 1968, pp. 157-161.

169. PEDINOFF, M.E. and WALDNER, M., "Refraction and Reflection of Ultrasonic Surface Waves by Thin-Gold-Film Layers on Lithium Niobate Substrates", Electronics Lett., vol. 6, no. 17, Aug. 1970, pp. 533-534.

170. PEDINOFF, M.E., WALDNER, M. and JONES, W.R., "Refraction and Reflection of Surface Acoustic Waves at Boundaries of Layered Anisotropic Substrates: Gold on Lithium Niobate", Jrnl. Appl. Phys., vol. 42, no. 8, July 1971, pp. 3025-3034.

171. COLE, P.H. and BURGESS, A.S., Dept. Elect. Eng., University of Adelaide. - Private Communication.

LIST OF PUBLICATIONS.   P.V.H. SABINE.

1.   SABINE, H. and COLE, P.H., "Communication Applications of Surface
          Acoustic Waves," Elect. Eng. Trans., Institution of
          Engineers, Aust., vol. EE6, no. 1, March 1970, pp. 11-
          17.

2.   SABINE, H., "Rayleigh-wave Propagation on a Periodically Roughened
          Surface", Electron. Letts., vol. 6, no. 6, March 1970,
          pp. 149-151.

3.   SABINE, H. and COLE, P.H., "Surface Acoustic Waves in Communica-
          tion Engineering", Ultrasonics, vol. 9, no. 2, April
          1971, pp. 103-113.

4.   SABINE, H. and COLE, P.H., "Surface Acoustic Wave Devices: A
          Survey", Proc. I.R.E.E. Aust., vol. 32, no. 12, Dec.
          1971, pp. 445-458.

5.   SABINE, H., "Surface Acoustic Wave Reflectors", Electron. Letts.,
          vol. 7, no. 22, Nov. 1971, pp. 653-654.

Reprints of publications 2, 4 and 5, which relate most closely to
the subject matter of this thesis, are enclosed in the pocket attached
to the back cover.

TECHNICAL REPORTS.

The following technical reports have been submitted, in bound form,
to the A.P.O. Research Laboratories, Melbourne, Aust., in accordance
with Research Contract CO/35513.

1.   SABINE, H. and COLE, P.H., "Communication Applications of Surface
          Acoustic Waves", Tech. Report 1-68, Dept. Elect. Eng.,
          University of Adelaide, Nov. 1968.

2.   SABINE, H., "Communication Applications of Surface Acoustic Waves.
          Launching and Analysis Techniques", Tech. Report 1-69,
          Dept. Elect. Eng., University of Adelaide, March 1969.

3.   SABINE, H., "Communication Applications of Surface Acoustic Waves.
          Scattering from Surface Roughness", Tech. Report 2-69,
          Dept. Elect. Eng., University of Adelaide, June 1969.

4.   SABINE, H. and COLE, P.H., "Communication Applications of Surface
          Acoustic Waves. Acoustic Amplification", Tech. Report
          3-69, Dept. Elect. Eng., University of Adelaide, Nov.1969.

5. SABINE, H., "Communication Applications of Surface Acoustic Waves. Microsonic Components on Anisotropic, Piezoelectric Surfaces", Tech. Report 2-70, Dept. Elect. Eng., University of Adelaide, Nov. 1970.

6. SABINE, H., "Surface Wave Propagation in Anistropic Media. Programme Listings for Numerical Solution", Supplement to Tech. Report 2-70, Dept. Elect. Eng., University of Adelaide, Nov. 1970.

7. SABINE, H. and COLE, P.H., "Communication Applications of Surface Acoustic Waves. Analysis and Design of the Microsonic Crossbar Coupler", Tech. Report 1-72, Dept. Elect. Eng., University of Adelaide, Jan. 1972.

PAPERS READ AT ENGINEERING CONFERENCES.

1. SABINE, H. and COLE, P.H., "Communication Applications of Surface Acoustic Waves", presented at Conference of Inst. Engineers, Aust., on 'The Applications of Modern Science to Electrical and Electronics Engineering', Adelaide, June, 1969.

2. SABINE, H. and COLE, P.H., "Surface Acoustic Wave Devices: A Survey", presented at 13th National Radio and Electronics Engineering Convention, Melbourne, May 1971.

3. SABINE, H. and COLE, P.H., "Design Data for Anisotropic Surface Acoustic Wave Devices", presented at Conference of Inst. Engineers, Aust., on 'Materials for the Electrical and Electronics Industries', Perth, Aug. 1971.

4. SABINE, H. and COLE, P.H., "Materials for Surface Acoustic Wave Technology", presented at Conference of Inst. Engineers, Aust., on 'Materials for the Electrical and Electronics Industries', Perth, Aug. 1971.

5. SABINE, H. and COLE, P.H., "Reciprocity Relationships and Coupled Mode Theory Applied to Guided Microsonic Waves", presented at Radio Research Board Symposium on Microwaves, Adelaide, Feb. 1972.

Sabine, P. V. H. (1970). Rayleigh-wave propagation on a periodically roughened surface. *Electronics Letters, 6*(6), 149-151.

Sabine, P. V. H. (1971). Surface-acoustic-wave reflectors. *Electronics Letters, 7*(22), 653-654.

Sabine, P. V & Cole, P. H. (1971). Acoustic surface wave devices: a survey. *Proceedings I.R.E.E.* 445-458.